Investigation of Energy Storage Options for Thermal Management in Hybrid Electric Vehicles

By

NADER JAVANI

A Thesis Submitted in Partial Fulfillment
of the Requirements for the degree of Doctor of Philosophy
in
Mechanical Engineering

Faculty of Engineering and Applied Science
University of Ontario Institute of Technology

Oshawa, Ontario, Canada

© Nader Javani, 2013

Abstract

Fossil fuelled-dominant ground transportation faces heavy challenges due to ever increasing binding regulations on pollutants and carbon footprints. Electric and hybrid electric vehicles could have a significant role in future sustainable transport. Important issues in electric and hybrid electric vehicles are the energy and power density of battery packs, which directly affect the efficiency and driving range of the vehicle. When higher current is extracted from the Li-ion cells, heat is generated due to ohmic law. Therefore, it is vital to create a successful thermal management system to prevent temperature increase and temperature excursion in the battery pack beyond its specified operating range. In the current study, integration of a phase change material (PCM) in the cell and sub-module level is investigated in regard to thermal management. During the phase changing process, PCMs absorb heat and create a cooling effect. In the discharging solidification process, they release heat and create a heating effect. The first considered scenario is to use the phase change material in different thicknesses around the Li-ion cells integrated with the sub-module. Experimental study along with numerical results using the finite volume-based commercial software of ANSYS FLUENT 12.0.1 show that maximum temperature in the cell and temperature excursion in the sub-module are reduced when phase change material is applied. In addition, for the case when PCM is introduced in between the cells through the porous foam, up to a 7.7 K temperature decrease is observed in the sub-module compared with the case without phase change material. Phase change material with 12 mm thickness decreases the maximum temperature more than that of the case with 3, 6, 9 and 12 mm thicknesses (within 2.77 K to 3.04 K). Furthermore, the effect of phase change material on cell temperature is more pronounced when the cooling system is under transient conditions.

The second scenario is to design and optimize a shell and tube latent heat energy storage system to integrate with the active cooling system of the vehicle to decrease the cooling load. The length of the heat exchanger is defined as an objective function and optimized length and diameter of the latent heat storage system is obtained using the genetic algorithm method.

Energy and exergy analyses have been conducted in the next section of the thesis for a new cooling system of the vehicle, in which the passive latent heat storage thermal management system is integrated with the active refrigeration cycle. The exergy destruction rate and the exergy efficiency for each component of the system are calculated. In addition, the effects of

specific parameters such as PCM mass fraction, evaporator temperature, and compressor pressure ratio on the system performance are investigated. The findings of exergy analysis reveal that the heat exchangers have less exergy efficiencies as compared to other components. The overall exergy efficiency of the system with PCM presence is 31%, having the largest exergy destruction rate of 0.4 kW. In addition, a parametric study is carried out and the results show that an increase in PCM mass fraction results in an increase in exergy efficiency of the system, which is due to the decrease of compressor work. The studies in this section are carried out using EES software. Environmental impact assessment is also conducted and the results show that an increase in exergy efficiency of the cooling system reduces greenhouse gasses and also increases the sustainability of the system. In addition, a multi-objective optimization using the genetic algorithm is performed by incorporating two objective functions, namely exergy efficiency to be maximized and total cost rate of the system to be minimized. The multi-objective optimization shows that the maximum exergy efficiency of the system is 34.5% while the minimum total cost rate is 1.38 $/hr.

In order to improve the thermal conductivity of n-octadecane as the selected phase change material, carbon nano-tubes and graphene nano-platelets are introduced with different mass concentrations. Morphological structure of pure and technical grade PCMs mixed with nano-particles is studied through the transmission and reflection optic microscopic method. Results show that 6% concentration of carbon nano-tubes increases effective thermal conductivity of pure PCM four times that of technical grade phase change material. Furthermore, partial agglomeration of the nanoparticles is observed in the experiments.

Acknowledgements

I would like to express my deep and sincere gratitude to my supervisor Dr. Ibrahim Dincer and my co-supervisor Dr. Greg F. Naterer, for their support of my research and for supporting me thoroughout my studies.

My sincere appreciation and special thanks to Dr. Greg Rohrauer for providing me with the direction and help I needed to undertake this project. He was also very helpful with providing the test facilities and equipment. I have been extremely lucky to know Prof. Yilbas, whose consistent guidance, support, unparalleled knowledge, and encouragement helped me so much in accomplishing this thesis. I would like to extend my appreciation to my committee members for their valuable time in reading and providing their comments to improve the content of my thesis.

I would like to thank and acknowledge the Automotive Partnerships Canada and the Natural Sciences and Engineering Research Council of Canada (NSERC) for their financial support. In addition, I would like to thank General Motors of Canada for providing me the opportunity to work in their energy systems lab in the Canadian Regional Engineering Centre (CREC), Oshawa. My thanks extend to Jasmine Wang and Mike Kobylecky, who were helpful and supportive throughout the project. Furthermore, I acknowledge the Scientific and Technical Research Council of Turkey (TUBITAK), Dr. Evren Bayrmaoglu for providing crucial test results.

Moreover, I would like to offer my deepest thanks to Halil Sadi Hamut, for all his helps during my studies. Also, I must express my gratitude to Hassan Hajabdollahi, Pouria Ahmadi, Shahid Ahmed, Dr. Shahryar Rahnamayan, Mohammad Ali Khalvati, Hadi Ganjeyi, Stephen Petryana, Masoud Ramandi and Ahmet Ozbilen for their support throughout my research at the University.

Last but not least, I would like to thank my mother Roghayeh, my brothers Naser and Hadi, and my sister Bahareh Javani for their understanding and encouragement throughout my education. In the last months of my study, I lost my dearest friend—my father. I will never forget you and may your soul rest in peace.

Table of Contents

List of Tables

List of Figures

Nomenclature

A	area (m^2)
Cp	specific heat coefficient (J/kg K)
C	mass concentration (%)
D	diameter (m)
D_H	hydraulic diameter (m)
$\dot{E}x$	Exergy rate (W)
ex	specific exergy (kJ/kg)
f	friction factor
h	specific enthalpy (kJ/kg)
h_s	convective heat transfer coefficient (W/m^2 K)
I	current (A)
k	thermal conductivity of a cell (W/m K)
L	length scale (m), latent heat of fusion (J/kg)
$\dot{m}$	mass flow rate (kg/s)
n	number of electrons
N	number of copper tubes in heat exchanger
P	pressure (N/ m^2)
$\dot{q}$	heat generation rate (W/m^3)
R	resistance (Ω)
S	entropy (J/K)
t	time (s)
T	temperature (K)
U	open circuit potential (V)
V	cell potential (V)

Greek letters

β	coefficient of thermal expansion (1/ºC)
Ω	cooling effectiveness index
θ	Overall temperature coefficient
Δ	change or differences
δ	thickness (m)
ε	effectiveness
η	efficiency
η_o	finned heat transfer surface efficiency
μ	dynamic viscosity (kg/ms)
ρ	density (kg/m^3)
γ	specific heat ratio
ε	porosity, volumetric concentration
ρ	density (kg/m^3)
β	arbitrary variable
φ	dissipation function (m^2/s^3)

Subscripts

0	ambient

act	actual
b, bat	battery
$comp$	compressor
$cool$	coolant
$chil$	chiller
$comp$	compressor
cnt	carbon nanotube
$ctxv$	thermal expansion valve before chiller
$cond$	condenser
$crit$	critical
D	destruction
dis	discharge
e	exit
$elect$	electricity
en	energy
$etxv$	thermal expansion valve before evaporator
ex	exergy
$evap$	evaporator
f	final
g	gas
gen	generation
H	height
i, in	in
max	maximum
min	minimum
o, out	outside
P	product
pcm	phase change material
q	heat
ref	refrigerant
s	isentopic
St	Stefan number
sc	subcooling
sh	superheating
tot	total
w	work

Acronyms

ARC	Accelerating Rate Calorimetry
BEV	Battery Electric Vehicle
BTMS	Battery Thermal Management System
CENG	Compressed Expanded Natural Graphite
CFD	Computational Fluid Dynamics
CNT	Carbon nanotube
DOD	Depth of Discharge
DSC	Differential Scanning Calorimeter

EV	Electric Vehicle
FEV	Full Electric Vehicle
GHG	Greenhouse Gas
GA	Genetic Algorithm
HEV	Hybrid Electric Vehicle
HTF	Heat Transfer Fluid
ICE	Internal Combustion Engine
LCA	Life Cycle Analyses
LHTES	Latent Heat Thermal Energy Storage
LIB	Lithium-ion Battery
LMTD	Log Mean Temperature Difference
MP	Melting Point
OTR	Onset-of- Thermal Runaway
PCM	Phase Change Material
PDE	Partial Differential Equation
PHEV	Plug-in Hybrid Electric Vehicle
SOC	State Of Charge
TEM	Transmission Electron Microscopy
TGA	Thermal Gravimetric Analysis
TIM	Thermal Interface Material
TMS	Thermal Management System
UDF	User Defined Function

Chapter 1 Introduction

The importance of using a latent heat thermal energy storage system, as well as the motivations and objectives of this thesis are presented in this chapter. The role of energy and its effects on society are explained and the importance of the transportation sector on energy employment is discussed. In addition, this chapter sheds some light on the role of electric and hybrid electric vehicles. Motivations behind the current research, along with the scope, are explained.

1.1 Hybrid Electric Vehicles (HEVs) and Energy Aspects

The change in recent global average temperature cannot be justified only as a specific phenomenon of nature. Designs and modifications in industrial processes can leave an impact on the environment and lead to related issues [1-3]. This shows the deterministic effect of energy systems in the development of human society and its shift to sustainability. Ever-increasing evidence depicts the side effects of air pollution and its destructive impact on human health, ecology, and the environment. Therefore, any effort to recognize energy trends and effective parameters on production and consumption of energy will have a key role in the future of society. In the 1970s, three global events shaped the trend of energy usage, and the traditional perspective on energy changed in an irreversible way. First, the awareness of societies and relevant publications about the absolute global limit in exploiting non-renewable energy sources was increased. The second event was the oil crisis in 1973, which raised the price of oil and gas—people in Norway still remember the empty highways during the weekends, the result of a prohibition against the use of private vehicles. The third factor was the nuclear power debates in 1970s [4].

As a result, the search for renewable energies was initiated, and energy scenarios based on non-fossil fuels began in almost every country. The current global energy consumption pattern predicts that world energy consumption will increase by over 50% before 2030 [5]. Extending the use of global energy resources is the leading reason to make energy sustainability a global necessity, and the link to the broader concept of sustainability will affect most of the world's civilizations [6].

In the past century, fossil fuel consumption by internal combustion engine vehicles had a major contribution to the emission of various air pollutants. Life cycle studies of these vehicles reveal a wide range of impacts. Among the various industrial activities, on-road transportation has the biggest disruptive effect on the environment [7], therefore green electricity produced by solar cells, wave and wind energy could be applied to hybrid and electric vehicles, making potentially the greatest contribution to resolving air pollution problems. Power plant-based electricity generation has been shown not to have anywhere near the level of emissions or consumption of fossil fuels found in vehicular transportation [8]. Several major cities have planned to drastically reduce the number of cars to prevent air quality degradation. In the move towards clean vehicles, the development of electrically-driven vehicles is the top priority in reducing harmful exhaust gases and attaining a sustainable transport policy [9]. Introducing modifications to electric vehicles will create new opportunities for the transportation sector. Figure 1.1 shows the share of transportation in petroleum consumption in the US, and the high contribution of transportation systems [7].

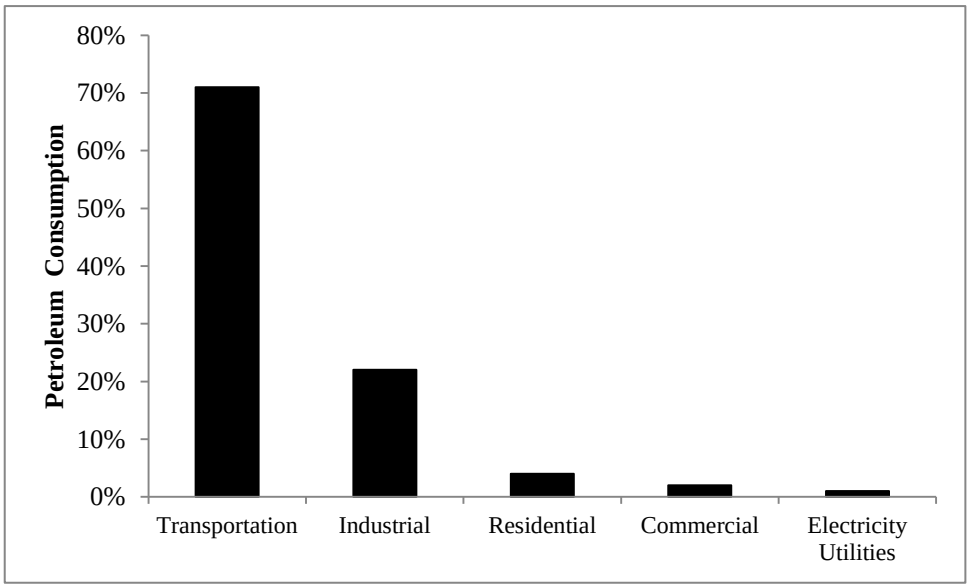

Figure 1.1 Petroleum consumption of end-use sector in U.S (adapted from [5]).

For many parts of the transportation sector, the proper use of energy will benefit total electrical and thermal energy storage [10]. Electric energy storage within batteries is a potential option. Complementary systems such as regenerative braking in HEVs can recover the energy that is dissipated and, in this way, make the vehicle more efficient. The main difference between

electric-powered and Internal Combustion Engine (ICE) cars, from the energy point of view, is the source of energy. While petroleum is a fossil-based energy source used in the ICE mode (apart from new developments like cold flame combustion for conventional vehicles), the exploited electricity that is stored in the battery packs in EV or HEVs can be produced either from power plants with fossil fuels or from renewable energy sources. The source from which the electricity is produced and used in electric and hybrid electric vehicles is the critical criterion in the further development of these vehicles. If the trend is to use more renewable energies to produce electricity, the environmental impacts of EVs and HEVs will be reduced. Furthermore, excessive amounts of greenhouse gasses (GHG) in the atmosphere are a result of conventional fossil fuelled-vehicle usage. It is worth mentioning that the transportation sector is the largest contributor to these gasses in the United States, with over a quarter of the total GHG emissions [11].

The main argument behind using the energy storage systems is the discrepancy between electricity production and high demand periods. Energy storage systems with different configurations such as thermo-chemical and mechanical can be utilized in off-peak power, load levelling, or to store renewable energies produced by temporal power sources such as wind turbines or photovoltaic plants. Electric energy storage systems can also store the energy produced by an ICE in hybrid vehicles or from the electrical grid and assist the propulsion system in transportation.

In conclusion, several studies in government and research centers show that the electrification of the transport sector is a key solution for power sector and transportation issue [12, 13]. A shift to Electric Vehicles (EV) and Hybrid Electric Vehicles (HEVs) can increase the efficiency of the vehicles and, subsequently, reduce energy (fuel) consumption. They can reduce CO_2 emission, which is a function of the carbon intensity of the charged electricity. In this way, they may help the growth of renewable energies, potentially drawing the required electricity from wind and solar energies as well as other non-fossil-based sources. Reduction of noise problems in urban regions and improvement of air quality will be achieved using this technology [13]. This is only possible by improving the battery pack performance, and thermal management is the first priority in achieving this goal. In the following sections, some of the main types of electric storage systems are introduced and briefly explained.

1.2 Motivation

The power and speed of a vehicle are not the only determining parameters anymore as they were in past decades. Nowadays, there are other criteria for auto making companies as well as customers in the production and selection of a vehicle. Increased considerations about fuel consumption and global climate disruption of vehicles have led to the rebirth of HEVs after an inert period in their history. Significant improvement can be obtained in HEVs by proper application of the energy storage systems. These vehicles, in all-electric range, can greatly reduce gasoline consumption. Vehicular transportation is responsible for 23% of global energy-related greenhouse gas emissions, and that contribution is increasing rapidly [14].

Despite recent progress in EV and HEV technology, they retain certain shortcomings, such as relatively long charging times, limited range, and lower efficiencies under extreme temperatures, which prevent the widespread commercialization of these vehicles. Among the shortcomings, the main difficulty comes from achieving ideal battery performance. To be able to encourage the shift towards HEVs and improve their efficiency, the battery pack should allow the vehicle to operate in a safe and economical manner. Li-ion batteries with higher energy and power density as electric energy storage systems are expected to be the power source of the next generation of HEVs. A target for different HEV configurations has been addressed by tje US Department of Energy (DOE) [12]. One of the main issues in battery packs is the high and uneven temperature distribution in the module and across the pack. Of all possible complications, high temperature has the most destructive effect on the performance of battery cells and modules, as it can lead to thermal runaway, capacity fading, limited driving range, and other safety issues. Thermal runaway in stressful conditions can decrease the life span of the battery pack, and creates the risk of fire and explosion. Smoldering of Li-ion batteries grounded Boeing's 787 Dreamliner airplanes, and federal aviation administration issued an emergency airworthiness directive (AD) to address a potential battery fire risk [15].

Major parameters need to be considered in thermal management systems of electric driven vehicles: battery pack maximum temperature, temperature gradients within the cells and modules for uniform temperature distribution, battery life, weight of the battery, compactness, safety, driving range, and cost. Moreover, thermal management systems (TMSs) are also responsible for preventing thermal runaway, which can have catastrophic outcomes. Temperature non-uniformity among the cells in the battery pack will lead to thermal runaway. A

number of thermal management systems have been developed based on battery characteristics, vehicle applications, drive cycle, size and weight limitations, and cost, along with environmental impact. These thermal management systems vary in their objectives (cooling vs. cooling and heating), method, (passive vs. active), heat transfer medium (air vs. liquid) and application (series vs. parallel or direct vs. indirect). Temperature also affects the discharge power in start-up and during acceleration, charge acceptance, and energy and life cycle of the battery, which are among the main characteristics of every battery pack. Most of the time, the objective of a thermal management system is to improve the system efficiency, decrease the investment in vehicle production and reduce the operating costs and corresponding environmental impacts. To achieve these goals, a systematic way is required to analyse these systems.

1.3 Scope of research and objectives

Despite the availability of EVs and HEVs and their ability to address issues related to fossil fuel-based transportation, there are still challenges that prevent their widespread commercialization. Among all of their components, the battery is the most significant stumbling block. Any improvement in the efficiency of the battery will directly affect the performance of EVs and HEVs, since the vehicle performance, range, cost and safety are highly linked to battery characteristics and efficiency. In order to access high power in EV/HEVs, more power must be extracted from the cell and, therefore, the battery pack. This means that higher current is required which, in turn, generates more heat (according to Ohm's Law). Therefore, the main issue is the temperature increase in the battery pack and non-uniform temperature distribution across the battery cells. This is why different TMSs have been created to tackle this problem. Without an effective TMS, the temperature in the interior parts of the battery pack will increase in a nonlinear fashion. This can lead to local hot spots and the onset of thermal runaway, which is a destructive process in the battery pack. Thus, a more effective TMS must be employed in order to limit the temperature range and non-uniformity in the battery packs and provide sufficient cooling into the cabin as well.

Currently, liquid TMSs are used for this purpose. Though these systems are more capable than passive or active air coiling TMS systems, they use the net power extracted from the battery, which leads to reduced driving range. Considering the type of heat transfer in battery thermal management (BTM) systems, the three options available are active, passive and phase

change material (PCM) cooling systems [16]. Active air and liquid systems have been used to remove the heat generated by the cells and modules in the pack and to regulate the operating temperature. For abusive operational conditions, such as high discharge rate in full load conditions and high ambient temperature, passive and even active air cooling systems cannot remove the heat sufficiently [17]. Active cooling systems impose the addition of further components into the system such as compressors, pumps and connections which make the system more complicated. By contrast, PCMs have the potential to absorb the heat generated in the cell as a thermal energy storage medium and keep the cell temperature almost constant during their phase change process, minimizing temperature excursion in the cells and battery pack.

In the current study, the effect of different parameters on cooling effectiveness in the passive thermal management of prismatic lithium-ion cells and sub-modules with PCMs are investigated. The goal is to integrate the passive PCM thermal energy storage system with electric energy storage systems in HEVs in order to remove the accumulated heat in the system and improve the overall efficiency of the vehicle, which directly affects the performance of the HEVs. Alternative configurations of the cooling systems and materials are also considered to analyze the efficiency of the energy storage systems.

In relation to direct use of PCM in contact with the battery pack, the Li-ion cells are investigated and, based on the different heat generation rates, maximum temperature in a steady-state condition is attained. PCM is applied around the cell. The reason for peripheral integration of PCM is the orthotropic behaviour of thermal conductivity of the cell. Considering the vehicle's available space, different thicknesses of the PCM layer around the cell are studied. The efficacy of PCM as a solution to the heating problem has been investigated by defining the cooling effectiveness in the cell. In the second step, the numerical simulation is extended to include the PCM around the battery pack itself. By defining a sub-module, which has different components, the PCM is applied all around the sub-module that represents the battery pack unit. In the third step, dry foams that are located between the cells are soaked with PCM and the simulation conditions for the heating problem are re-arranged accordingly. Once the battery pack (sub-module) generates heat, the PCM in the foam absorbs it and turns into liquid through the phase change process. This leads to a decrease in the overall temperature rise within the battery

pack unit and effectively manages the cooling process. The above mentioned studies are carried out using commercial Computational Fluid Dynamics (CFD) software, ANSYS FLUENT 12.0.1.

Experiments are carried out to examine the selected PCM's ability to be absorbed by different foams. After specifying the proper foam, the soaked foams are placed in between the cells in the sub-module and the cooling effect of the resulting system is measured. Furthermore, the proper PCM is placed in the shell side of a shell and tube heat exchanger. The latent heat thermal energy storage system is arranged to work in parallel with the available chiller in the cooling loop. Therefore, once the heat transfer fluid extracts the heat from the battery, part of the flow enters the storage system and charges the PCM as part of the TMS. To do this, a shell and tube heat exchanger has been designed and constructed with respect to the existing constraints. The genetic algorithm is used to optimize the length of the storage system as the objective function in the designing of the heat exchanger.

Considering the very low thermal conductivity of PCMs, the method of adding nanoparticles to the PCM has been introduced. In this way, the effective thermal conductivity becomes a function of the carbon nanotube (CNT) concentration and their arrangement in series or parallel. Two configurations of helical tubes and straight copper tubes are designed and optimized. Considering the manufacturing processes, the heat exchanger with optimum straight tubes is selected and manufactured to be integrated with the cooling cycle. The overall efficiency of the cooling cycle has been evaluated using exergy analysis and exergy destruction of each component has been calculated to give a big picture about the functionality of each main component. Total cost rate and exergy efficiencies are considered as objective functions in a multi-objective optimization method. Therefore, this thesis covers four main objectives along with their specific sub-objectives as follows:

a) To develop a model and introduce a relevant mathematical analysis for micro/macro scale integration of phase change material with Li-ion cells and the created sub-module.
b) To introduce, design and manufacture an optimized latent heat thermal energy storage system by selecting the proper PCM and nanoparticles for effective thermal management.
c) To conduct energy and exergy analysis of the vehicle’s thermal management loop with respect to the PCM tank and to carry out exergoeconomic analysis and multi-objective optimization of the system.

d) To establish a test bench to integrate the PCM and cells along with the sub-module to verify the simulation results. Furthermore, to conduct opto-image studies of the PCM and nanoparticle mixture such as transmission electron microscopy along with thermography tests.

The main objectives of this study involve the following tasks related to the mentioned objectives:

a) To develop a model and introduce a relevant mathematical analysis for micro/macro scale integration of phase change material with Li-ion cells and the created sub-module:
   - To develop a numerical model (CFD) to simulate a battery cooling system incorporating PCM.
   - To introduce a mathematical analysis for cooling effectiveness of cells and modules incorporating different configurations in a Li-ion cell that is to be used used in HEVs (prismatic cell), and to define the geometry of the model.
   - To model two-dimensional steady-state model and developing the model to three dimensional and transient model in using commercial finite-volume solver of ANSYS FLUENT 12.0.1.
   - To study and select a PCM and holding material (porous foam) with respect to melting temperature and operating conditions.
   - To analyse different thicknesses for the PCM around the cell and to compare the cooling effect in each case.
   - To consider a layout for a sub-module consisting of Li-ion cells, foam and cooling plate. The PCM is first introduced as a jacket around the sub-module surfaces.
   - To analyse temperature excursion along with maximum temperature in the sub-module and compare results with and without the PCM.
   - To apply the PCM in between the cells in the sub-module, and to analyse temperature distribution and thermal management assessment of the sub-module with and without the PCM.

b) To introduce, design and manufacture an optimized latent heat thermal energy storage system by selecting the proper PCM and additives:

- To design a proper heat exchanger to apply a PCM for thermal management purposes.
- To optimize the dimensions of the heat exchanger with respect to the available space in the vehicle.
- To manufacture the designed thermal storage unit for measurements.
- To study and apply a suitable thermal conductivity enhancement method. The new mixture of PCM and additive is considered as a designing criterion for the energy storage system. The optimization method is used to find the optimum design values.

c) To conduct energy and exergy analyses of vehicle thermal management systems with an integrated PCM storage unit:
   - To conduct thermodynamic analysis and to apply the energy and exergy method for assessment and improvement of the overall energy and exergy efficiency of the system.
   - To conduct exergoeconomic analysis and multi-objective optimization of the system to reduce the associated costs.
   - To conduct a parametric study to investigate the effect of coolant mass fraction passing through the PCM tank on cooling load, compressor work and related operating parameters.
   - To investigate the effect of the latent heat storage with the conventional thermal management system on overall efficiency of the system.
   - To conduct multi-objective optimizations in the system.
   - To conduct a transient exergy analysis in the heat exchanger.

d) To conduct experiments and set up the test bench for model validation and simulation assessment:
   - To establish a cell–level test setup and measure the temperature on the cell surface to obtain the transient response of the sub-module.
   - To validate the numerical model and initial testing of phase change material performance.

- To select the proper foam material based on thermal stability and governing conditions.
- To assemble a TMS test bench (based on Chevrolet Volt Gen 1) to find the most suitable location for the PCM tank.
- To study and select the proper additive to enhance the thermal conductivity of the PCM.
- To prepare PCM and CNT mixtures and study the improved thermal conductivity.
- To analyse the thermal characteristics of the PCM with the inclusion of CNTs and graphene nano-platelets via differential scanning calorimetry (DSC).
- To conduct opto-image analyses for different mixture samples of phase change materials.

1.4 Outline of the thesis

This thesis is organized in 7 chapters as described below. Following the current chapter, which highlights the motivation and objectives of the research, Chapter 2 introduces the concept of and different types of electrified vehicles. The causes of their failure in the beginning of the century, and the recent rebirth of EV/HEV technologies are presented. Battery technology and a comparison between the available batteries are carried out. The motivations behind the TMSs are explained along with available systems and methods. PCMs are introduced and categorized according to their characteristics and properties, which leads to the selection of a proper PCM for the current study. Different methods to increase the thermal conductivity of these materials are also explained. CNTs are introduced as a candidate for this purpose. Heat exchangers for phase changing heat transfer processes are explained and at the end the exergy concept and advantages of exergy analysis are covered.

Chapter 3 provides a literature review on the EV/HEV and battery technologies as well as their proposed TSMs. Heat exchangers are then reviewed and the effective properties of the PCM and nanoparticle mixtures are examined. A detailed study about the PCMs is followed by information on the exergy analyses conducted on various TMS applications along with key gaps on the current state of knowledge.

Chapter 4 establishes model development of three cases: simulation studies using computational fluid dynamics (CFD) and governing equations in mathematical modeling

.Thermal modeling of heat exchangers is introduced along with the optimization method used in designing the shell and tube heat exchangers. Exergy modelling and the main components in the system are covered in third part of this chapter.

Chapter 5 illustrates the experimental setup and instrumentation of the test bench. A brief description of tools and methods used to gather data as well as brief explanations of the output are provided.

Chapter 6 presents the numerical results based on ANSYS FLUENT 12.0.1 simulations. Different PCM application options are studied comparatively. Designing of the finned and bared copper tube heat exchanger with straight and helical configurations is explained. The effect of CNT configuration in the optimum length of the heat exchanger is presented in detail. The results of energy- and exergy-based analyses of the cooling system with EES software along with the PCM tank are illustrated in chapter 6.

Chapter 7 summarizes the conclusions and provides recommendations for future research.

Chapter 2 Background

Basic concepts and definitions for EVs and HEVs are presented in this chapter. The battery pack as the key element of an EV/HEV is explained, and thermal management necessity in the battery is emphasized. PCMs are the main focus of this study and so their basic concepts are introduced. Heat exchangers that are applied in thermal management of HEVs are also explained in the following chapter.

2.1 Electric and hybrid electric vehicles: Development and commercialization

The advent of EVs dates back to 1880, when the first vehicle was a tricycle. The years between 1890 and 1905 are called the golden age of EVs [4]. For example, in the 1893 World Exhibition in Chicago, 6 types of electric vehicles were shown, and in 1903, more than 4000 registered motor vehicles (about 20% of total cars) were EVs. Then, an inactive period spanning from the 1930s to the 1950s occurred, mainly due to the invention of the ICE. The early 1960s marked the re-birth of interest in EVs.

For the first time, major car producers in the world showed interest in the mass production of EVs. In the mid-1960s, General Motors started a development program for EV; around this time, the difficulties in developing electric cars, such as driving range, acceptable performance and cost were revealed. The oil crisis in 1973 and various other problems made the 1970s an active decade for electric car development. Due to competition, there was resistance in the development of EVs. The main obstacles were the dominance of conventional car producers on the market, along with the absence of suitable battery packs to compete with ICE vehicles. Some efforts to mass produce EVs in the UK and France failed(for a number of case studies from this period, refer to [4]). In the early 1980s, the focus was on EVs again, due to increasing concern over air pollution in big cities. In the early 1990s, California released its first zero-emission regulations, which provided some motivation for car producers to move toward sustainable transportation development.

Compared to conventional vehicles (CVs) with ICEs, conventional HEVs and PHEVs provide significant reduction in emissions while having competitive pricing due to government incentives, increasing oil prices, and high carbon taxes combined with low-carbon electricity

generation [18]. Briefly, the 1990s was the main decade in which most producers engaged in projects to develop electric and hybrid vehicles. Toyota launched its Prius model—a hybrid four-door sedan—to the Japanese market in 1997 and, in 1999, Toyota was the first car company to launch a hybrid vehicle to the North American market (Insight model). In 2003, the Honda Civic Hybrid became available. Most recently, General Motors introduced a new extended-range electric vehicle called the "Volt", which has been commercially available since fall of 2010.

Battery mass influences the design and application of the power source in EVs and HEVs. Usually, the capacity of a battery is nominal and reliable for a full charge state. In practice, it is not possible to deliver the full energy for the high repeating cycle of the battery. Different models of EVs are discussed here. EVs, also called electric drive vehicles, use one or more electric motors as the propulsion system. They appear in different models such as scooters, cars, buses, trains, boats, spacecraft, and other forms where power comes from electric motors. Major methods to provide an electrical energy source for EVs are as follows:

a) Full Electric Vehicles (FEV): on-board systems using rechargeable electricity storage systems. These on-board systems can store the power in the following forms:
    i) Energy stored in chemical form. Battery Electric Vehicles (BEV) as on-board storage with different types of battery;
    ii) Energy stored in capacitors in static form (electric fields);
    iii) Energy stored as kinetic energy in flywheels;
b) Electric vehicles with renewable sources: these types store energy from renewable sources, such as solar vehicles.
c) Direct-connected vehicles, normally in the form of buses and trains, which get energy continuously by wires connected to a ground source generator.
d) On-board systems using diesel motors to produce the electricity as the energy source. These types are suitable for heavy applications like locomotives, etc. because of the large weight and volume of diesel motors.
e) Fuel-cell vehicles as on-board systems, which produce electricity through a specific combination of fuel cells.
f) Nuclear energy-based electric propulsion systems, like nuclear submarines and other massive systems.

g) Hybrid vehicles: the power source to drive the vehicles can be more than one source, unlike in full electric vehicles (FEVs). For example, a hybrid vehicle can use internal combustion and compressed air as power sources. Hybrid Electric Vehicles (HEVs) use both an electric motor and a conventional ICE in combination to provide the power.
h) Plug-in hybrid vehicles refer to any kind of above mentioned EV that use an external electricity source like wall sockets to charge the batteries.

In HEVs, the driving power can be generated by the primary and secondary power sources. In general, the primary energy source is an ICE. The arrangement between the power sources can be in series, parallel or combined parallel/series configuration. In series HEV systems, the ICE provides the mechanical work by using fuel in the engine and drives a generator that produces the electricity, and through an electric traction motor, power is transferred to the wheels. Plug-in HEVs and power assisted HEVs are very similar in their components and operation, but in plug-in vehicles, it is possible to recharge larger energy storage systems from an off-board electric power source[19, 20]. In this configuration, the output of the heat engine is converted to electrical energy. The main advantage of this configuration is the ability to size the engine for average rather than peak energy needs and therefore have it operate in its most efficient zone. Moreover, the engine-generator set is easy to locate because of its relatively simplistic structure and the absence of clutches. When peak power is required, bigger batteries and motors are needed to satisfy this which, in turn, causes significant losses to occur due to energy conversion from mechanical to electrical and back to mechanical again.

In parallel HEV systems, both an ICE and electric energy storage systems produce mechanical energy to drive the vehicle. Series and parallel systems are used in HEVs. While braking, the motor acts as a generator and transforms the energy in the wheels into electrical energy, which is then stored in the batteries. These two power sources can be combined in order to propel the car, or they can be used independently so that the combustion engine can drive the wheels as in a conventional ICE vehicle where an auxiliary electric motor can boost its power. The parallel and series hybrid vehicle configurations can be seen in Figure 2.1.

When a parallel configuration (such as in Honda's Civic and Accord hybrids) operates, both the engine and motor provide torque to the wheels, which leads to much more power and

torque being delivered to the vehicle's transmission. Therefore, it is an electric-assisted conventional vehicle for attaining lower emissions and fuel consumption.

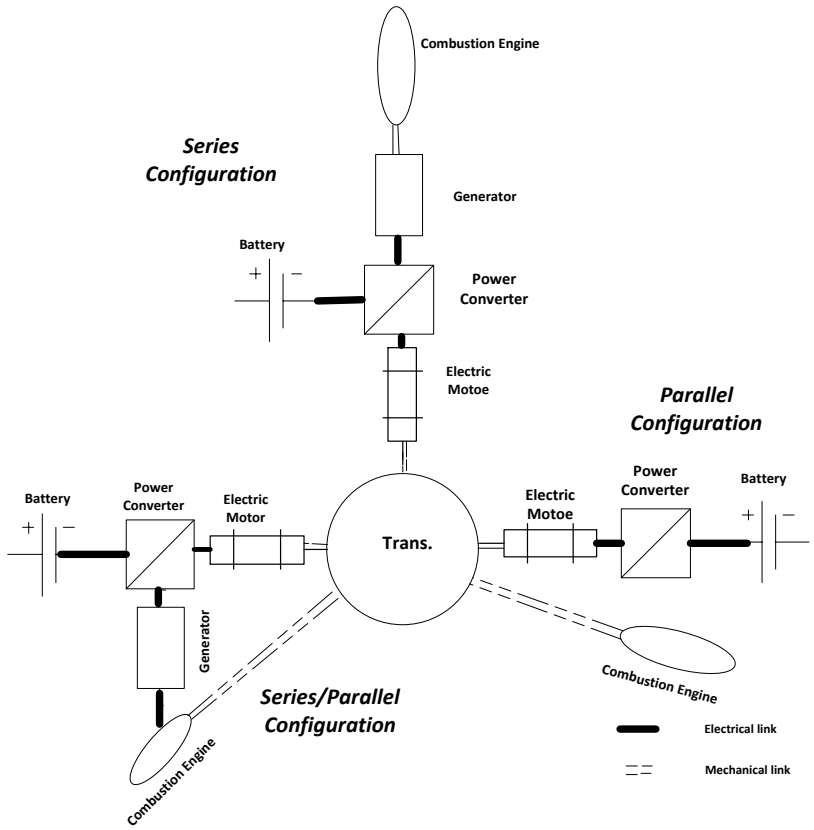

Figure 2.1 Hybrid vehicles configurations in series, parallel and series/parallel (adapted from [18]).

In case of excess demand beyond the engine's capability, the engine shaft provides power directly to the drive train where the battery is parallel to the engine. In a split parallel/series power train (such as in the Toyota Prius), a planetary gear system power split device is used along with a separate motor and generator in order to allow the engine to provide torque to the wheels and/or charge the battery through the generator. In this way, by using additional components, the benefits of both the parallel and series configurations can be attained [18, 20, 21]. However, the advantages of each configuration are solely based on the ambient conditions, drive style and length, electricity production mix, and overall cost.

In each cycle, EVs can have their full capacity withdrawn, where the batteries in HEVs have a capacity that operates around 10% of the nominal level which, in turn, is half the of state of charge (SOC). This operating range is required to prevent overcharging (beyond 75%) and deep discharge (below 25%) of the state of charge. This implies that only half of the battery capacity is being used in HEVs [22]. For this reason, after charging PHEVs through conventional electrical outlets, they operate in charge-depleting mode (CD-mode) as they drive until the battery is depleted to the target state of charge, which is generally around 35%. At this point, the vehicle switches to charge-sustaining mode (CS-mode) by utilizing the ICE to maintain the current SOC. Despite the recent progresses in EVs and HEVs in terms of performance and cost with much less environmental impact, their benefits depend mainly on the battery technology utilized in these vehicles. Thus, in order to understand the effects of EVs and HEVs, further analysis is needed for these battery technologies based on various criteria.

2.2 Battery technologies

Batteries are categorized into different types. In vehicle applications, there are specific constraints on choosing the proper battery. Energy density of the battery, for example, is one of the most important criteria. Regardless of the recent technological advancements in this area, there are still specific limits in the application of batteries that makes it difficult to meet all the requirements for vehicle applications. Therefore, a trade-off is necessary in order to derive an optimized solution from among the available technologies. Current battery technologies are evaluated based on their specific power and specific energy to provide sufficient amounts of both under various operating and ambient conditions. Furthermore, being compact, long lasting, low cost and environmentally friendly are other decision making parameters. Based on these assessment criteria, the battery technologies are evaluated. A battery with high specific energy and lower specific power will not meet the aforementioned criteria and cannot be used in HEV applications. This indicates that for vehicle application, only limited types of batteries such as Lead-acid, Ni-Cd, Ni-MH and Li-ion can be considered. Various performance characteristics based on the limitations of the chemical components of the batteries can be employed to investigate their technology. In the following section, characteristics of battery types are presented and the reasons behind choosing Li-ion batteries as the most promising technology in portable applications (such as full and hybrid EVs) are explained.

2.2.1 **Lead-acid batteries**

Lead-acid batteries have served for a century as a power supply in various fields of industry. They have been used in a sealed structure as Valve-Regulated Lead Acid batteries (VRLA) in certain commercial EVs. Among the secondary batteries, this is the oldest battery type with a known technology [12]. Lead and lead oxide are negative and positive electrodes respectively, with sulphuric acid as the electrolyte. Lead-acid batteries are cheaper than their competitors. The partial SOC problem in these electric storage systems is a limiting factor for a plug-in vehicle. In lead-acid batteries, the temperature rise is not as high as it is in Ni-MH and Li-ion batteries, and therefore thermal management is not very important in lead-acid battery packs [23]. Lead-acid batteries encounter serious problems such as their massive battery pack due to their low specific power capacity, which decreases the performance of the EV.

2.2.2 **Ni-Cd batteries**

Compared to lead-acid batteries, Ni-Cd batteries have relatively higher energy density, lower maintenance requirements and better cycle life. Their popularity was superseded heavily by the adverting of Ni-MH batteries. Interior cycle life, memory effect, energy density and toxicity of the cadmium in Ni-Cd compared to Ni-MH batteries were among the chief reasons. The endothermic nature of the discharge reaction in Ni-MH gave them a higher rate of capability along with high tolerance to over-discharge compared to Ni-Cd batteries. Cadmium is the main element in these batteries, which is a toxic component making their disposal environmentally challenging. [24]. On the other hand, the resources for cadmium, such as zinc ore—the main source of cadmium—are assumed to be limited. It is believed that extraction of resources for cadmium will peak by mid-century or earlier [25]. This makes Ni-Cd batteries more expensive than lead-acid batteries.

2.2.3 **Nickel metal hydride batteries**

The specific energy of these batteries is about 50 Wh/kg, which is not as high as those of Li-ion batteries; the main advantage is their high power density, which is about 1000 W/kg. They are similar to Ni-Cd batteries, where a metal hydride alloy has been replaced with anode metal for Ni-MH batteries. For the future of this type of electric energy storage system, the price is an issue, as the price of nickel is not expected to decrease in the near future based on the current

market trends. The other challenge for development of these batteries is competition between Ni-MH and Li-ion batteries, whereby progress with Li-ion technologies will have a larger effect on the trend of battery applications [12].

2.2.4 **Lithium based batteries**

Lithium-ion batteries (LIB) are one of the rechargeable battery types in which lithium ions move from the negative electrode (anode) to the positive electrode (cathode) during discharge, and back when charging. These batteries are produced in different types where four main categories are lithium metal, lithium metal polymer, lithium-ion polymer and lithium-ion batteries. The last one is the most common type [12]. Lithium-ion batteries are used in laptops, cellular phones and other electronic applications like EVs. Wide-range cycling requirements for batteries, especially for PHEVs, are a limiting factor for their proper operation. A number of challenges that prevent their widespread use in HEVs can be addressed as follows:

- Temperature range: low temperature decreases the conductivity of the cell and electrolyte so it cannot be lower than a minimum temperature. On the other hand, higher temperatures damage the cell. A narrow temperature band is an inherent feature in these types of batteries.
- Safety: issues like overcharging and over-discharging, mechanical stress and high temperature can cause specific problems [26].
- Calendar life: electric batteries are partly in use and most of the time they are in standby mode in HEVs so calendar life is important.
- Cost: the costs are relatively higher than other components and need to be decreased.

One of the main advantages of this type of energy storage system is their higher energy density. They have nearly 4 times higher energy density than lead-acid batteries. At normal ambient temperatures, Li-ion cells have very high performance. Their energy density is about 200 Wh/kg, which is among the highest. Because of the compactness and lightness of Li-ion batteries, they are considered as a potential candidate for EVs, regarding extended driving range, life-time and vehicle acceleration [27]. On the other hand, as will be discussed ahead, the compactness compromises effective heat removal and therefore safety issues should be under consideration for Li-ion batteries. These kinds of batteries are very sensitive to overcharging, more so than Ni-MH or other Li-ion polymer batteries. Higher cycle life and specific energy give Li-ion batteries

superiority over other kinds of batteries such as Ni-MH. As electrochemical systems, they are very dependent on temperature variations within the cell.

The increasing demands of energy storage systems, particularly for transportation applications such as PHEVs require continued research. Lithium-ion batteries are widely considered to be one of the most promising technologies in the coming decades, and many research and development activities are taking place to improve their performance. A report from the Global Industry Analysts (GIA) on the researchable battery markets predicts that the global market for rechargeable batteries is to reach US $16.4 billion by the year 2015 [16].

Huge interest has been generated due to nanotechnology applications. Graphite (which is currently used in electrodes) fails to fulfill the ever-increasing demand in this field. Inspired by high conductivity, flexibility, surface area, and Li-ion insertion ability, the best suitable material for next-generation energy storage devices is believed to be individual or composite nano carbon materials. Many of these CNT-based structures are considered the future replacement for current electrodes [28]. Lithium Metal Polymer (LMP) batteries are related to Li-ion batteries. Instead of a lithium intercalation anode, the metallic lithium is applied for anode material. It is predicted that the use of a metallic anode should improve the specific energy of the cell [29]. Lithium-Sulfur (Li-S) batteries are other types of lithium-based batteries where sulphur is paired with the carbon and have a sulfur cathode. Lithium-air (Li-air) uses lithium as anode material and air (oxygen) from the ambient air plays the role of a cathode. The Lithium-Sulfur and Lithium-air batteries have specific energy levels of 350 and 260 Wh/kg respectively, which are higher than the 150 Wh/kg of Li-ion batteries [30]. Because of their low specific energy and power, lead-acid batteries apply significant extra mass for EVs and HEVs. Ni-Cd batteries, on the other hand, have adequate specific power and good specific energy (still significantly larger than lead-acid batteries) and a reasonable low temperature performance [31]. Ni-Cd batteries were replaced with Ni-MH batteries because of their good power capability. At the same time, Ni-MH batteries have lower specific energy than Li-ion. Li-ion has the highest energy density among the compared batteries making it highly compatible with EVs and HEVs without significantly increasing the overall mass of the vehicle [32]. Comparisons among the batteries with respect to the criteria outlined above are provided in Table 2.1.

Table 2.1 Battery characteristics for today's most common battery technologies

Battery	Specific Energy (Wh/kg)	Specific Power (W/kg)	Operating Temp. Range (℃)	Cost ($/kWh)	Env. Impact (mPts)	Voltage (V)	Self-Discharge (%/month)	Number of cycles
Lead-Acid	20-40	80-300	-30 - 60	150	503	2.1	4-6	200
Ni-Cd	50-60	200-500	-40 - 70	400-500	544	1.2	10	2000
Ni-MH	40-70	500-1300	-20 - 50	400 – 500	491	1.2	20	>2500
Li-ion	100-130	800-3000	-20 - 55	500-800	278	~3.6	1-5	<2500

Data from [12, 33].

In order to compare the Li-ion and Ni-MH batteries, Table 2.1 gives specific data for these two promising formats [34]. The data is for a battery pack-level storage system where voltage is important. Because of higher voltage for Li-ion cells (3.6 V), it is observed that Li-ion cells act more efficient compared to Ni-MH batteries.

Figure 2.2 is another comparison between different types of batteries. Considering these data and the above mentioned characteristics, it is clear why EV and HEV manufacturers prefer Li-ion cells to other types.

Table 2.2 Comparing different types of battery packs for PHEVs

Battery Type	**Li-ion**	**Ni-MH**
No. of cells	102	280
Nominal voltage (V)	367	350
Energy Capacity (kWh)	15.1	14
Peak Power (kW)	100	80
Total system weight (kg)	180	352
Cooling medium	Liquid	Air

(Data adapted from [34]).

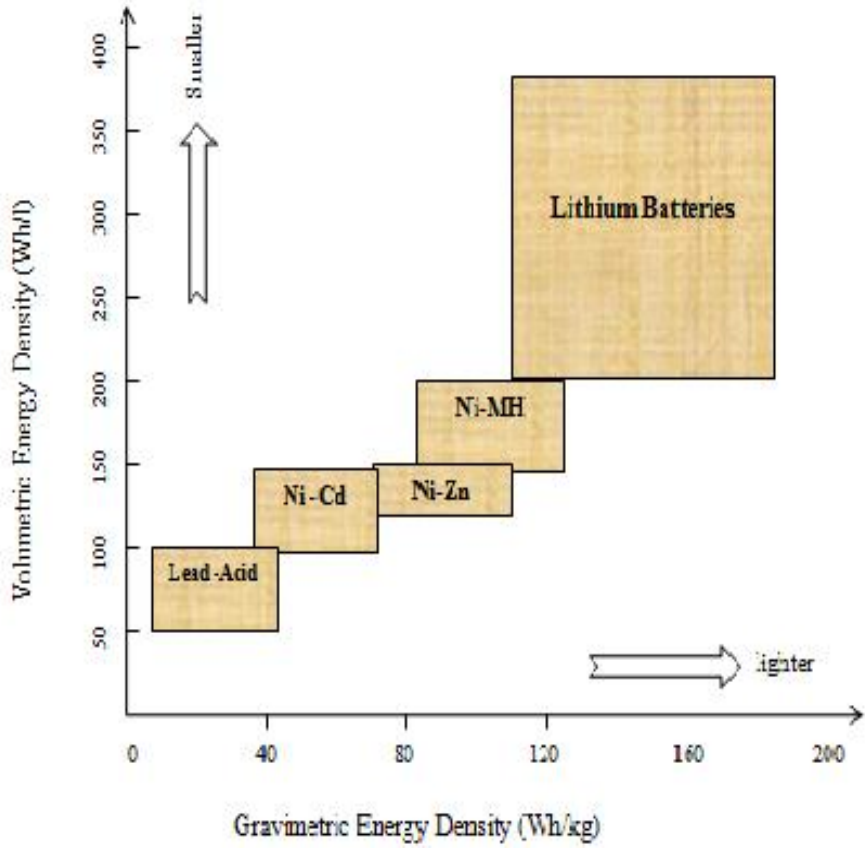

Figure 2.2 Comparing different types of energy storage systems (adapted from [35]).

2.3 Thermal management systems in EV/HEVs

Conventional TMSs that are used in EVs and HEVs can be categorized as active or passive systems, with the two primary active systems being:

- Active air cooling
- Liquid-cooling (active system)

PCMs can be considered a passive TMS. In passive air cooling, ambient air is used to ventilate the cells. Extra elements such as fans and manifolds will not be used. In active air cooling, a large area for the heat exchanger, higher temperature rise for air and parallel air distribution through manifolds for all modules are among the disadvantages when compared to liquid active cooling systems [20]. These two active systems have been developed in recent years. Disadvantages of these two systems are the complexity, bulkiness and high cost due to the

need to use fans and blowers for air cooling as well as pumps in liquid cooling, and pipes with other accessories impose parasitic power on the system [23]. Using PCMs can eliminate this parasitic power loss, which has been under investigation for various applications of thermal energy storage and TMSs. The other important parameter is initiation of Onset-of-Thermal Runaway (OTR), which produces very high heat and can fail the whole pack. When a PCM is used for cooling the battery pack, the temperature will be damped within the PCM and should not propagate to other cells.

The main steps for thermal management design are listed below[36]:

1. To define the objective of the Battery Thermal Management System (BTMS) and constraints. Specifications of the desired thermal performance are to be identified. (Safety requirements such as temperature limits for safe operation, packing requirements and ventilation of the pack if there are hazardous gases during the operation also need to be considered).
2. To estimate or calculate module/pack heat generation rate and heat capacity. Overall heat generation can be estimated or directly measured by experimental methods like calorimetry. Overall heat capacity of the module can also be determined.
3. To perform a first-order BTMS evaluation. Steady-state and transient responses of the module and battery pack to select the operating fluid as liquid (water) or air. Different flow models like parallel, series and their combinations will be assessed in this step.
4. To predict the module and battery pack behaviour. The heat transfer rate between the pack and environment is calculated by defining the overall thermal conductivity of the system and employed software.
5. To design a preliminary BTMS.
6. To build and test the BTMS. Based on the results in step 5, a prototype BTMS is built and then tested with respect to constraints and different conditions.
7. To optimize the BTMS.

A module is made by adding a number of cells to each other in series or parallel to meet power requirements. Similarly, these modules form the battery pack with the specified voltage and power. Since the cells are basic units in the structure of a battery pack and their performance is strongly related to temperature range, it is important to keep the battery pack temperature in a

safe range to avoid the thermal runaway and power fading of the system. Temperature affects the discharge rate of the pack and its cycle life, and can fade the capacity, energy, and power density.

When one of the interior cells fails because of a short circuit (or various other reasons), the total heat energy saved in that cell will flow to neighbouring cells in a short time. Local heat generation will increase drastically and the maximum temperature in the cell stack increases from the initial temperature up to 453 K, whereby hot spots extend to nearby locations and will lead to battery failure. Thermal runaway is a destructive phenomenon that is normally a result of abusive or stressful battery operation[37].

Parameters such as variations of temperature in different points of the pack, non-uniformity of distribution of impedance in the cells, heat transfer coefficient and differing efficiency between locations lead to temperature variations among the cells. This is not a favourable phenomenon [38]. Therefore, the main concern among other issues in thermal management of Li-ion battery packs is to avoid the large temperature rise in the battery pack or cell stack. PCMs can solve this problem and also transfer the heat propagation in the pack. The above research also states that using PCMs will lead to more uniform temperature profiles in various discharge rates. In order to meet the requirements for HEVs, the batteries should accommodate high electrical currents over many charging-discharging cycles.

The TMS utilizes the available and waste heat sources in order to minimize heat loss and increase efficiency. Future improvement of HEVs will revolve around better employment of heat sources and sinks to decrease the amount of net energy extracted from the high voltage battery pack. This will lead to longer battery pack life and extended drive range for HEV/EVs. By addressing the need to increase the energy density to electrify the vehicles, safety and long-term durability become significant issues due to potential overheating or thermal runaway under extreme conditions [39]. Therefore, a well-designed cooling system is very crucial in EVs/HEVs to control and cool down the battery pack and avoid these issues. Such a cooling system may be active or passive, which will be defined later.

Furthermore, effective TMSs in HEVs will not only prevent the safety issues, but can also improve the life span of the battery pack and vehicle. Li-ion battery cells are sensitive to higher temperatures such that for each degree of temperature rise in the range of 30-40℃, a decrease of about two months can occur in their life time [40]. In order to have a full life span,

the maximum cell temperature should not exceed 40℃ and the temperature excursion in the cell should be less than 5℃. The battery pack used in Chevy Volt HEV, which is studied in this thesis, employs 288 cells and can encounter thermal runaway and related issues. Therefore, a well-designed TMS is required. These systems are utilized to improve the battery efficiency by keeping the battery temperature within desired ranges. Thus, freezing and overheating of the electrochemical systems in the battery can be avoided, preventing reductions in power capability, charge/discharge capacity and premature aging of the battery [41, 42].

Different cooling loops are used in the Chevy Volt TMS. Even though the components and structure of these loops may vary from vehicle to vehicle, their purpose is usually the same; creating an efficient and robust system that is not adversely affected by internal and ambient temperature variations. The TMS of the Chevrolet Volt is comprised of various heat source and cooling loops. The cooling loops significantly affect the performance and energy consumption of the vehicle. TMSs in Chevy Volt consist of four different cycles to keep the associated components in their ideal temperate range in order to operate safely and efficiently. These cooling loops are listed as

- Power electronics cooling system
- High voltage battery cooling system
- Electric drive unit and lubricating system
- Cooling system and heater loop for engine

These four loops operate fully independently. A brief explanation of the battery loop cooling system will be presented later. Heat transfer fluid is a premixed solution of Dexcool coolant in the loops. For the electric drive cooling and lubrication system, the working fluid is Dexron VI. The water used in the cooling system should be deionized water in all hybrids and EVs. This will ensure high-voltage isolation and at the same time will prevent the internal corrosion of cooling system components. Figure 2.3 shows the radiator arrangement in the Chevy Volt. An overview of the loops is shown in Figure 2.4.

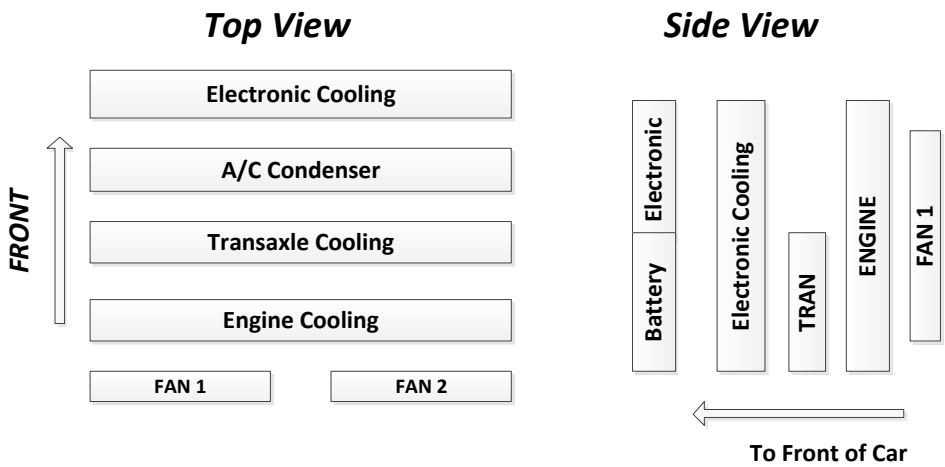

Figure 2.3 Sandwiched radiators for the cooling loops of Chevy Volt radiators [43].

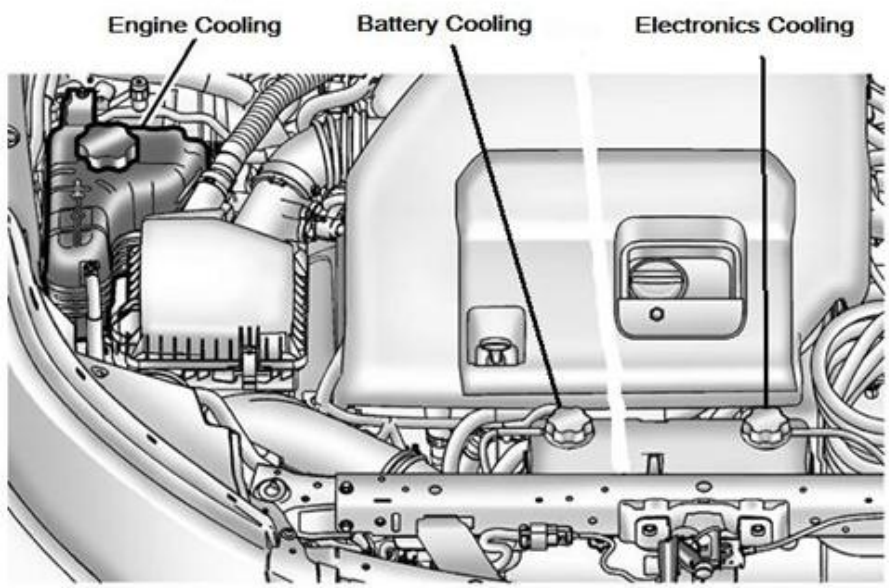

Figure 2.4 Under the hood view of the Chevy Volt [43].

2.3.1 **Battery cooling loop**

The 360 V Li-ion high voltage battery is a T-shaped pack that is positioned underneath the vehicle. A pair of quick-coupler fittings guides the coolant flows in and out of the battery. To make the coolant flow in between the cells inside the modules, thermal passages are placed in the battery housing. Heating or cooling is carried out by this thermal passage, depending on the operational requirements. A heating element with variable high voltage, heats the coolant accurately to maintain the temperature in the desired operational range. This heater gets its power directly from the battery pack.

Refrigerant cooling is a compact way of cooling the battery, with more flexibility, compared to a fan with ducts, through connecting the battery evaporator parallel to the evaporator in the cooling loop. Heat generated by the battery is transferred to the evaporating refrigerant. This system only requires two additional refrigerant lines, namely suction and pressure lines. The battery evaporator uses some portion of the compressor output that was reserved for the air conditioning, and thus this might cause conflict in some conditions. However, the compressor work needed to cool the battery is usually considerably lower than the air conditioning evaporator need.

It was mentioned before that the main component of note in the TMS of the vehicle is the battery pack. Battery cooling can also be carried out with PCMs. In the current research, the option to employ PCMs to cool down the battery are investigated. PCMs have significant advantages over the aforementioned TMSs, due to their simple design, light weight and compact size, safety and relatively low cost, especially when thermal conductivity is improved with the addition of aluminum foam and fins [23].

Liquid cooling utilizes the previous cooling method with the incorporation of an additional liquid cooling loop specifically for the battery that connects to the refrigerant. This additional cooling loop usually has water or a 50/50 water-glycol mixture and it is kept cool via different procedures depending on the cooling load and ambient conditions. The coolant can be cooled either by ambient air through the battery cooler (if the ambient temperature is low enough) or by transferring the heat to the refrigerant through the chiller. Both methods increase the efficiency of the system since the additional compressor work (that is used in refrigerant cooling) is no longer needed.

As will be discussed later in more detail, one of the options is to integrate the PCM with the loop that uses chiller to exchange the battery heat. This is done by exploiting a latent heat thermal energy storage system (LHTES). PCMs are capable of keeping the magnitude and uniformity of the cell temperatures under stressful operating conditions without the need of a complicated system or fan power. Moreover, the heat transfer associated with adding PCMs to a cell can prevent the propagation of thermal runaway, when the cell temperature reaches critical levels. Furthermore, PCMs can be used to have both an active and passive role (complementary/secondary) in thermal management of the battery packs, which can reduce the complexity and cost of the system. There are specific drawbacks in these systems, such as the

long charging time of the storage system due to low thermal conductivity, which current study examined. New methods are being applied to overcome these drawbacks. Figure 2.5 shows the components of a battery pack. The PCM is going to be applied at the cell and module level in the battery pack. The PCMs are explained in the following section, while the application of these materials to the Li-ion cells will be explained in detail in the current study.

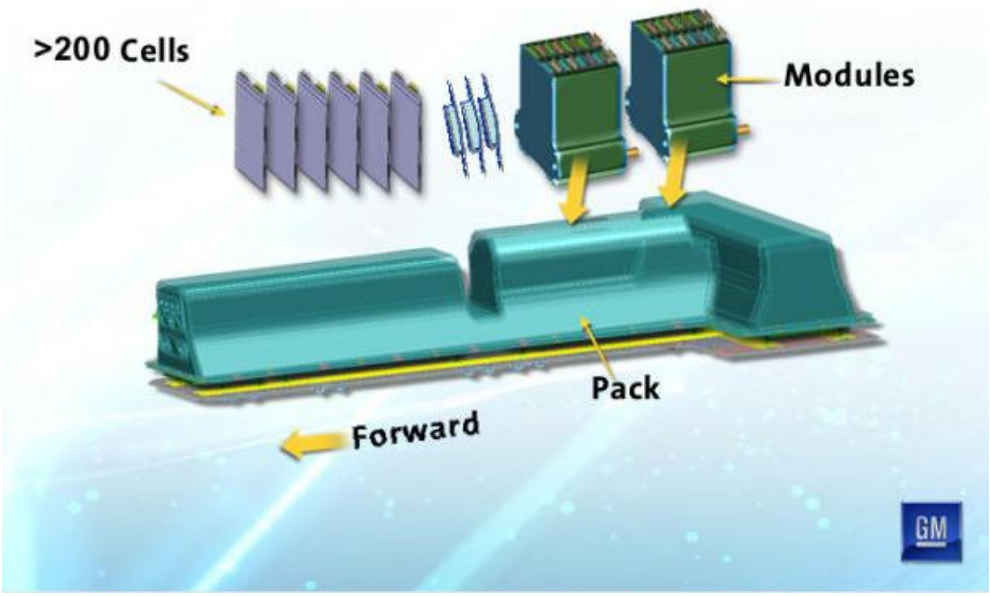

Figure 2.5 Inside the Chevy Volt (HEV) battery pack with the cells and components [44]

2.4 PCMs for thermal energy storage systems

For thermal energy storage, the main three methods are sensible heat, latent heat and chemical reactions. Since the amount of energy being stored in latent heat is higher than sensible heat, it is preferable to use PCMs as latent heat storage materials in different industrial fields such as solar energy, building heating and cooling, spacecraft storage applications and many others. In thermal management systems for HEVs, these materials can be used to maintain a uniform temperature distribution and meet other requirements of TMSs. In this way, parasitic power losses that exist in active cooling systems will be eliminated. The melting point in pure PCMs determines the application of the material. To maintain the temperature at a constant value without variations, constant temperature during phase change is the main advantage of PCMs. For cooling applications in the battery pack, it is important to select the appropriate operating temperature.

Using phase change materials can meet the requirements for TMS that were introduced earlier. They can remove the excess elements like a pump and fan in the system, leading to a decrease in parasitic power extracted from the battery as net electric output. This system will not use any power from the battery to run the cycle. Because of its latent heat of fusion, PCM-based thermal management can remove large amounts of heat during the discharge of battery, which is an exothermic process.

The heat is absorbed in the PCM, which has been integrated between the cells in the module. In this way, heat generation in the cell will be absorbed by a heat sink of the PCM. When the overall temperature of cells and subsequently the pack temperature reach the melting point of the PCM, the resulting process absorbs the produced heat and keeps the temperature constant. In this process, selecting an appropriate PCM with a melting point near the required operating temperature of the system is important. Heat removal can be enhanced over that of the pure PCM by introducing additives like graphite, whereby the thermal conductivity of the composite will increase [45].

The application of PCMs has its own benefits and disadvantages in thermal energy storage systems. Some of the main advantages of PCMs are listed as follows:

- Reduced temperature of TMS
- Temperature uniformity in battery
- Low system maintenance
- Reduced system volume
- No parasitic power requirements
- Constant temperature during phase change period

PCMs as an energy storage material also have certain disadvantages for different applications. Their importance varies substantially. For example, additional weight in stationary applications is not as unfavourable as in vehicle applications. Some of them can be addressed as follows:

- Volume expansion encountered upon solidification of the PCM after melting (leads to mechanical stresses on the casing and battery pack)
- Additional weight

- Undesirable thermal inertia
- Higher costs compared to sensible heat storage

The application of phase change material is important in selecting the PCM. For instance, battery pack cooling and latent heat of fusion are among the most influential criteria to choose the appropriate material, but their melting temperature will dictate the type of material to be chosen. If phase change occurs in temperatures higher than what is required, it cannot be considered. When a material is used for thermal energy storage, it should satisfy some basic requirements as follows:

- High latent heat of fusion
- Compactness, due to higher density
- Melting temperature near the operating temperature (slightly higher)
- High thermal conductivity to reduce thermal resistance in the solid phase
- Higher specific heat to allow to store greater energy in the form of sensible heat
- Lower material cost and availability
- Lower stresses applied to a container due to smaller volume changes in phase change period
- Smaller negligible corrosion effect on PCM container
- Non-toxic material
- Environmentally friendly
- Chemical stability
- Congruent melting (phase segregation)
- No chemical decomposition
- Small or negligible supercooling effect

2.4.1 **Classification of PCMs**

There are many studies on the various applications of PCMs. In this work, the selected materials should have properties that make them compatible with vehicle standards such as weight, latent heat storage and safety. These materials have varied morphologies. Figure 2.9 shows the classification of the various PCMs.

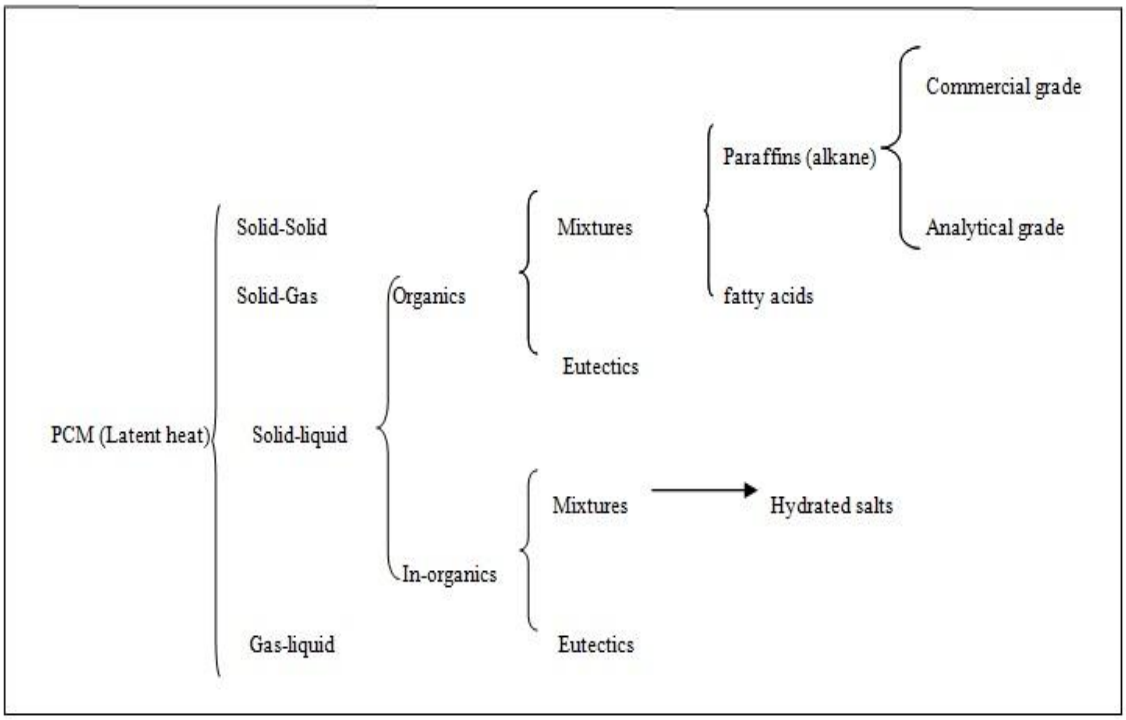

Figure 2.6 Classification of PCMs (adapted from [46]).

For scaled-up battery packs, the candidate PCM for Li-ion batteries normally should have a melting point less than 40℃ with a small mushy phase and small temperature interval for melting [40]. Also the material should have a high latent heat per mass, thermally high cycle life and be light, safe and chemically stable, as well as non-toxic and inert to other battery components.

2.4.1.1 Organic PCMs

Organic PCMs are materials with carbon elements in their compound. They are chemically stable and non-corrosive. Two main groups of these materials are paraffin and non-paraffin organic materials.

- **Paraffins**

Paraffin waxes are normally a mixture of alkanes with a number of carbons between 20 and 40. Paraffin wax is a solid phase of paraffin. Alkanes are hydrocarbons with single bond molecules. The general formula for alkanes is $C_n\ H_{2n+2}$, where n is the number of carbon atoms. If the

number of carbon atoms is an even number, it is called n-paraffin, while an odd number denotes an iso-paraffin.

Organic paraffin waxes are studied in two groups: commercial waxes and pure alkanes. Commercial paraffin and pure alkanes are of the same compounds except in their number of carbons. For commercial paraffin, the number of carbons are between 8–15, while for pure alkanes, carbon atoms are between 14 to 40 with a melting point of 6℃ and 80℃ [47]. The melting point of paraffin increases by increasing the number of carbon atoms in their structure. For n >17, the paraffin is normally solid at room temperature. This kind of paraffin material has a lower latent heat of fusion than n-paraffin. If the number of carbons increases, there will be a higher increase in latent heat of fusion for n-paraffin than iso-paraffin material [46].

- **Non-Paraffin organics**

Other non-paraffin organics are similar to fatty acids. These organic materials have a relatively high latent heat of fusion and have small volume changes during phase change.

2.4.1.2 Inorganic PCMs

The second main group of PCMs is inorganic materials. Inorganic PCMs are divided into mixtures and eutectics. Mixtures are salty hydrate PCMs and have a higher heat of fusion. The density of these materials is high which makes them more compact and suitable for storage applications. In salty hydrate (compound) materials, an important advantage is their high density leading to their compactness. From their thermal conductivity values, it can be observed that inorganic PCMs are 2 to 3 times higher than organic materials. This property makes them suitable in some applications where their corrosiveness is not very important. Salty hydrates are not flammable but they are not safe if a person comes into direct contact, as they can cause skin irritation.

The problem of segregation occurs in these materials, which is a disadvantage and prevents their proper use as a PCM. It means that after separation occurs during melting, the solid phase will not be solved in the aqueous phase, and will thus not recombine and the form the same material, due to the irreversibility of the process. This will cause the PCM to lose its structure. This means that these kinds of materials cannot be practically used as PCMs. To address the incongruent melting problem, the extra water principle and employment of

suspension media can be used. Another disadvantage of salty hydrates is that they have a super-cooling property. In order to decrease this property, nucleating materials can be added to the salt hydrates, such as the Borax that is added to Glauber's salt, to decrease its super-cooling problem.

2.4.1.3 Eutectics

Eutectics are mixtures of different compounds with melting points lower than the constituent compounds. Thus, they can be adjusted to give specific melting temperatures for specific applications. In order to have congruent melting, all components should be miscible in the liquid phase.

In general, commercial paraffins are cheaper than pure alkanes. One solution to address the high costs of pure alkanes is to mix them with other similar paraffin waxes. This will lead to very similar properties for an equal amount of matter with a lower price. For eutectics, the main part of their compound is inorganic materials, which hold the same problems stated above. Also, more investigations are needed into the properties of this class of PCMsin comparison with their organic counterparts [47]. It should be noted that eutectic materials don't have the disadvantage of incongruent melting. However, eutectic materials are made mainly from inorganic salts because of their high latent heat of fusion, rather than organic compounds, with high volumetric changes. This expansion in volume is not homogenous, which can damage the container and impose stress on the structure. Since eutectics are made based on specific requirements, they are more expensive than other PCMs with a lower latent heat of fusion.

2.4.2 Thermal conductivity enhancement methods in phase change materials

Though latent heat storage methods offer a higher energy density to be stored, these materials possess a nearly isothermal situation in heat transfer which acts as the main barrier to their applicability in storage systems. Therefore, to tackle the low thermal conductivity drawback of these materials, it is essential to find methods to increase their thermal conductivity. The various methods to improve the heat transfer rate can be grouped into four main categories [48]:

- Utilization of extended surfaces
- Employment of multiple PCMs
- Microencapsulation of the PCM
- Thermal conductivity enhancement

2.4.2.1 Utilization of extended surfaces

Fins are the most common form of extended surfaces. In this method, the heat transfer area is increased by adding additional surface area. Extended surface can have different configurations. It can be a tube or plate shape to transfer the heat between the PCM and heat transfer fluid (HTF). Normally, the PCM side has a lower heat transfer coefficient, therefore the fins should be placed on the PCM side. Another important concept is to check whether adding the fins and increasing the surface will improve the rate of heat transfer. If the heat transfer coefficient can afford the heat exchange, adding fins can have opposite effect due to increased wall resistances.

2.4.2.2 Employing multiple PCM method

Using more than one PCM has the benefit of making temperature more uniform in the heat transfer period. This is another interesting method. Some researchers have reported the benefits of using multiple PCMs.

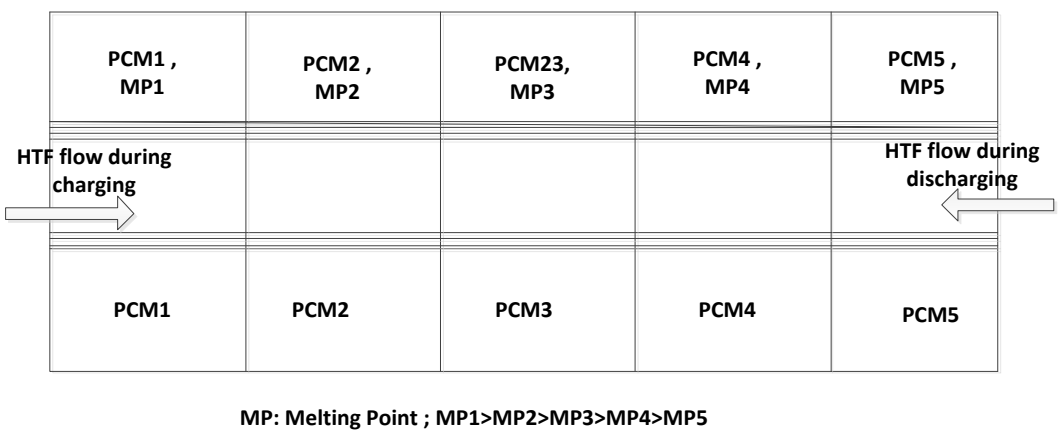

Figure 2.7 Multiple PCM configurations in a shell & tube heat exchanger (adapted from [48]).

If $T_{m,,aver}$ is considered as the average melting temperature of the PCM located in the middle of a multiple PCM system, the following equation gives the optimum temperature difference for the charging period between the highest and lowest melting temperatures [49]:

$$T_{MP,first} - T_{MP,last} = \frac{NTU}{1+\frac{NTU}{2}}(T_{HTF,in} - T_{m,aver}) \quad (2.1)$$

where NTU represents the number of heat transfer units.

2.4.2.3 Microencapsulation of PCM

Microencapsulating the PCM increases the heat transfer rate between the PCM and the source/sink. In this method, micro-size PCM in liquid/solid form are surrounded in the carrying fluid. Two methods are used to prepare microencapsulation of PCMs: chemical methods (such as coacervation, complex coacervation and interfacial methods) and mechanical or physical methods (like spray drying).

2.4.2.4 Thermal conductivity enhancement

The low rate of charging and discharging processes limits the potential application of PCMs in latent heat storage systems. Both organic and inorganic PCMs have very low thermal conductivity, ranging from 0.1 to 0.6 W/m.K [47, 50].

A high thermal conductivity material can be added to the PCM to increase their thermal conductivity [48]. There are specific methods to achieve this goal which can be categorized as follows:

- Impregnation of highly conductive porous material with the PCM
- Dispersion of highly conductive particles in the PCM
- Placing of metal structures in the PCM
- Using of high conductivity, low density materials

In all of these methods, by adding a specific percent (volume or mass percentage) of an additive, the thermal conductivity can increase, but at the same time, heat capacity also increases. This is due to replacing the PCM with another material that has a lower latent heat of fusion compared to the PCM's. In the current research, certain methods such as adding a metal matrix or balls to the languid are not applicable. The reason is the portability requirements of LHTES. There is a limit to the weight of the component to be added to the TMS of the vehicle. Therefore, the method of applying high conductivity and low density materials is examined in this study. For this purpose, CNTs are used as additives in the PCM. These materials are briefly explained in the following section:

2.4.3 **Carbon Nanotubes (CNT) and effective properties of PCM and CNT**

CNTs were first introduced in 1991 [51]. They are considered a specific form of carbons in which the length is in the order of micrometer size and diameter of nanometer size. If the layers of graphitic sheets (which are called graphene) are rolled up and formed into a cylinder (seamless and with a size in the nanometer range), then the resultant morphology will be a CNT. In this form, their aspect ratio (length to diameter ratio) will be greater than 1000 (Figure 2.11). Therefore nanotubes can be considered as a nearly one dimensional structure. A molecule composed solely of carbons hollow structures is called a fullerene. Spherical fullerenes are also known as buckyballs. The two ends of CNT cylinders can be open or closed with full fullerene caps. The notable thermal and electrical properties of CNTs make them a preferable candidate for their application in nano fluids. CNTs are generally produced by three main techniques: arc discharge, laser ablation, and chemical vapour deposition [52].

Multi-wall CNTs have specific properties such as very high axial thermal conductivity. Due to nano-scale effects on the properties of the material, the measurement of thermal conductivity for CNTs has been reported with different values in a wide range. The axial thermal conductivity of CNT is reported theoretically to be as high as 3000 W/mK [53] or even up to 6600 W/mK [54] for individual multiwall CNTs and single-wall CNTs, respectively.

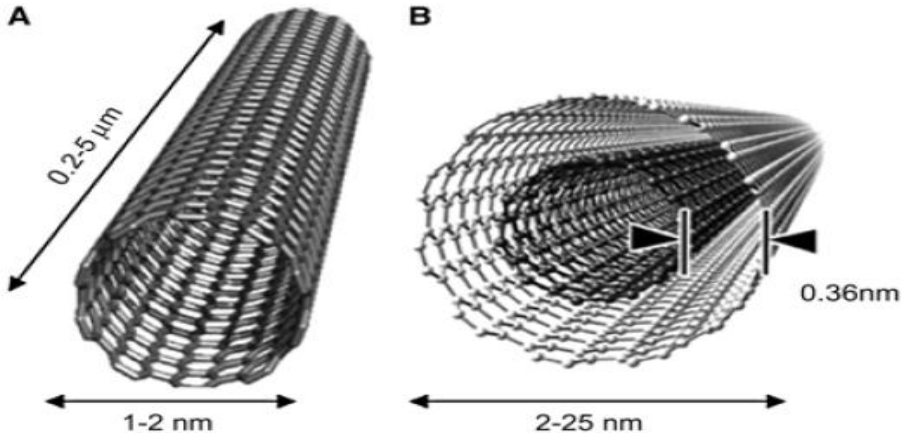

Figure 2.8 Single wall (SWCNT) and multi wall carbon nanotubes (MWCNT) ([55]).

The orientation of layers in the nanotubes is different. Depending to the cutting line in the planar surface, different shapes can be obtained for the CNTs. Figure 2.12 shows the possible orientations. Two main structures of CNTs are single wall (SWCNT) and multiwall (MWCNT) nanotubes.

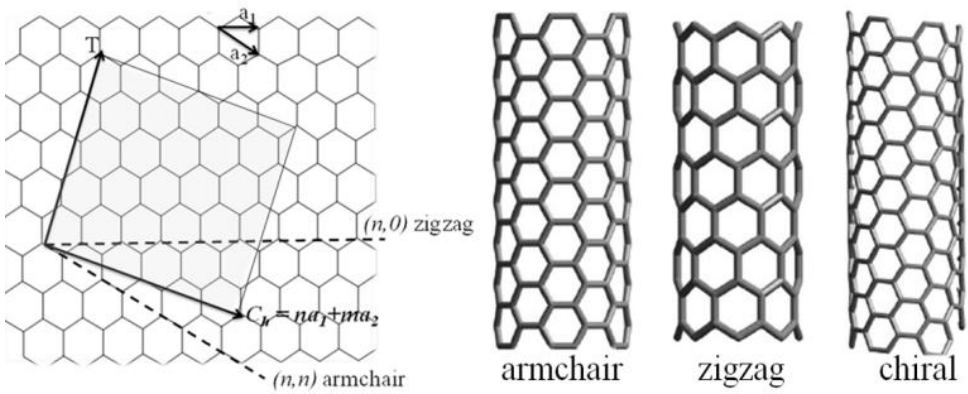

Figure 2.9 Graphene sheet rolled into carbon nanotube [52].

SWCNTs are generally narrower than the multi-walled tubes, with diameters typically in the 1–2 nm range, and tend to be curved rather than straight. MWCNTs contain at least two layers, often many more, and range in outer diameter from about 3 nm to 30 nm. The interlayer distance in MWCNTs is close to the distance between graphene layers in graphite, approximately 3.3 A˚. The special case of MWCNTs—double-walled carbon nanotubes (DWCNTs)—must be emphasized here since they combine very similar morphology and properties, as compared to SWCNT.

Even though the CNTs have very high thermal conductivities, which makes them an ideal candidate to be added to the PCM and thereby increase the thermal conductivity of the fixtures, their molecular attractive forces, or Van der Waals forces, have a negative effect on their thermal applications. It should be considered that CNTs cannot form stable and reliable bonds with the other molecules around them and tend to form agglomerates, or large masses, with neighboring nanotubes. To overcome this deficiency, different dispersion methods are used to ensure homogeneity of the CNTs throughout the nano fluid [52].

Thermal interface material (TIM) is an example of the application of CNTs in increasing thermal conductivity. TIMs are important in the efficient removal of heat in electronics packaging applications. Improvement in TIM performance is dependent on developing materials that have both high thermal conductivity and high compliance. The introduction of CNTs into TIMs has the potential to improve the bulk thermal conductivity. In preliminary testing, introducing of CNTs into a commercial TIM, Arctic Silver VR5, increased the thermal resistance and hence reduced the performance. At the same time, the CNT-AS mixtures show greater compliance. The performance change can be attributed to the increase in thickness due to the

difficulty of spreading the mixture. In a second test, a mixture composed of CNT-AS and silicone oil yielded comparable or slightly improved performance over the CNT-AS mixture and the commercial TIM. The CNT/oil mixture also showed high compliance and reduction of total resistance with increased pressure [56].

2.4.3.1 Measurement of PCM properties

MWNTs are widely used in lithium ion batteries for notebook computers and mobile phones, marking a major commercial success. In these batteries, small amounts of MWNT powder are blended with active materials and a polymer binder, such as 1 wt. % CNT loading in LiCoO2 cathodes and graphite anodes. CNTs provide increased electrical connectivity and mechanical integrity, which enhances rate capability and cycle life [57]**.** As nano-scale graphitic structures, CNTs are of great interest not only for their electronic and mechanical properties, but also for their thermal properties. 1-D quantization of the phonon band structure can be observed from the low-temperature specific heat and thermal conductivity. This is due to the importance of quantum effects because of their small sizes [58].

There are specific techniques to measure the latent heat of fusion and melting temperature of PCMs. Thermogravimetric Analysis (TGA) measures the amount and rate of change in the weight of a material as a function of temperature or time in a controlled atmosphere. Measurements are primarily used to determine material composition and to predict thermal stability at temperatures up to 1000°C. The technique can characterize materials that exhibit weight loss or gain due to decomposition, oxidation, or dehydration [59]. Another two of these methods are differential thermal analysis (DTA) and differential scanning calorimetry (DSC) [60].

As discussed in the previous sections, the thermal conductivity of CNTs is noticeably high compared to PCMs. The considered value in the present study is 2000 W/m K. Effective thermal conductivity mainly depends on the direction of the nanotubes. If they are placed in series configuration, the effective thermal conductivity increases tremendously. On the other hand, the effective thermal conductivity will possess the minimum value once the nanotubes are in parallel arrangement in the worst scenario.

2.5 Heat exchangers for PCM

In order to transfer heat from the cooling loop of the battery to the PCM, a compact heat exchanger is required. Because of the low thermal conductivity of PCMs, the effectiveness of the heat exchanger is an important criterion. The constraint of limited available volume in the hybrid vehicle to place the heat exchanger is another parameter which leads the heat exchanger design in the EV and HEVs toward compactness. Compact heat exchangers are characterized by a large heat transfer surface area per unit volume. The plate fin heat exchanger (PFHE) is a typical compact heat exchanger that is widely used in many industrial power generation plants, and in the chemical, petrochemical, and petroleum industries. Fins or extended surface elements are introduced to increase the heat transfer area.

It is concluded that thermal loss from shell and tube configurations is minimal [61]. In addition, it has been shown that most engineering systems use shell and tube technology which makes them inexpensive, easier to manufacture and cheap to maintain [62]. The charging and discharging times are important in latent heat storage systems. The less melting/solidification time, the better latent heat storage will behave. The research shows that shell and tube type heat exchangers require less charging and discharging time [63].

2.6 Heat generation and thermal management systems

The heat source in the battery pack is the volumetric heat generated in the Li-ion cells. The main problem emerging in compact electric energy storage systems using Li-ion cells is this volumetric heat generation. A proper TMS is required to remove the excess dissipated heat from the modules and cells. A reliable safety circuit design is also important in Li-ion batteries. Heat generation is a function of the SOC, temperature and heat capacity of the cell. Liquid electrolyte mixtures, along with single and multiphase solids, make Li-ion cells complicated from a thermodynamic point of view. Mixing, electrochemical reactions and phase changes cause heat generation, which will not be simple to determine. In order to reliably and effectively predict temperature profiles within the cells, heat generation data of the cell is required. Selman et al. [64] considered the heat generation as a summation of three parameters as follows:

- Reversible heat released or absorbed as a result of chemical reactions. It increases linearly as the level of current increases. In most Li-ion batteries, this term is the main

cause for a temperature rise in the discharging mode of batteries. Two methods can be used to calculate this effect accurately: calorimetry techniques and thermodynamic equations.

- Irreversible heat generation by ohmic resistance and polarization effects that increase quadratically with the current load.
- Side reactions which include parasitic reactions, corrosion reactions and chemical shorts.

For normal operational conditions, reversible and irreversible effects are small and, since the temperature is low, no thermal runaway or capacity fading can occur even with long battery operation. Under abusive conditions, reversible and irreversible effects will be important. Abusive conditions mean a higher rate of discharge current (excessive load) and accidental shorts. In these situations, the reversible reaction temperature increases linearly and irreversible temperature increases quadratically, which can lead to thermal runaway conditions and battery failure. In most cases, for Li-ion discharge, the dominant heat effect is reversible and should be considered. Then, further calculations can be done to estimate side reactions and their contribution to heat generation. By contrast, in abnormal or harsh conditions, like high discharge current (excessive load) and short connection, reversible heat generation due to chemical reactions and irreversible heat produced by ohmic resistance and polarization leads to a high temperature rise in the cell and a non-uniform temperature distribution will be caused. The hot spots that may form for this reason can bring about thermal runaway by accelerating the side reaction heat generation [64]. Heat generation can be obtained experimentally by an Accelerating Rate Calorimeter (ARC) test in charge and discharge cycles.

2.7 Exergy analysis method

The efficiency of the TMSs in EVs and HEVs has great importance due to the onboard energy availability as well as the overall impact on vehicle performance, operational cost and environmental impact. Thus, it is imperative to have a good understanding of the efficiencies associated with the system and its components. Exergy analysis represents the amount of energy that may be totally converted to work. Even though energy analysis is the most commonly used method for examining thermal systems, it is only concerned with the conservation of energy, which neither takes the corresponding environmental conditions into account, nor provides how, where and why the system performance degrades. Consequently, the energy analysis only

measures the quantity of energy and does not reveal the full efficiencies of the system. By analyzing both the quality (usefulness) and the quantity of the energy, the true magnitude of losses, and their causes and locations are identified by investigating the sites of exergy destruction in order to improve the individual components and overall system.

Thus, in this study, the TMS is examined with respect to exergy analysis in order to have better understanding of the true efficiencies of the components and battery cooling loop. More information about the exergy analysis and its applications and advantages can be found in literature [65-67].

Chapter 3 Literature Review

The main objective of the present research is to determine how to thermally manage the heat generation in the battery of an EV or HEV. Due to increasing environmental concerns and technological developments, there is both an increased need and greater capability to produce more effective EVs and HEVs. This has resulted in a significant increase in the amount of studies conducted on this subject in various scientific disciplines. Among the available options to improve the efficiency of the battery and in turn, the vehicle, application of PCMs is the focus of this work. In this chapter, there follows a review of the studies carried out about the vehicles (full electric or hybrid) including full scale level with the related cooling loops and the battery loop where the PCM has been applied. Also, a review of PCMs and their related application will be conducted. As discussed in Chapter 2, materials that can increase the thermal conductivity of PCMs are studied briefly. The chapter concludes with an exergy model review and analysis of associated exergy models for the corresponding cycles.

3.1 EVs and HEVs

There is an ever increasing concern about the health and environmental effects of modern road transport. Societal response and growing economic constraints are putting regulatory pressure on the automotive industry to develop more fuel-efficient vehicles. Therefore, it stands to reason that improvements for EVs and HEVs should be prioritized to alleviate the burdens of increasing fuel costs and environmental impact, the legacy of decades of dependence on conventional ICE technology. Various applications and configurations as well as their associated operating costs and environmental impact are reviewed below.

Different HEV designs and applications (defined by the Department of Energy Partnership for New Generation of Vehicles Program) are reviewed by Nelson [31] with respect to their specifications and operational requirements imposed on the batteries. Furthermore, he evaluated the pros and cons for each battery technology in order to evaluate the compatibility with the proposed systems and made various corresponding recommendations. He concluded that even though most of the DOE PVNG goals are unlikely to be achieved at this time, significant improvements have been made in this field and these targets can be met in the near future.

Fan et al. [17] investigated the cooling effect of air and gap spacing on heat transfer rate. They show that forced convection is required in thermal management of Li-ion battery cells and free convection is not enough. Also, they showed the positive effect of higher gap spacing in air flowing channels. Different charging behaviors of PHEVs in the United States have investigated by Wieller [68]. with a focus on electricity demand profiles and energy use. Calculations also showed that PHEVs with all-electric ranges up to 40 miles allow drivers in the US to cut their gasoline consumption by more than half by shifting 45%-77% of miles traveled from gasoline to electricity. For this purpose, 2003 National Household Travel Survey (NHTS) load profiles and the average US electricity production mix are used as base lines. The new range also corresponds to a $0.09 per kWh reduction of energy cost and 53% to 58% reduction in environmental impact. The second statistic could be further improved with the use of electricity produced from renewable energy sources.

The source from which the electricity is produced is important from the standpoint of environmental impact. Using fossil fuel-based electricity can lead to further environmental impacts and lowered overall efficiency. There are many aspects that can affect the efficiency of EVs and HEVs. For example, if the electricity used to charge the battery is produced from petroleum-based power plants, there will be reduced net benefit due to the energy conversion losses. The average efficiencies of power plant boilers, transmission systems, battery chargers and the battery charging process are approximately 33%, 93%, 70% and 90% respectively. Therefore, overall efficiency will be around 23%, which is not meaningfully higher than the 20% of conventional ICEs [8]. Needless to say, there is motivation to produce cheaper, renewable electrical power. Once this valuable net energy is stored in the battery, the idea is to use the energy for propulsion and extended driving range. One of the main obstacles to achieving this goal is the heat generated, which needs to be extracted by TMSs from the battery packs. In this way, passive TMSs, such as using PCMs to improve the TMS will be highlighted.

Doucette and McCulloch [69] along with Samara and Meisterling [70] compared EVs and PHEVs with CVs featuring ICEs in terms of CO_2 emissions. They expressed the emissions in terms of CO_2 intensity, defined by “the average amount of CO_2 emitted per unit of electrical energy generated by all the power production processes in a mix weighted by the amount of power obtained from each of those processes”. They showed that EVs have the lowest emissions over the entire driving range and mid-range CO_2 intensity (such as France's and the US's

electricity production mixes, respectively), where PHEVs have higher CO_2 intensity. In all scenarios, EVs and PHEVs had significantly lower emissions than CVs with ICEs.

The effects of additional batteries on total cost, fuel consumption and greenhouse gas was investigated using simulation models by Shiau et al. [18]. In order to account for the additional weight needed to support the extra battery weight, they used a structural weight multiplier and calculated the emissions based on the average US electricity mix. In conclusion, they determined that among PHEVs, HEVs and EVs, the lowest lifetime cost and emissions are produced by small capacity PHEVs, provided they are charged frequently (under 20 miles). However, when PHEVs are charged between 20 to 100 miles, HEVs provide lower costs. Despite this, they determined that the impact of PHEVs and HEVs, even with increased battery specific energy or carbon taxes, would have only limited impact without decarburization of the electricity grid.

3.2 Thermal management systems: PCM applications

To predict the thermal behaviour of a system**,** heat generation is required to be known. Some studies treat thermal management of lithium-ion batteries as simple and one-dimensional with constant heat generation and constant properties.

As a one dimensional study, Al Hallaj et al. [27] used lumped system parameters for temperature profiles inside the lithium-ion cell. In their model for heat generation, they used experimental data. For C/2, C/3 and C/6 discharge rates, the model predictions and measurements showed good agreement for temperature profiles. For low heat transfer rates from the cell, temperature gradients are not high; therefore the lumped system with uniform temperature governs the cell. For higher rates of heat removal, the Biot number could exceed 0.1 and temperature gradients will exist in the cell. They also determined the Onset-of-Thermal-Runaway (OTR) temperature using an Accelerated Rate Calorimeter (ARC). Other one dimensional studies were carried out elsewhere [71-74]. Some investigators applied transient heat generation and temperature-dependent thermo-physical properties in their studies [37, 75].

Kelly et al. [76] showed that for air cooling systems used in the Toyota Prius, parasitic power losses decrease the efficiency of the Ni-MH battery by 40%. Different cells operate at different temperatures. For Li-ion batteries, the operating temperature is normally defined by the manufacturer. Chemical components of the cell and their characteristics will determine this

temperature. Along with the other properties of PCMs, their melting temperature is an important parameter in their selection.

Khateeb et al. [23] studied a scooter and replaced the lead acid battery with lithium-ion batteries with PCMs for thermal management. In order to enhance the low conductivity of the PCM, aluminum foam was added along with the application pf cooling fins to the battery pack. They showed that without active air cooling, the natural convection will have a lower heat transfer coefficient. Their study also confirmed the effective role of using PCMs in EV TMSs. Cell capacity degradation is affected dramatically for temperatures higher than 60° C in Li-ion cells. To prevent this phenomenon, the heat transfer coefficient of the surrounding air should be raised via forced air recirculation or other mechanisms like high efficiency fans and blowers. This, in turn, will increase the complexity and bulkiness of the system. The study also examined the PCM/battery ratio, and found that PCMs alone cannot manage the heat removal and that thermal conductivity must be enhanced to overcome this problem. Heat coefficients are considered to be 5 W/m^2K for free or natural convection and 20 $W/m^{2\cdot}K$ for forced cooling with air. Since the thermal conductivity of PCMs is low, they added aluminum foam to the PCM, increasing heat transfer by as much as an order of magnitude. Another issue is ambient temperature in the summer. It can exceed 40℃ and, as discharging initiates, the PCM will start to melt too soon, and sensible heat will come into play. In the second charging/rest cycle, the PCM does not recover to its former solid phase, and the mushy phase will be present until the end of the cycles. Though the PCM at the second and third cycles cannot act as a heat sink and the resultant rise in temperature can be as much as 11℃ at the end, the operating range remains within safe limits and it is still better than air cooling the case or the PCM without the addition of aluminum foam.

By adding aluminum foam to the PCM, the thermal conductivity improved by an order of magnitude, which in turn reduced the temperature of the battery module to 25℃. On the other hand, the PCM still failed to provide adequate cooling due to the material being completely melted during the second cycle (in a three cycle experiment). To overcome this drawback, aluminum fins were also added to the battery. As a result of this analysis, they concluded that PCMs can be a simple and cost effective solution for Li-ion battery applications including HEVs, especially in cases where passive air cooling is insufficient. The result of their study showed the heat dissipation rate of the PCM is not sufficient and aluminum foam is an effective way to

overcome this deficiency. They considered the volume expansion in the re-solidification phase of the PCM after melting.

Lee et al. [77] studied averaged properties and a quasi-homogeneous model for the composite electrode stack to simulate the temperature profiles of the battery. They showed that space between cells, number of cells, capacity and discharge rate of the battery pack, along with cooling orientation, affect the thermal behaviour of the module. Al-Hallaj and Selman [38] investigated a scaled-up battery pack that used cylindrical cells and PCMs among the cells in the module. They showed that a PCM is effective and capable of controlling the temperature. Their work was among the first studies that showed passive thermal management with PCMs can be used in these batteries, removing the need for external power. Al-Hallaj et al. [45] studied a module with cylindrical Li-ion cells and PCM within a graphite matrix as a TMS. They placed thermocouples at critical locations in the module—one in the corner and the other in the middle of the module—and measured the temperature. The capacity fading of cells and output power of the pack with and without PCMs were tested under normal conditions at room temperature. For the module without PCMs and with high discharge rates, the temperature increased until a failure in battery pack operation occurred, which shows the need for an effective TMS. Results also showed that about 90% of nominal capacity was accessible when a PCM was used and battery cycle life was longer than the case without a PCM.

Duan and Naterer [78] experimentally investigated the effect of PCMs on thermal management of cylindrical cells. They used a line heat source to represent a battery cell which generates heat. In the experimental part of this study, they considered two cases. In the first, the cell (line heater) was surrounded by PCM and, in the second, a cell was wrapped with a PCM jacket. They concluded that both designs were capable of keeping the cell temperature within a narrow band and therefore a similar design could be considered for TMSs in HEVs.

Selman et al. [64] showed that in the scaled-up cells, temperature increases due to high discharge rates and that natural convection is not sufficient for dealing with the generated heat. Their experimental studies showed that for commercial secondary batteries, temperature rise in the cell is strongly dependant on the chemistry of the cell and discharge rate. The surface cooling rate is effective in the temperature distribution in the cell. In abusive conditions, an effective TMS is required.

Kizilel et al. [79] used a scaled-up Li-ion battery pack, consisting of 67 modules, each module with 20 cylindrical Li-ion cells (type 18650 high power, each cell with 1.5 Ah capacities and 3.6 V nominal voltages). They studied each module under normal and stressful or abusive conditions, using air cooling and a PCM latent heat TMS. Five strings of 4-cell units connected in series gave the nominal voltage and capacity of 14.4 V and 7.5 Ah. They also used a graphite-PCM matrix to overcome the low thermal conductivity of pure PCMs and studied the temperature distribution in a cell. The results of the simulation showed that under normal discharge conditions (ambient temperature and discharge rate), air cooling is almost enough for thermal management. For stressful operating situations, air cooling failed to effectively remove the heat and high temperature gradients with an uneven temperature distribution predominated in the system. In another attempt, Kizilel et al. [80] used PCM as a passive TMS in Li-ion as high energy power packs in normal and stressful situations. They tried different higher rates of discharge and stressful operating conditions and increased ambient temperature (up to 45 ℃). They showed the advantage of using PCMs over conventional active cooling systems and concluded that using PCMs can significantly reduce safety issues in Li-ion batteries.

Sabbah et al. [81] compared the effectiveness of air active cooling and passive cooling, using PCMs in the compact battery pack of a PHEV. The cell array in their study was surrounded by a micro-composite graphite-PCM matrix where cooling air passes the gaps between the cells. Their study showed that for abusive conditions, like a higher discharge rate or high operating temperature, an active air cooling system cannot provide the cooling requirements or cope with the high parasitic power loss required by an air fan, and thus could not keep the battery pack temperature in the safety range. By contrast, PCM cooling systems can remove the heat from the pack and meet the TMS's requirements. Nelson et al. [20] pointed out that for a vehicle parked outdoors on a hot day, the temperature in the battery pack and under the hood of the car can reach as high as 50 ℃. If the battery temperature goes as high as 60℃, it will be difficult to reduce this temperature to within safe operating range. Therefore, a refrigeration system was developed to overcome this problem. They confirmed PCM can reduce temperature but required parasitic power to cool the system when the vehicle is at rest.

Refrigeration is considered to be the main cycle in vehicular TMSs. The efficiency of the cooling cycle along with the integrated latent heat thermal energy storage system is investigated in this thesis. The refrigeration circuit of automotive air conditioning systems (AACSs) was

considered in a steady state experimental study by Jabardo et al. [82] and compared against their numerical analyses. Effects of various parameters on the system were also predicted in the study. The COP was calculated with20% error with respect to experimental results. Moreover, they specified that the refrigeration capacity is significantly affected by the evaporator return air temperature and that refrigeration capacity, mass flow rate and COP vary linearly with condensing and return air temperatures and compressor speed.

The effect of various parameters in the cooling cycle and mass flow rate have been studied by Kaynakli and Horuz [83]. The performance of an AACS with respect to various cooling loads, compressor power consumption and refrigerant mass flow rates was investigated by using an experimental vapor compression refrigeration system. The results showed that increasing condensing temperature and compressor speed will lead to an increase in the cooling capacity.

Pesaran [84] conducted a comparison among various TMSs based on their capabilities and functionality, including cooling vs. heating, passive vs. active, parallel vs. serial and air vs. liquid for VRLA, NiMH and Li-ion batteries. He compared the heat generation for these batteries and their behavior with respect to different temperature and cycles. He concluded that the passive TMS is less complicated, though less effective, and it can be used for relatively small battery packs; however, the ambient air must be between 10℃ and 35℃ for the thermal management to work for passive systems, otherwise the battery pack can suffer in extreme temperature ranges. For any other condition, active components might be needed to provide adequate thermal management. On the other hand, for EVs and series HEVs, more elaborate liquid-based systems may be required for optimum thermal performance. He also suggested that it is imperative for Li-ion batteries to have a good TMS due to their safety and low temperature performance concerns.

The effects of batteries operating in extreme temperatures and their corresponding effects on the vehicle characteristics such as range for a Griffon Electric Vehicle equipped with a CMP 3ET205 lead-acid battery were studied by Keller and Whitehead [85]. To make a comparison, they initially conducted tests on the vehicle with no TMS and then with an air and liquid TMS. In the absence of a TMS, vehicle range significantly decreases due to high ambient temperatures and heat spread across the battery pack. This can cause the seasonal driving variability and premature cell failure. Based on the experiments, they determined that the vehicle can achieve up

to 20% greater mileage with TMS. Furthermore, temperature distribution can be reduced or eliminated significantly with the use of TMS, where they achieved a 4.0ºC and 2.3ºC temperature spread in the pack for a circulating-air and circulating-liquid TMS respectively compared to 11.6ºC for the non-managed pack. Heat generation in the battery cells as well as different types of active cooling systems with air, liquid and refrigerant cooling mediums were investigated by Kuper et al. [41]. They formulated the increase in battery temperature over time based on internal heating and cooling rates. The results if their study showed that in order to prevent 25% acceleration of the aging kinetics and up to 50% variance in power capability (in a high temperature power degradation range), maximum and minimum cell temperatures should be maintained within a 3 – 5 K range. They also recommended keeping the inlet and outlet coolant temperature difference to be less than 3 K to keep the cell temperatures sufficiently uniform.

The transient response of the battery pack is more important than the steady-state solution of the model since the vehicle's operation is transient behavior and there is a specific time interval in which the thermal management should satisfy the requirements. There are number of studies about this situation in the literature. For example, Mi et al. [86] estimated thermal loss, predicted the temperature rise and modeled the gradients of the battery pack under various operating conditions for a TMS using a Li-ion battery pack designed for HEVs. Considering the battery impedance and charge rate, they calculated the heat generation to be 2.0 kW. In addition, their results show that it would take approximately 16 minutes to cool the battery below the threshold temperature of 40℃. They assumed the scenario of the vehicle parked under the sun (vehicle compartment temperature of 55℃) to attain the above mentioned result.

A new method using enthalpy potentials to calculate the heat generation rate is presented by Rao and Newman [75]. They compared this method with the energy balance method of Bernardi et al. [87]. The components and species in the cell were taken into account to calculate the heat generation rate of the total cell. They showed that the ohmic drop in the pores of electrodes creates a large portion of the heat generation in the porous electrodes

Studies for Li-ion cells are generally done for cylindrical cells. Prismatic cells act in a similar way, and the heat generation pattern is almost the same except for geometry effects. Krein [88] showed that lithium-ion cells are more effective than other types regarding their high input, output energy efficiency and their wide operating range. For the safety characteristics of Li-ion cells, some experimental tests have been performed. Kitoh and Nemoto [26] conducted

nail penetration, external short circuit and external heating tests for different safety levels of these batteries. They did not report potential ignition or explosion of the battery during the safety tests and concluded that Li-ion cells can be applied to HEVs. Among several batteries under study in a European project (SUBAT), comparisons based on technical, economic and environmental aspects showed that Li-ion is the preferred solution [89]. Also, Khateeb et al. [23] stated that Li-ion cells are a potential choice for the next generation of EVs. The current research will focus on these types of electric energy storage systems and related thermal management.

3.3 Phase change materials

Solid-liquid PCM systems are of interest in heat storage systems because of their high storage density and constant phase change temperatures. Low melting temperature PCMs that are applicable to Li-ion battery cooling systems have been receiving attention because of their wide use in solar energy storage systems. ([47, 90, 91]. A rather comprehensive study about PCMs can be found in a study carried out by Sharma et al. [10]. They studied various aspects of more than 200 PCMs and reported their benefits in decreasing energy use of solar water heating and space heating, as well as other PCM applications. Their report also covers various other properties of PCMs . Trp [92] studied a shell and tube-type energy storage system where the PCM fills the shell side. Heat Transfer Fluid (HTF) exchanges heat with the PCM. Experimental data verified their numerical results in an isothermal solidification process. The reduced volume of storage material is important in energy storage applications. Sharma et al. [10] have studied PCMs for latent heat thermal energy storage applications.

Abhat [47] studied organic and inorganic PCMs and stated that organic fatty acids have much better phase change characteristics than organic paraffin wax materials. The author also showed that n-paraffin waxes have a narrow or constant phase change temperature and they are preferred to iso-paraffin materials. The author showed that Lauric acid is compatible with all common construction materials without corrosion effects. These materials have negligible supercooling and phase segregation during the heat transfer process, thus there is no need to add nucleating agents to overcome these disadvantages. Nucleating agents are materials with a crystal structure and lattice spacing similar to heat storage materials which help in crystallization and preventing phase segregation. For inorganic mixture PCMs, he reported that the main drawbacks for these materials are their corrosive property and relatively higher cost.

Paraffin wax is the solid phase of paraffin materials. Benefits of paraffin waxes are their negligible change in properties over heating/cooling cycles without corrosion effects, and their ability to be used with many materials [46]. In this study, Dennis showed that for non-paraffin materials, fatty acids have up to a 10% increase in volume upon their phase change between room temperature and a temperature of 80℃. After 450 heating and cooling cycles, nearly 10% reduction in latent heat of fusion occurred. Dennis concluded that the energy stored as latent heat can be up to 50 times higher than sensible heat stored energy. Dennis obtained a freezing curve of paraffin 6403 (iso-paraffin), paraffin 6035 (iso-paraffin) and paraffin 6106 (n-paraffin). Comparing the graph showed that n-paraffin has a constant cooling temperature where the iso-material had variable melting temperatures. This is an advantage of n-paraffin materials over iso-paraffin materials because this behaviour is in contrast with the assumption that constant temperature is required to have effective thermal management in the battery pack. Therefore, for commercial waxes, n-paraffin waxes are preferred to iso-paraffin waxes for energy storage purposes. This is in contrast with the expectation of a PCM application, which makes them useless for practical purposes [46, 91].

Table 2.1 shows basic properties of organic and inorganic materials to give an overall understanding of characteristics of organic and inorganic PCMs. Quanying et al. [93] studied miscible paraffin and pure alkanes with different mass proportions and showed that mixed PCMs have higher latent heat energy and can be used in industrial applications. The cooling curves are rather typical for n-paraffin waxes. The melting point (MP) or phase change temperature for a combination of n-heptadecane (mass content), paraffin, n-eicosane, and n-octadecane were studied. Their study showed that the highest latent heat of fusion was for a mixture of n-heptadecane and n-eicosane. The other mixtures have lower latent heat and more variable phase change temperatures. (For mass content of 0% - 50% of n-heptadecane, the latent heat of fusion is about 232-246 kJ/kg). For inorganic PCMs, the containers with salty hydrates will have better performance when they are sealed, which leads to the use of air tight containers their corresponding complexity [46]. n-eicosane, which is one of the shortest pure alkanes (with 20 carbon atoms), can be mixed with other alkanes like n-octadecane to reduce the price of the obtained PCM. Therefore, there will be a trade-off between higher latent heat and price. For mixtures with a mass content of n-eicosane greater than 90%, the latent heat of fusion will be more reasonable, though it depends on the price of these mixtures [93].

Table 3.1. Properties of some organic paraffin waxes and inorganic PCMs

Materials/Organic Commercial Paraffins	Melting Point (°C)	Heat of Fusion (kJ/kg)	Thermal Conductivity (W/mK)	Density (Solid) (kg/m^3)	Density (Liquid) (kg/m^3)	Specific Heat (solid) (kJ/kgK)
5913 (n-paraffin)	23	189	0.21	900	760	2.1
6106 (n-paraffin)	43	189	0.21	910	765	2.1
P116 (n-paraffin)	41	210	0.21	817	786	2.1
5838 (n-paraffin)	49	189	0.21	912	760	2.1
6035 (iso-paraffin)	59	189	0.21	920	795	2.1
6403 (iso-paraffin)	63	189	0.21	915	790	2.1
6499 (iso-paraffin)	67	189	0.21	930	830	2.1
n-Alkane						
Hexadecane	18	236	0.21		770	2.2
Heptadecane	22	213	0.21		778	2.2
Octadecane	28	244	0.21	814	774	1.90
Nonadecane	32	222	0.21	782		1.91
Eicosane	37	246	0.21	778		1.92
Docosane	44	249	0.21	791		1.93
Tricosane	48	232	0.21	764		1.93
Tetracosane	51	255	0.21	796		1.93
Parrafin wax	55	146	0.21	880		1.93
Hexacosane	57	256	0.21	770		1.85
Heptacosane	59	235	0.21	802		1.91
Dotriacontane	70	266	0.21	809		1.92
Octatriacontane	100	271	0.21	815		1.93
Inorganic PCMS (Salty Hydrates)						
$LiClO_3$	8.1	253		1720	1530	2.11
$KF.4H_2O$	18.5	231		1455	1447	1.84
$CaCl_2.6\ H_2O$	29.7	171	0.454	1710	1496	1.45
$Na_2SO_4\ .10\ H_2O$	32.4	254	0.544	1485		1.93
$Na_2HpO_4\ .12\ H_2O$	35	281	0.476	1520	1442	1.7
$Na_2CO_3\ .10\ H_2O$	36	247		1438		
$Zn(NO_3)_2\ .\ 6\ H_2O$	36.4	147		2065		1.34
$KF.2H_2O$	42	117		1670		1.51
$Na_2S_2\ O_3\ .5\ H_2O$	48	201		1730	1670	1.46
$NaCH_3COO.3H_2O$	58	270	0.5	1150		1.90
$NaOH\ .\ H_2O$	61	260		1720		
$Ba(OH)_2\ .8H_2O$	78	267		2180		1.17
$Mg(NO_3)_2\ .6\ H_2O$	89	159		1640	1532	1.99
$MgCl_2\ .6\ H_2O$	116	165		1570		

(Data from [46]).

For a lower operating range of below 35℃, n-octadecane with a high latent heat of fusion (244 kJ/kg) can be considered. For eutectic materials the melting point is mainly above 50 ℃, which is out of the range of the current study. The heat of fusion is lower for eutectics than salty hydrates or organic substances. Research on eutectic materials is still in an early phase, and limited data about their thermo physical properties are available compared to other types of PCMs. Properties of known eutectic materials can be found in [47].

3.3.1 **Heat generation and temperature variations in cell**

Parameters such as possible phase change inside the cell, electrochemical reactions, mixing effects and Joule heating can all affect cell temperature. The heat generation rate is equal to heat generation due to cell polarization minus the entropy coefficient due to reversible processes in the cell. Bernardi et al [87] considered mixing effects that were not addressed in previous works. They also assumed uniform temperature variations in the cell that allow temperature changes with time uniformly in the cell. The ohmic heating is the main heat-generating component. It is a second order function of current and internal resistance of the Li-ion cells. The battery internal resistance is a function of SOC of the battery and cell temperature [72].

Chen and Evan [37] studied thermal behaviour of Li-ion batteries for transient heat generation rates and temperature rise and its profile regarding module dimension and operating variables with a mathematical model. For temperature ranges from 25℃ to 50℃, they assumed that cell electrochemical change is not significantly affected by temperature variation. For heat generation, they showed that the rate of charge or discharge is more effective and for medium-rate discharge (such as C/2), heat generation for the cell is about 10 kW/m^3, which increases with an increase in the discharge rate and also at the end of discharge. Their study also included the temperature rise in the cell. For the center of the battery stack, they used different heat transfer coefficients of adiabatic discharge, natural convection and forced convection. Their results show that for high discharge rates, even forced convection cannot remove the heat from the pack and thermal runaway can occur at approximately 453 K.

The Biot number is used for lumped system analysis. Pals and Newman [72] introduced a model for a lithium/polymer/insertion cell. Results showed that temperature has a crucial effect on degree of utilization of lithium-polymer batteries. They also used the Biot number to estimate

the number of cells in the stack that maintain the Biot number to be less than 0.1, which means the temperature gradient in the stack is ignorable.

A battery cycler integrated with an accelerated rate calorimeter can be used to measure the heat dissipation and heat accumulation in cells. The operational limits in experiments are normally derived from recommendations by the manufacturer. Using this method, Hong et al. [94] found that the heat capacity of commercial cells is almost independent of temperature. Doughty et al. [95] studied the thermally abused operational conditions and corresponding safety issues. They obtained data to use in thermal models for different Li-ion batteries by different calorimetric methods.

Selman et al. [64] considered three main sources of heat generation in cells that are responsible for capacity fading and thermal runaway, listed below. The first two sources of heat generation are not effective under normal operation, but become the main source of heat in abusive or excessive load conditions. The abnormal conditions generate very non-uniform temperature distribution including hot spots. By forming hot spots in the cell, the third source of heat generation (side reactions) can cause thermal runaway in the cell and thereby in the battery pack.

- The reversible heat absorbed or released due to chemical reactions in the cell.
- Irreversible heat generated that increases quadratically with the current load. This heat is caused mainly by ohmic resistance and polarization.
- Side reactions including parasitic and corrosion reactions and chemical shorts.

Wu et al. [96] assumed that heat generation is uniformly distributed throughout the cell, and used the equation of Bernardi et al. [87]. They did not consider radiation. A constant heat transfer coefficient is assumed for the external surface of the battery. They showed that for a cylindrical battery, temperature variations are more uniform in the z-direction than the radial direction. For the state of discharge, temperature depends on the amount of extracted current. The study also showed that for discharge currents less than 10 A, the temperature at the center line is almost enough to be dissipated by natural convection except for the end of the discharge situation, where temperature increases. For higher discharge current, heat generation cannot be dissipated by free convection. For this cylindrical shape battery, temperature at the center line increases stepwise by increasing the state of discharge. They stated that increases of temperature

at the center of the cell are very high at the end of the discharge period and suggested that this increase can be due to large polarization at the end of discharge. Observations suggest that heat can be dissipated even by free convection when there is a lower discharge current, while for higher discharge currents (usually higher than 10 A), the heat cannot be dissipated without active cooling, which in turn makes the cooling system more complicated. In this case, at the end of discharge, temperature can rise up to 65℃. Experimental and simulated results show that for heat removal from the battery pack, cooling by natural convection is not adequate to keep the temperature within safe margins [96].

Overcharging and complete discharging can accelerate cell aging. For discharging effects in Li-ion cells, Saito et al. [97] experimentally studied heat generation for various cells in the overcharge condition and showed that the amount of heat generation during overcharging is almost proportional to charging current. This experiment also showed that in the overcharge period, thermal runaway can be avoided if the cooling system is capable of removing the equivalent heat input to the cycle. Heat generated from lead acid batteries is not noticeable and their thermal management is not a critical issue. By introducing Ni-MH batteries, depending on discharge rate, the heat generation was removed.

3.4 Latent heat thermal energy storage systems (LHTES)

A survey of the previous studies reveals that rectangular and cylindrical geometries are commonly used among the other configurations. Furthermore, the most interest has been shell and tube systems (more than 70 % of all studies) and it has been concluded that thermal loss form shell and tube configurations is minimal [61]. Considering the flow pattern, the parallel flow configuration is better than counter-current flow in terms of charging and discharging time (improved by 5%). Due to the shorter time required for charging/discharging, the pipe model is recommended. This configuration possesses lower heat loss rate to the ambient [63]. In addition, it is found that most engineering systems use shell and tube technology which are inexpensive, easier to manufacture, and with lower maintenance costs [62]. For shell and tube heat exchangers, the Length/Diameter of the cylinder is important. Small ratios are not practical. On the other hand, for larger L/D, there will be negligible entry length effects, which will lead to better performance of the unit [98]. In an experimental study, shell and tube heat exchangers

have shown promising performance. This configuration is more appropriate for limited volumes [99, 100].

Melted PCM can be absorbed in expanded graphite (EG) to obtain form-stable composites and at the same time provide higher thermal conductivity. The paraffin/EG composites with different mass fractions of 2% to 10% have been investigated. The results show that 10% mass fraction makes the mixture stable with higher thermal conductivity [101], while the experiments carried out in the current research show that higher concentrations such as 10% decrease the specific heat of the mixture and are thus not recommended.

Another method is to apply metals in different configurations. Copper can be used as an additive to make the heat transfer 1.7 times higher for melting and 3.8 times for freezing with the specified flow rate (0.050 L/S) [102]. Comparative studies about the charging (melting) time of PCM storage systems with three different configurations have been conducted [103]. The mass, volume and the surface area of all three configurations were the same. Results show that cylindrical shell containers provide the least time required to absorb the same amount of heat. For the range of inlet temperature of heat transfer fluid (HTF), an increase in the temperature leads a decrease in charging period. At lower temperature ranges for the inlet temperature of HTF, there is a sharp increase in the energy storage time corresponding to an increase in inlet temperature, while for higher temperature ranges, storage time will not be affected considerably [103]. [103]. Spherical capsules filled with paraffin wax and metal beads are another approach to enhance the effective thermal conductivity. A decrease of 15% in melting and solidification time has been reported with different diameters and numbers of metal beads [104].

Composite PCM/CENG thermal conductivity is about 4 to70 W/mK compared to 0.2 or 0.3 W/mK for paraffin waxes. Therefore compressed expanded natural graphite (CENG) can be exploited for thermal storage systems. This, in turn, decreases the solidification time, but it should be mentioned that their application reduces the latent heat of fusion of the mixture [105]. Carbon fibres can be used in two different configurations: 1) randomly oriented fibres, and 2) fibres in brush arrangement.

Optimization methods are applied in designing heat exchangers to meet requirements while remaining within constraints. Foli et al. [106] tried to maximize the heat transfer rate and minimize the pressure drop in a micro heat exchanger by these two objective functions. Sanaye

and Hajabdollahi [107] applied a multi-objective genetic algorithm to optimize the performance of a shell and tube heat exchanger.

Other related works can be found in the literature about heat exchanger optimization. In brief, it was found that shell and tube heat exchangers are more suitable for latent heat energy storage, the reasons for which are:

- Shell and tube heat exchangers have minimal thermal loss.
- Charging and discharging times are smaller than other types of heat exchangers.
- They are widely used in various industrial fields. This makes them easier to order or manufacture.

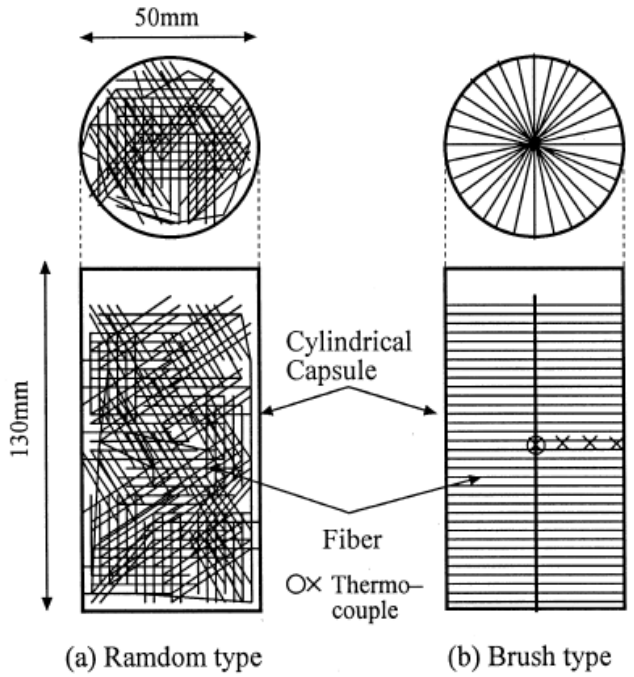

Figure 3.1 Carbon fibre in brush configurations enhances the thermal conductivity [108].

3.4.1 **PCM and nanoparticle mixtures**

The main drawback of PCMs is their low thermal conductivity. Many investigations have been aimed at addressing this shortcoming. Adding solid particles is a method which has attracted much attention, especially after Maxwell's theoretical observation in 1904 [109]. Energy storage capacity of LHTES systems featuring PCM doped with CNTs is a new field of interest. Shaikh et. al [110] studied SWCNTs, MWCNTs, and carbon nano-fibres for heat exchanging purposes. DSC was used to measure the latent heat of fusion for these samples. Compared to pure wax, the measured values of latent heat for all samples showed an improvement. A maximum

enhancement of approximately 13% was observed for the wax/SWCNT composite corresponding to 1% loading of SWCNT.

By dispersing a small fraction of MWCNTs in the liquid paraffin, a novel class of nano-fluid PCMs with enhanced thermal conductivity is obtained. In the research of Kumaresan et.al [111] the stable NFPCMs were prepared by dispersing the MWCNTs in liquid paraffin at 30°C with volume fractions of 0.15, 0.3, 0.45 and 0.6% without any dispersing agents. For the shear stress range of 1-10 Pa, Newtonian fluid behaviour is obtained based on the rheology measurements. The DSC results showed that there is no observable variation in the freezing/melting temperature of the NFPCM, and only a small observable change in the latent heat values. As an important property, the thermal conductivity of various NFPCMs were measured. The enhancement in thermal conductivity increases with the increased volume fraction of MWCNTs where the effect of temperature is not crucial. Furthermore, for the NFPCM with a volume fraction of 0.6%, there was an appreciable increase in heat transfer with a reduction of 33.64% in solidification time.

Heat transfer augmentation in micro-channel flow by introduction of encapsulated PCM was investigated by Alquaity et. al [112] to analyse entropy generation in the microchannel flow due to heat transfer and fluid friction. Effective properties of the flow were determined to study the heat transfer method in the microchannels. Zhang et. al [113] studied novel HTF, containing a water based suspension with microencapsulated PCM (MEPCM) and MWCNTs. DSC, thermal gravimetric analysis (TGA), a thermal conductivity meter, and a rheometer were applied to experimentally obtain the thermal and rheological properties of the sample. The study showed an effective improvement in thermal conductivity of the suspensions. It wass found that the addition of MWCNTs into MEPCM slurry can effectively improve the thermal conductivity of the suspension. It is also found that a blend of 10 wt. % MEPCMs and 1 wt. % MWCNTs suspensions can lead to optimal thermal performance and stability.

Carbon nanotubes are dispersed in a compliant polymer matrix in order to enhance the effective thermal conductivity of the composite [53]. Thermal interface resistance between CNTs and the matrix along with mechanical stress at CNT-matrix boundaries have adverse effects on the thermal conductivity in these structures, which resulted in only modest improvements. Reduced speed at which phonons propagate in the CNTs (i.e., the surrounding elastic medium alters phonon dispersion and reduces the intrinsic thermal conductivity in CNTs) is the main

reason for the moderate improvement in the thermal conductivity [114]. CNT-polymer composites remain an active research focus and several companies are developing products based on this technology as highlighted in a recent article [115].

3.5 Exergy model

Currently, examples of exergy models in the literature are very limited for EV and HEV TMSs. A recent study was done by Hamut et al .[116, 117] to assess the thermal management of a HEV. The authors employed an exergy analysis in order to calculate the exergy destruction of the components and overall system with an active cooling cycle. The study provides information about the component-based exergy efficiencies and their effect on each other. Furthermore, exergy-based economic study about electrified vehicles was carried out.

Liquid cooling systems of HEV battery packs mainly consist of the same components as a vapor-compression cycle. Various studies regarding these cycles have been conducted for many applications, from oil refineries and chemical processing plants to large public buildings. For optimization purposes, there are many studies in the literature. Ahmadi et al. [118] conducted a comprehensive exergy, exergoeconomic and environmental impact analysis. They established a multi-objective optimization model for combined cycle power plants (CCPPs) with respect to exergy efficiency, total cost rate and CO_2 emissions of the overall plant.

Endo et al. [119] used exergy analyses for assessment of a Rankine cycle, which uses waste heat recovery in an automotive engine. The study demonstrated that fuel economy in automobiles can be improved using this system[119]. Li [120] used the exergy analysis method to assess the automotive cooling system of an engine. They concluded that to maximize the engine performance, exergy-based methods can be a useful design decision tool. Exergy based methods are also employed as a design decision tool for integrated aircraft thermal systems. Comparing a traditional energy-based method with exergy analysis reveals that component and overall efficiencies can be obtained more readily through the exergy concept, which can greatly aid the designing process[121]

Chapter 4 Model Development

In order to conduct numerical heat transfer using ANSYS FLUENT or thermodynamic analysis of a vehicle cooling cycle using EES software and a heat exchanger design in Matlab software, there should be a mathematical model which shows the physics of the problem, input variables and relationship between these parameters through the governing Equations and their valid range of variation with initial and boundary conditions. Furthermore, such a model is required to achieve the determined objectives by assigning constraints for the problem and defining the corresponding methodology Therefore, this chapter starts with a mathematical model developed for sub-module and cell level heat transfer process. Next, the thermal modeling of the heat exchanger will be explained and the thermodynamic model of cooling loop in the HEV will be described. The location of phase change material tank in the liquid thermal management system will be defined and the overall efficiencies will be determined based on this model.

4.1 Model development for cell and sub module simulations

For the ANSYS FLUENT simulations, initially the physical domain of the model is presented, followed by the assumptions. Furthermore, the governing conservation equations in the cell zone along with the PCM is defined, which is discretized to be used by numerical methods. Boundary and initial conditions required to complete the model formulation are also illustrated.

Developing a transient three dimensional model is one of the major objectives of this research. A layout for a sub-module is introduced along the physical domain, and the boundary conditions are presented. Existing assumptions and governing equations will form the model. Experiments have been carried out to select the main elements of the sub-module. Basic elements are a lithium-ion cell, cooling plate and foam which will be applied to the system. The model can be applied to scaled-up LHTES systems to investigate the effect of various conditions on their efficiency.

4.1.1 Physical model for numerical study of PCM application

In order to explain the model, a single Li-ion cell and the surrounding PCM is initially modeled. This single cell model, later on, is improved to include a sub-module which includes foam and

cooling plates. Dimensions of the cell are introduced later in this chapter. In addition, figures in chapter 6 illustrate the temperature contours where the physical domain can also be seen. Figure 4.1 illustrates the cell geometry and aspect ratio of the Li-ion cell, foam and cooling plate. The heat generation rate is assumed to be the only heat source in the cell zones. In this study, a sub-module with 4 cells is modeled.

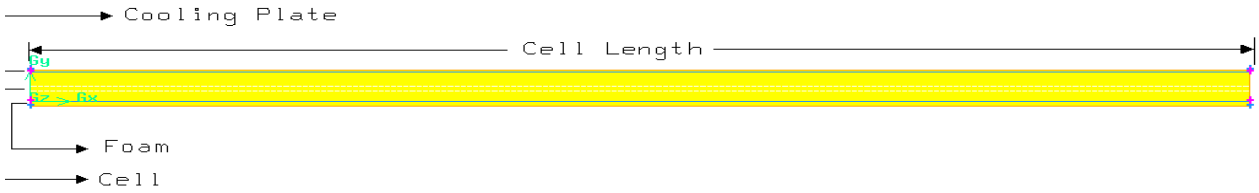

Figure 4.1 Single cell model in the sub-module

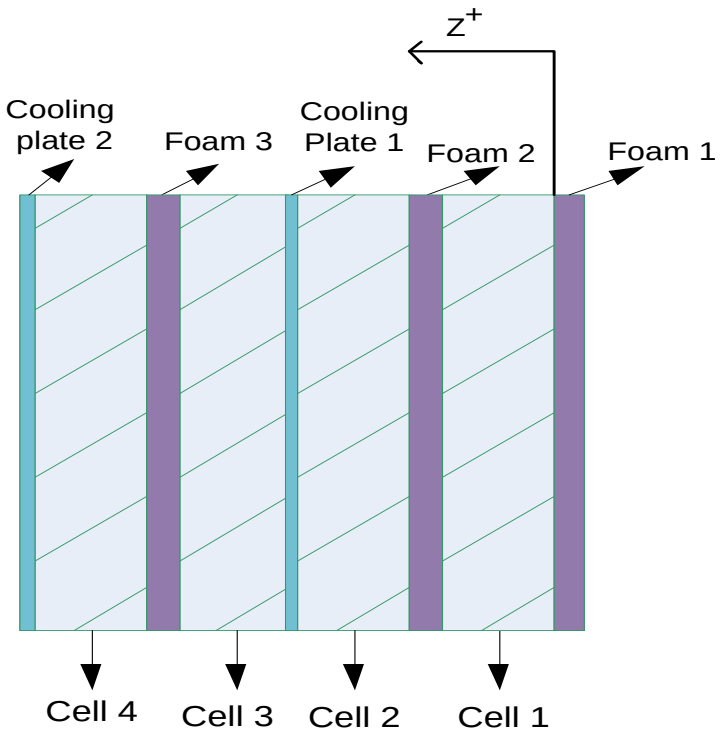

Figure 4.2 Physical domain for the sub-module.

Figure 4.2 shows a sample configuration for the sub-module. In order to have reasonable values in the transient solution, first a steady state condition will be solved and the results will be used as initial conditions. This method is normally used in ANSYS FLUENT software [122].

4.1.2 **Boundary and initial condition; model assumptions**

In the layout for the sub-module, boundary conditions for the interface between the cells and the foam have been defined as "wall boundary conditions". In addition, for the cell and cooling plate, "wall" boundary condition has been considered for locations where there is no mass transport. Free convection has been considered for both ends of the system. For the zone condition, the source term for heat generation rate has been applied to the system. The upper and lower surfaces are also exposed to free convection. For this conjugate heat transfer problem, free convection has been considered for all surfaces (h= 7 W/m^2 K and T_{amb} = 294.15 K).

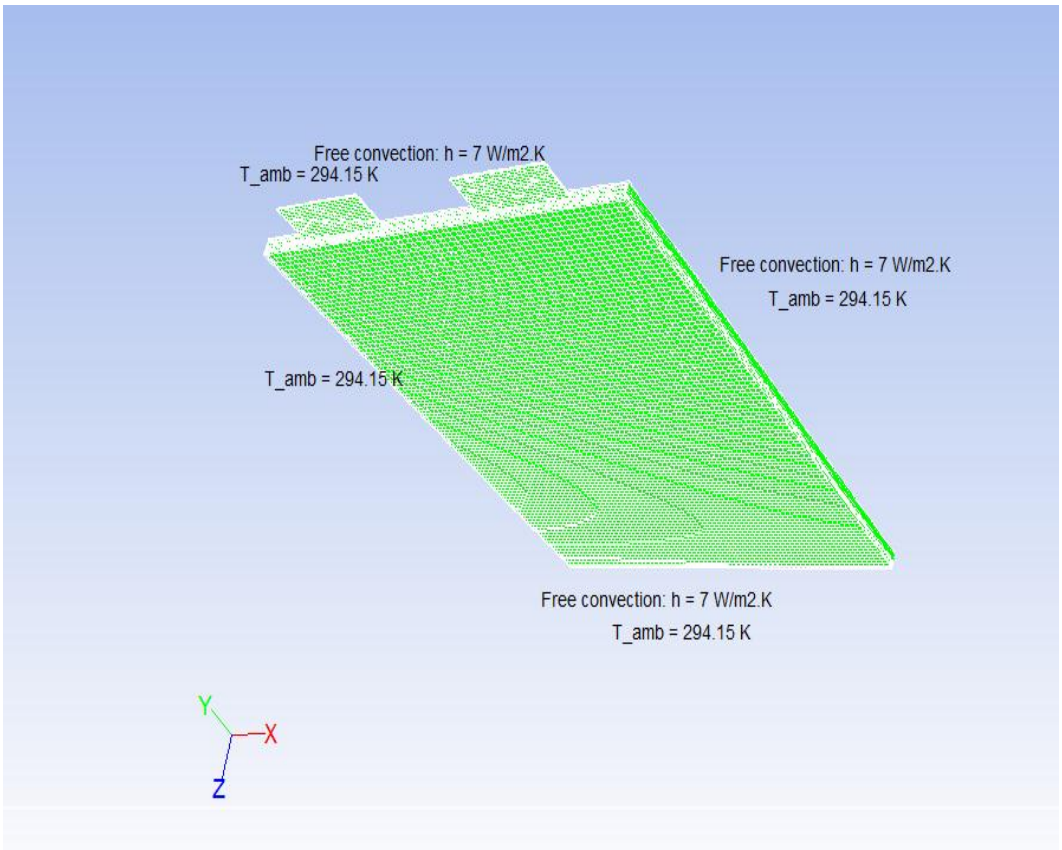

Figure 4.3 Boundary conditions for the cell

The boundary conditions and initial conditions for the single cell and sub-module are as follows:

- The volumetric heat generation rate: $\dot{q}_v$ = 63,970 W/m^3 for 2C (C-rate) (4.45 W/cell). (This assumption is in accordance with a lumped system analysis, which is applicable for these elements based on the insignificance of their thickness)

- The heat transfer from the terminal surfaces and ambient temperature is free convection.
- The boundary between the terminal and cell itself is “coupled” type boundary conditions which assures the continuity of the temperature across the defined boundary
- The initial temperature is considered to be 294.15 K equal to the ambient temperature.
- The cell has orthotropic thermal conductivity.
- The specific heat for the cell, plate and fin is averaged.
- Thermal conductivity of foam is considered as the value for insulation foams.
- No flow filed for the liquid phase of PCM.
- Radiation is not considered.

4.1.3 **Material properties; model input parameters**

The physical domain contains different zones, each one having different material. The properties for the material have been used based on the following information in the simulations. Herein, the data for cell, phase change material, foam and cooling plates are presented.

4.1.3.1 Li-ion cell properties

The prismatic cells are used in the Chevy Volt hybrid electric vehicle (HEV). Heat generation rate, in turn, is the main reason for thermal runaway in the battery pack. Heat generation rate in the cell, is determined by the calorimeter tests. Spatial distribution of heat generation sources inside the cell depends on the chemical reactions in the cell. The new generation of the li-ion cells have almost uniform heat generation in the cell [123]. In this study, different scenarios have been considered for the heat generation rate in the cell depending on the operational conditions. The value for heat generation is considered constant in the volume.

Some studies refers to isotropic thermal conductivity of 0.27 W/m K [27]. In simulation study, the option of applying of PCM around the cell has been selected because of the orthotropic behavior of the cell. This means that the planar (or surface) thermal conductivity of the cell is 25 W/m K and the value for the direction normal to the cell surface is considered as 1 W/m K.

4.1.3.1.1 Heat generation rate in the cell

The C-rate will determine the rate at which the current is discharged from the cell as described in chapter 2. The generated heat is mainly due to the internal resistance, which, in turn depends on the C-rate of the battery. Thermal stability of the cell strongly depends on the internal resistance. For the state of the charge (SOC) equal to 50% and discharge rate of C/1, the heat generation rate for the cylindrical cells is estimated to be 20 W/Liter [27]. For the case of 2C, the heat generation rate is 4.45 W/cell [124].

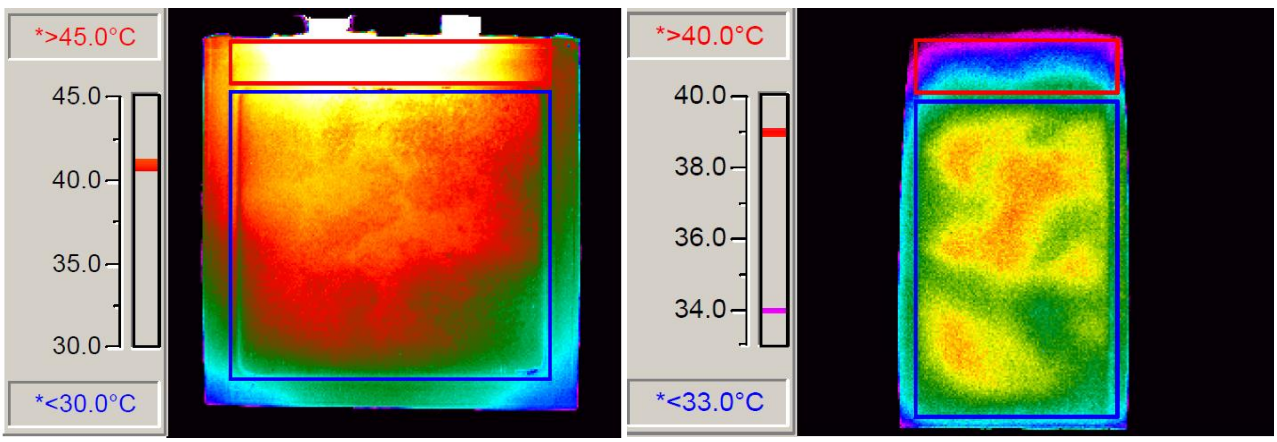

Generation II Generation III

Figure 4.4 Thermal image of li-ion cell after 30.0-amp discharge [123].

From Figure 4.4 it is obvious that the heat generation is more uniform in the new generations of Li-ion cell. This is in accordance with the assumption of uniform heat generation in cell zone. For C/1 rate and heat generation of 1.33 Watts in the cell, the heat generation rate will be 19,120 W/m^3 and for 2C, heat generation rate is 63,971 W/m^3

For the current study, the following ranges of heat generation of the battery cells have been used:

$\dot{q}_v$ = 6855 W/m^3	by Standard US06
$\dot{q}_v$= 22,800 W/m^3	at 135 Amps (150 kW), 3.6 W/cell
$\dot{q}_v$= 63,970 W/m^3	at 2C, 4.45 W/cell
$\dot{q}_v$= 200,000 W/m^3	at full power, uphill condition

Heat generation can be stored as sensible and latent heat in the pack, if the phase change process occurs, then it can be written as

$$Q = m_{PCM} C_p (T_m - T_i) + m_{PCM} LHV \quad (4.1)$$

Heat generation in the cell can be obtained by a calorimetric method or can be modeled mathematically by considered assumptions. Parameters like possible phase change inside the cell, electrochemical reactions, mixing effects and Joule heating will change the heat generation whereby the cell surface temperature. Bernardi et al. [87] developed the following formulation for the heat generation in the cell:

$$\dot{q} = I \left(U - V - T\frac{dU}{dT}\right) = h_s A(T - T_a) + M_A C_p \frac{dT}{dt} \quad (4.2)$$

where U and V are open circuit and cell potentials, respectively. h_s is per-cell heat transfer coefficient. Term I (U-V) is the heat generation due to cell polarization and $-IT\frac{dU}{dT}$ is entropy coefficient due to a reversible process in the cell. M_A is the cell mass per unit area and C_p is the weight-averaged value of cell heat capacity. Temperature variations were assumed to be uniform in the cell. Equation (4.31) can be rewritten as follows [96]:

$$\dot{q} = \frac{I}{V_b}\left[(E_0 - E) + T\frac{dE_0}{dT}\right] \quad (4.3)$$

Here, $\dot{q}$, V_b, E_0, E and I are heat generation rate per unit volume , battery volume, open circuit potential, cell potential and current (< 0 for charging and > 0 for discharging), respectively. If heat generation include reversible and irreversible effects, Selman et al. [64] states that reversible heat released or absorbed in the cell as a result of chemical reactions is

$$Q_{rev} = n_{Li} T\Delta S = T\left(\frac{\partial E_{eq}}{\partial T}\right) It_{dc} \quad (4.4)$$

For obtaining heat generation with thermodynamic relations, the Gibbs free energy can be considered as:

$$\Delta G = -n \times F \times U \quad (4.5)$$

where F is Faraday`s constant and n is the number of electrons.

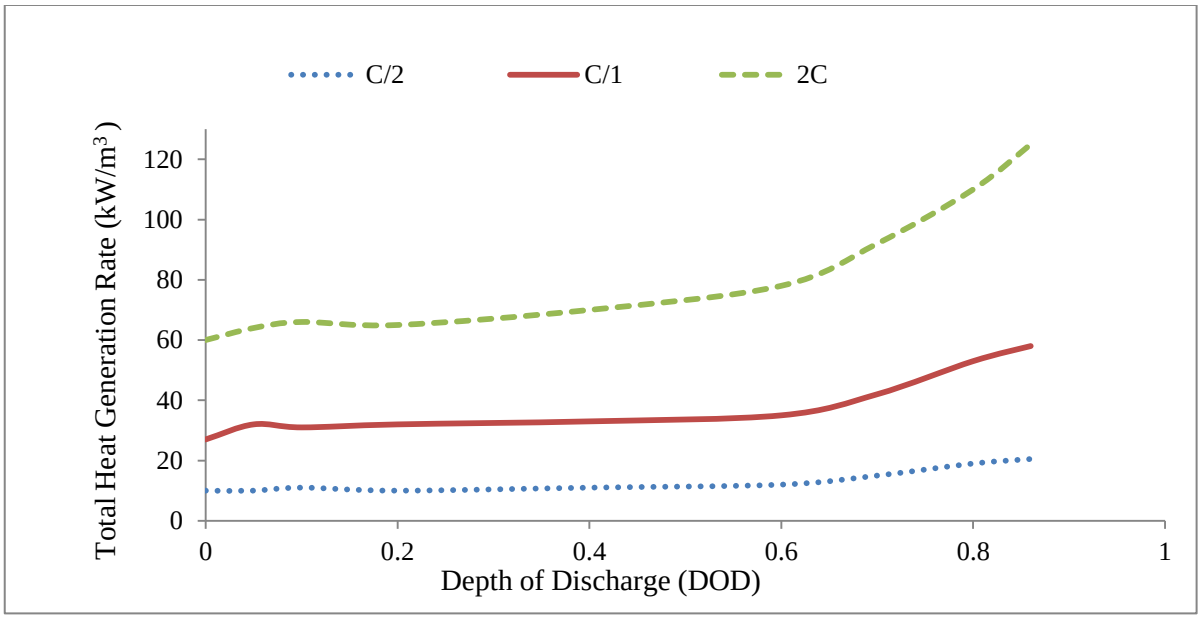

Figure 4.5 Heat generation for the Li-ion cell at different C-Rates (adapted from [27]).

4.1.3.2 Phase change material

The selection of proper PCM which can meet the requirements of the present study is explained in detail. Considering the operating temperature of the cycle, the organic normal Octadecane is selected. Solidus and liquidus temperatures are also depending on the materials purity. Based on the literature review, the considered values for n-Octadecane are:

$T_{solidus} = 301.15\ K\ \ and\ \ T_{liquidus} = 303.15\ K$

The variations of the specific heat are considered as a step function between these two values. In order to find the different values for the PCM with respect to the experimented time, the values can be interpolated based on the curve fitting method. In this section, a method of predicting the behavior of the specific heat with respect to the time is presented.

4.1.3.2.1 Application of Chebyshev polynomials

In order to find a closed form function for the obtained set of data from our experiment, it is needed to use a certain type of fitting algorithms. There are a large number of methods to obtain a function for fitting a set of data such as Chebyshev polynomials, least squares, Levenberg-Marquardt and Gauss-Newton algorithms. In this section, Chebyshev polynomials are utilized to obtain a closed form function for the objective set of data. Chebyshev polynomials are succinctly introduced and then it is employed to find a closed form function for the given data in Table.4.1.

There are two types of well-known Chebyshev polynomials, namely, first and second kinds. In this project, Chebyshev polynomials of the first kind are used to find a closed form function and therefore, this algorithm is initially illustrated. The Chebyshev polynomials of the first kind are defined by the recurrence relation. Based on this algorithm, one could have

$$T_0(x) = 1. \tag{4.6}$$

$$T_1(x) = x. \tag{4.7}$$

$$T_{n+1}(x) = 2xT_n(x) - T_{n-1}(x) \tag{4.8}$$

The conventional generating function for T_n is

$$\sum_{n=0}^{\infty} T_n(x)t^n = \frac{1-tx}{1-2tx+t^2}. \tag{4.9}$$

The generating function relevant for 2-dimensional potential theory and multiple expansions is

$$\sum_{n=1}^{\infty} T_n(x)\frac{t^n}{n} = \ln\frac{1}{\sqrt{1-2tx+t^2}}. \tag{4.10}$$

The Chebyshev polynomials of the first kind are employed to find an accurate closed form function for the presented data. Table 4.1 shows the obtained data from our objective model. Eventually, an explicit form is found for the objective system based on the super position rule and Chebyshev polynomials. Using six orders of Chebyshev polynomials, the following functions are obtained (Figure 4.6)

$$y_a = \frac{1-0.06}{\sqrt{1-0.09^2 T_6^2(\frac{1}{0.018}(x-0.95))}}. \tag{4.11}$$

$$y_b = \frac{0.007}{\sqrt{1-0.09^2 T_6^2(\frac{1}{0.0125}(x-0.987))}}. \tag{4.12}$$

$$y_c = 0.0065.$$

$$T_6(x) = 32x^6 - 48x^4 + 18x^2 - 1. \tag{4.13}$$

Based on the superposition rule and by summation of the above functions, an explicit form could be found for the objective system. This function can correctly predict behaviour of the objective system. Figure 4.6 represents the superposition rule which has been utilized to obtain the closed form function for the objective problem.

$$y_{total} = 0.0065 + \frac{1-0.06}{\sqrt{1-0.09^2 T_6^2(\frac{1}{0.018}(x-0.95))}} + \frac{0.007}{\sqrt{1-0.09^2 T_6^2(\frac{1}{0.0125}(x-0.987))}}. \quad (4.14)$$

Table 4.1 Effect of temperature variations on specific heat

Temperature (K)	$C_p(J/kgK)$	Normalized Temperature	Normalized C_p
299.15	2150	0.983561	0.00881148
300.15	2150	0.986848	0.00881148
300.65	2150	0.988493	0.00881148
300.95	2150	0.989479	0.00881148
301.05	5000	0.989808	0.0204918
301.13	122000	0.990071	0.5
301.15	244000	0.990136	1
301.2	244000	0.990301	1
301.25	244000	0.990465	1
301.35	244000	0.990794	1
301.55	244000	0.991452	1
301.75	244000	0.992109	1
301.95	244000	0.992767	1
302.05	244000	0.993095	1
302.25	5000	0.993753	0.0204918
302.35	2180	0.994082	0.00893443
302.95	2180	0.996054	0.00893443
303.15	2180	0.996712	0.00893443
304.15	2180	1	0.00893443
302.25	5000	0.993753	0.0204918
302.35	2180	0.994082	0.00893443
302.95	2180	0.996055	0.00893443

Figure 4.6 illustrates the curve fit for the Variation of the normalized specific heat. Figure 4.7 shows the superposition method used to obtain the resultant piecewise function of specific heat with respect to the normalized temperature. The above mentioned Chebyshev estimation is used to find the curve. In ANSYS FLUENT, there is an option to enter input data as discrete numbers. Thus, once the variations of the considered property are known, the values can be entered to the software. In the piecewise polynomial option, which is available in the software, the abrupt increase of properties can lead to divergence. (For example, specific heat has a very low value, namely, 2150 J/kgK for solid phase and at phase change stage, roars to a very large

number of 244000 J/kg. This step-wise behaviour may cause instability in the simulation which should be noticed).

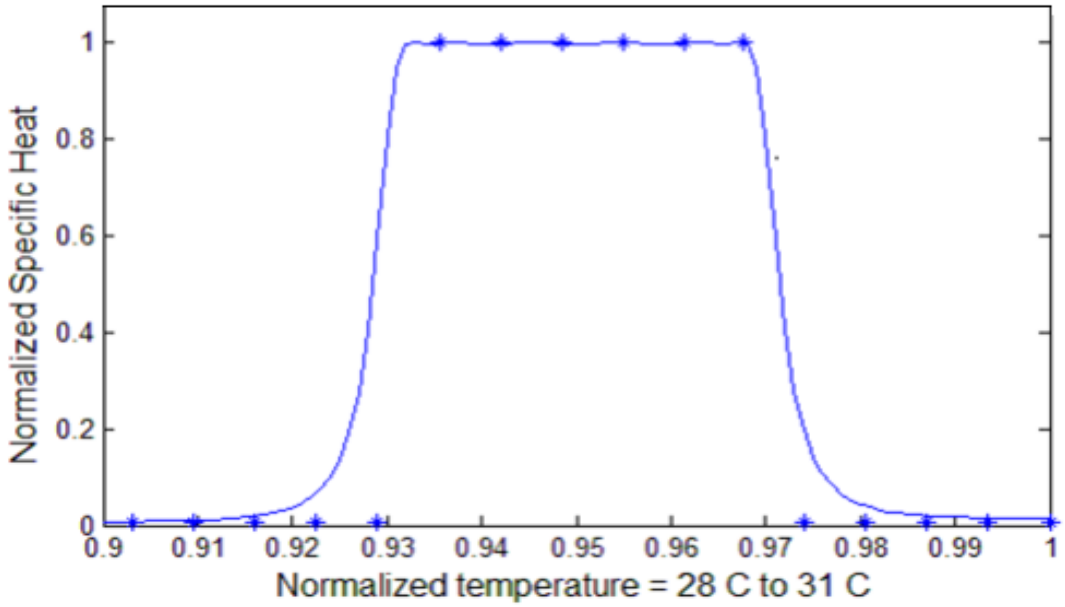

Figure 4.6 Chebyshev polynomial to interpolate specific heat

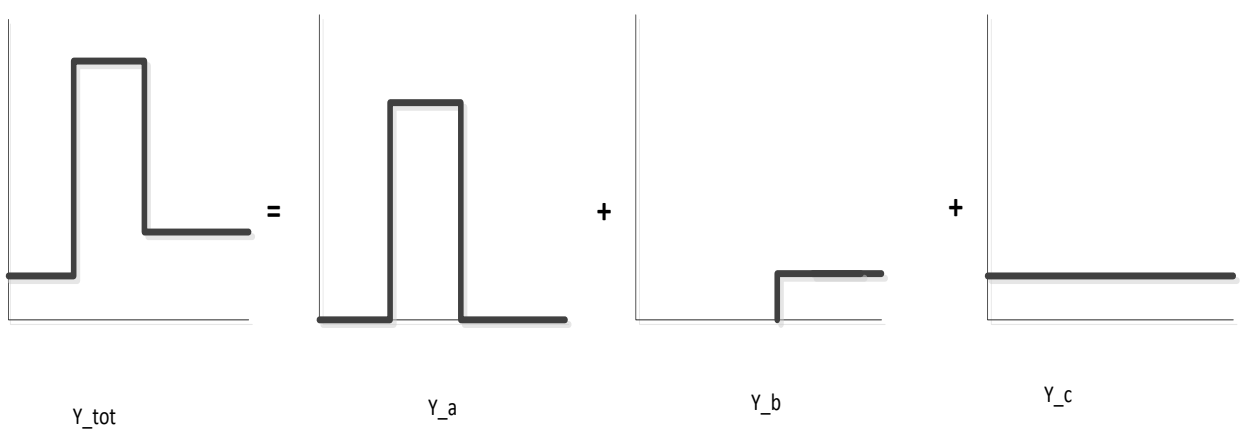

Figure 4.7 Representation of superposition rule for our system

The second method which can be used is Gauss function. For the available data, Gauss function has the following form:

$$C_p = 0.0088 + Gauss(54.79 \times Gauss(1.628e - 7/(T^4 - 3.687 \times T^3 + 5.0713 \times T^2 - 3.108 \times T + 0.7144))) \quad (4.15)$$

The accuracy of the above formula is approximately 97%. The values for the specific heat, thermal conductivity and density of the phase change material are given in the following form to be used in simulations

$$C_p = \begin{cases} 2150 \quad J/(kgK) & T_{solidus} > T & \text{solid phase} \\ 0.255 \quad J/(kgK) & T_{solidus} < T < T_{liquidus} & \text{Mushy zone} \\ 0.152 \quad J/(kgK) & T > T_{liquidus} & \text{liquidus phase} \end{cases} \tag{4.16a}$$

$$k = \begin{cases} 0.358 \quad W/(mK) & T_{solidus} > T & \text{solid phase} \\ 0.255 \quad W/(mK) & T_{solidus} < T < T_{liquidus} & \text{Mushy zone} \\ 0.152 \quad W/(mK) & T > T_{liquidus} & \text{liquidus phase} \end{cases} \tag{4.16b}$$

$$\rho = \begin{cases} 814 \quad kg/m^3 & T_{solidus} > T & \text{solid phase} \\ 769 \quad kg/m^3 & T_{solidus} < T < T_{liquidus} & \text{Mushy zone} \\ 724 \quad kg/m^3 & T > T_{liquidus} & \text{liquidus phase} \end{cases} \tag{4.16c}$$

Octadecane as the selected PCM for this research can be found in two categories: Technical grade and pure PCM. In the literature, latent heat of fusion for this material is considered 244 kJ/kg (243.5 KJ/kg is reported in reference [61]). The DSC tests that have been carried out in this study, shows this value to be 225 kJ/kg. This difference can be a result of impurities in the material. The technical grade even will have lower values depending on the technical grade.

4.1.3.3 Foam material

The foam used in the battery pack has a higher thermal stability and acts as a separator once it is placed in between the cells. They are normally Urethane foams. The following specifications for the foam have been provided by a company in GM vendor list. For thermal conductivity, Polyurethane foam has been considered. Time-dependent thermal conductivity is $k(T) = 0.02064 + 11.28 \times 10^{-5}$ T , where in this thesis, the average value of k = 0.083 W/m K is considered. Density of foam, in general varies between 240 kg/m^3 to 400 kg/m^3, though experimental results are used to calculate this value for the employed foam in the lab. Measured mass of the foam in the experiments is 4.150 grams; The foam dimensions are 107 mm in 140 mm in 1 mm and specific density of the ρ = mass of the sample/ volume of the sample = 277 kg/m^3.

This value has been used in the simulations which are in accordance with the standard values. Specific heat of the foam is considered as 1500 J/kg K from the data provided by the supplier. For absorbed PCM in the foam, the following relation can be used to estimate effective specific heat and thermal conductivity. Effective thermal and density (K_{eff} and ρ_{eff}) are defined similarly and used in the simulations. The relations between the volume percentage and weigh percentage of the foam and absorbed PCM in the foam are presented in chapter 6.

$$Cp_{aver} = \frac{1}{m_{tot}} \times \sum m_i \, Cp_i = \frac{m_{pcm}}{m_{tot}} Cp_{pcm} + \frac{m_{foam}}{m_{foam}} Cp_{foam} \tag{4.17}$$

The porosity is defines as

$$\varepsilon = \frac{V_{pcm}}{V_{tot}} \tag{4.18}$$

Therefore, the average specific heat can be formulated as

$$Cp_{aver} = \frac{\rho_{pcm}}{\rho_{tot}} \times \varepsilon \times Cp_{pcm} + \frac{\rho_{foam}}{\rho_{tot}} \times (1 - \varepsilon) \times Cp_{foam} \tag{4.19}$$

4.1.3.4 Cooling plate

Physical and thermophysical properties of aluminium have been considered for the cooling plate. Corrections should be applied for the thermal convection effect [36]. Corresponding properties for the coolong platr, then, is as follows:

- ρ= 2719 kg/m^3
- C_p= 871 J/kgK
- K = 202.4 W/mK

Table 4.2 shows the elements' properties used in the simulation. In order to have the exact heat generation rate, experimental methods such as calorimetry readings would give more reliable data whereby model verification will be more accurate.

Table 4.2 Thermo-physical properties of materials for simulation

Property/Component	**Cell**	**Cooling fin**	**Foam**
Density (kg/m^3)	4035	2719	277
Specific heat (J/kgK)	1027	871	1500
Thermal conductivity (W/mK)	$K_{x,y} = 25$, $K_z = 1$	202.4	0.083
Heat generation rate (kW/m^3)	22.8	0	0

4.1.4 Governing equations and constitutive laws

A specific partial; differential equation are used to describe each phenomena which comprises a transient term, diffusion term, convection term and a source term. By taking all these terms into account, a general equation can be derived as follows:

$$\frac{\partial}{\partial t}\left(\rho\Theta\right)+\nabla\cdot\left(\rho\vec{u}\Theta-\Gamma_{\Theta}\nabla\Theta\right)=S_{\Theta} \tag{4.20}$$

where Θ is 1, u, Y and h, in the continuity, momentum, species and energy equations, respectively. Γ_{Θ} and S_{Θ} are the diffusion coefficient and source terms which have consistent units. The main governing equation is energy equation to analyze the heat transfer in the model. In order to obtain the cell temperature distribution, an energy balance is applied. The expression for the conservation of energy is stated as

The net rate of change for internal and kinetic energy = The net rate energy change by convection (fluid flow) + The net rate of energy change by heat by conduction (heat) + The net rate of work

Here, the rate of change for internal and kinetic energy of element and is represented by the following formula

$$\frac{\partial}{\partial t}\left[\rho\left(\hat{u}+\frac{V^2}{2}\right)\right]dx\,dy\,dz \tag{4.21}$$

where $\hat{u}$ is internal energy.

The net rate of energy change by convection (fluid flow contribution) is

$$-\left\{\nabla.\left[\left(\hat{u}+\frac{V^2}{2}\right)\rho V\right]\right\}dx\,dy\,dz \tag{4.22}$$

The net rate of energy change by heat by conduction (heat contribution in the balance equation) is formulated as

$$-(\nabla.\ddot{q})\ dx\ dy\ dz \tag{4.23}$$

The net rate of work by element on the surroundings (works by body forces and surface forces), is

$$-\rho\ (V.g)dx\ dy - \left[\frac{\partial}{\partial x}\left(u\sigma_{xx} + v\tau_{xy} + w\tau_{xz}\right) + \frac{\partial}{\partial y}\left(u\tau_{yx} + v\sigma_{yy} + w\tau_{yz}\right) + \frac{\partial}{\partial z}\left(+u\tau_{zx} + v\tau_{zy} + w\sigma_{zz}\right)\right] dx\ dy\ dz \tag{4.24}$$

Substituting all terms into the Equation 4.1, yields the following equation:

$$\frac{\partial}{\partial t}\left[\rho\left(\hat{u} + \frac{V^2}{2}\right)\right] = -\nabla.\left[\left(\hat{u} + \frac{V^2}{2}\right)\rho V\right] - (\nabla.\ddot{q}) + \rho\ (V.g) + \left[\frac{\partial}{\partial x}\left(u\sigma_{xx} + v\tau_{xy} + w\tau_{xz}\right) + \frac{\partial}{\partial y}\left(u\tau_{yx} + v\sigma_{yy} + w\tau_{yz}\right) + \frac{\partial}{\partial z}\left(+u\tau_{zx} + v\tau_{zy} + w\sigma_{zz}\right)\right] \tag{4.25}$$

In Equation 4.21, the stress tensor has 9 normal and shear stresses which have symmetry and can be extracted from the momentum equation to simplify this equation, therefore

$$\rho\frac{D\hat{u}}{Dt} = -\nabla.\dot{q} + \left(\sigma_{xx}\frac{\partial u}{\partial x} + \tau_{yx}\frac{\partial u}{\partial y} + \tau_{zx}\frac{\partial u}{\partial z}\right) + \left(\tau_{xy}\frac{\partial v}{\partial x} + \sigma_{yy}\frac{\partial v}{\partial y} + \tau_{zy}\frac{\partial v}{\partial z}\right) + \left(\tau_{xz}\frac{\partial w}{\partial x} + \tau_{yz}\frac{\partial w}{\partial y} + \sigma_{zz}\frac{\partial w}{\partial z}\right) \tag{4.26}$$

In order to relate heat flux $\dot{q}$ to temperature field and eliminate normal and shear stresses, a constitutive equation is needed. For temperature fields, the constitutive equation is Fourier's law

$$\dot{q}_n = -k_n\frac{\partial T}{\partial n} \tag{4.27}$$

A Newtonian approximation can relate the stresses and velocity fields as the other set of constitutive equation

$$\tau_{xy} = \tau_{yx} = \mu\left(\frac{\partial v}{\partial x} + \frac{\partial u}{\partial y}\right) \tag{4.28}$$

Using these two equations, the principle equation of energy conservation (Equation 4.22) is arranged to

$$-\rho \frac{D\hat{u}}{Dt} = -\nabla . k\nabla T - p\nabla . V + \mu\varphi \tag{4.29}$$

where enthalpy h is $\hat{u} + \frac{p}{\rho}$. Differentiation of this equation and combining with the main equation leads to the energy equation in form of

$$\rho \frac{D\hat{h}}{Dt} = \nabla . k\nabla T + \frac{Dp}{Dt} + \mu\varphi \tag{4.30}$$

If temperature is of interest, enthalpy can be replaced by temperature as follows:

$$D\hat{h} = C_p dT + \frac{1}{\rho}(1 - \beta)\, dp \tag{4.31}$$

Here, β is coefficient of thermal expansion as

$$\beta = -\frac{1}{\rho}\left(\frac{\partial p}{\partial T}\right)_p \tag{4.32}$$

The resulting energy conservation equation is

$$\rho C_P \frac{DT}{Dt} = \nabla . k\nabla T + \beta T \frac{Dp}{Dt} + \mu\varphi \tag{4.33}$$

4.1.5 **Numerical implementation**

In order to obtain the thermal behaviour of the battery pack and cells, numerical simulations will be used based on the Finite Volume Method (FVM). In order to discretize the energy equation and other governing equations, FVM is one of the most applicable procedures in CFD. The computational domain is divided into a number of control volumes and the variable to be studied is set in the center. The governing equation in the differentiable form is integrated over each control volume. Between a cell's centroid, the variables are interpolated to have a profile for variations of the parameter like pressure or temperature. The resulting equation is a discretized equation in the domain. After obtaining a discretized equation, it is solved by a solver, along

with other equations and numerical techniques are employed to make the solution to be converged. For this purpose, there are specific steps briefly introduced in this section [125]. Due to the widespread application of ANSYS FLUENT software, there are many references and technical CFD forums that provide information about different aspects of software.

4.1.5.1 Mesh generation

By defining the domain and zones that require detailed analysis, a pre-processor like Gambit or ICEM can be used to generate the mesh. Because of the simple geometry of the sub-module, a structural mesh will be used in this step. The bottom-up method is used where the "edges" are meshed first. Depending on a successive ratio, zones adjacent to the interface or boundaries where the PCM is applied will be meshed in detail. Then "face" mesh will be generated by selecting the element of the mesh. The structured mesh will have the required specifications such as the mesh density in the zones of interest and other preliminary defined zones and boundary conditions. Refining of the mesh will lead to an increase in the number of grids which will increase the accuracy of the solution, but can increase the calculation time and cost at the same time. In simulation software, three steps of pre-processing, solver and post-processing are used to complete the analysis. In the finite volume method, each node of the grid should be enclosed by a corresponding control volume. The grid network with attributed characteristics will be exported to the solver software which is the commercial ANSYS FLUENT 12.0.1 in this study. In the mushy zone, there is pull velocity effect. Similar to the free convection, the change in the density can cause the pull velocity to be noticeable. Pull velocity effects are not effective in this study, since the mushy zone and leted part forms a very small fraction of study domain. Also discrete phase is not dominant here because the particles in the PCM do not exist unlike the case with the carrier fluid.

4.1.5.2 Employed solver and discretization scheme

The ANSYS FLUENT as a powerful solver will process the mesh file produced in a pre-processor. The governing integral equations for conservation of mass, energy, momentum and properties can be solved either by pressure-based or density-based solvers [122].

a) Pressure-Based solver

In this method, a pressure (or pressure correction) equation is solved to obtain the constraint of mass conservation of the velocity field. The pressure equation is derived from the continuity and the momentum equations in such a way that the velocity field, corrected by the pressure, satisfies the continuity. Due to non-linearity of governing equations, the solution process involves iterations wherein the entire set of governing equations is solved repeatedly until the solution converges. In each iteration, the coupled equations will be considered. There are two pressure-based solver algorithms in ANSYS FLUENT 12.0.1 software.

I. Pressure-Based segregated algorithm

In this method, sequentially (i.e., segregated from one another) solution of governing equations is employed by the solver. Again, the governing equations are non-linear and coupled, therefore, the solution loop must be carried out iteratively in order to obtain a converged numerical solution. Each governing equation is solved one after another. While being solved, each of the equations is “decoupled” or “segregated” from other equations. With the segregated algorithm, each iteration consists of the steps illustrated in Figure 4.8a.

II. Pressure-Based coupled algorithm

Unlike the segregated algorithm, the pressure-based coupled algorithm solves a coupled system of equations comprising the momentum equations and the pressure-based continuity equation. Steps 2 and 3 in the segregated solution algorithm, thus, are replaced by a single step in which the coupled system of equations are solved (Figure 4.8b).

b) Density-Based solver

The governing equations of continuity, momentum, energy and species transport are solved by density based solver, simultaneously. Governing equations for additional scalars will be solved afterward and sequentially (i.e., segregated from one another and from the coupled set). The iteration of solution loop is required again, to satisfy the convergence criteria. The nonlinearity of the equation, requires this approach. Each iteration consists of the steps illustrated in Figure 4.8c.

In both of the above mentioned methods, if the fluid flow is of interest, the velocity field is obtained from the momentum equations. Discretization used by both methods is similar and based on a finite volume approach. In order to solve the discrete equation, different approaches are used. In a pressure based solver, coupled and segregated approaches are used for discretization. In segregated methods, the governing equations are solved sequentially and separate from each other. Thus variables of interest like u, v, w, p, T and etc. will be solved one after another. In a coupled algorithm, a coupled system of equations is solved.

In preliminary versions of FLUENT software, a density based approach was developed to solve the compressible flows, but later on, both pressure-based and density- based solvers could solve the compressible flows. Furthermore, the pressure-velocity coupling is achieved by solving a pressure correction equation which is derived from the continuity and momentum equations. In this way, the velocity field, corrected by the pressure, satisfies the continuity. In order to model the transient and steady state problems, PISO and SIMPLE algorithms are employed respectively. An initialization step assigns the initial values to the variables. The proceeding algorithm can be summarized as follows:

- To obtain density, specific heat and other fluid properties.
- To solve the momentum equations based on updated values in the first step for pressure and face mass fluxes.
- To solve the pressure correction equation using the recently obtained velocity field and the mass flux.
- To correct face mass fluxes, pressure and the velocity field using the pressure correction obtained before. (This is used for the case that fluid flow is considered in the problem. For cases discussed in this proposal, PCM flow has not been considered).
- To solve the equations for the remaining scalar energy, using the current values of the solution variables.
- To update the source terms.
- To check for the convergence of the equations via the convergence criteria.

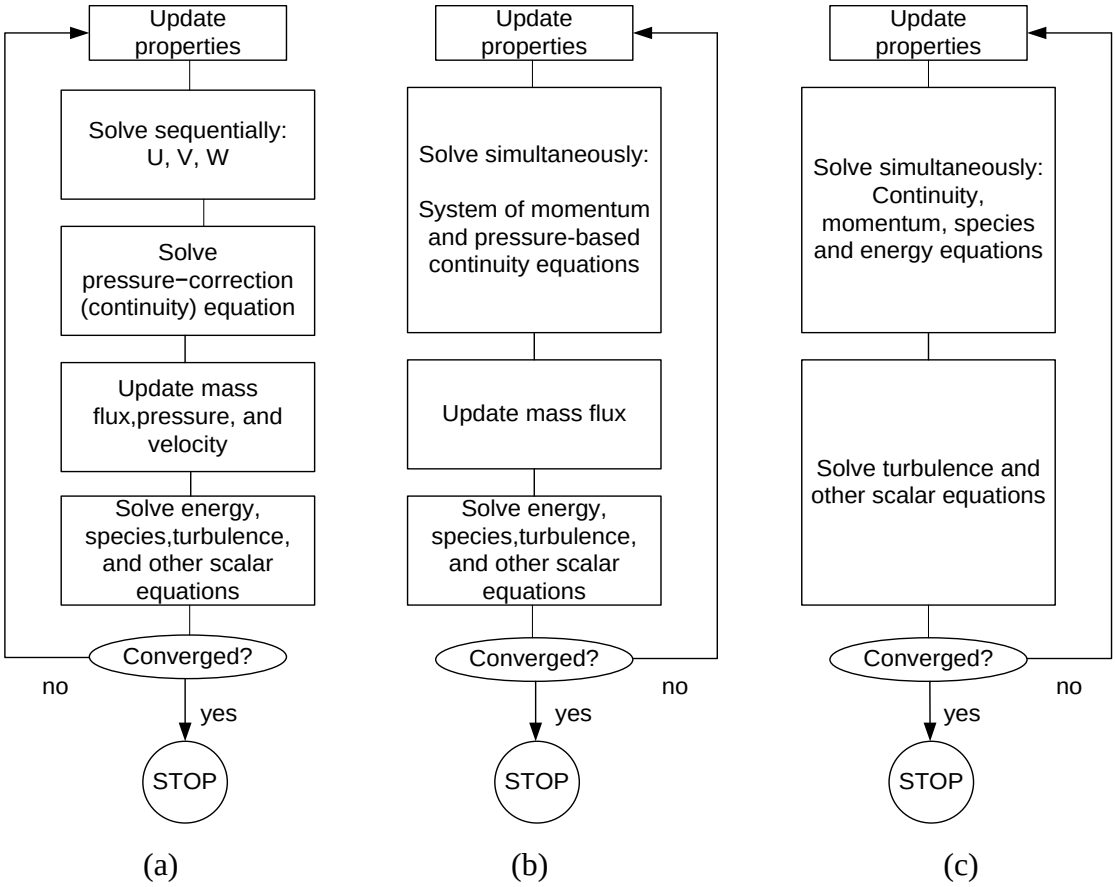

Figure 4.8 Overview of the available solvers in ANSYS FLUENT 12.01: (a) Pressure-Based Segregated Algorithm, (b) Pressure-Based Coupled Algorithm, (c) Density-Based Algorithm (adapted from [126]).

4.1.5.3 Discretization scheme

In order to convert a Partial Differential Equation (PDE) to an algebraic equation, a discretization technique is used and solved by numerical methods. The control volume technique consists of integrating the transport equation about each control volume. In this way, the conservation law on a control-volume is expressed by a discrete equation. Discretization of a transient, convection, diffusion and source terms and general form of governing equations, can be demonstrated by the following equation written in integral form for an arbitrary control volume V

$$\int_V \frac{\partial \rho\theta}{\partial t} dV + \oint \rho\theta\vec{v} d\vec{A} = \oint \Gamma_\theta \nabla\theta \, d\vec{A} + \int_V S_\theta dV \tag{4.34}$$

where $\rho, \vec{v}, \vec{A}, \Gamma_\theta, \nabla\theta$ and S_θ are density, velocity vector, surface area vector, diffusion coefficient, θ gradient and source of θ per unit volume, respectively. The above equation is applied to all cells or control volumes in the computational domain. A discretization of equation on a given cell leads to

$$\frac{\partial \rho\theta}{\partial t} V + \sum_{f}^{N_{force}} \rho_f \vec{v}_f \theta_f \vec{A}_f = \sum_{f}^{N_{force}} \Gamma_\theta \nabla\theta \, d\vec{A} + \int_V S_\theta dV \tag{4.35}$$

A common method to obtain temporal discretization for an arbitrary variable of β is

$$\frac{\partial \beta}{\partial t} = F(\beta) \tag{4.36}$$

Using backward differences as a first-order accurate method, a spatial discretization function of F can be written as

$$\frac{\beta^{n+1} - \beta^n}{\Delta t} = F(\beta) \tag{4.37}$$

First order implicit time integration leads to

$$\frac{\beta^{n+1} - \beta^n}{\Delta t} = F(\beta^{n+1}) \tag{4.38}$$

The final form to be solved at each time level iteratively is expressed as

$$\beta^{n+1} = \beta^n + \Delta t \, F(\beta^{n+1}) \tag{4.39}$$

The same methods are applicable to spatial discretization.

4.1.5.4 Under-Relaxation scheme

Changes of a dependent or auxiliary variable should have specific controlling possibility and constraints, which under-relaxation can be considered such a criteria. It is required to maintain the stability of the coupled, non-linear system of equations. In this concept, under-relaxation is a technique to stabilize the solution in order to achieve convergence. Basically well-posed problems with proper boundary conditions and grid network usually do not require a high reduction of under-relaxation factors. On the other hand, for non-linear and stiff problems, a

proper under-relaxation scheme is essential. When the under-relaxation applies, the process divides in steps in a way that the under-relaxed variable does not reach its final value directly, but technically, under-relaxation factors make the solution take a lot longer to converge.

4.1.5.5 Convergence criteria

There should be limiting criteria to control the variable, undertaking steps of iteration. In a numerical approach, this is used to stop the iterations. In order to control the convergence trend, a parameter called "residual" is defined to begin the solution procedure. When the residual sum for each of the variables is higher than a pre-defined value, iteration will continue until it reaches the defined amount. In this study, the residual for energy equations is set to 1×10^{-15}.

4.2 Heat exchanger design and optimization model

Based on the survey and operational condition, the shell and tube heat exchanger is selected as latent heat thermal energy storage system (LHTES). The main reasons for selecting shell and tube model of heat exchanger are as follows:

- Thermal loss form shell and tube configurations is minimal [61].
- Shell and tube heat exchangers require less charging and discharging time compared to other types [63].
- Shell and tube technology is inexpensive, easier to manufacture with lower maintenance costs [62].

4.2.1 Physical domain and heat exchanger configuration

As Figure 4.9 shows the coolant will flow through the copper tubes and PCM will be located in the shell space. The design process is explained in the following sections. Outer surface of the tank is considered to be insulated. This will lead to an increase in the heat exchanger effectiveness.

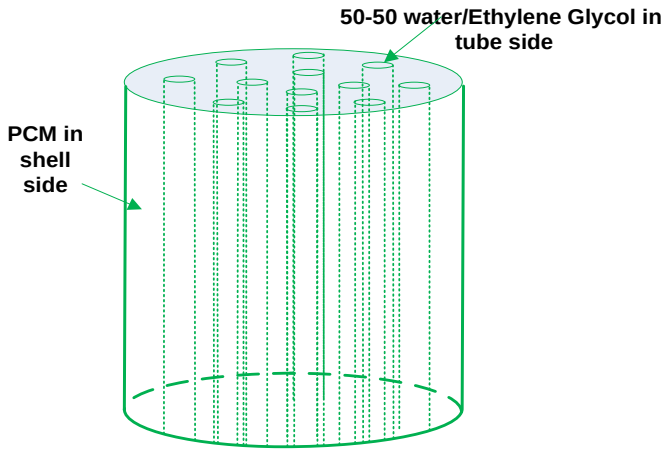

Figure 4.9 Physical model of heat exchanger

4.2.2 **PCM selection for the application**

Properties like congruent melting, neglected super-cooling due to their self-nucleating ability and compatibility with other materials like container materials (corrosivity and possible reactions) are advantages of organic PCMS. As explained earlier, inorganic materials have a high latent heat of fusion and their density is two times higher than organic materials. This property gives them the advantage of small volume and compactness, but incongruent melting and some corrosion and toxic properties make them unfavourable to use in sensitive cases like the current research. For instance, sodium hydroxide, as a salty hydrate PCM has a good thermal conductivity and less volume change, but it is very toxic and has corrosive properties. Therefore it cannot be considered as a thermal storage material here, though its latent heat of fusion is as high as 260 kJ/kg. For eutectics, the main part of their compound is inorganic materials which hold the same problems of inorganic materials in eutectics.

In order to narrow down the selection, with respect to properties of PCMs, iso-paraffin is not applicable to this research, because these PCMs have the disadvantage of temperature variations during freezing. This is in contrast with the assumption that constant temperature is needed to have effective thermal management in battery. For non-paraffin materials, like fatty acid, their high costs which can be as high as 2 times other PCMs is the main disadvantage of this group of organic materials comparing with paraffin organics. Characteristics of studied PCMs have been shown in Table 4.3 as important characteristics of PCMs.

Table 4.3 Characteristics of different PCM types

Inorganic compounds		Organic-paraffin						
Inorganics - Salty Hydrates	Inorganic compounds	Alkane-paraffin wax	Alkane-paraffin wax	paraffin wax(Alkanes)	paraffin wax(Alkanes)	Organic	Organic	**PCM Type**
Na2SO4.10H2O	satly hydrates	A20	A18	P-116 (n-paraffin)	6106 (n-paraffin)	n-paraffin	General	**Name**
32.4	various	36.4	28.2	47	43	various range	various range (6°C – 80°C)	**Melting Point (°C)**
254	high	248	244	210	189	relatively high	relatively high	**Latent Heat of Fusion (KJ/kg)**
1485		"	"	low (817 in solid phase)	low (910 in solid phase)	"	lower density comparing to salt hydrates and eutectics	**Compactness, Density ,solid (kg/m^3)**
0.544	higher than organic	"	"	0.21	0.21		low	**Thermal Conductivity (W/m*K)**
1.93 (S)				2.10 (S)	2.1 (solid)			**Specific Heat (KJ/kg*K)**
	low in cost	"	"			Relatively inexpensive	relatively inexpensive	**Material cost & availability**
						Relatively high (about 10%)	relatively high	**Volume Changes (Thermal Stresses)**
no (except Al.)	normal	No	No	No	No	No	No	**Corrosion**
harmful to contact direct	non-flammable					non-toxic	non-toxic flammable	**Non-toxic Material /Safety**
No					high	inert	good	**Chemical Stability**
incong.	incogr.					cong.	cong.	**Incongruent Melting**
Yes (max 14 °C)	yes						no	**Sub-cooling**

Organic Non-paraffin			Eutectics							
"	"	Non-paraffin organic	Eutectics	Eutectics	Eutectics	"	"	"	"	"
acid (Lauric Acid	fatty acid (Capric Acid)	fatty acids	Propionamide-25.1% Palmitic Acid -74.9%	Ca(NO3)2.4H20-67% Mg(NO3)2.6H2O-33%	-	Na2S2O3.5H2O	KF.2H2O	Zn(SO3)2.6H2O	Na2Co3.10H20	Na2HPO4.12H2O
43	32	various range	50	30	Low	48	42	36.4	36	35
178	153	Medium	192	136	higher than organic	201	117	147	247	281
870	886	760 -910	1160 (liq.)	-		1730	1670	2065	1438	1520
0.147	0.149	"			higher than organic	-	-	-	-	0.476
1.60 (Solid)	-					2.39(lis) 1.46 (S)	1.51 (s)	2.26 (liq) 1.34 (s)	-	1.7 (s)
		Less expensive than paraffin waxes.			higher than other PCMs					
"	10% (23 degree-80 deg)	small 10% (23 degree-80 deg)			high and non homogenous					
					corrosive	no (except Al.)	no (exept Al.)	no (except Al.)	no (except Al.)	No (exept Al.)
			Depending	Depending	Depending	harmful to contact direct	harmful to contact direct	harmful to contact direct	harmful to contact direct	harmful to contact direct
						No	No	No	No	No
					cong.	incongg.	incong.	incong.	incong.	incong.
no	no	no				yes	yes (max 35 °C)	yes	yes	yes

Characteristics such as incongruent melting, high latent heat of fusion, and no corrosivity lead to the selection of organic, paraffin wax PCM. It can be seen that pure alkanes such as A18 or A20, are more convenient to use, though the prices should be taken into account. For example, A20 has a higher latent heat of fusion (248 kJ/kg) than P116 (210 kJ/kg) and at the same time its melting point is about 37℃ which is more reasonable for thermal management of Li-ion batteries to keep their temperature constant. The disadvantage of low thermal conductivity can be improved by certain methods like encapsulation or embedding the PCM inside a graphite matrix and other methods. Normal or linear Alkanes like Eicosane are colorless, non-polar and non-reactive and insoluble in water.

By considering the operating temperature, the melting point of Eicosane is large to be used for cooling the Li-ion cells. From the same category, normal-Octadecane is selected for the current study. Its melting point is around 29.5℃, which makes it more suitable for the current application and for controlling the temperature, and was selected to use for experiments.

4.2.3 Nano-particles and PCM mixture for thermal conductivity enhancement

By mixing the nanotubes in the PCM, the effective properties will be changed. The predicted thermal conductivity of the mixture is introduced as a designing parameter of the heat exchanger. The equations have been derived for the case that there is carrying fluid (f) and PCM as additive. Thus, in a similar way, it is assumed that PCM particles are carried by the CNT as it has replaced the flow. Note that the series configuration for PCM means the parallel arrangement for CNTs. In this case, the following equations are obtained. C is defined as the mass concentration in the foam and PCM.

$$c = \frac{V_{pcm}}{V_{tot}} = \frac{V_{pcm}}{V_{pcm}+V_{cnt}} \tag{4.40}$$

$$k_{eff,parallel} = \left(\frac{c}{k_{pcm}} + \frac{1-c}{k_{cnt}}\right)^{-1} \tag{4.41}$$

$$k_{eff,series} = ck_{pcm} + (1-c)k_{cnt} \tag{4.42}$$

As defined before, the ratio of thermal conductivities is given as follows:

$$\frac{k_{eff}}{k_{cnt,parallel}} = \left(c\frac{k_{cnt}}{k_{pcm}} + (1-c)\right)^{-1} \tag{4.43}$$

$$\frac{k_{eff}}{k_{cnt,series}} = c\frac{k_{pcm}}{k_{cnt}} + (1-c) \tag{4.44}$$

4.2.4 Thermal modeling of heat exchanger

LMTD method is applied here for predicting the heat exchanger performance. The rate of heat transfer is estimated as [127]

$$Q = UA_{tot}\Delta T_{lm} = (\dot{m}c_p\Delta T)_h = (\dot{m}c_p\Delta T)_c \tag{4.45}$$

where ΔT_{lm} is the logarithmic mean temperature as

$$\Delta T_{lm} = \frac{(T_{h,i} - T_c) - (T_{h,o} - T_c)}{\ln((T_{h,i} - T_c)/(T_{h,o} - T_c))} \tag{4.46}$$

Here, h and c are subscripts of hot and cold stream. U is the overall heat transfer coefficient and A_{tot} is total heat transfer surface.

$$U = \frac{1}{\frac{A_o}{A_i}\frac{1}{h_i} + \frac{1}{\eta_o h_o} + \frac{R_{f,o}}{\eta_o} + \frac{A_o}{A_i}R_{f,i} + A_o R_w} \tag{4.47}$$

$$A_{tot} = A_b + N_f \times s_f \tag{4.48}$$

$where\ A_b$ and A_i are outside base and internal heat transfer surface area defined as

$$A_b = \pi d_o N_f (s_f - t) \tag{4.49}$$

$$A_i = \pi d_i N_f s_f \tag{4.50}$$

Here, d_i, d_o, t, N_f and s_f are inside and outside tube diameters, fin thickness, number of fins and distance between the fins. Moreover η_o in Equation 4.47 is overall surface efficiency defined as follow and R_w is wall thermal resistance.

$$\eta_o = 1 - \frac{N_f A_f}{A_{tot}}(1-\eta_f) \tag{4.51}$$

where η_f is the efficiency of a single fin. It is worth mentioning that the fin's efficiency is unit when there is no fin. Considering the circular fin [127] for the external surface, the fin efficiency is defined as

$$\eta_f = \frac{C_2\left[K_1(mr_1)I_1(mr_{c2}) - I_1(mr_1)K_1(mr_{c2})\right]}{\left[I_0(mr_{r1})K_1(mr_{c2}) + K_0(mr_1)I_1(mr_{c2})\right]} \tag{4.52}$$

where I and K are modified Bessel function of first and second kind. In addition C_2 and m are given as follows:

$$C_2 = \frac{2r}{m(r_{2c}^2 - r_1^2)} \tag{4.53}$$

$$m = \sqrt{\frac{2h_o}{k_w t}} \tag{4.54}$$

Here, convection heat transfer coefficient in tube side, h_i is calculated based on the corresponding Reynolds number as follows [128]:

$$h_i = \frac{k_f}{d_i}.\left(3.657 + \frac{0.0677.(\mathrm{Re}.\mathrm{Pr}.d_i / L)^{1.33}}{1 + 0.1.\mathrm{Pr}(\mathrm{Re}.d_i / L)^{0.3}}\right) \qquad for \qquad \mathrm{Re} \le 2300 \tag{4.55}$$

$$h_i = \frac{k_f}{d_i}.\left\{\frac{\frac{f}{2} \times (\mathrm{Re} - 1000).\mathrm{Pr}}{1 + 12.7.\sqrt{\frac{f}{2}}\left(\mathrm{Pr}^{0.67} - 1\right)}\right\} \qquad for \qquad 2300 < \mathrm{Re} \le 10000 \tag{4.56}$$

where friction factor for this case is $f = (1.58\log(\mathrm{Re}) - 3.28)^{-2}$

$$h_i = \frac{k_f}{d_i}.\left\{\frac{\frac{f}{2} \times \mathrm{Re}.\mathrm{Pr}}{1.07 + \frac{900}{\mathrm{Re}} - \frac{0.63}{1 + 10\,\mathrm{Pr}} + 12.7.\sqrt{\frac{f}{2}}\left(\mathrm{Pr}^{0.67} - 1\right)}\right\} \qquad for \qquad \mathrm{Re} > 10000 \tag{4.57}$$

Here, friction factor $f = 0.00128 + 0.1143(\mathrm{Re})^{-0.311}$ and *Re* is Reynolds number which is defined as

$$\mathrm{Re} = 4\dot{m}/(\pi d_i \mu N) \tag{4.58}$$

Here, N is the number of tubes. Furthermore, the pressure drop and outside convection heat transfer coefficient (h_o) are calculated as

$$\Delta P = 4NfL\dot{m}^2/(\rho\pi^2 d_i^2) \tag{4.59}$$

Once the heat transfer inside the tube is calculated, the heat transfer coefficient for the outer surface is required. To calculate this value, the outer surface Nusselt number is calculated first.

$$h_o = \frac{Nu \times k_f}{\Delta r_m} \tag{4.60}$$

Here, k_f, Δr_m and Nu are PCM conductivity, thickness of heat storage material and Nusselt number. Similar to internal surface of the tube, the equivalent Reynolds number is the criterion to select the proper equation

$$Nu = 0.28\left(\frac{\Delta r_m Ra}{L}\right)^{0.25} \qquad for \qquad Ra \geq 1000\, and\, \Delta r_m \leq 0.006 \tag{4.61}$$

$$Nu = 1 \qquad for \qquad Ra < 1000\, and\, \Delta r_m \leq 0.006 \tag{4.62}$$

$$Nu = 0.133(Ra)^{0.326}\left(\frac{\Delta r_m}{L}\right)^{0.0686} \qquad for \qquad \Delta r_m > 0.006 \tag{4.63}$$

where R_a = Gr. Pr amd Grashof number is $Gr = \dfrac{g\beta(T_{h,i} - T_c)\Delta r_m{}^3}{\upsilon^2}$

$$D_s = 0.637\, p_t \sqrt{(\pi N_t)CL/CTP} \tag{4.64}$$

Here, D_s, L and Ra are diameter of the heat exchanger, length of the tubes and Rayleigh number, respectively. Also, p_t tube is pitch and CL is tube layout constant that has a unit value for 45° and 90° tube arrangement and 0.87 for 30° and 60° tube arrangement. Also CTP is tube count

constant which is 0.93, 0.9, 0.85 for single pass, two passes and three passes of tubes, respectively [129].

4.2.5 **Genetic algorithm**

Optimization algorithms have received increasing attention by research communities and industry. In the area of evolutionary computation (EC), an optimization algorithm an evolutionary process is simulated. The idea behind this method is to evolve solutions by means of crossover, mutation, and selection based on their quality (fitness) with respect to the optimization problem at hand [130].

Due to capability of evolutionary algorithms (EAs), they are highly relevant for industrial applications, because they can handle problems with non-linear constraints, multiple objectives, and dynamic components properties that frequently appear in real problems [131]. Genetic algorithms (GAs) are an optimization technique based on natural genetics. Holland [132] developed this genetic algorithm (GA) as an optimization method in an attempt to simulate growth and decay of living organisms in a natural environment. It is proved that GAs are powerful optimization technique, Even though they are originally designed as simulators. This method is capable to find the global optimum, or a near-optimal point, for any optimization problem. A set of points inside the optimization space is created by random selection of points. In the next step, the selected set of points is transferred into a new group. Moreover, this new set will contain more points that are closer to the global optimum. The only required information in GA is how optimal each point is in the optimization space. This simplicity makes GAs attractive as optimizers. Two major advantages of the GAs are that i) Constraints of any type can be easily implemented and ii) GAs usually finds more than one near-optimal point in the optimization space, thus permitting the use of the most applicable solution for the optimization problem at hand.

The basic steps for the application of a GA for an optimization problem are summarized in Figure 4.9 [130]. A set of strings is created randomly. This set, which is transformed continuously in every step of the GA, is called population. This population, which is created randomly at the start, is called initial population. The size of this population may vary from several tens of strings to several thousands. The criterion applied in determining an upper bound

for the size of the population is that further increase does not result in improvement of the near-optimal solution.

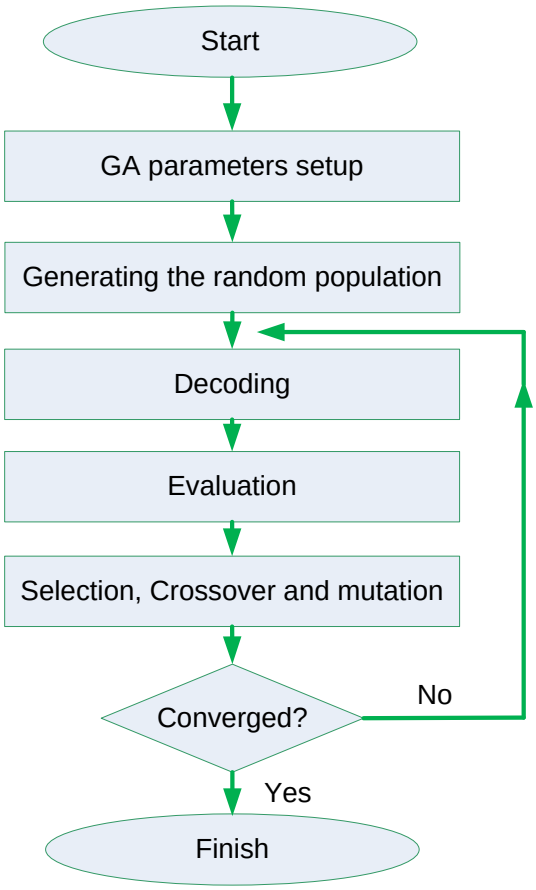

Figure 4.10 Genetic algorithm flowchart for heat exchanger

This upper bound for each problem is determined after some test runs. Nevertheless, for most applications the best population size lies within the limits of 10-100 strings .The "optimality" (measure of goodness) of each string in the population is calculated. Then on the basis of this value an objective function value, or fitness, is assigned to each string. This fitness is usually set as the amount of "optimality" of each string in the population divided by the average population "optimality". An effort should be made to see that the fitness value is always a positive number. It is possible that a certain string does not reflect an allowable condition. For such a string there is no "optimality". In this case, the fitness of the string is penalized with a very low value, indicating in such a way to the GA that this is not a good string. Similarly, other constraints may be implemented in the GA. A set of "operators", a kind of population transformation device, is applied to the population. These operators will be discussed later.

A new population is created as a result of the operators. It is expected to consist more strings in the next generations. Usually a maximum number of generations to be performed by the GA, which is considered as a predefined stopping criterion, are checked. If this criterion is not satisfied a new generation is started, otherwise the GA terminates. In this way, it is clear that a set of points (final population) has been defined, when the GA terminates. This population contains more than one equivalently good (optimal) point may exist. This property is considered as an advantage of the Gas which permits the selection of the most appropriate solution for the optimization problems.

4.3 Exergy model

The efficiency of the thermal management systems in EVs and HEVs is very crucial due to the limited onboard energy resources in electrified transportation systems as well as the overall impact on vehicle performance, operational cost and the environmental impact. Therefore, It is of great importance to have a good understanding of the efficiencies associated with the system and its components. Considering this priority in the vehicle, an effective assessment method is very deterministic. As it is mentioned in Chapters 2 and 3, energy-based efficiencies may lead to inadequate and misleading conclusions. This is because of ignoring the ambient temperature and also assuming the energy as number which can be added, without notice to the direction of the energy flow. The second law of thermodynamics defines the energy conversion limits of this available energy based on irregularities between different forms of energies. Reference environment as well as the success level of this conversion capacity, and needs to be considered to prevent any incomplete and/or incorrect results, are effective on defining the quality of the energy. An analysis for examining the work potentials of the initial and final stages of a system can give an evaluation criterion for the quality of the energy which will be related to overall efficiency. Such analysis is called “exergy analysis”, which represents the amount of energy that may be totally converted to work [65, 66].

As a definition, exergy of a system is the “maximum shaft work that can be done by the composite of the system and a specified reference environment” [133]. In every thermal management system, heat transfer within the system, or between the system and surrounding environment, occurs at a finite temperature difference. This effect is very important in creating irreversibilities for the system. All real processes, including natural events are irreversible and

the system performance degrades as a result of these irreversibilities in each individual thermodynamic process that makes up the system. Irreversibilities reduces the work potential which in turn, makes the corresponding amount of energy becomes unusable [65]. Entropy generation plays an important role in measuring the effect of these irreversibilities in a system during a process. By calculating the irreversibilities and comparing them with each other, it helps compare each component in the system based on how much they contribute to the operation inefficiencies of the overall system. Even though energy analysis is almost traditional method in analysing the engineering processes, but it possesses specific short comes and is only concerned with the conservation of energy, which neither takes the corresponding environmental conditions into account, nor provides how, where and why the system performance degrades. As a result, the energy analysis only measures the quantity of energy and does not reveal the full efficiencies of the system [134]. Recalling these disadvantage of energy analysis, in this present, exergy analysis is used to assess the thermal management system efficiency and to have a big picture about true efficiencies of the components by determining the irreversibilities in each cycle, as well as the overall exergy efficiency of the system and how nearly the respective performances approach ideal conditions. The true magnitude of losses, and their causes and locations are identified by investigating the exergy destruction By analyzing both the quality and the quantity of the energy, in order to improve the individual components and overall system [133, 134].

Similar to any other system to be analysed, first components of the system should be clarified in detail which can help the to increase the efficiency. The following section, describes the considered passive thermal management system.

4.3.1 Energy and exergy analyses

In the first step of the exergy analysis, the mass, energy, entropy and exergy balances are needed in order to determine the heat input, rate of entropy generation and exergy destruction as well as energy and exergy efficiencies.

4.3.1.1 Governing equations

In general, a balance equation for a quantity in a system may be written as follows:

$$Input + Generation - Output - Consumption = Accumulation \quad (4.65)$$

where input and output terms refer to quantities entering and exiting through the system, respectively. Generation and consumption terms refer to quantities produced or consumed within the system, and the accumulation term refers to potential build-up of the quantity within the system [135]. In steady-state conditions, however, all properties are unchanging with time and therefore, all the transient accumulation terms become zero. Thus, under the steady-state assumption, the balance equations for mass, energy, entropy and exergy can be written as follows:

$$\dot{m}_{in} = \dot{m}_{out} \tag{4.66a}$$

$$\dot{E}_{in} = \dot{E}_{out} \tag{4.66b}$$

$$\dot{S}_{in} + \dot{S}_{gen} = \dot{S}_{out} \tag{4.66c}$$

$$\dot{E}x_{in} = \dot{E}x_{out} + \dot{E}x_{D} \tag{4.66d}$$

where $\dot{S}_{gen} = \dot{m}\Delta s$ and $\dot{E}x_D = T_0\,\dot{S}_{gen}$, $\dot{m}$ and $\dot{E}$ are associated with the mass flow rate and energy transfer rate and show that the respective total rates in / out across the boundary are conserved (neglecting reactions). $\dot{S}$ is the entropy flow rate or generation rate. The amount transferred out of the boundary must exceed the rate in which entropy enters, the difference being the rate of entropy generation within the boundary due to associated irreversibilities. As the previous equations, in these balance equations, $\dot{E}x$ is the exergy flow rate and it shows that exergy transferred out of the boundary must be less than the rate in which exergy enters, the difference being the rate of exergy destruction (or lost work) within the boundary due to associated irreversibilities. *Gouy-Stodola* theorem is used to calculated these values by using dead-state temperature (T_0) multiplied by the entropy generation rate.

Minimum exergy destruction, or minimum entropy generation, design characterizes a system with minimum destruction of available work, which in the case of refrigeration plants, is equivalent to the design with a maximum refrigeration load, or minimum mechanical power input [136]. In cooling systems, T_0 usually equals to the temperature of the high-temperature medium T_H [137]. In addition, the specific flow exergy associated with the coolant medium is given below:

$$ex_{coolant} = (h - h_0) + \frac{1}{2}V^2 + gZ - T_0(s - s_0) \tag{4.67}$$

Considering a system at rest relative to the environment, kinetic and potential terms can be ignored:

$$ex_{coolant} = (h - h_0) - T_0(s - s_0) \tag{4.68}$$

The exergy rate is determined as

$$\dot{E}x = \dot{m}\, ex \tag{4.69}$$

After describing the TMS configuration and parameters along with the fundamental principles of the exergy, the TMS can be studied with respect to energy and exergy analyses based on the aforementioned system model. Ideally, in the thermal management system, the refrigerant travels through the condenser at constant pressure by heat absorption and exits the condenser as a saturated liquid. Moreover, the refrigerant is compressed isentropically in the compressor before entering the condenser and expanded isenthalpically in the thermal expansion valve before entering the evaporator. The refrigerant also flows through the evaporator at constant pressure by heat rejection and exits the evaporator as a saturated vapor. However, practical applications deviate from ideal conditions due to pressure and temperature drops associated with the refrigerant flow and heat transfer to/from the surroundings. During the compression process, entropy changes due to the irreversibilities and heat transfer to / from the surroundings. There is also some pressure drop as the refrigerant flows through the condenser and evaporator as modeled in the previous section. Furthermore, the refrigerant is sub-cooled as it is leaves the condenser (and may drop further before reaching the expansion valve) and slightly superheated (due to the pressure losses caused by friction) as it leaves the evaporator (and enters the compressor).

As the refrigerants flows to the compressor, its e temperature increases more , increasing its specific volume, which increases the work of the compressor. On the coolant side, the coolant is pumped to the battery, where the pressure increases significantly with a slight increase on its temperature. The coolant then exchanges heat with the battery module without any phase change in the medium. Subsequently, the coolant enters the chiller in order to transfer the heat to the refrigerant cycle and enters the pump again to make up for the lost pressure before re-entering the battery.

For the compressor:

M.B.E $$\dot{m}_1 = \dot{m}_2 = \dot{m}_r \quad (4.70a)$$

E.B.E $$\dot{m}_1 h_1 + \dot{W}_{comp} = \dot{m}_2 h_2 \quad (4.70b)$$

En.B.E $$\dot{m}_1 s_1 + \dot{S}_{gen,comp} = \dot{m}_2 s_2 \quad (4.70c)$$

Ex.B.E $$\dot{m}_1 ex_1 + \dot{W}_{comp} = \dot{m}_2 ex_2 + \dot{E}x_{D,comp} \quad (4.70d)$$

where $\dot{E}x_{D,comp} = T_0\,\dot{S}_{gen,comp} = \dot{m}T_0(s_2 - s_1)$ and exergetic efficiency is defined as

$$\eta_{ex,comp} = \frac{(\dot{E}x_{2,act} - \dot{E}x_1)}{\dot{W}_{comp}} = 1 - \frac{\dot{E}x_{D,comp}}{\dot{W}_{comp}}$$

where $\dot{W}_{comp}$ is the compressor power input in kW. Moreover, the isentropic efficiency of the adiabatic compressor is defined as

$$\eta_{comp} = \frac{\dot{W}_s}{\dot{W}} = \frac{h_{2,s} - h_1}{h_2 - h_1} \quad (4.71)$$

Here, $\dot{W}_s$ is the isentropic power and $h_{2,s}$ is the isentropic (i.e, reversible and adiabatic) enthalpy of the refrigerant leaving the compressor.

For the condenser:

M.B.E $$\dot{m}_2 = \dot{m}_3 = \dot{m}_r \quad (4.72a)$$

E.B.E $$\dot{m}h_2 = \dot{m}h_3 + \dot{Q}_{cond} \quad (4.72b)$$

En.B.E $$\dot{m}_2 s_2 + \dot{S}_{gen,cond} = \dot{m}_3 s_3 \quad (4.72c)$$

Ex.B.E $$\dot{m}_2 ex_2 = \dot{m}_3 ex_3 + Ex_{Q_H} + \dot{E}x_{D,cond} \quad (4.72d)$$

where $\dot{E}x_{D,cond} = T_0\,\dot{S}_{gen,cond} = \dot{m}T_0\left(s_3 - s_2 + \frac{q_H}{T_H}\right)$ and similar to compressor, the efficiency of condenser can be defined as

$$\eta_{ex,cond} = \frac{\dot{E}x_{\dot{Q}_H}}{\dot{E}x_2 - \dot{E}x_3} = 1 - \frac{\dot{E}x_{D,cond}}{\dot{E}x_2 - \dot{E}x_3} \text{ and } \dot{E}x_{\dot{Q}_H} = \dot{Q}_H\left(1 - \frac{T_0}{T_H}\right)$$

Here $\dot{Q}_H$ is the heat rejection from the condenser to the high-temperature environment.

For the thermal expansion valve before the evaporator (the expansion process is considered isenthalpic)

M.B.E $\dot{m}_3 = \dot{m}_4 = \dot{m}_r$ (4.73a)

E.B.E $h_3 = h_4$ (4.73b)

En.B.E $\dot{m}_3 s_3 + \dot{S}_{gen,TXV} = \dot{m}_4 s_4$ (4.73c)

Ex.B.E $\dot{m}_3 ex_3 = \dot{m}_4 ex_4 + \dot{E}x_{D,TXV}$ (4.73d)

where $\dot{E}x_{D,TXV} = T_0\, \dot{S}_{gen,TXV} = \dot{m}T_0(s_4 - s_3)$ and exergetic efficiency is defined as

$$\eta_{ex,TXV} = \frac{\dot{E}x_4}{\dot{E}x_3}$$

For the evaporator:

M.B.E $\dot{m}_4 = \dot{m}_1 = \dot{m}_r$ (4.74a)

E.B.E $\dot{m}h_4 + \dot{Q}_L = \dot{m}h_1$ (4.74b)

En.B.E $\dot{m}_4 s_4 + \dot{S}_{gen,evap} = \dot{m}_1 s_1$ (4.74c)

Ex.B.E $\dot{m}_4 ex_4 + Ex_{Q_L} = \dot{m}_1 ex_1 + \dot{E}x_{D,evap}$ (4.74d)

Here $\dot{E}x_{D,evap} = T_0\, \dot{S}_{gen,evap} = \dot{m}T_0\left(s_1 - s_4 + \frac{q_L}{T_L}\right)$

Efficiency: $\eta_{ex,evap} = \frac{\dot{E}x_{\dot{Q}_L}}{\dot{E}x_4 - \dot{E}x_1} = 1 - \frac{\dot{E}x_{D,evap}}{\dot{E}x_4 - \dot{E}x_1}$ And exergetic efficiency is $defined\ as$

$$\dot{E}x_{\dot{Q}_L} = -\dot{Q}_L\left(1 - \frac{T_0}{T_L}\right) \quad (4.75)$$

where $\dot{Q}_L$ is the heat taken from the low-temperature environment to the evaporator. For the chiller the balance equations will be similar. Ina similar way, the exergetic efficiency is

$$\textit{Efficiency} \quad \eta_{ex,ch} = \frac{\dot{E}x_{\dot{Q}_{ch}}}{\dot{E}x_5 - \dot{E}x_{1''}} \quad (4.76)$$

Here, $\dot{Q}_{ch} = \dot{m}_{cool}(h_7 - h_6)\ \ and\ \ \dot{E}x_{\dot{Q}_{ch}} = -\dot{Q}_{ch}\left(1 - \frac{T_0}{T_7}\right)$

The enthalpy and entropy changes in the water/glycol mixture of 50/50 by weight are calculated by assuming the specific heat remains constant as follows[138]:

$$h_7 - h_6 = C_{wg}(T_7 - T_6)\ and\ s_7 - s_6 = C_{wg}\ln\left(\frac{T_7}{T_6}\right) \quad (4.77)$$

For the pump the exergetic efficiency is defined as follows:

$$\eta_{ex,pump} = \frac{(\dot{E}x_{8,act} - \dot{E}x_7)}{\dot{W}_{pump}} \tag{4.78}$$

For the battery

M.B.E $$\dot{m}_8 = \dot{m}_6 = \dot{m}_{cool} \tag{4.79a}$$

E.B.E $$\dot{m}_{cool}h_8 + \dot{Q}_{bat} = \dot{m}_{cool}h_6 \tag{4.79b}$$

En.B.E $$\dot{m}_{cool}s_8 + \dot{S}_{gen} = \dot{m}_{cool}s_6 \tag{4.79c}$$

Ex.B.E $$\dot{m}_{cool}ex_8 + \dot{E}x_{\dot{Q}_{bat}} = \dot{m}_{cool}ex_6 + \dot{E}x_{D,bat} \tag{4.79a}$$

For the phase change material heat exchanger the balance equations are as follows:

M.B.E $$\dot{m}_{10} = \dot{m}_{11} = \dot{m}_{PCM} \tag{4.80a}$$

E.B.E $$\dot{m}_{pcm}h_{10} + \dot{Q}_{pcm} = \dot{m}_{cool}h_{11} \tag{4.80b}$$

En.B.E $$\dot{m}_{pcm}s_{10} + \dot{S}_{gen} = \dot{m}_{pcm}s_{11} + \frac{\dot{Q}_{pcm}}{T_0} \tag{4.80c}$$

Ex.B.E $$\dot{m}_{pcm}ex_{10} + \dot{E}x_{\dot{Q}_{pcm}} = \dot{m}_{pcm}ex_{11} + \dot{E}x_{D,pcm} \tag{4.80d}$$

For the entire cooling system, the energetic coefficient of performance (COP) becomes

$$COP_{en,system} = \frac{\dot{Q}_{evap} + \dot{Q}_{ch} + \dot{Q}_{pcm}}{\dot{W}_{comp} + \dot{W}_{pump}} \tag{4.81}$$

Ideal energy models are more efficient which is mainly because of irreversibilities in the real systems. As given in the previous equations, a smaller temperature difference between the heat sink and heat source provides higher cooling system efficiency. Thus, the aim of the exergy analysis is to determine the system irreversibilities by calculating the exergy destruction in each component and to calculate the associated exergy efficiencies. This methodology helps to focus on the parts where the greatest impact can be achieved on the system since the components with larger exergy destruction also have more potential for improvements. Table 4.4 gives the exergy destruction calculations and results for each component. For the overall system, the total exergy destruction of the cycle can be calculated by adding the exergy destruction associated with each component that was previously calculated.

Table 4.4 Exergy destruction rates for each component in the TMS.

Component	**Exergy Destruction Rate Equations**
Battery	$\dot{E}x_{D,bat} = T_0\dot{m}_{cool}\left(C_{wg}\ln(T_6/T_8)\right)$
PCM tank	$\dot{E}x_{D,pcm} = T_0\dot{m}_{pcm}\left(C_{wg}\ln(T_{11}/T_{10})\right)+\dot{Q}_{pcm}$
Evaporator TXV	$\dot{E}x_{D,evap,TXV} = T_0\dot{m}_{r1}(s_4 - s_3)$
Chiller TXV	$\dot{E}x_{D,ch,TXV} = T_0\dot{m}_{r2}(s_5 - s_3)$
Evaporator	$\dot{E}x_{D,evap} = T_0[\dot{m}_e(s_{e2} - s_{e1}) - \dot{m}_{r1}(s_4 - s_1)]$
Chiller	$\dot{E}x_{D,ch} = T_0\left[\dot{m}_{cool}\left(C_{wg}\ln(T_6/T_7)\right) - \dot{m}_{r2}(s_5 - s_1)\right]$
Pump	$\dot{E}x_{D,pump} = T_0\dot{m}_{cool}\left(C_{wg}\ln(T_6/T_0)\right)$
Condenser	$\dot{E}x_{D,cond} = T_0[\dot{m}_c(s_{c2} - s_{c1}) - \dot{m}_r(s_2 - s_3)]$
Condenser	$\dot{E}x_{D,cond} = T_0[\dot{m}_c(s_{c2} - s_{c1}) - \dot{m}_r(s_2 - s_3)]$

For the overall system, the total exergy destruction of the system can be calculated by adding the exergy destruction associated with each component that was previously calculated.

$$\dot{E}x_{D,system} = \dot{E}x_{D,comp} + \dot{E}x_{D,cond} + \dot{E}x_{D,evap,TXV} + \dot{E}x_{D,ch,TXV} + \dot{E}x_{D,evap} + \dot{E}x_{D,ch} + \dot{E}x_{D,pump} + \dot{E}x_{D,battery} + \dot{E}x_{D,pcm} \quad (4.82)$$

Finally, for the thermodynamic analysis, using the aforementioned exergy equations, the exergetic COP of the system can be calculated as

$$COP_{ex,system} = \frac{\dot{E}x_{\dot{Q}evap} + \dot{E}x_{\dot{Q}ch} + \dot{E}x_{\dot{Q}pcm}}{\dot{W}_{comp} + \dot{W}_{pump}} \quad (4.83)$$

4.3.2 **Exergoeconomic analysis**

Exergy analyses can be used to improve the efficiencies of the components and corresponding systems,. However, the feasibility of applying these improvements is generally constrained by the limitation of financial resources and providing the required equipment for the analyses. In addition to taht, the approaches taken by purely scientific motivation may not always be cost

effective , in many cases Thus, in order to achieve the optimum design for energy systems, techniques combining scientific disciplines (mainly thermodynamics) with economic disciplines (mainly cost accounting) should be utilized.

Conventional based methods are normally used to design various thermal management systems. Scientific analyses, experimental data and practical experience are employed in these methods. Most of these systems are often operating outside of their optimum parameters which results in inefficient use of resources, increasing production costs and adverse environmental impact. The objective of exergoeconomic analysis is to determine the inefficiencies in the system and calculate the associated costs [139]. In this section, an exergy costing method (SPECO method) is used for the analysis [140, 141].

4.3.2.1 Cost Balance equations

In order to conduct an exergoeconomic analysis, the cost flow rate, $\dot{C}$ ($\$/h$), is defined for each flow in a system, and a cost balance is written for each component to provide exergy costing as follows:

$$\dot{C}_{q,k} + \sum_i \dot{C}_{i,k} + \dot{Z}_k = \sum_e \dot{C}_{e,k} + \dot{C}_{w,k} \tag{4.84}$$

where $\dot{C}_j = c_j \dot{E}x_j$

Exergy rates for streams, work and heat transfer are written as follows:

$$\dot{C}_i = c_i \dot{E}x_i = c_i \, \dot{m}_i ex_i \tag{4.85a}$$

$$\dot{C}_e = c_e \dot{E}x_e = c_e \, \dot{m}_e ex_e \tag{4.85b}$$

$$\dot{C}_w = c_w \dot{W} \tag{4.85c}$$

$$\dot{C}_q = c_q \dot{E}x_q \tag{4.85d}$$

However, before the analysis can be conducted, the fuel and product exergies are needed to be defined for each component. The product exergy is defined according to the purpose of owning and operating a component under consideration, while the fuel represents the resources consumed in generating the product, where both are expressed in terms of exergy [142]. The fuel and products for each component can be seen in Table 5.4.

Table 4.5 Fuel and product definitions with respect to the system.

Component	**Fuel**	**Product**
Compressor	$\dot{W}_{comp}$	$\dot{E}x_2 - \dot{E}x_1$
PCM Tank	$\dot{W}_{pump}$	$\dot{E}x_{11} - \dot{E}x_{10}$
Condenser	$\dot{E}x_2 - \dot{E}x_3$	$\dot{E}x_{10} - \dot{E}x_0$
Evaporator TXV	$\dot{E}x_{3a}$	$\dot{E}x_4$
Chiller TXV	$\dot{E}x_{3b}$	$\dot{E}x_5$
Evaporator	$\dot{E}x_4 - \dot{E}x_{1a}$	$\dot{E}x_9$
Chiller	$\dot{E}x_{1b} - \dot{E}x_5$	$\dot{E}x_7 - \dot{E}x_6$
Pump	$\dot{W}_{pump}$	$\dot{E}x_8 - \dot{E}x_7$
Battery	$\dot{W}_{bat}$	$\dot{E}x_6 - \dot{E}x_8$

The volumetric cost balance equation is written as follows:

$$\sum_e \left(c_e \dot{E}x_e\right)_k + c_{w,k}\dot{W}_k = c_{q,k}\dot{E}x_{q,k} + \sum_i \left(c_i \dot{E}x_i\right)_k + \dot{Z}_k \tag{4.86}$$

which states that the total cost of the exiting exergy streams equals the total expenditure to obtain them, namely the cost of the entering exergy streams plus the capital and other costs [143]. In general, there are "n_e" exergy streams exiting the component, "n_e" unknowns and only one equation, the cost balance. Thus, "$n_e - 1$" auxiliary equations need to be formulated using F and P rules.

4.3.2.2 Purchase equipment cost correlations

The capital investment rate can be calculated with respect to the purchase cost of equipment and capital recovery as well as maintenance factor over the number of operation hours per year as given below

$$\dot{Z}_k = \frac{Z_k \cdot CRF \cdot \varphi}{N} \tag{4.87}$$

where N is the annual number of operation hours for the unit and φ is the maintenance factor, generally taken as 1.06 [142]. CRF is the capital recovery factor which depends on the interest rate (i) and equipment life-time in years (n) as

$$CRF = \frac{i \times (1+i)^n}{(1+i)^n - 1} \tag{4.88}$$

Here, Z_k is the purchase equipment cost of the thermal management system components that should be written in terms of design parameters. The correlations for each component are given below [144].

$$Z_{comp} = \left(\frac{573\dot{m}_{ref}}{0.8996 - \eta_s}\right)\left(\frac{P_{cond}}{P_{evap}}\right)\ln\left(\frac{P_{cond}}{P_{evap}}\right) \tag{4.89}$$

where

$$\eta_s = 0.85 - 0.046667\left(\frac{P_{cond}}{P_{evap}}\right) \tag{4.90}$$

Here, $\dot{m}_{ref}$ is the refrigerant mass flow rate (kg/s) and η_s is the isentropic efficiency of a scroll compressor. For the heat exchangers the cost correlations developed[139] are used. The fixed cost associated with the heat exchangers is neglected due to being insignificant relative to the variable costs as well as a lack of reliable data.

$$Z_{cond} = 516.621 A_{cond} \tag{4.91}$$

$$Z_{evap} = 309.143 A_{evap} \tag{4.92}$$

$$Z_{chil} = 309.143 A_{chil} \tag{4.93}$$

where A_{cond}, A_{evap} and A_{chil} are the heat transfer areas associated with the condenser and evaporator respectively [139].

$$Z_{pump} = 308.9 \dot{W}_{pump}^{C_{pump}} \tag{4.94a}$$

$$C_{pump} = 0.25 \text{ for } 0.02 \text{ kW} < \dot{W}_{pump} < 0.3 \text{ kW} \tag{4.94b}$$

C_{pump} = 0.45 for 0.3 kW < $\dot{W}_{pump}$ < 20 kW (4.94c)

C_{pump} = 0.84 for 20 kW < $\dot{W}_{pump}$ < 200 kW (4.94d)

Here, $\dot{W}_{pump}$ is the pumping power in kW and C_{pump} is the pump coefficient with respect to the corresponding pumping power ranges, provided below [145].

$$Z_{evap,txv} = k_{txv}\dot{m}_{ref,a} \tag{4.95}$$

$$Z_{chil,txv} = k_{txv}\dot{m}_{ref,b} \tag{4.96}$$

where k_{txv} is the cost per mass flow rate of refrigerant which is taken to be $5,000 [146].

$$Z_{bat} = C_{bat}K_{bat} \tag{4.97}$$

Here, C_{bat} is the typical lithium-ion battery pack costs per kilowatt-hour, taken as $500 [147]. a K_{bat} is the battery pack energy that is associated with powering the thermal management system. The EV/HEV battery analyzed in the study has an energy storage capacity of 16 kWh, where only 12.9 kWh can be utilized for charging and driving in order to extend the life of the battery. Among this, only 9.6 kWh is used to propel the car and the accessories [148]. Of the remaining energy, the TMS can draw anywhere between 4% and 24% by just using the fans and turning the A/C all the way on a very hot day, respectively [149].

4.3.3 System configuration

Hybrid electric vehicle thermal management systems (HEV TMSs) are considerably different systems due to their exclusive necessities. The TMS needs to handle significant thermal load deviations and provide comfort under highly instable conditions, while being compact and efficient. They should also last several years without any need for major maintenances. Moreover, the airflow volume, velocity and temperature must be adjustable over a wide range of enveloped temperatures and manage cycles without having a significant influence on the all-electric vehicle performance features.

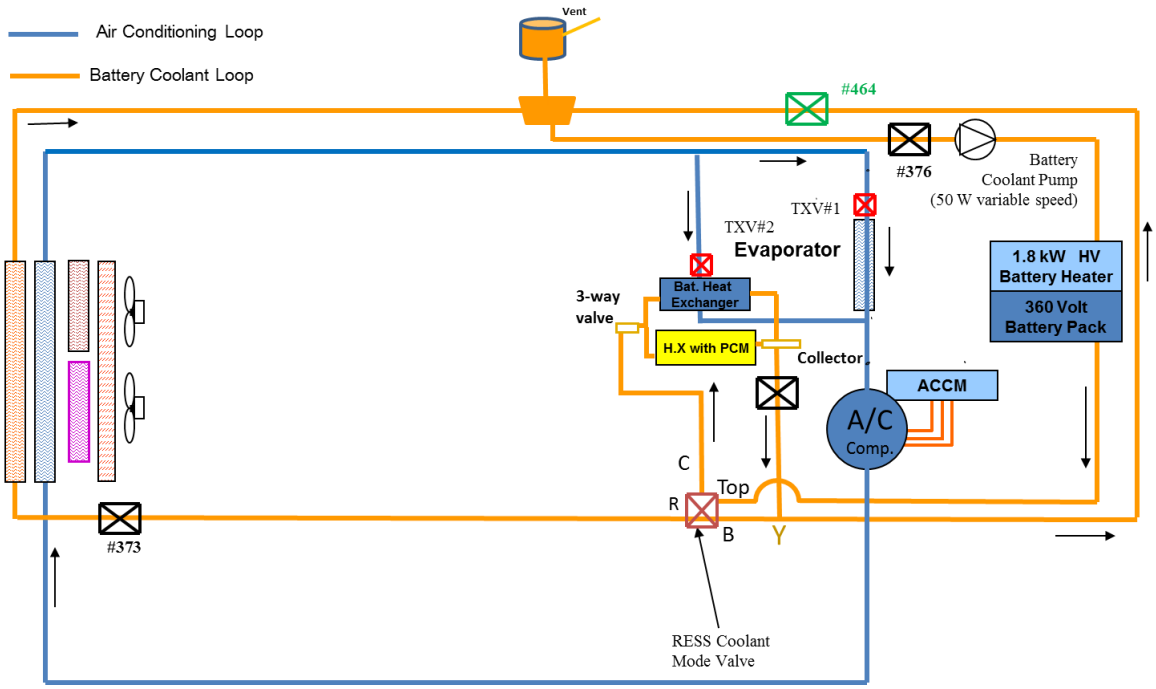

Figure 4.11 Simplified representation of the hybrid electric vehicle thermal management system.

Additionally, since the time spent in the vehicles compared to buildings is much limited, while the energy requirements between the cabin and the battery are challenging, the thermal management systems must be able to condition the air in the passenger cabin rapidly and silently, They should also keep the vehicle mechanisms operating under ideal functional temperature ranges (especially the electric battery) in order to extend their lifetime, increase the fuel efficiency and all electric range. Therefore, special attention needs to be given to hybrid electric vehicle TMSs [82, 150].

A simplified thermal management system of an electric vehicle with liquid battery cooling is shown in Figure 4.11. The system is consisted of two loops, a refrigerant and battery coolant loop. These two loops are connected through a chiller, which allows heat exchange among the loops to deliver super cooling to the battery cooling as it passes through the chiller unit. The refrigerant loop permits air conditioning of the vehicle cabin, while the coolant loop keeps the electric battery functioning within its ideal temperature range.

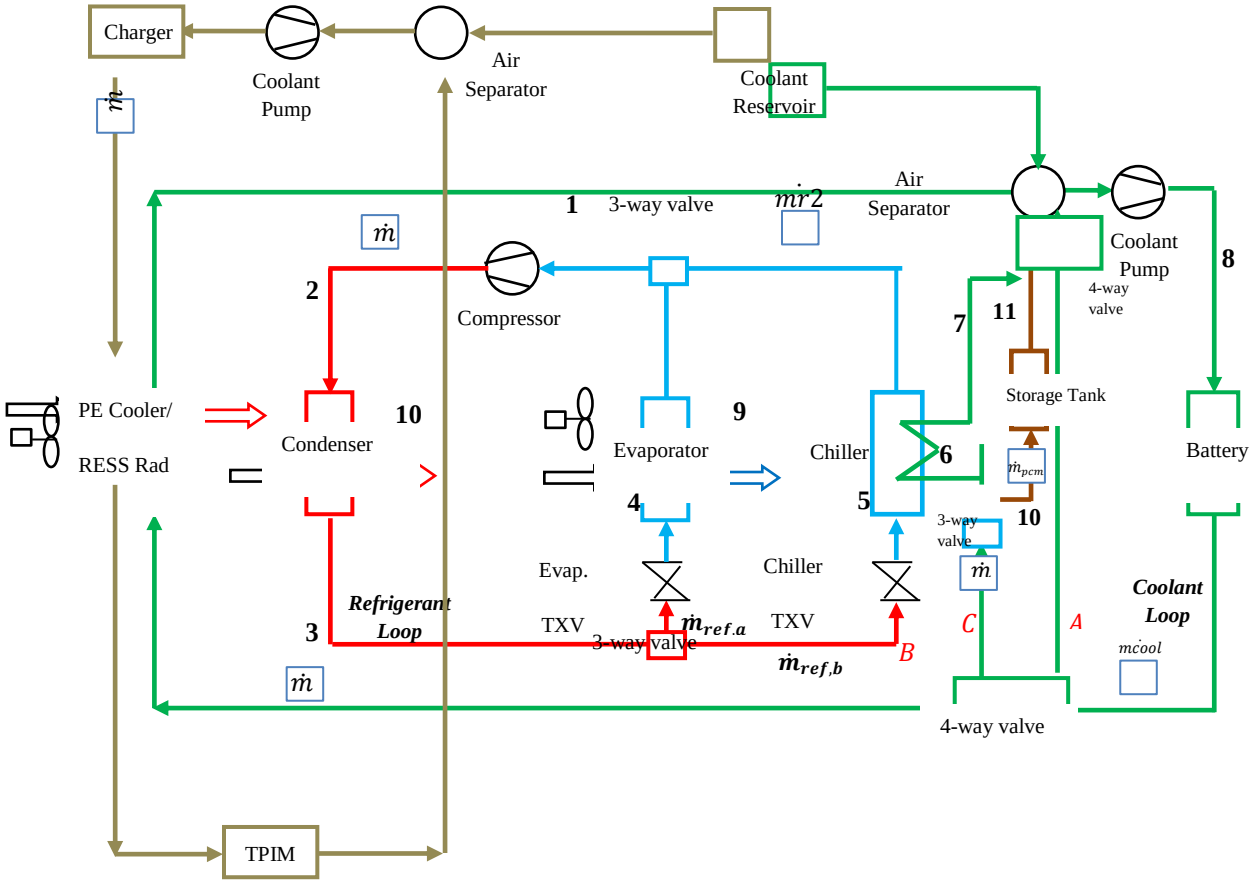

Figure 4.12 Cooling cycle integrated with PCM cooling cycle

Since the battery coolant circuit need the air compressor, cooling via refrigeration circuit would consume more energy. Therefore, an improvement in cooling system enhances the efficiency of the system considerably.

The thermal management system unites the advantages of both the air cooling and refrigerant based cooling if the help of the additional battery cooler and chiller is provided. The additional cooling loop is kept cool through different procedures, which depends on the cooling load and circumfused conditions. The battery coolant circuit would bypass the thermal management systems, if a stable temperature within the ideal range is granted. This will result in re-circulating battery coolant before getting pumped into the battery (Route A as shown in Figure 4.12). Temperature constancy is permitted by controlling cell temperatures through pump control in this loop. When the battery temperature is high and the ambient temperature is lower than the desired temperature of the battery, the ambient air flow in the battery cooler is used to keep this coolant circuit cool (Route B). In the condition of higher battery temperature while the ambient temperature is higher than the desired battery temperature, by operating the electric air

conditioning (A/C) compressor, regulation of the R134a refrigerant is reached via the thermal expansion valve (TXV) which allows super-cooling of the battery coolant while it passes through the chiller unit (Route C). Therefore the efficiency of the system increases significantly since cooling via a cooling circuit would consume more energy compared to operating the battery coolant circuit since it needs the air compressor in the first case.

In the baseline model, the refrigerant mass flow rates are determined from thermal expansion valve correlations and the cooling capacity is calculated accordingly. To study the effects of the TMS on the battery, ambient air conditions of 35ºC and 1 ATM are used. For the baseline model, temperatures of 5ºC and 55ºC are used for evaporating and condensing temperatures along with 5ºC superheating and sub-cooling in the evaporator and condenser, while the temperature of the passenger cabin is set at 20ºC. The refrigerant mass flow rate in the chiller is determined regarding to the amount of battery heat transferred from the water/glycol mix in the coolant circuit to the refrigerant circuit through the chiller. In the refrigerant cycle, the refrigerant flow in the evaporator and chiller is combined in the system before it is compressed to the condenser. For the coolant circuit, the battery coolant temperature is assumed to be 19ºC (since it functions in a temperature span of 19ºC to 25ºC) before entering the battery, and the heat generated by the battery is considered to be 0.35 kW (GM information) and [116], where the mass flow rate of the battery coolant is determined accordingly. The system is mainly consists of a compressor, heat exchangers, thermal expansion valves, pump and the battery. These components are described in more detail below. The coolant pump is not described further since its relatively has negligible impact on the overall system. Different refrigerants can be applied to the system and their effect on the overall efficiency of the cooling system can be compared with other systems.

4.3.4 **Multi-objective optimization**

A multi-objective problem consists of optimizing (i.e. minimizing or maximizing) several objectives simultaneously, with a number of inequality or equality constraints. Genetic Algorithms (GA) are semi-stochastic methods, based on an analogy with Darwin’s laws of natural selection [131]. The first multi-objective GA, called vector evaluated GA (or VEGA), was proposed by Schaffer [151]. An algorithm based on non-dominated sorting was proposed by Srinivas and Deb [152] and called non-dominated sorting genetic-algorithm (NSGA). This was

later modified by Deb et al. [153] which eliminated higher computational complexity, lack of elitism and the need for specifying the sharing parameter. This algorithm is called NSGA-II which is coupled with the objective functions developed in this study for optimization.

Tournament selection

Each individual competes in exactly two tournaments with randomly selected individuals, a procedure which imitates survival of the fittest in nature.

Controlled elitism sort

In order to preserve diversity, the influence of elitism is controlled by choosing the number of individuals from each subpopulation, according to the geometric distribution [154]

$$S_q = S\frac{1-c}{1-c^w}c^{q-1}, \tag{4.98}$$

In order to form a parent search population, P_{t+1} (t denote the generation), of size S, where $0 < c < 1$. And w is the total number of ranked non-dominated.

Crowding distance

The crowding distance metric proposed by Deb [155] is utilized, where the crowding distance of an individual is the perimeter of the rectangle with its nearest neighbours at diagonally opposite corners. So, if individual $X^{(a)}$ and individual $X^{(b)}$ have same rank, each one has a larger crowding distance is better.

Crossover and mutation

The uniform crossover and random uniform mutation are employed to obtain the offspring population, Q_{t+1}. The integer-based uniform crossover operator takes two distinct parent individuals and interchanges each corresponding binary bits with a probability, $0 < p_c \leq 1$. Following crossover, the mutation operator changes each of the binary bits with a mutation probability, $0 < p_m < 0.5$.

Final optimum solution

The selection of a single optimum point from existing points on the Pareto front needs a process of decision-making. In fact, this process is mostly carried out based on engineering experiences

and importance of each objective for decision makers. The process of final decision-making is usually performed with the aid of a hypothetical point named as equilibrium point (at which both objectives have their optimal values independent of the other objectives) which is shown in Fig. 4.13 it is clear that it is impossible to have both objectives at their optimum point, simultaneously. Therefore the equilibrium point is not a solution located on the Pareto frontier. In this paper, LINMAP method was used to find the final optimum solution in Pareto [156]. In LINMAP method, each objective is non-dimensionalized using the following relation

$$F_{ij}^{n} = \frac{F_{ij}}{\sqrt[2]{\sum_{i=1}^{m}(F_{ij})^{2}}} \tag{4.99}$$

where *i* is the index for each point on Pareto front, *j* is the index for each objective and *m* denotes the number of points on the Pareto front. Then the distance of each point on Pareto front from the ideal point was obtained:

$$d_i = \sqrt{\sum_{j=1}^{2}\left(F_{ij}^{n} - F_{ideal,j}^{n}\right)^{2}} \tag{4.100}$$

where ideal is the index of ideal objective functions. The closest point of Pareto frontier to the equilibrium point might be considered as a desirable final solution.

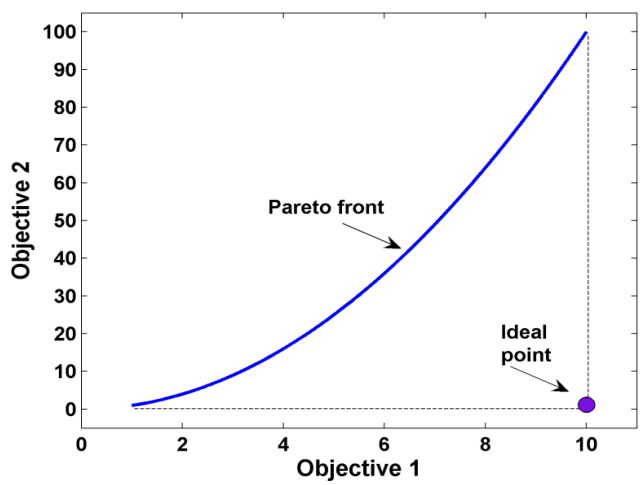

Figure 4.13 Concept of ideal point in the Pareto frontier for maximizing the objective 1 and minimizing the objective 2

Chapter 5 Experimental Setup and Procedure

In order to obtain the temperature distribution in Li-ion cells of the undertaken HEV battery pack, related experiments are carried out. The effects of the proposed TMS using PCM integrated with the Li-ion cells and battery pack are measured and data are compared with the simulation results. The experimental setup and process, instrumentations utilized along with the gathered data are described in this chapter. In order to investigate the dispersion of nanoparticles in the PCM mixture, opto-image techniques are used. In the reflection microscopic study, the surface of the PCM and nanoparticles during the phase change is observed to understand the surface arrangement of the particles. Using transmission microscopic images, the samples are studied during the phase change process, as well as the rate of agglomeration for graphene nano-platelets and carbon nanotubes. Furthermore, the fine extended surface and other methods are studied to investigate their effect on preventing convection of particles in the mixture.

5.1 PCM integrated to sub-module

To verify the sub- module simulation results, experimental data is required. A test bench with a layout for sub-modules is carried out using available facilities. The sub-module has been set, according to the simulation layout. Thermocouples (K-type) have been attached to the cell surface. The data acquisition system is coupled with IPEmotion software. To analyze the selected sub-module, its components such as PCM and foam have been studied and selected based on the available time and facilities. Their selection is briefly explained as follows.

5.1.1 Preparing foam and phase change material cooling jacket

In order to select the foam, several experiments have been done based on physical properties of the material. The experimental procedure was constant for all foams and the same PCM was used throughout. From the foams in Table 5.1, the foam in row 3 is selected. The main reason is the high absorption of PCM by this foam due to the porosity of its structure

Figure 5.2 shows the different samples that are used in the experiments to absorb the PCM. All these foams are specifically fabricated for thermal management applications.

Table 5.1 Tests with different foams

Foam	**Sample color**	**Sample size (mm^2)**	**Surface area (mm^2)**	**M1, dry mass (g)**	**M2 after soaking (g)**	**PCM, absorbed mass (g)**	**PCM density in foam (g/mm^2)×1000**
1	Yellowish	106×155	16,430	1.92	8.24	6.32	0.38
2	Black	107×140	14,980	4.15	5.68	1.53	0.10
3	Black (porous)	105×140	14,700	2.27	7.75	5.48	0.37
4	Blue (strip)	35×150	5,250	0.84	2.48	1.64	0.31
5	Blue	105×150	15,750	0.731	1.601	0.87	0.06

Figure 5.1 The Temptronic device to heat and cool the test chamber.

The Temptronic is a device which is used along with the heat chamber to control the test environment conditions (Figure 5.1). It is also used to melt the solid phase PCM for the experiments. Solidus and liquidus temperatures are considered as 35.5℃ and 38.6℃, which show a three degree interval for the segregation temperature due to impurities.

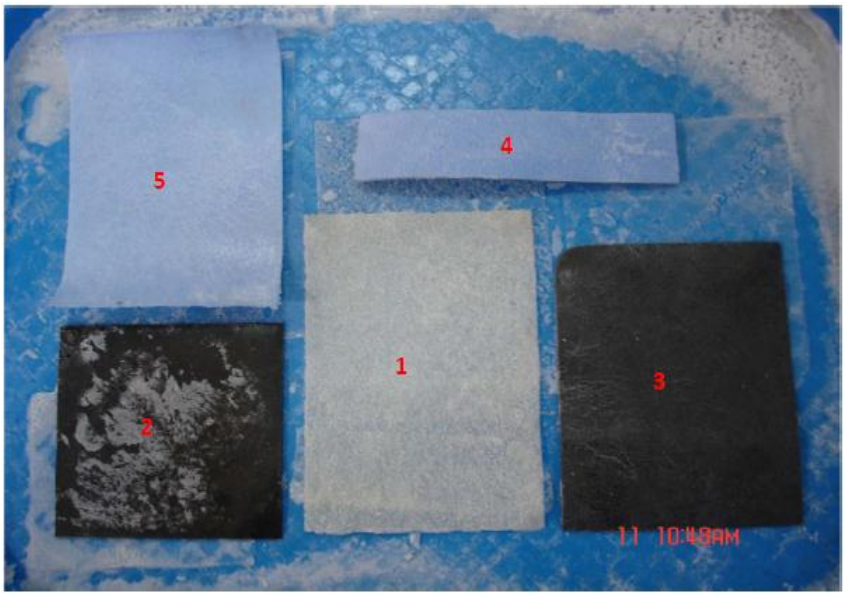

Figure 5.2 Foams after soaking in the PCM to assess their absorption

Cell surface temperature measurements in sub-module

Thin thermocouples are connected through a thermal paste material to the surface of the second (the critical) cell in the sub-module as illustrated in Figure5.3. The other side of the cells are also connected to the thermocouples as can be seen in Figures 5.4 and 5.5. Temperatures on the cell surface have been recorded through the IPEmotion software and data acquisition system. The parts of the experiments for the sub-module are carried out in the GM Canadian Regional Engineering Center (CREC). Results of the experiments are discussed in Chapter 6.

5.2 Heat exchanger model

Based on the optimization results, two heat exchangers are manufactured. The minimum diameter for the copper tubes is selected from the available sizes in the market. For the manufactured model, the selected size for copper tubes is 5/16 inch, which is among the smallest diameters available in the market. The advantage of nanoparticles is to be tested through the available data.

Figure 5.3 Connecting thermocouples on the surface of the Li-ion cells

Figure 5.4 Cooling plate and other surface of the cells connected to thermocouples

Figure 5.5 Sub-module with 3 cells under test

5.2.1 **Test apparatus for temperature measurements and applied materials**

Heat fluid enters into the heat exchanger. Four thermocouples are positioned with equal distances from the copper tube. Figure 5.6 shows the configuration of the thermocouples from above. All four thermocouples are placed inside the PCM; therefore, they represent temperature variations in the PCM. Results for these thermocouples are presented later. The melting process in the heat exchanger and location of four thermocouples can be observed in Figures 5.6 and 5.7.

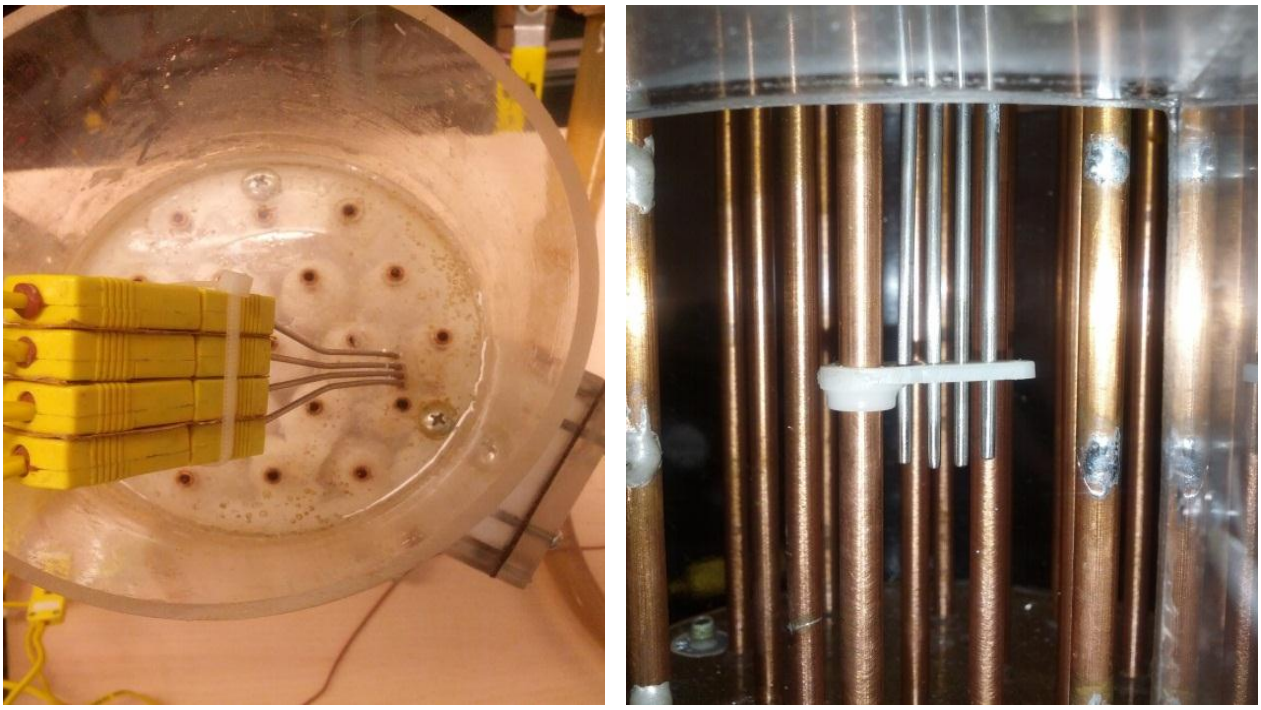

Figure 5.6 Position of four thermocouples in equal distances from the copper tube

Due to the lower melting temperature of the PCM, the ambient temperature could handle the solidification process after charging (melting); therefore, after a specific time, the liquid PCM turns to solid. Fig. 5.8 shows the heat exchanger with optimum dimensions. Length and diameter of the tank, along with the number of copper tubes and their diameters were obtained based on the genetic algorithm optimization. Mass flow rates of 1.2 liter/min to 7 liter/min and heat transfer of 350 W to 700 W are considered in designing the heat exchanger. Fig. 5.9 shows the PCM when it is in solidus phase.

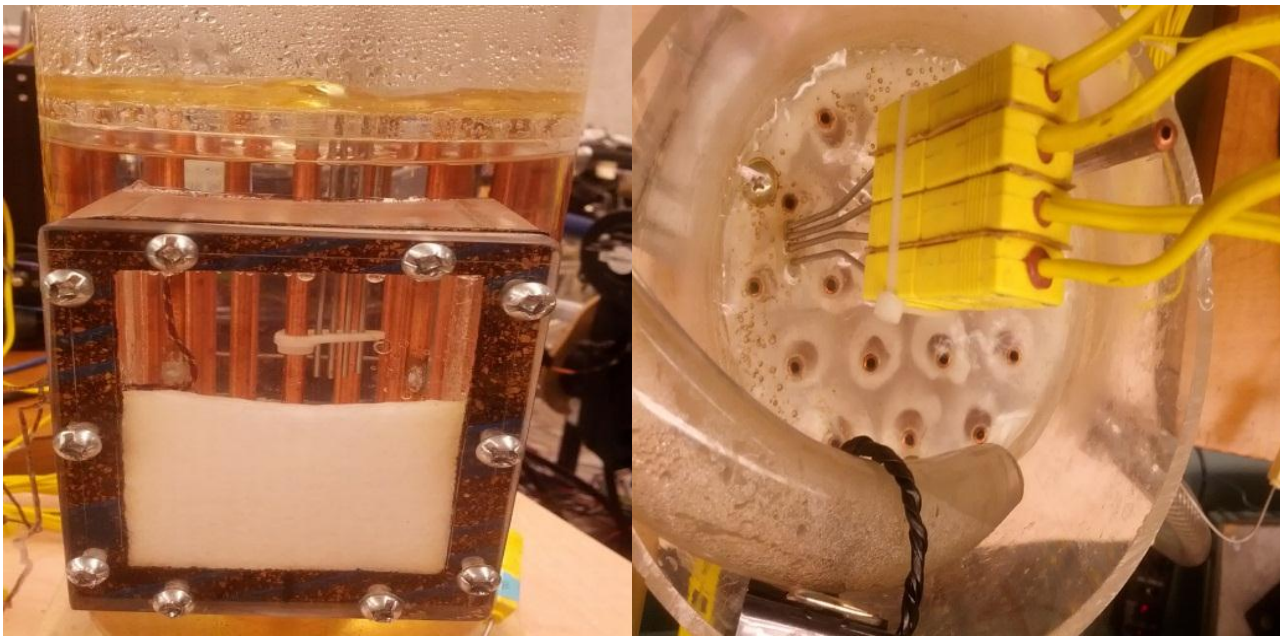

Figure 5.7 Position of thermocouples 1 to 4 from tube surface respectively

Figure 5.8 Manufactured heat exchanger with optimized dimensions

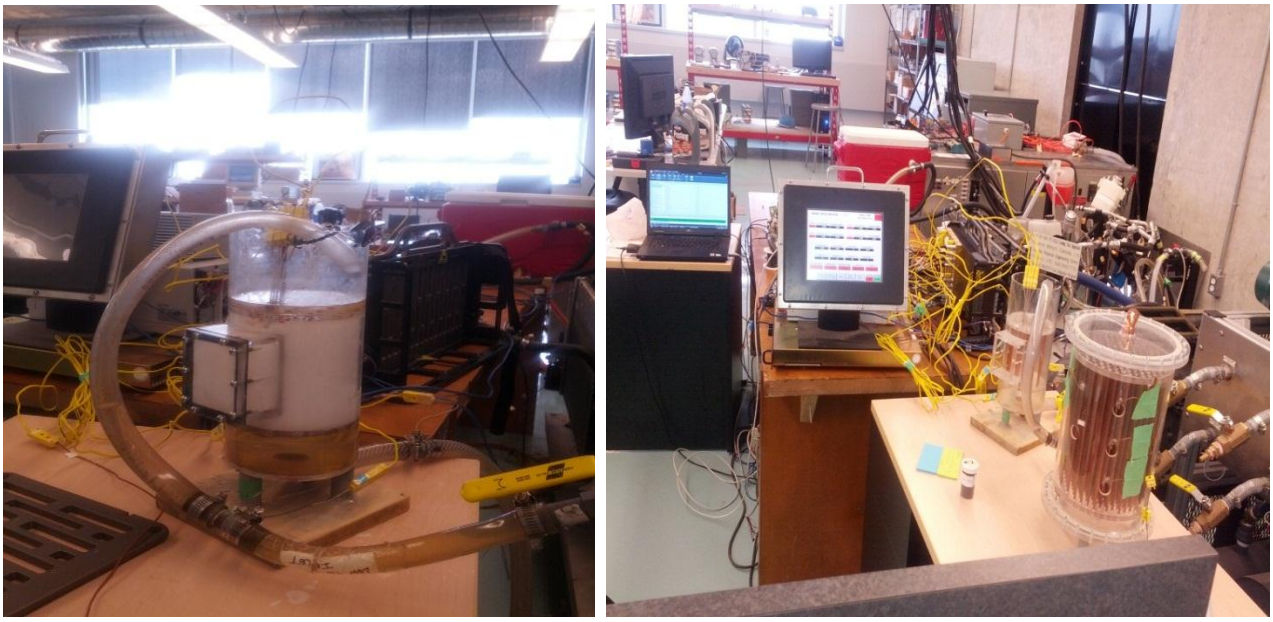

Figure 5.9 Solid phase of the PCM in the heat exchanger and Test set up

5.2.2 **Phase change material and nano-particle mixture properties**

The material used in the shell side is n-octadecane in different combinations. Pure PCM (99% purity) and technical grade (90.8%) are used (Fig. 5.10a). CNTs and graphene platelets are used in the tests in different mass concentrations (1.25%, 3% and 6%) using the scale (Fig. 5.10b). An ultrasonic unit in the lab is used for preparation of the CNT and PCM. As discussed in Chapter 3, ultrasonic waves are used to disperse the nanotubes in the PCM properly (Fig. 5.10c). The advantage of the ultrasonic method is the prevention of agglomeration of nanoparticles through the phase change process. Also, by increasing the elapsed usage time of the ultrasonic device, thermal conductivity of the mixture will be increased [157].

The prepared PCM and nanoparticle mixture is used for DSC tests and thermal conductivity analyses. Prepared samples (Fig. 5.10d) are also used in optical microscopic studies.

Octadecane is supplied in two types of technical grade (90.8%) and pure material (99%). In addition, the nanoparticles used in this investigation are carbon nanotubes and graphene nano-platelets. Physical properties of these materials are explained here. The properties of graphene nano platelets are as follows:

- Purity: 97 wt%
- Diameter: 2 μm
- Grade 3

- Ash: <1.5 wt%

For the carbon nanotubes (CNT), the corresponding properties are

- Outer diameter: 8-15 nm
- Length: 10-50 μm
- Purity: >95 wt %

The graphene platelets and CNTs are mixed with technical grade and pure octadecane (the chosen PCM) in different mass concentrations. The values used for the present study are 1.25%, 3%, 6% and 9%. For concentrations greater than 10%, the mixture becomes less viscous and the latent heat of fusion for the mixture decreases. The lower specific heat will be a disadvantage.

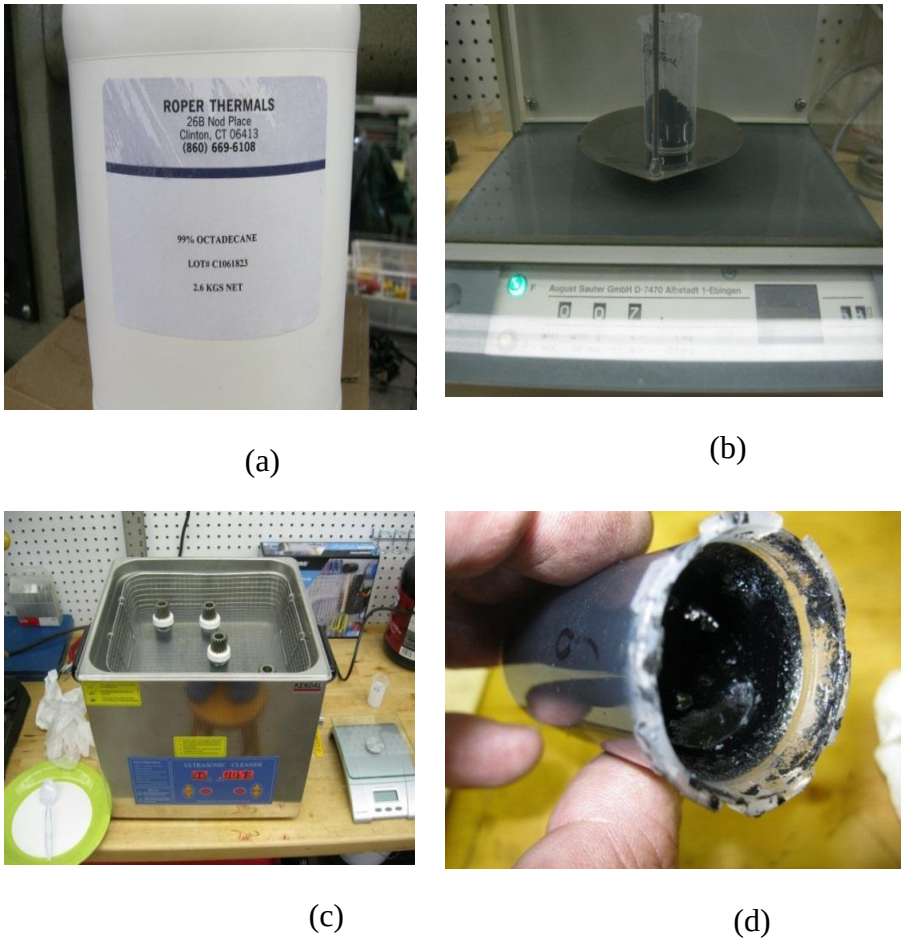

Figure 5.10 Preparation of samples using ultrasonic unit

Bayramoglu [158] has shown that in 5% weight concentration of MWCNT, the latent heat will decrease by 6%, which can reach 12% when 10% MWCNT is mixed with the pure octadecane. This study also shows the thermal stability of the mixture of n-octadecane and nano-tube after 1440 cycles. This is mainly due to the characteristics of organic materials and paraffin waxes explained in Chapter 2. These mixtures are prepared in the lab and are analysed with the differential scanning calorimetry (DSC) method and optical microscopic images.

5.2.3 Opto-image study: Transmission electron microscopy (TEM) and reflection electron microscopy

Transmission electron microscopy (TEM) is a microscopy technique whereby a beam of electrons is transmitted through an ultra-thin specimen, interacting with the specimen as it passes through. An image is formed from this interaction of the electrons transmitted through the specimen; the image is magnified and focused onto an imaging device, such as a fluorescent screen, on a layer of photographic film, or to be detected by a sensor such as a CCD camera. TEMs are capable of imaging at a significantly higher resolution than light microscopes. In a reflection microscope, light is reflected off a sample. Image contrast can arise in different ways.

One of the main drawbacks of a PCM and nano-particle mixture is the agglomeration of nanoparticles when the mixture gets melted. This will decrease the thermal conductivity of the mixture. As a method to prevent this phenomenon, a very fine mesh of stainless steel is used in the mixture and experiments are done through (TEM) and reflection microscopy imaging. Figure 5.12 illustrates the micro-mesh employed in the mixture for this purpose.

The test bench is used to obtain overall data about the thermal management of the vehicle. Furthermore, the auxiliary bench is used to simulate the battery loop with the corresponding heat and mass flow approximately that of the vehicle. The complex bench is connected to the auxiliary bench through a screen touch control system to set up the temperature, pressure and mass flow rates. Figure 5.12 shows the location of the PCM tank proposed for the current TMS.

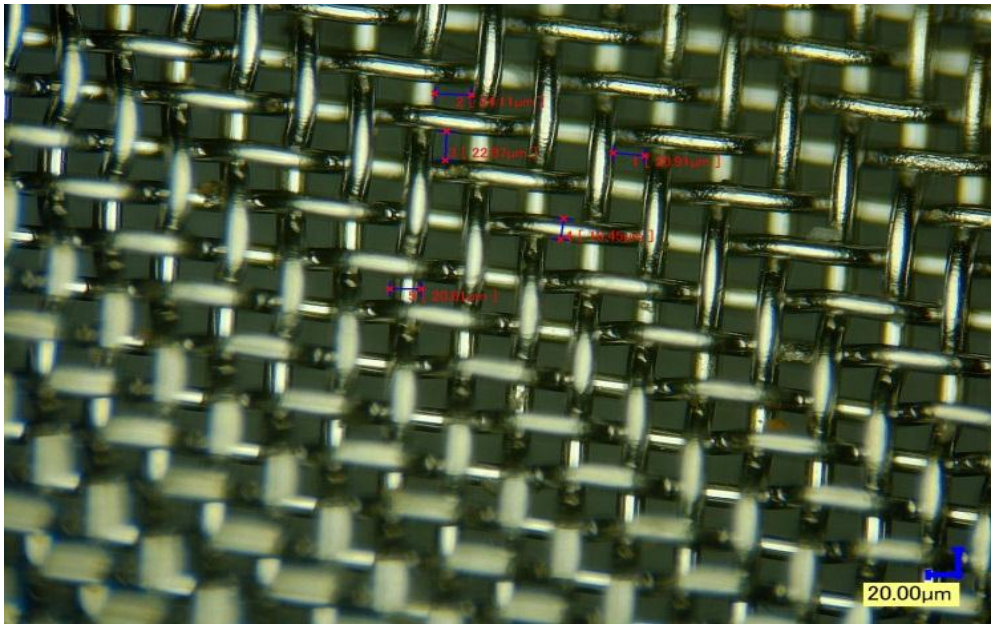

Figure 5.11 Stainless steel micro-mesh with mesh size of 20 μm

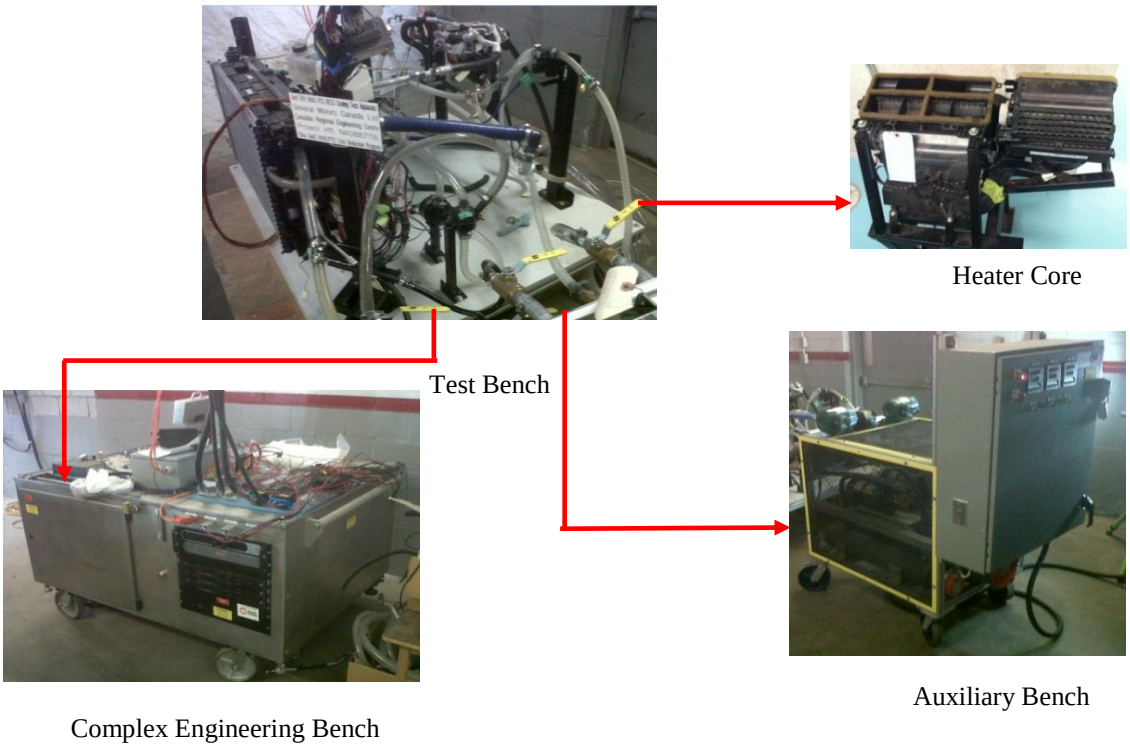

Figure 5.12 Test bench components

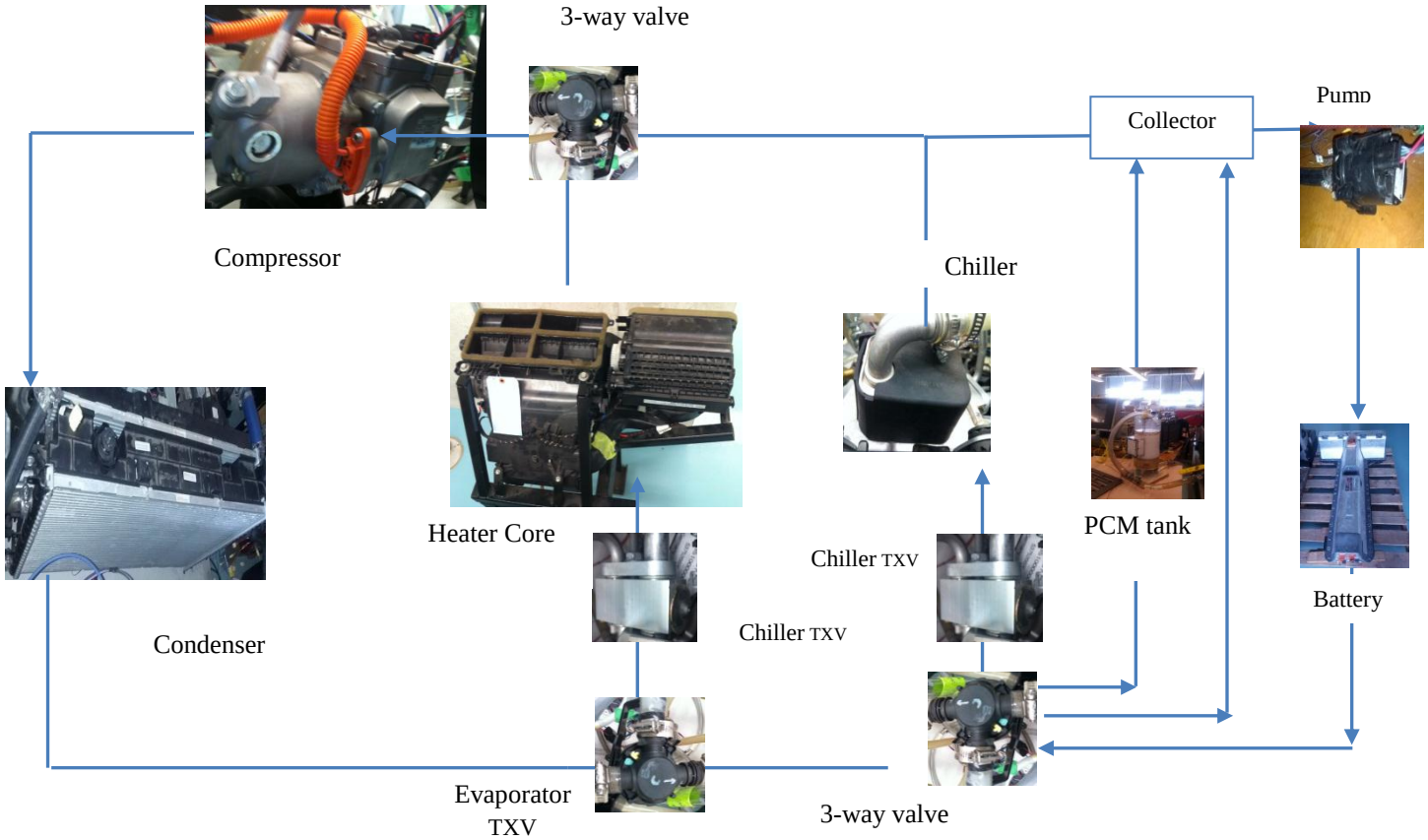

Figure 5.13 Location of PCM tank integrated with other components

Chapter 6 Results and Discussion

The main purpose of this thesis is the investigation of passive methods of battery thermal management using phase change materials (PCMs). Introducing the PCM into the vehicle cooling cycle can mitigate the net energy extracted from the pack. Energy used by the compressor in the current active cooling systems can be saved in order to extend the driving range of the vehicle.

The results for PCM application at the cell and module levels are presented and discussed. Using refrigerant to extend the driving range will have ramifications in the thermal management of HEVs. There is a compromise of life span of the vehicle and driving range. The effect of the PCM on heat transfer from the cells and sub-module in the cooling cycle is shown.

Using LHTS in the cooling/heating loop is studied later. The proper type, design and optimization of such a heat exchanger are presented. Methods to improve the thermal conductivity using carbon nano-particles are studied. Then Results for energy and exergy analysis of the current active cooling integrated with the experimental latent heat energy storage system to increase cooling capacity are presented in this chapter. The cooling loops were explained in Chapter 4. Energy and exergy efficiencies of the overall cooling loop are presented herein. Results for optical microscopic techniques are also presented in this chapter.

6.1 Phase change material application integrated with battery pack

Passive cooling systems have the advantage of having lower energy demands. This is due to the lack of components required to extract the energy from the battery pack. In active air cooling, the fan consumes energy, while in passive cooling system there is no need for a chiller or other devices. As was discussed before, the passive air cooling load is not sufficient to manage the thermal issues in the pack, and that is the reason that liquid cooling systems are used. In this section, the PCM is going to be used as a passive TMS at the cell and sub-module levels. Firstly, the PCM is placed around a single cell and its effects on the cooling of the cell are studied. The second option examined is to use the PCM in the foam between the cells. The foam is soaked with the liquid PCM and, after solidification, it is placed between the cells. The third option investigated is to use the PCM around the sub-module. The main components in the battery pack

are Li-ion cells, foam as separator between them, and the casing. The selected PCM was introduced in model development section (Chapter 4).

6.1.1 Peripheral application of the PCM in the cell level

The higher thermal conductivity in the planar direction is considered an advantage of the cells, as it makes it possible to extract heat from the sides of the cell when there is no interest in manipulating the layers between the cells. The heat generation rate at the cell level will cause a temperature increase. The way that heat is generated and distributed mostly depends on the cell type. Dimensions of the cell have been shown in Figure 6.1. Different thicknesses of the PCM are considered to investigate the effect of each thickness in reducing the temperature and giving uniform temperature distribution throughout the cell and sub-module. Cooling effectiveness has been defined in the cell to use as a criterion for various applications of PCMs.

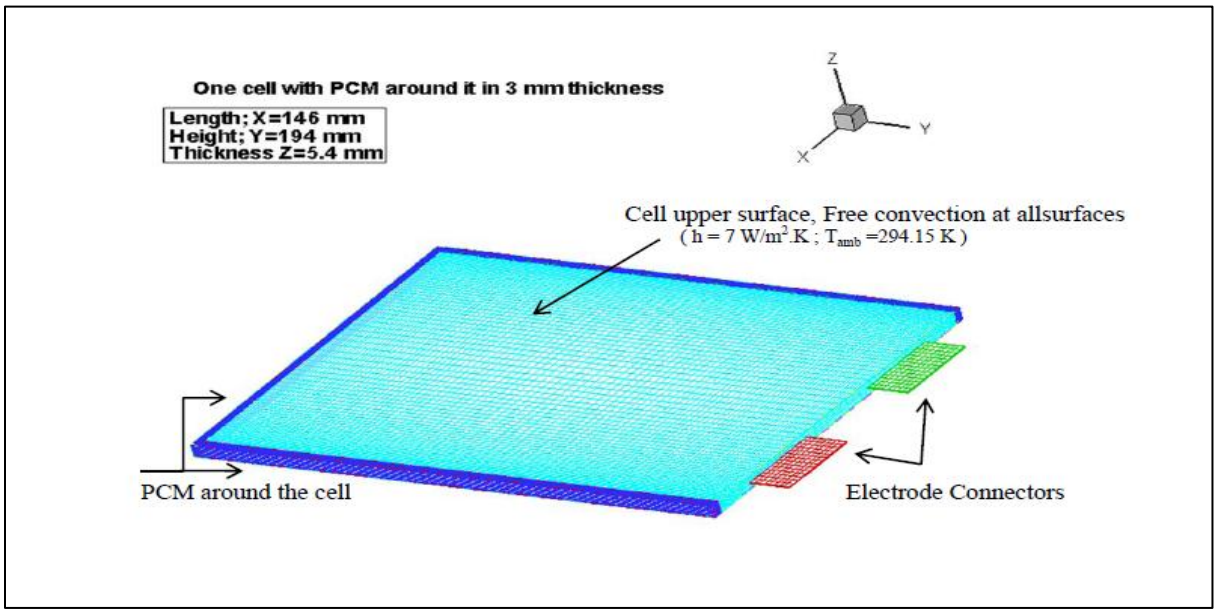

Figure 6.1 Cell dimensions and the PCM around the cell

The considered thicknesses are 3 mm, 6 mm, 9 mm and 12 mm, discussed in the following sections. It should be noted that the selection of PCM thicknesses is based on the practical applicability of the PCM in the undertaken HEV battery pack. Two terminals in the cell have been placed symmetrically. There is no heat generation in terminals and they behave like a cooling fin in the cell. This may be an accurate representation in reality. The reason is that the space between the cell margin and the terminals has been decreased due to the compressed

electrolyte between two thin layers, which forms the prismatic shape. This decreases the heat transfer area between the cell and terminals. The contact resistance has been considered in this section. Contact thickness is considered to be 0.6 mm to represent the actual case. Table 6.1 shows the different thicknesses for the PCM.

Table 6.1 Dimensions of cell and terminals

Zone	Length (x, mm)	Height (y, mm)	Thickness (z, mm)
Cell	146	194	5.4
Terminals	35	15	0.6
PCM	3, 6, 9 and 12	3, 6, 9 and 12	5.4

6.1.1.1 Grid Space Independency Test

A grid independency test is carried out to affirm that mesh size will not affect output in the simulation. Normally a point inside the domain is monitored to investigate the convergence history of a property such as temperature. In this study, a rake crossing the cell has been monitored as convergence criteria. Temperature distribution along a constant rake in the cell is given for three meshes with different sizes.

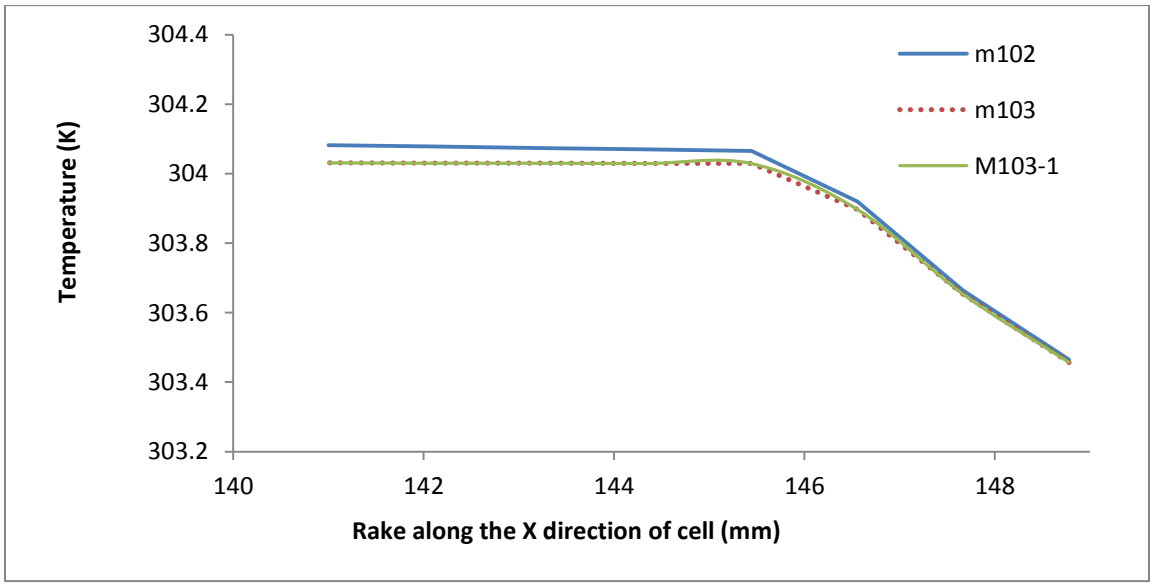

Figure 6.2 Grid space-independency test for cell and PCM

Figure 6.2 shows the convergence history for the rake in each case. Three meshes are considered for grid space-independency. For the first mesh the grid size is 97×73. The

successive ratio of the cell in the x and y directions (Figure 6.1) are 1.02 and 1.05, respectively. The present mesh sizes are given as follows:

- M102: 87,700 volume elements
- M103: 196,300 volume elements
- M103-1: 300,800 volume elements

For the PCM thickness around the cell, the grid number in an x-y plane is 9×9. Based on Figure 6.2, the mesh with 196,300 elements has been selected.

6.1.1.2 Contact resistance in the terminals

Contact resistance (thermal barrier resistance) can be effective in any location with two or more different layers due to the surface roughness effect. Contact resistance is important when the heat flux or temperature difference is low. In the current mode, the electrolyte in the Li-ion cell is encapsulated by a thin metal sheet where the terminals have been connected. There can be contact resistance in this interface that affects heat transfer rate. In addition, when the PCM is placed around the cell, an enclosure is required to prevent the leakage of melted PCM. If a thin layer of aluminum cover (0.5 mm thickness) is considered, the contact resistance (R) can be written in the following form:

$$R_{tot} = \frac{\Delta T}{\dot{q}} = \frac{L_{Al}}{k*A} + \frac{1}{hA} + R_{contact,casing} \tag{6.1}$$

Also for the connectors:

$$R_{contact} = \frac{T_{cell} - T_{terminal}}{Thickness} \tag{6.2}$$

where "h" is the heat transfer coefficient between the cell surface and ambient and L is the thickness of the casing. For the case of aluminum interface (10 micrometer surface roughness, 10^5 N/m^2 with air as interfacial fluid, the contact resistance is 2.75×10^{-4} m^2 K/W).

Also, $R_{thcikness} = \frac{L_{Al}}{k*A} = 0.1 /(202\times194\times146) \times1000 = 1.7\times10^{-5}$ (6.3a)

$R_h = 1/hA = 1/(10\times146\times194) \times10^6 = 3.531\times10^1$ (6.3b)

$R_{contact} = 2.75\times10^{-4} \times (146\times194) \times1e\text{-}6 = 7.8\times10^{-6}$ (6.3c)

Order of magnitude for contact resistance is ignorable compared to the coefficient of heat transfer. So, contact resistance will not make a significant difference in the calculations. The

main reason behind the contact resistance is the high temperature differences and heat flux in the interface. At micro scale levels, this will be more dominant. The phonons in the micro-scale level will determine the contact resistance more effectively.

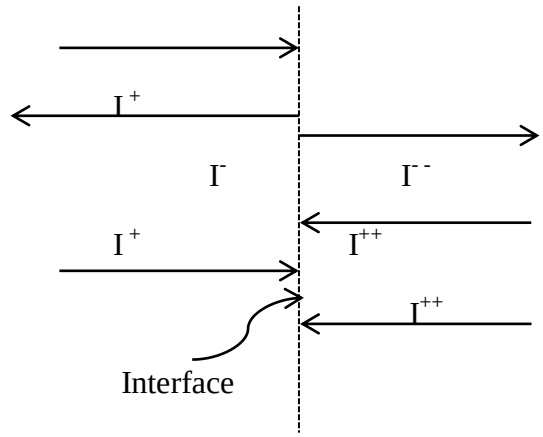

Figure 6.3 Phonon transport at the interface in relation to contact resistance

If the interface of two regions in thermal contact is considered as a finite control volume, then energy balance for phonons passing over the control surfaces can be written as (Figure 6.3)

$$I^{+} + I^{++} - (I^{-} + I^{--}) = \Delta I \tag{6.4}$$

where I is the phonon radiation intensity and ΔI is the net energy transport in terms of phonons passing through the interface (control surfaces of the finite control volume). This value is proportional to the heat flux.

Conduction takes place through the phonon radiative transport across the contact resistance. In order to examine the phonon intensity behaviour across the interface, equivalent equilibrium temperature is introduced in line with a previous study [159]. This temperature is the analog of the usual thermodynamic temperature defined in the diffusive limit in any medium. It represents the average energy of all phonons around a local point and it is equivalent to the equilibrium temperature of phonons when they redistribute adiabatically to an equilibrium state. It is defined as:

$$T(x,z,t) = \frac{\int_0^{k_{\max}} \int_0^{2\pi} \int_0^{\pi} I_k \sin\theta \, d\theta \, d\phi \, dk}{\int_0^{k_{\max}} \left(2C_{TA,k} v_{TA,k} + C_{LA,k} v_{LA,k} + 2C_{TO,k} v_{TO,k} + C_{LO,k} v_{LO,k}\right) dk} \tag{6.5}$$

The heat flux vector is defined at all points inside the layer as

$$q_x''(x,z,t) = \int_0^{k_{\max}} \int_0^{2\pi} \int_0^{\pi} \left(2I_{TA,k} + I_{LA,k} + 2I_{TO,k} + I_{LO,k}\right) \cos\theta \sin\theta d\theta d\phi dk \tag{6.6}$$

$$q_z''(x,z,t) = \int_0^{k_{\max}} \int_0^{2\pi} \int_0^{\pi} \left(2I_{TA,k} + I_{LA,k} + 2I_{TO,k} + I_{LO,k}\right) \sin\phi \sin^2\theta d\theta d\phi dk \tag{6.7}$$

$$\mathbf{q}'' = q_x''\mathbf{i} + q_z''\mathbf{k} \tag{6.8}$$

where I is the phonon radiation intensity, C is the sound wave in the solid ν is the frequency of the phonon, θ is the scattering angle of the phonons and φ is the azimuthal angle of the phonons. TA and LA represent transverse and longitudinal acoustic phonons due to the transverse and longitudinal motion of phonons at the interface. TO and LO are related to optical phonons instead of acoustic phonons.

6.1.1.3 Li-ion cell without PCM around it

As a baseline to compare the effects of applying PCM in various thicknesses, the cell without PCM is studied below. Steady-state simulations are presented followed by the transient response. Boundary and initial conditions are provided in the following section.

6.1.1.3.1 Steady-state heat transfer

For the heat generation rate of 63970W/m^3, the temperature contours are presented in Figure 6.4. For the considered boundary conditions and coefficient of heat transfer, the maximum volume – averaged and minimum temperatures of the cell will be compared with various other configurations. Three rakes have been defined for this problem. Rake 1, 2 and 3 in three different positions in the cell along with vertical rake throughout the height of the cell. Once the thermal conductivity is not constant in all directions, the heat transfer rate will be different in the cell surfaces. This will be investigated in the transient case later. The locations of rakes are shown in Figure 6.4, and the values are listed as follows:

- Rake 01: x=73 mm, y=127.75 mm, z ϵ [0 5.4] mm
- Rake 02: x=73 mm, y=97 mm, z ϵ [0 5.4] mm
- Rake 03: x=73 mm, y=24.25 mm,z ϵ [0 5.4] mm
- Rake 04: x=73 mm, y ϵ [0 194], z=2.7 mm

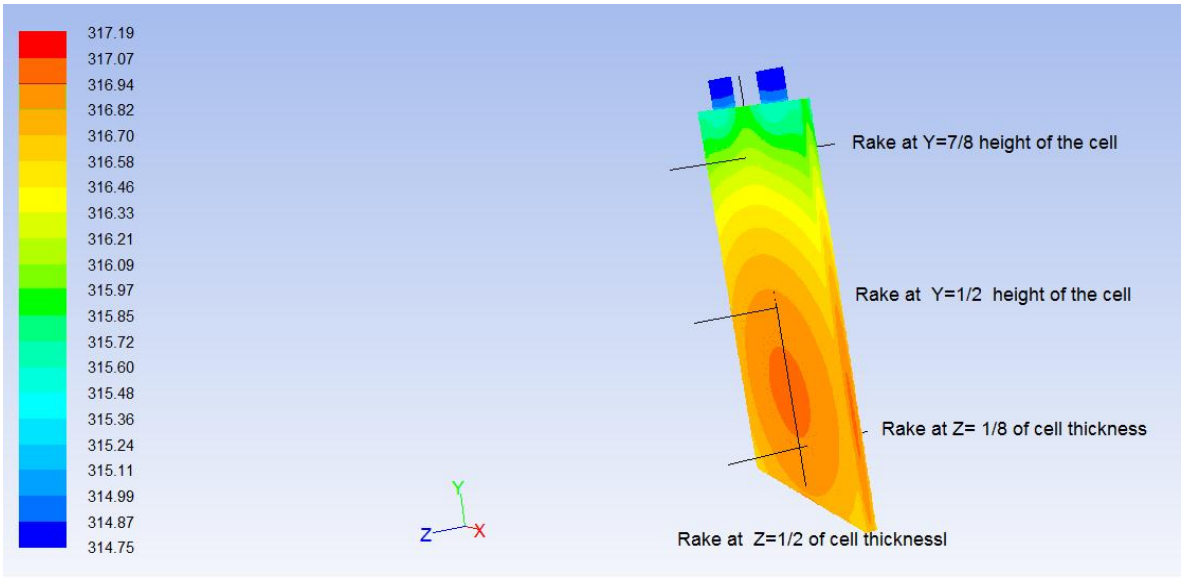

Figure 6.4 Temperature contours in the cell without applying cooling jackets of PCM

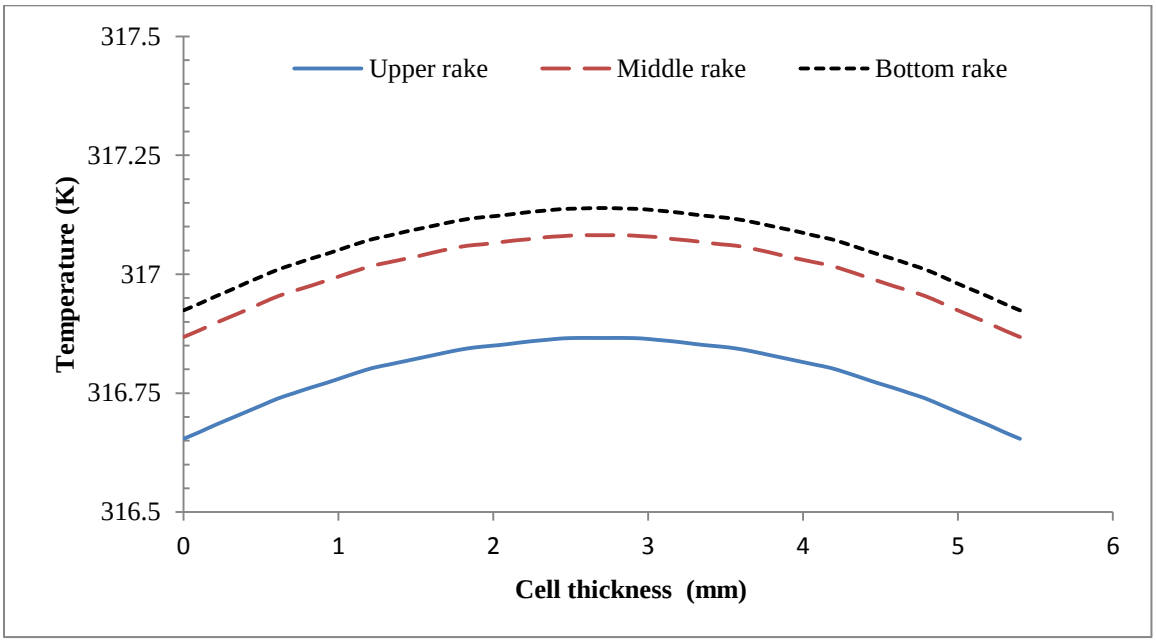

Figure 6.5 Temperature distribution along the horizontal rakes.

The temperature distribution in the created rakes is presented in Figure 6.5. It can be seen that the temperature increases its peak value in the middle portion of the cell, which is due to the symmetric boundary conditions. The vertical rake is created and the temperature distribution along this rake is shown in Figure 6.6 in order to find the location for the maximum temperature.

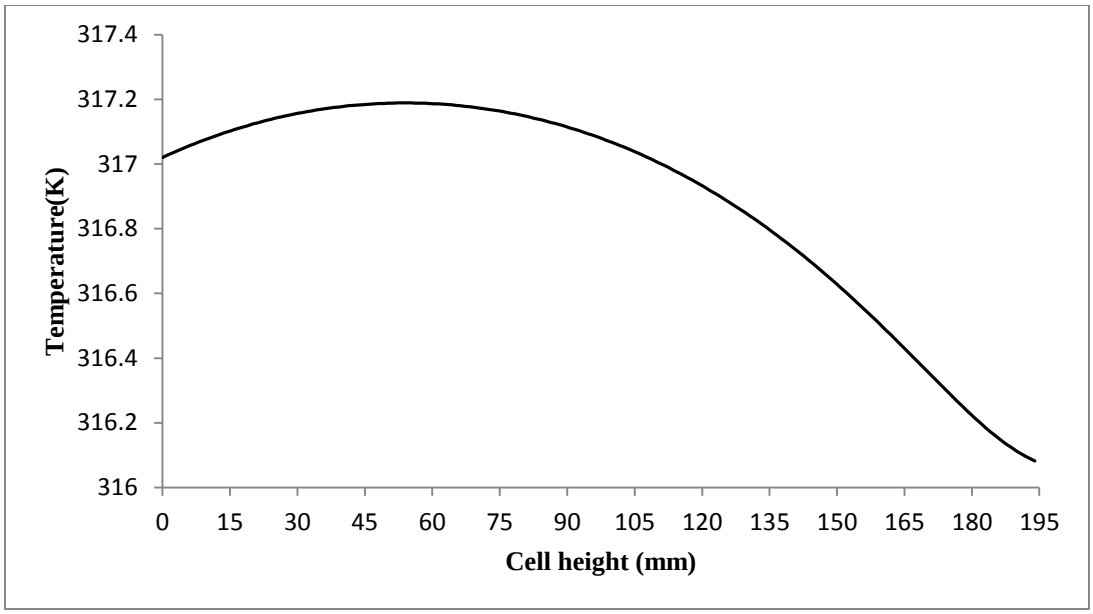

Figure 6.6 Temperature distribution along the vertical rakes

The curve fitting equation is obtained as

$$T = 2 \times 10^{-8} y^3 - 7 \times 10^{-5} y^2 + 6.9 \times 10^{-3} y + 317 \quad (6.9)$$

Therefore the maximum point of this graph is at y = 50.37mm. The main reason for this asymmetric profile is the boundary conditions of the problem. In the top boundary, where the connectors are attached, there is no PCM, which causes different conditions and imposes an asymmetrical pattern of temperature distribution. Another rake is created along the length of the cell (in the X direction). This is considered to be the critical rake in the cell. In the next steps, this rake will be the one considered when comparing the cooling of the different cases. This location is below the mid height of the cell due the cooling effect of terminals. Fig. 6.7 compares the temperature distribution in the critical rake and bottom rake. For all cases, where the cell has no PCM or different types of PCMs around it, three key values for temperature have been noted: minimum and maximum cell temperatures and volume-average temperature of the cell as bulk temperature.

Figure 6.8 shows these values for the steady-state case for the single cell as output from ANSYS FLUENT. For other cases, the values are presented at the end of this section.

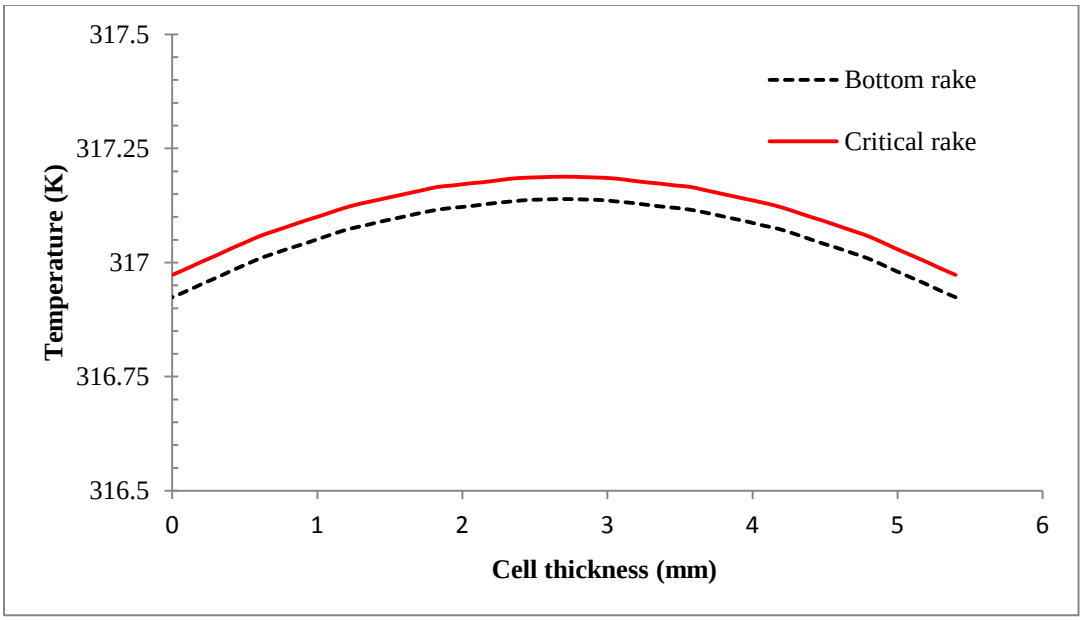

Figure 6.7 Temperature along the critical rake compared to the bottom rake

```
                                  Max
                Static Temperature                    (k)
-------------------------------- --------------------
                              cell             317.18939
                ---------------- --------------------
                               Net             317.18939

                                  Min
                Static Temperature                    (k)
-------------------------------- --------------------
                              cell              315.2774
                ---------------- --------------------
                               Net              315.2774

          Volume-Weighted Average
                Static Temperature                    (k)
-------------------------------- --------------------
                              cell             316.73862
                ---------------- --------------------
                               Net             316.73862
```

Figure 6.8 Average and extreme temperatures for the single cell in steady-state condition

6.1.1.3.2 Transient response of the cell

To start the transient responses of the models, the time-step independency of the mesh is shown in Figure 6.9. Time steps of 2.5, 5 and 10 seconds are considered.

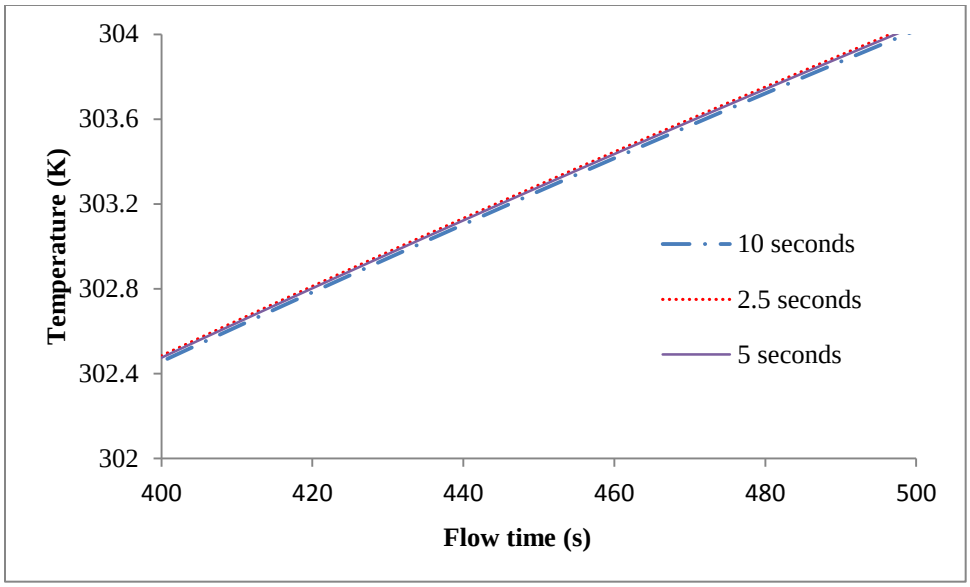

Figure 6.9 sensitivity of the mesh for time steps

The percent difference is used instead of the percent error (because none of the values are known or based on experiments).

$$\text{Percent difference} = \frac{|(T_{5s} - T_{2.5s})|}{(\frac{T_{5s} + T_{2.5s}}{2})} \times 100 \qquad (6.10)$$

For the time equal to 500 seconds, time steps of 2.5 and 5 seconds will give the temperature in the cell as 304.05 K and 304.04 K. The percent error in this case is 0.003%. The time step of 5 seconds is mostly used in transient analysis in this study unless higher heat generation rates are considered. Such a scenario is dominant for the heat generation rate of 200 kW/m^3 which will not last more than a couple of minutes. In these cases, smaller time steps have been used. The results for the transient solution will be used as comparison criteria with the other configurations.

6.1.1.4 PCM with thickness of 3 mm around the cell

The case with 3 mm of PCM around the cell is considered first (as shown in Fig. 6.10). In this case, the maximum cell squish of the mesh is 7.67886e-002, which allows better geometrical mesh stability. The steady-state and transient responses of the system will be compared with the previous case where there was no PCM around the cell.

The effect of PCM around the cell will give a shift in the location of maximum temperature in the cell as it can be seen in Figure 6.11.

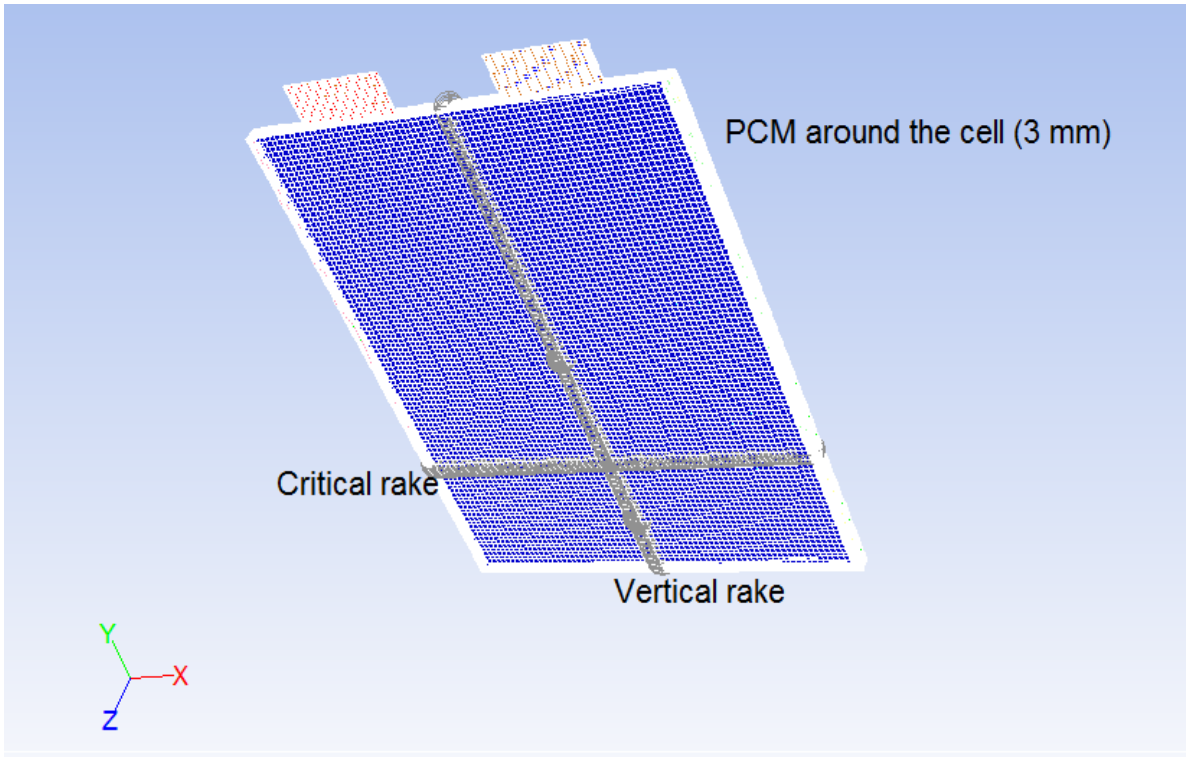

Figure 6.10 Location of vertical and critical rake in cell

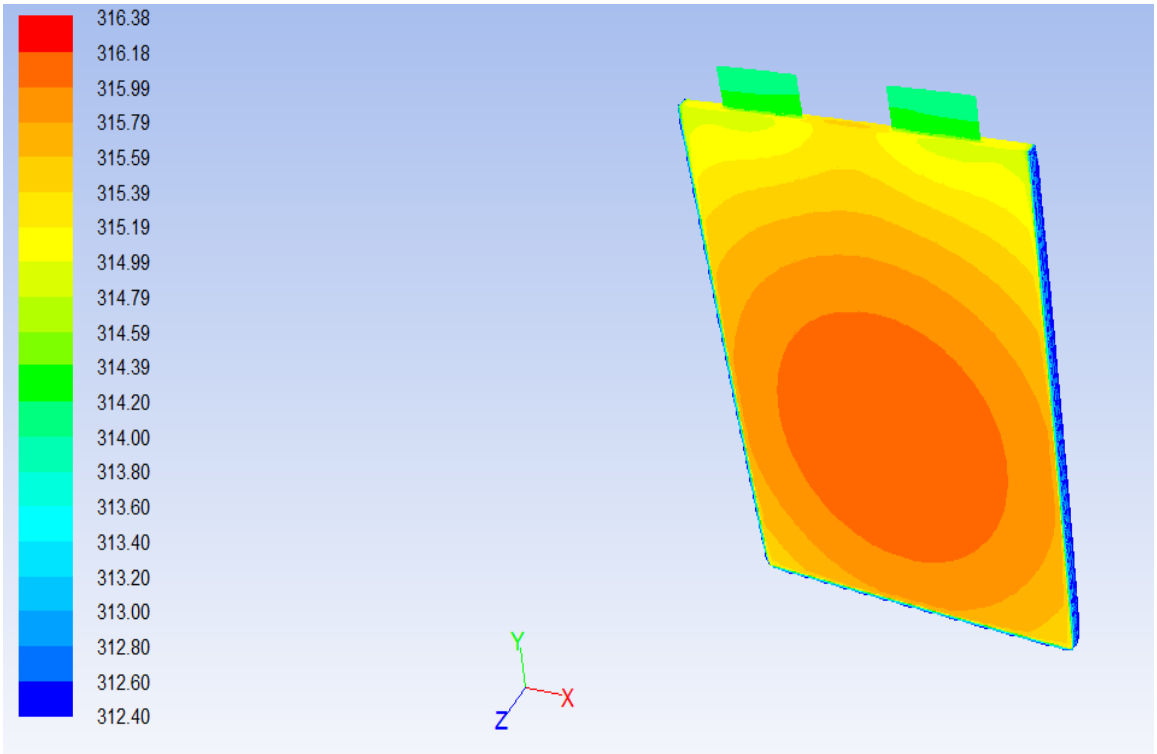

Figure 6.11 Temperature contours in the cell with PCM (3mm) around cell

Fig. 6.12 shows the shift in the location of the critical rake in the cell, caused by the application of the PCM. The curve fit method gives the critical height of the cell to be $y_{critical}$ = 72.8 mm; therefore, the new location is shifted 22.5 mm toward the cell interior. Fig. 6.12 also shows that using PCM around the cell should lead to better temperature uniformity. At the same time, the maximum temperature is reduced. As was mentioned in Chapter 2, decreasing the temperature and increasing the uniformity of temperature distribution are considered two critical criteria in the assessment of TMSs for the battery. A decrease in the maximum temperature of the cell is demonstrated in both cases, shown in Table 6.2.

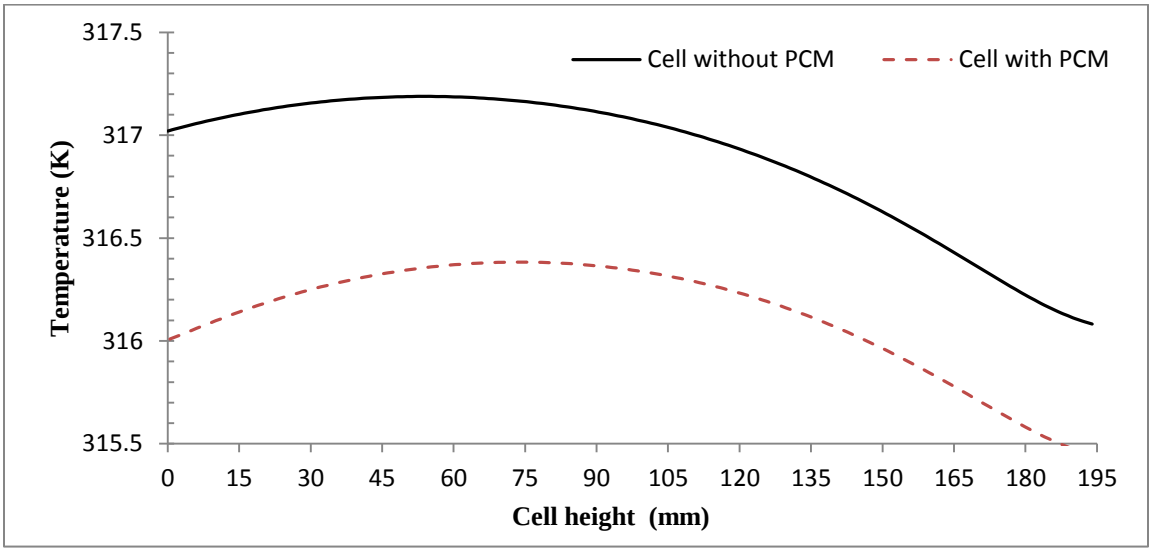

Figure 6.12 Change in the location of maximum temperature point in the vertical rake in the cell

Table 6.2 Maximum temperatures in cell with and without the PCM around it

Model	$T_{cell,\ min}$ (K)	$T_{cell,ave}$ (K)	$T_{cell,max}$ (K)
Cell without PCM	315.28	316.74	317.19
PCM (3mm thickness)	314.62	315.92	316.38

6.1.1.4.1 Transient response

The nature of the current study mostly relies on the transient behavior of the system. In a steady-state solution, the PCM has been already melted and the liquidus thermal conductivity will determine the solution. The mathematical difference between the steady-state and transient temperatures has been replaced by the quasi-steady-state and steady-state temperature differences in the cell. This means that when the average temperature (volume-average) in the

transient condition reaches a quasi-value (85% is used in this study), it is treated as the steady-state response.

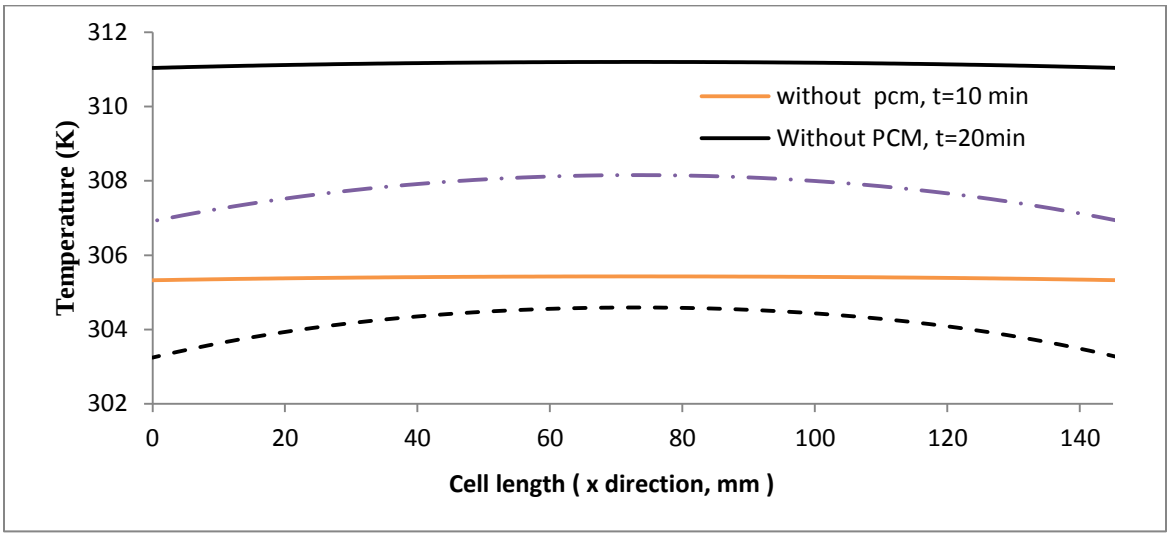

Figure 6.13 Transient response of the cell without PCM and with 3 mm thickness PCM around it

In order to monitor the temperature in the transient solution, a horizontal rake, created in the location of maximum temperature in the cell, is used with results to be compared with the other cases. Fig. 6.13 compares the temperature rise in two critical rakes for the case with no PCM and when there is a 3 mm thickness PCM around the cell.

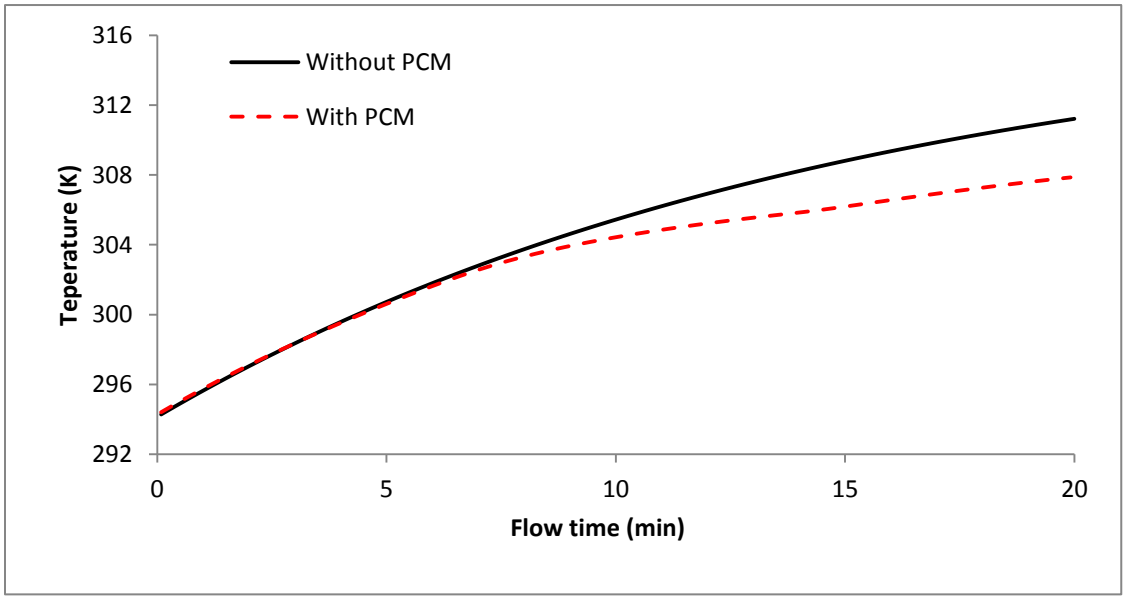

Figure 6.14 Effect of the PCM to prevent temperature increase in cell

Two results can be deduced from Figure 6.14. Firstly, the effect of flow time on the maximum temperature difference can be seen in both cases. The effect of PCM after 20 minutes

is clearer than the 10 minute effect. Secondly, the maximum temperature is reduced in the cell by using the PCM. Another monitoring possibility is the maximum temperature trend in the cell. Figure 6.14 shows the effect of the PCM in preventing the temperature increase in the cell.

6.1.1.5 PCM with 6mm thickness

The same method is applied for the case with 6mm PCM around the cell. In this case, the critical height for the highest temperature of the cell is calculated to be Y = 87.86 mm (critical height for vertical rake). Along the cell length (X-direction) and at the new height, the horizontal rake is created to monitor the critical temperatures in the cell. The results are recorded for the flow times of 10 minutes and 20 minutes.

6.1.1.6 Cell with PCM with 9 mm and 12 mm thicknesses

The new position is found to be Y = 84.37 mm, which may be considered close enough to the previous location of 87.86 mm. Temperature distribution in the cell is shown in Fig. 6.15, along with the shift of maximum temperature toward the upper side of the cell.

In the steady-state situation, the vertical temperature distribution equation is

$$T = 7 \times 10^{-8} y^3 - 10^{-4}\, y^2 + 0.0158y + 314.79 \qquad (6.11)$$

The maximum temperature along the rake happens at the height of y=86.94 mm. The temperature contours in the case shows the uniform cell temperature distribution.

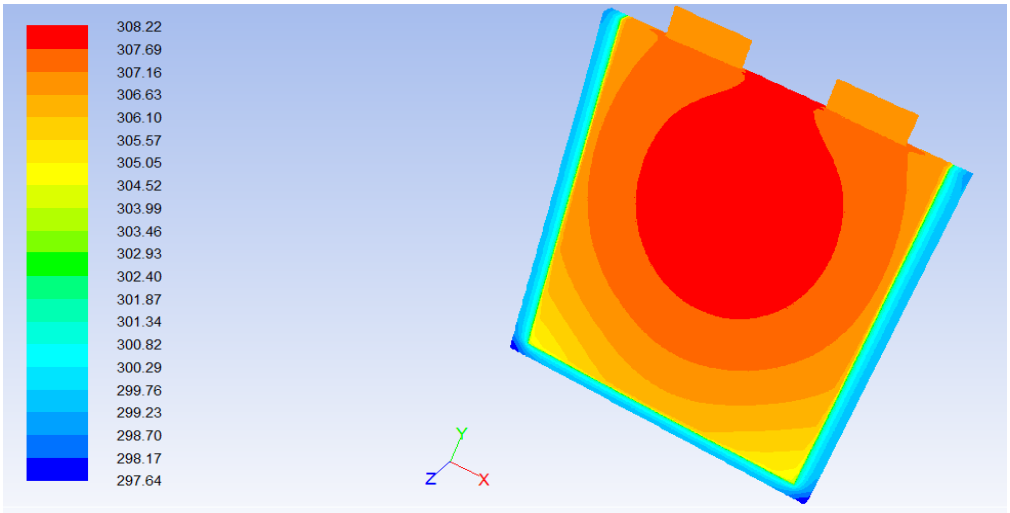

Figure 6.15 Temperature contours for PCM with thickness of 12mm

The PCM is melted by increasing the temperature. The amount of the PCM used will extend the time interval that temperature is absorbed in the PCM and prevents temperature increase. Fig. 6.16 shows the PCM around the cell, which is partly melted. The inside section represents the melted region of the PCM. Creating an animation in ANSYS FLUENT makes the speed and melting process within the cell easier to observe.

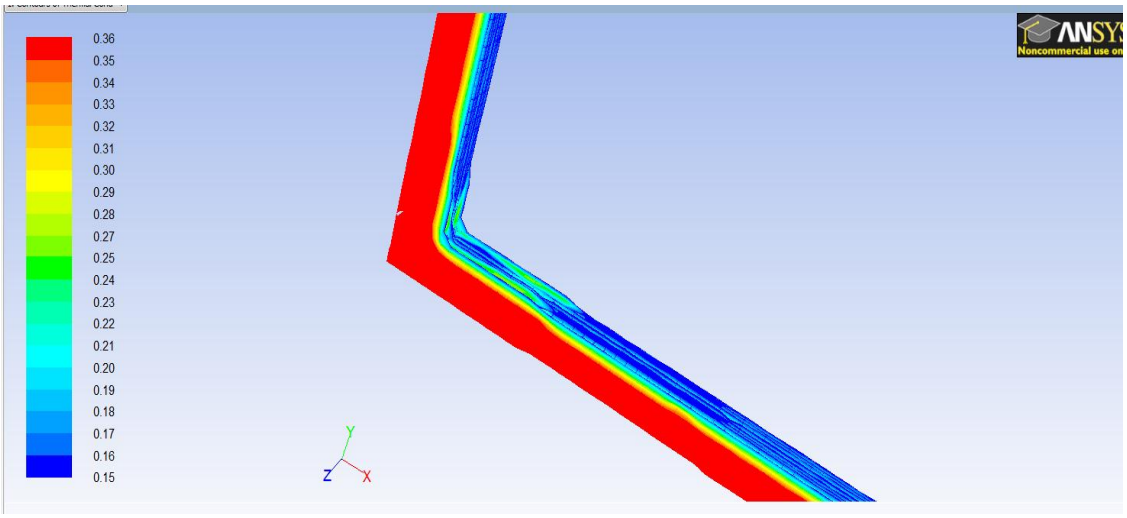

Figure 6.16 The mushy zone around cell during melting process

6.1.1.7 Discussion of the TMS for the cell and PCM around the cell

The overall results for the cell without the PCM and with 4 different thicknesses (3 mm, 6 mm, 9 mm and 12 mm) are presented below.

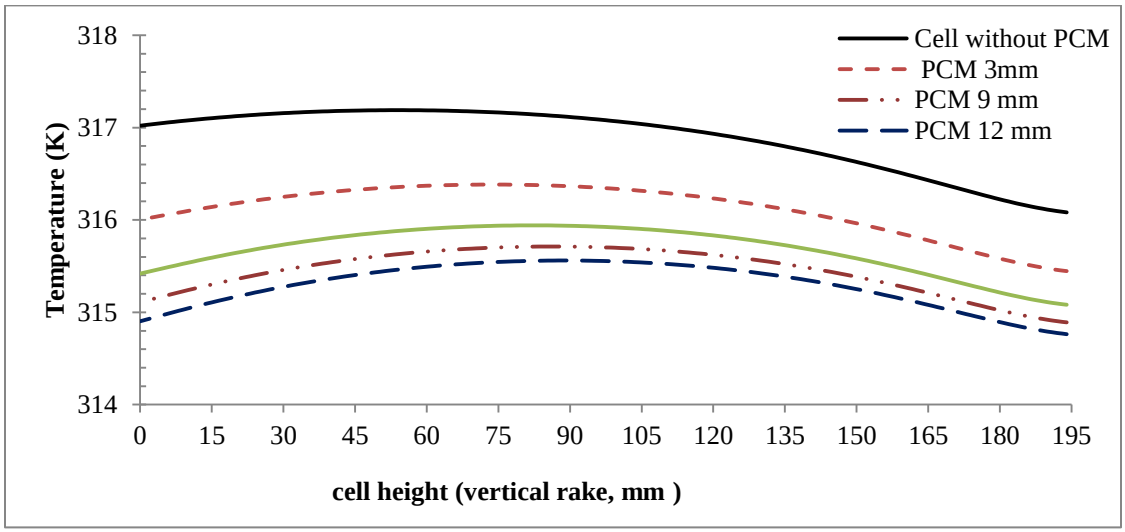

Figure 6.17 Steady-state temperature distribution along vertical rake in cell

The shift in maximum temperature can be observed in Figures 6.11 and 6.17, as previously noted. Figure 6.18 shows the temperature distribution in the horizontal rake at a flow time of 10 minutes. Time dependent response of different thicknesses is given in Figure 6.19.

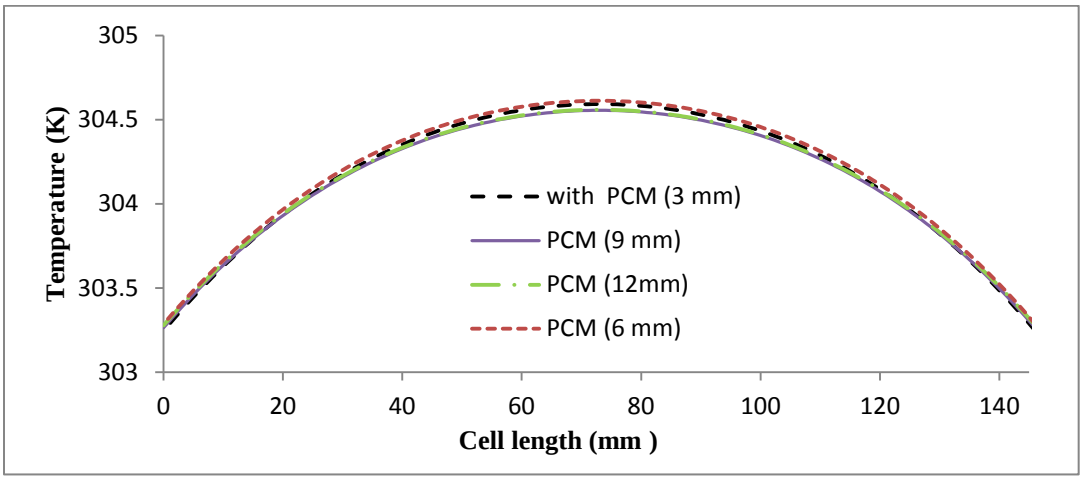

Figure 6.18 Transient responses of cells after 1 minute (heat generation rate of 63.970 kW/m^3)

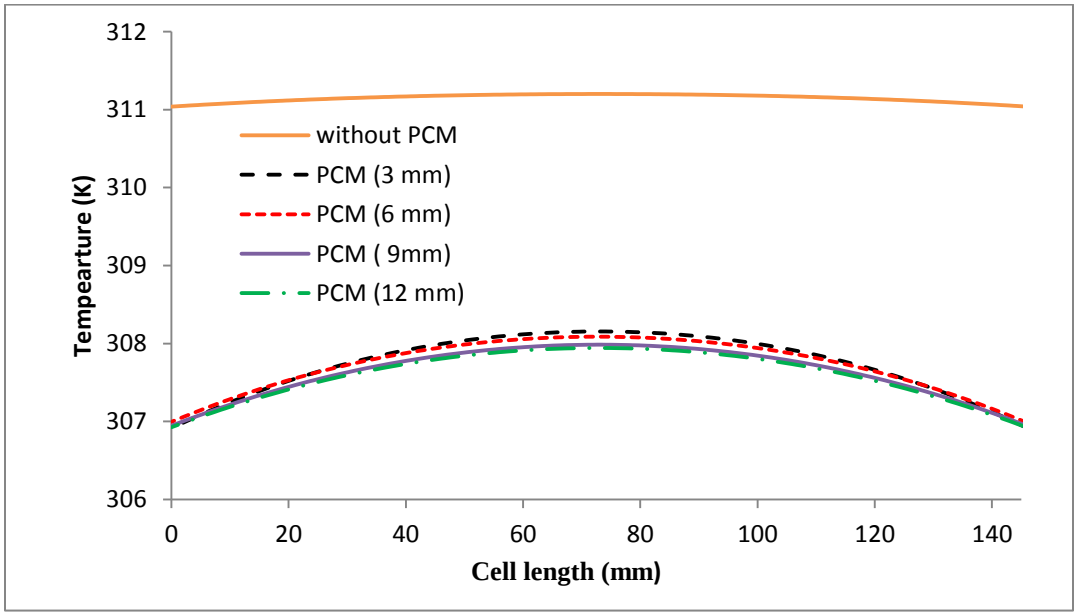

Figure 6.19 Temperature distributions in horizontal rake after 20 minutes

The higher temperature of 305.43 K refers to the case where there is no PCM thermal management in the cell. A similar comparison is shown in Figure 6.20 for the elapsed time of 20

minutes. In order to investigate the effects of PCM thickness on the temperature distribution along the horizontal rake, the temperature range has been modified in Figure 6.20.

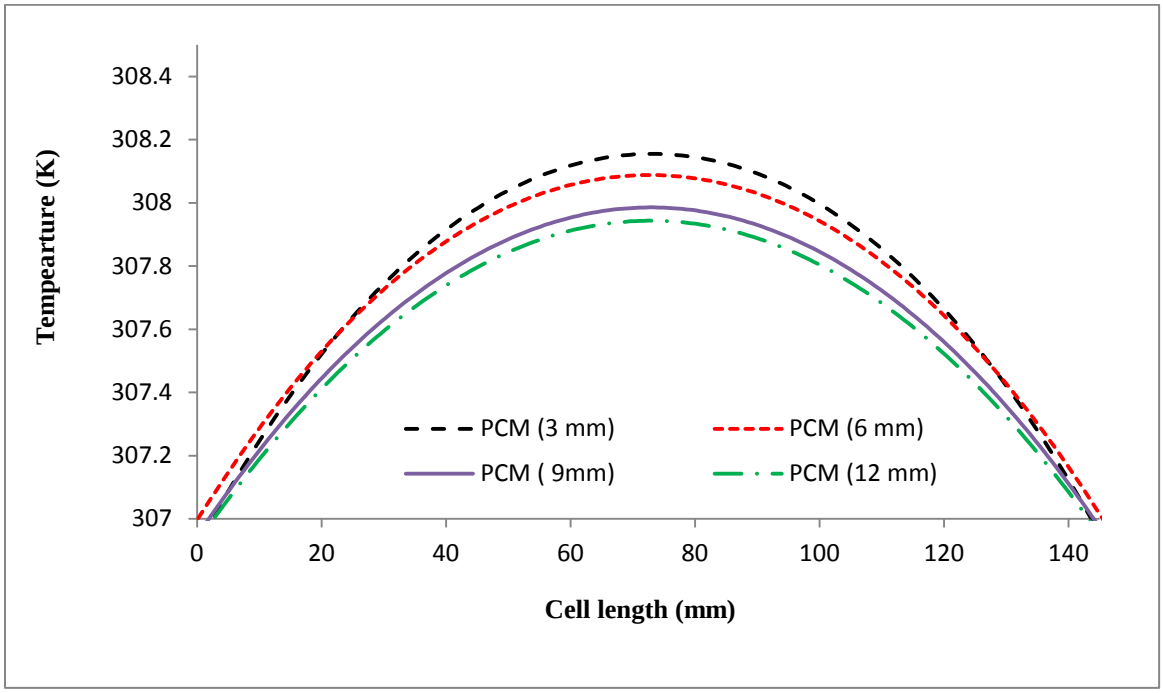

Figure 6.20 Temperature along the horizontal rake in the cell after 20 minutes

Figure 6.21 reveals that PCM with 12 mm thickness has the greatest thermal management effect on the cell. However, it should be noted that there is a geometrical restriction in putting thicker layers of PCM around the pack. Also, considering the melted PCM, the thicker layer will impose higher thermal resistance around the cell, which is detrimental to thermal management of said cell. The mid cell point has the following temperature response over time: with the studied heat generation rate (63.07 W/liter), in less than 7 minutes the effect of PCM around the cells will dominate in ameliorating the temperature increase in the cell.

As the maximum temperature in the cell might not represent the entirety of the physics behind the problem, the temperature distribution along the rake has been compared for different thicknesses. As Figure 6.22 shows, temperature values along the rake will have a slower rate of increase for higher PCM thicknesses, which prevent the maximum temperatures in the short time.

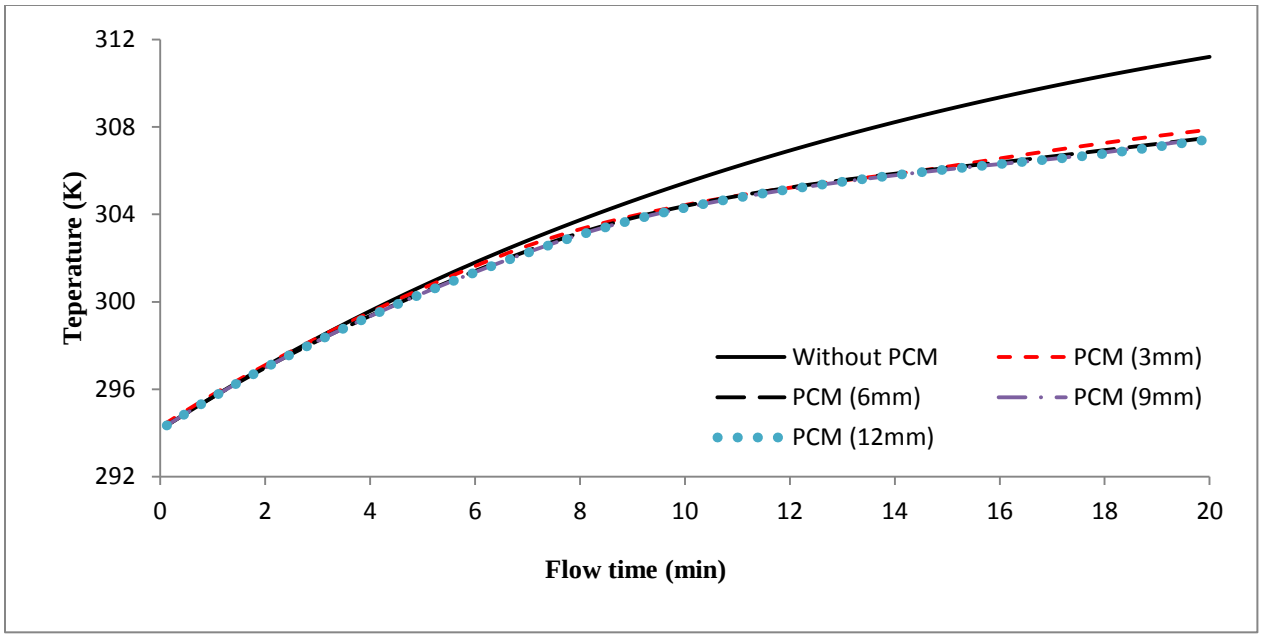

Figure 6.21 Cell maximum temperature

In order to compare the temperatures in the different models, minimum, volume average and maximum temperature values of the cell were measured and are shown in Table 6.3. The effect of PCM on average cell temperature with different PCM thicknesses has been illustrated in Fig. 6.23.

Table 6.3 Critical temperatures in the cell for different models

Configuration	**Cell minimum temp. (K)**		**Cell average temp. (K)**		**Cell maximum temp. (K)**	
	Flow time: 10 min	**Flow time: 20 min**	**Flow time: 10 min**	**Flow time: 20 min**	**Flow time: 10 min**	**Flow time: 20 min**
Cell without PCM around	304.54	309.82	305.24	310.89	305.43	311.20
Cell with PCM (3 mm)	302.37	305.05	303.98	307.58	304.70	308.43
Cell with PCM (6 mm)	302.48	304.72	303.97	307.37	304.64	308.30
Cell with PCM (9 mm)	302.34	304.63	303.92	307.34	304.61	308.22
Cell with PCM (12 mm)	302.35	304.58	303.92	307.28	304.60	308.16

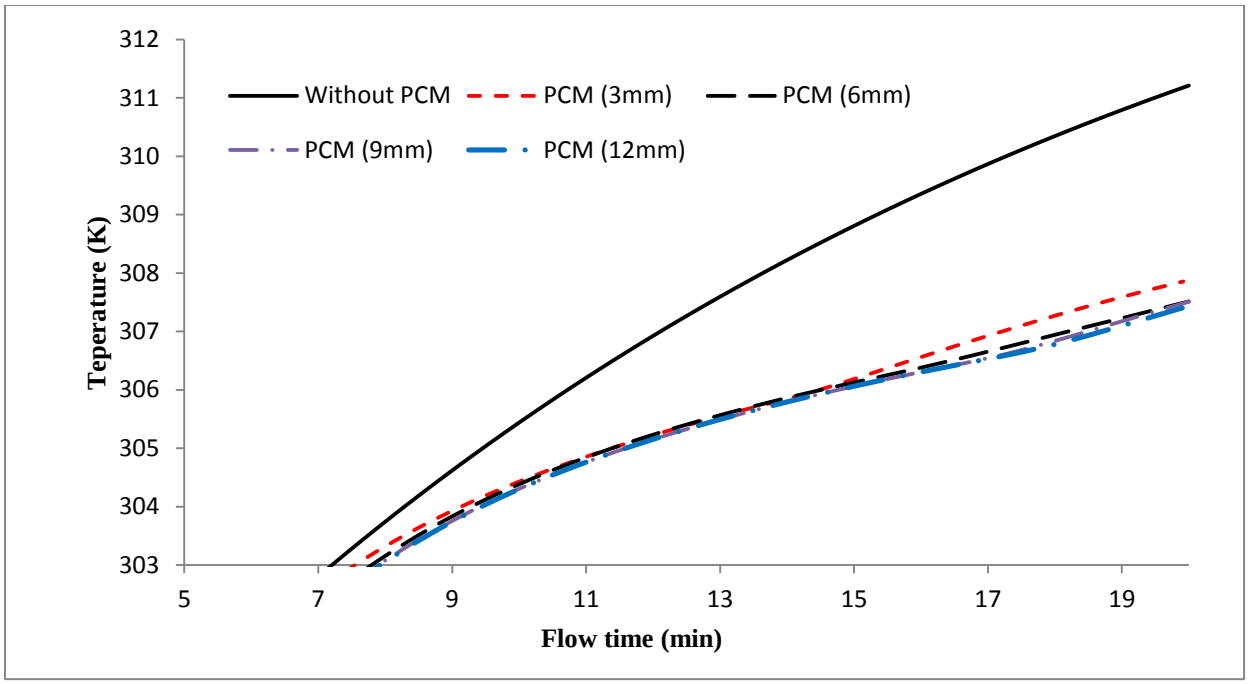

Figure 6.22 Effect of PCM with different thicknesses to prevent the temperature increase

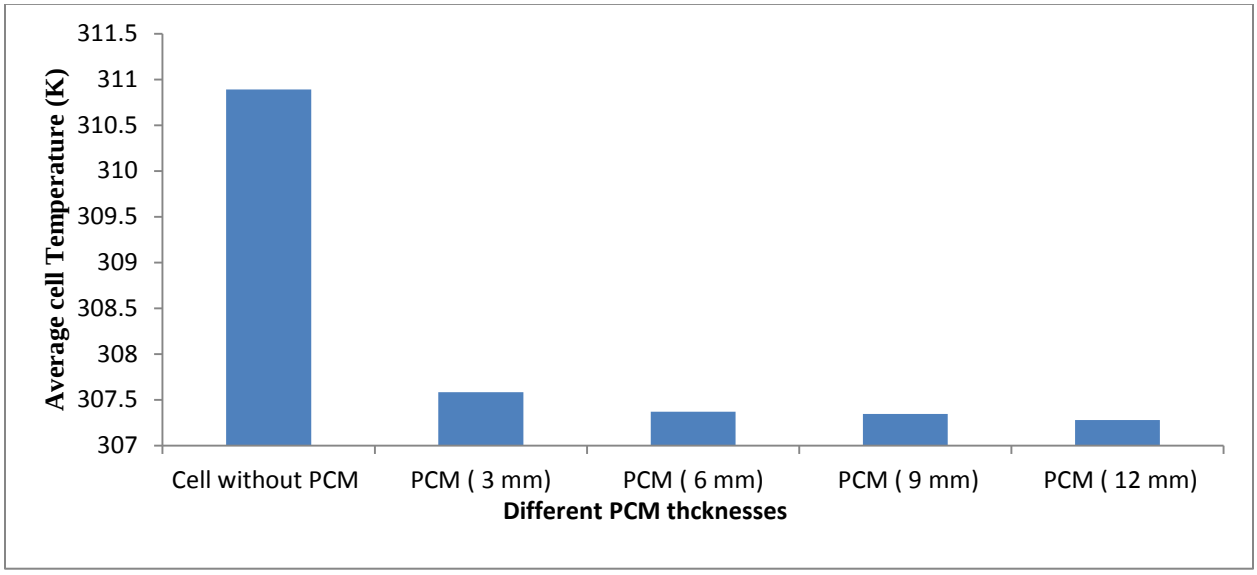

Figure 6.23 Average cell temeprature with different PCM thicknesses after 20 minutes

Cooling effectiveness

In order to investigate the cooling effectiveness, the following dimensionless parameter is defined for temperature variation along the critical horizontal rake in all five configurations (cell without PCM and with PCM in different thicknesses of 3, 6, 9 and 12 mm).

$$Cooling\ Effectiveness = \frac{T - T_{bulk,gen}}{T_{max,gen} - T_{bulk,gen}} \quad (6.12)$$

where $T_{bulk,gen}$ =Bulk temperature of all models and $T_{max,gen}$ = Maximum temperature of all models. Figure 6.24 shows the cooling effectiveness in the tested models.

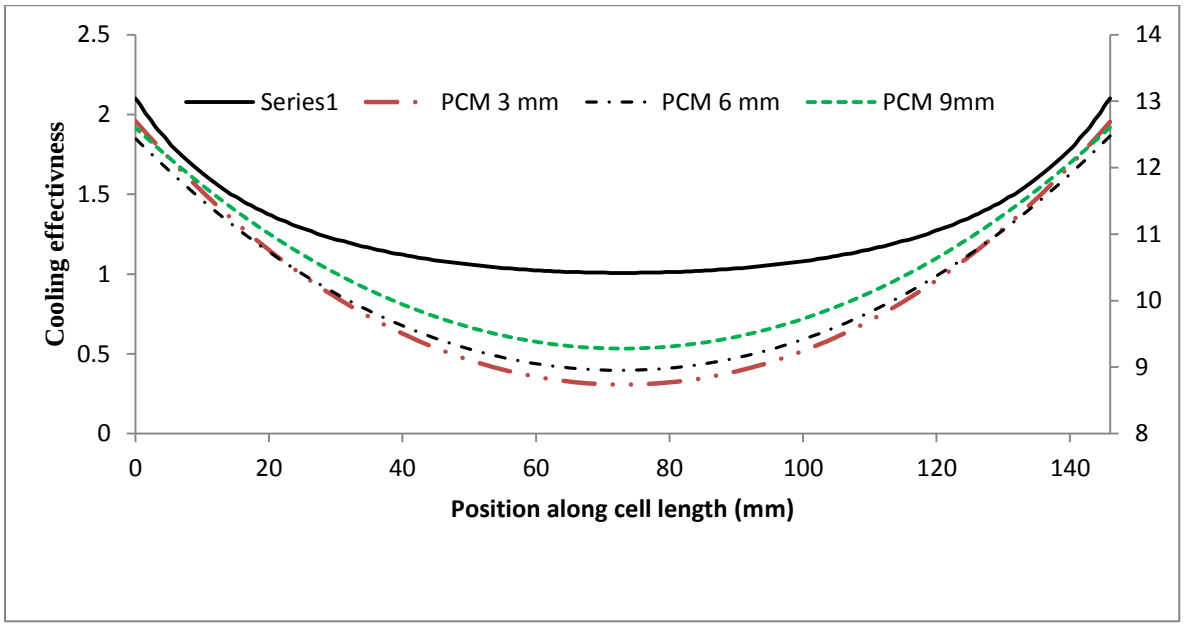

Figure 6.24 Cooling effectiveness for different configurations

The other parameter used to assess the cooling effect of the PCM on the cell is defined as the relative temperature ratio. Two temperature coefficients are defined below:

Overall temperature coefficient: $$\theta_1 = \frac{T - T_{max,local}}{T_{max,gen} - T_{max,local}} \quad (6.13)$$

Local temperature coefficient: $$\theta_2 = \frac{T - T_{bulk,local}}{T_{bulk,gen} - T_{bulk,local}} \quad (6.14)$$

where $T_{bulk,gen}$ =Bulk temperature of all models

Figs. 6.25 and 6.26 show temperature coefficient variations along the rake location for different thicknesses. Effectiveness Index **Ω** is defined as the depth of the curvature in Figs. 6.26 and 6.27. The larger Ω values represent higher local maximum (or local bulk) temperatures. Therefore, a large PCM thickness around the cell will have smaller depth in curvature which, in turn, provides better cooling in the cell. In this case, the maximum temperature in the cell attains low values and the difference between the maximum and the minimum temperature becomes small across the cell.

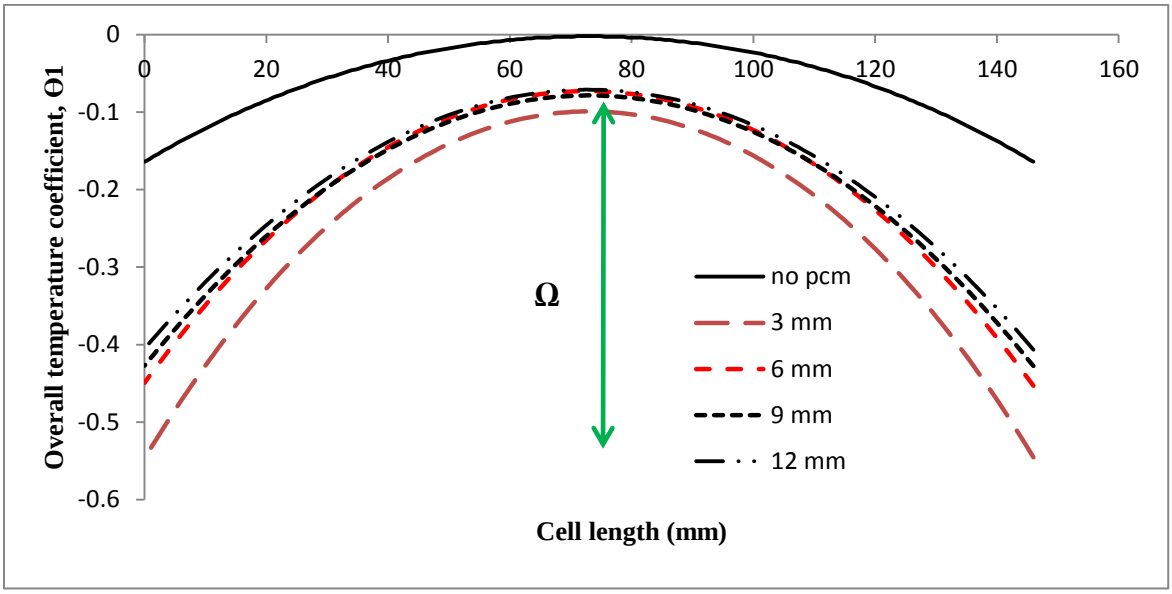

Figure 6.25 Overall temperature coefficient along cell for different PCM thicknesses

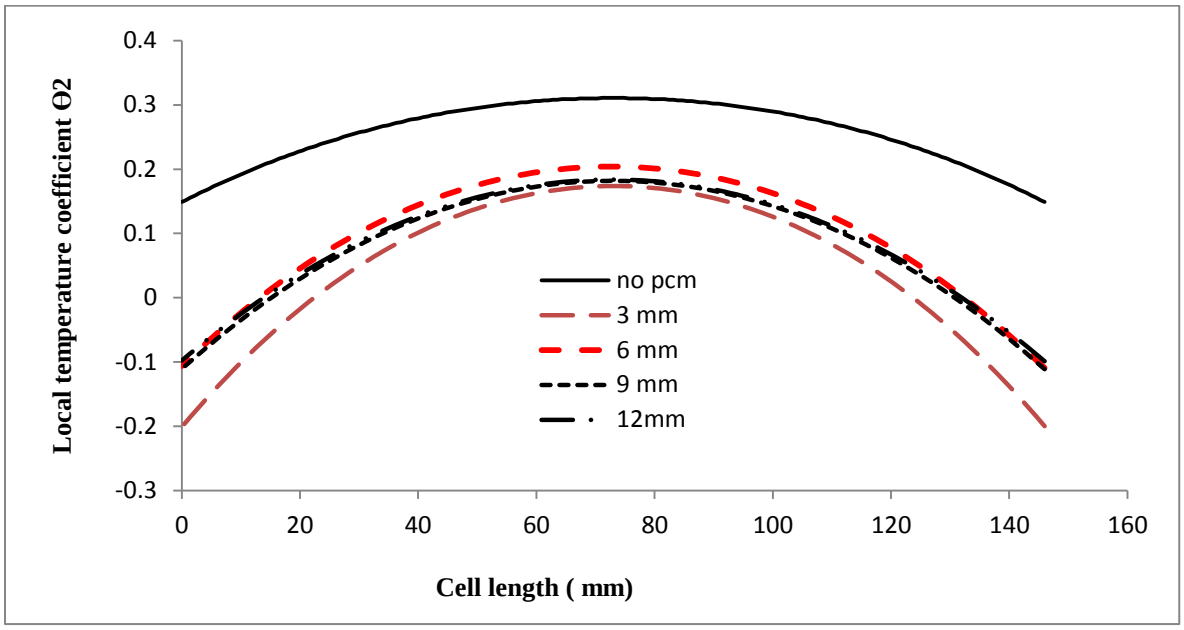

Figure 6.26 Local temperature coefficient along the horizontal rake in cell for different PCM thicknesses

6.1.1.8 Functional relation for characterization of thermal management system

In order to include the sensible and latent heat in the thermal management, a new parameter is required. This is because of the fact that the Stefan number only considers sensible heat storage

in the liquid phase over the latent heat of melting of the PCM. However, in such a thermal system, the presence of a solid phase requires inclusion in the sensible heat storage. The new parameter represents the functional relation for thermal characteristics of the system and system performance.

$$St = \frac{C_p \Delta T_L}{L} \tag{6.15}$$

Here, the denominator represents the sensible heat of melted phase and L is the latent heat of fusion.

$$\Delta T_L = T_f - T_m \tag{6.16}$$

where T_f and T_m represent final temperature and melting temperature of the PCM.

However, the PCM may not have a single phase change process and phase change may to take place across solidus and liquidus temperatures. To include the effect of solidus heat storage and the mush zone effect on TMS, it can be expressed in the following way:

$$Q_{in} = C_{ps}(T_{solidus} - T_{initial}) + x.L + C_{p_L} \Delta T_L \tag{6.17}$$

Hence in the case of complete melting:

$$\frac{Q_{in}}{L} = \frac{C_{ps} \Delta T_s}{L} + x.L + \frac{C_{p_L} \Delta T_L}{L} \tag{6.18}$$

In the case of complete melting it will be unit where “x” is the liquid fraction and is unit for the completed melted cases.

$$\frac{Q_{in}}{L} = \frac{C_{ps} \Delta T_s}{L} + 1 + \frac{C_{p_L} \Delta T_L}{L} \tag{6.19}$$

The last term in the equation is the Stefan number, therefore:

$$St = \frac{Q_{in}}{L} - (1 + \frac{C_{ps} \Delta T_s}{L}) \tag{6.20}$$

where $\frac{C_{ps}\Delta T_s}{L}$ corresponds to the ratio of heat storage in solid phase which is an important additional part of the total heat storage.

$$\text{New parameter} = 1+St+\frac{C_{ps}\Delta T_s}{L} \tag{6.21}$$

In designing the heat exchanger, this parameter is used and a mathematical equation is created based on genetic algorithm optimization—the relation between the optimum aspect ratios of the heat exchanger, number of straight tubes, and equivalent Reynolds number is found (Equation 6.43).

6.1.2 **Application of PCM around the battery pack side**

In the previous model, the PCM is applied around the cell. As results show, this TMS was effective at cooling down the cell. In this section, the PCM is going to be applied around the sub-module. As discussed earlier, the sub-module is formed by putting multiple cells together. The battery pack itself is formed by putting the sub-modules together in series, parallel or combined configurations. In this variant, the space between the cells does not change and, therefore, the related issues of manipulating the cells are avoided. The PCM is applied around the sub-module or battery pack by using enclosures or soaking into a material such as high stability foam. Fig. 6.27 shows the configuration of the cells and the foam with the cooling plate. In this sub-module, 4 cells are assembled with other components.

In the real sub module, there are plastic holders to keep the cells, foam and plates together. In the aforementioned configuration, there is foam, and then cell 1 will be in contact with this foam. The second foam acts as a separator between cell 1 and cell 2. Coolant, which is 50-50 water-ethylene glycol, flows through the plate and separates cell 2 and cell 3. In this section, the cooling effect of water has not been considered and the main focus is kept on the effect of the PCM and its role on thermal management of the battery.

In order to investigate the effect of the PCM on the pack, the baseline is the sub-module without PCM around it. The mesh possesses total volume elements of 261,000 cells. Sensitivity analyses have been carried out in the mesh, and mesh quality has been improved by using the Gambit mesh generator. In this system, there are 4 cells, 3 separating foams and 2 cooling plates,

which form 9 zones in total. Also, there are terminals that have been replaced symmetrically in the cells (Table 6.4).

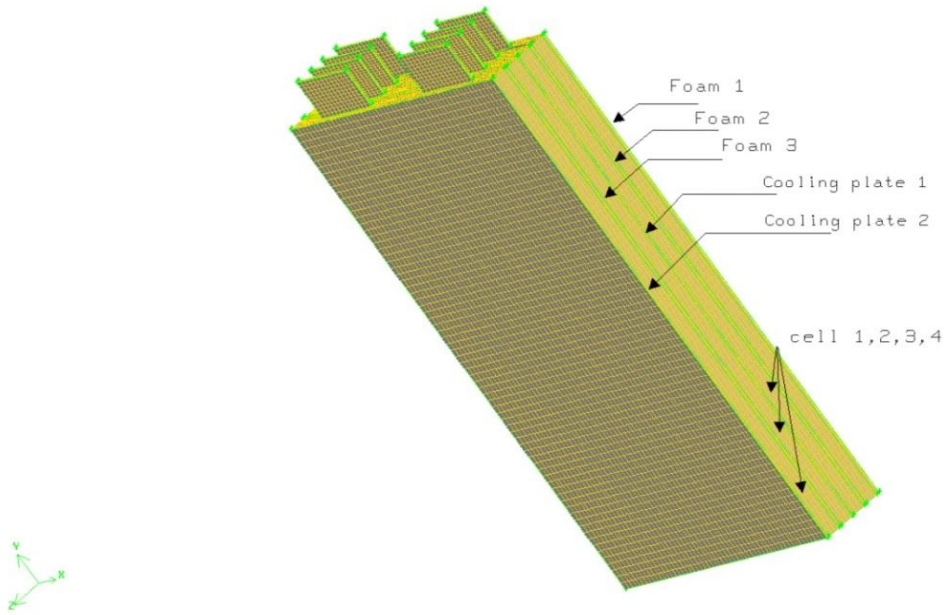

Figure 6.27 Configuration of cells, PCM sheets and cooling plates in the sub-module

Table 6.4. Dimensions of sub module without applying the PCM jackets

Dimension	Value (mm)
Wide (x)	146
Height (y)	196
Thickness (z)	25.6
Terminals dimensions (Length, Height and Thickness)	35, 15 and 0.6
Foam thickness	1
Cooling plate thickness	0.5

6.1.2.1 Steady-state response of the sub module without the PCM

First, the steady-state solution is studied. All the surfaces have convective heat transfer conditions with the ambient temperature. The cell has orthotropic thermal conductivity properties similar to the previous configuration. Initial conditions are the results of the steady-state results. The volumetric heat generation rate is 22,800 W/m^3 . Continuity in the properties is applied as coupled boundary condition between sub-module and surrounding PCM. The initial temperature in the domain is set to 294.15 K (21 °C)

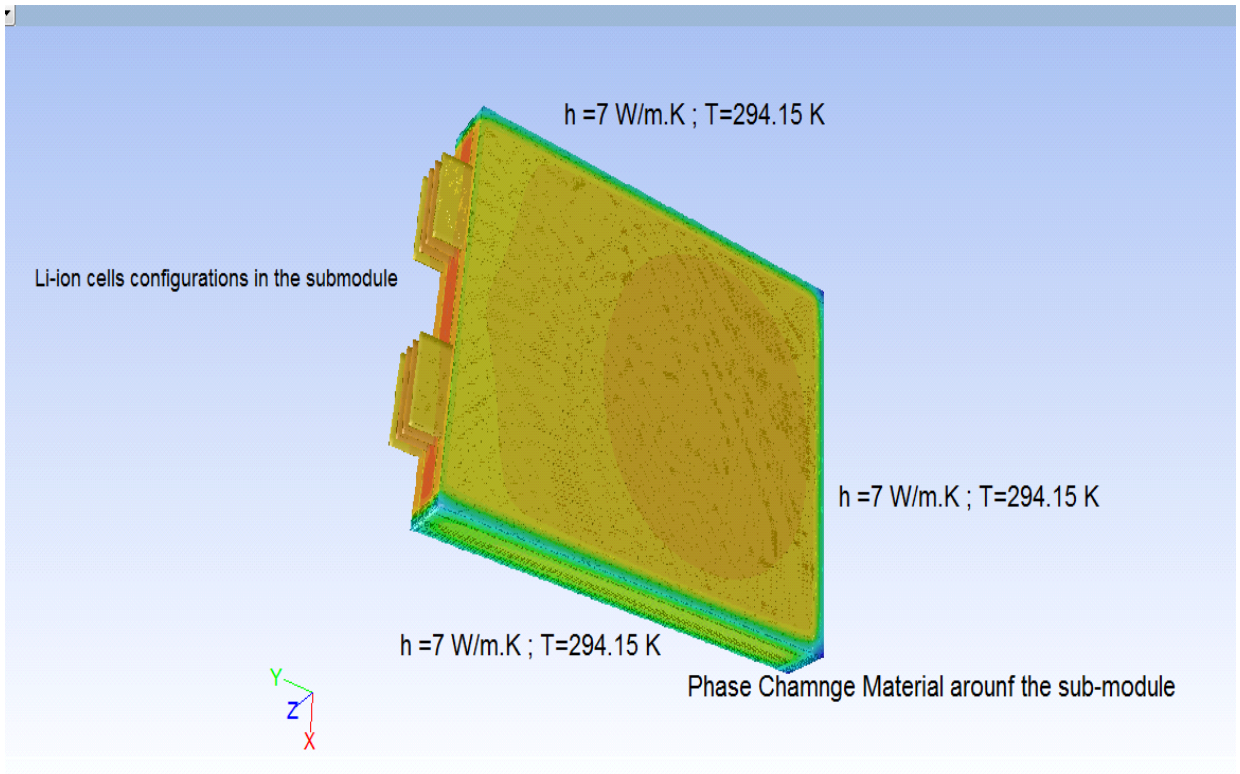

Figure 6.28 Boundary conditions in sub module

Fig. 6.28 illustrates the temperature contours. The high temperature contours are close to the base of the sub-module (away from the terminals). This location is traced in this section to assess temperature excursion. Temperature contours for the sub-module are shown in 6.30. Results show the maximum and minimum temperatures in the sub-module to be 321.28 K and 315.72 K respectively. In the real-life application in a vehicle, the cooling plate extracts the heat out of the pack by means of circulating coolant through the micro channels in the metal plates in between the cells. In this study, the minimum temperature occurs in foam 1, which is the foam in contact with the first cell as shown.

Because of the cooling effect of the terminals, the temperature distribution is not at the center of the cell. A rake has been created to determine the temperature along the Y-direction in the cell. Figure 6.29 shows the temperature profile along the vertical rake (along the cell height).

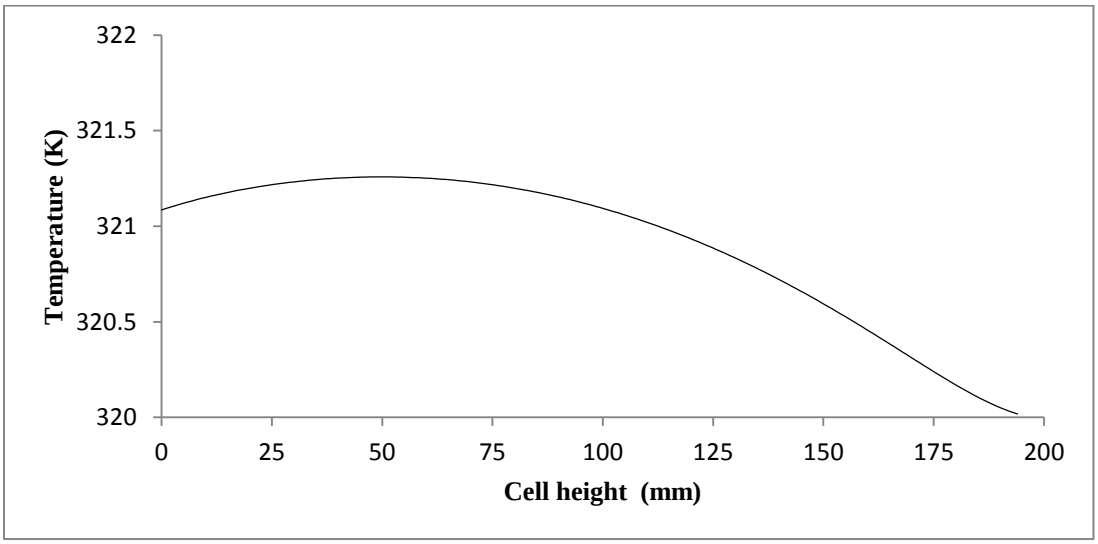

Figure 6.29 Temperature distribution in second cell

This shows that the maximum temperature will be closer to the base of the cell, with the above mentioned assumptions. To find the location, the curve fit will give y= 43.6 mm for the highest temperature in the cell. A new horizontal rake is created at this height and the results are compared with the other rakes. This is the same method that was explained in the previous configuration. The locations of the rake are shown in Table 6.5. Approximate locations of the rakes are shown in Fig. 6.30 in order to depict the geometry of the sub-module. The height of 43.6 mm has the maximum temperature along the sub-module thickness, as shown in Fig. 6.33. If this rake is defined as the critical horizontal rake in the sub-module, it can be used as an assessment location for the thermal management effect of the PCM..

Table 6.5 Position of the rakes in sub module to monitor the temperature distribution

Monitoring surface	x (Length, mm)	y (Height)	z (Thickness)
Rake 1	73	1/8 height, top	thickness
Rake 2	73	Half height	Throughout the thickness
Rake 3	73	1/8 height bottom	Throughout the thickness
Vertical rake	73	43.6	Thickness

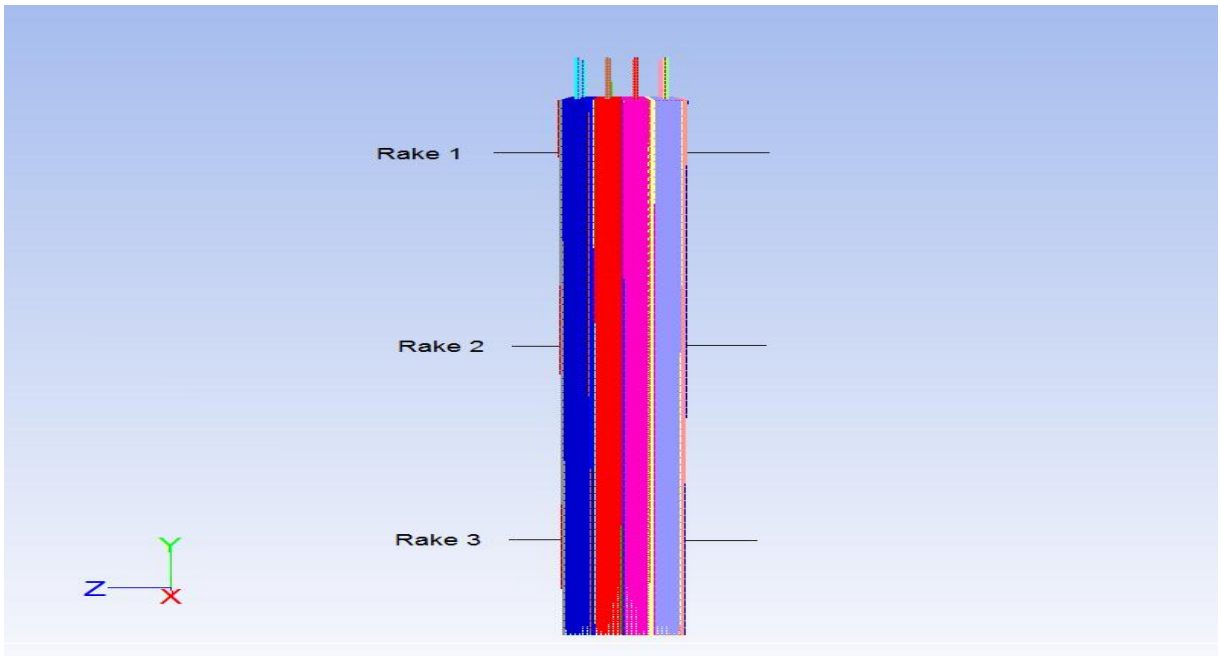

Figure 6.30 Rakes location in sub-module

A plane is created at the same height of the sub-module that illustrates the maximum temperature in different zones. The maximum temperature of the surface is the highest temperature in the sub module, which shows that the obtained height is the critical location. Animation for the temperature increase on this surface gives a better view from different layers in the sub module (Figure 6.31).

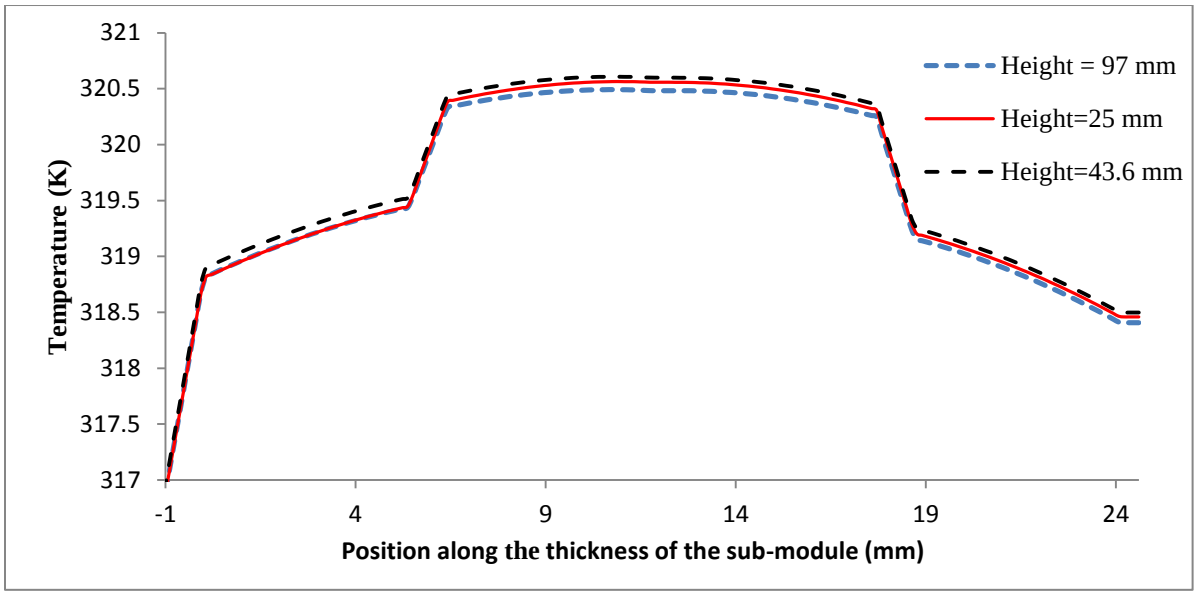

Figure 6.31 Comparison of temperature distribution along the rakes in vertical distance of sub-module

6.1.2.2 Steady-state response of the sub module with the PCM

In this model, The PCM is applied around the sub-module. The considered thickness for the sub-module is 6 mm. PCM foam has enclosed the sub-module all around except the northern face. When the heat propagates through the sub module, the PCM absorbs the heat and reaches the phase changing temperature. Then the heat is absorbed and in turn, will prevent the increasing rate of sub module temperature. Figure 6.32 shows the temperature contours in the sub module. Again, the rakes that have been created at the critical locations inside the sub module give the internal behaviour of the sub module. In the steady state, when the material turns to liquid completely, the lower thermal conductivity of the PCM will not act properly to extract the heat from the sub module and will behave as a thermal resistance. In the current condition, the PCM can operate in parallel to the conventional vapour compression cycle. This means that, the coolant will extract the heat from the battery pack. The PCM, which is either in encapsulated form or has been integrated with proper foam in the form of cooling jacket, can be cooled down by an auxiliary cooling system such as heat pipe or part of the cooling loop returning from the cabin air. The options depend on the operating temperature as well.

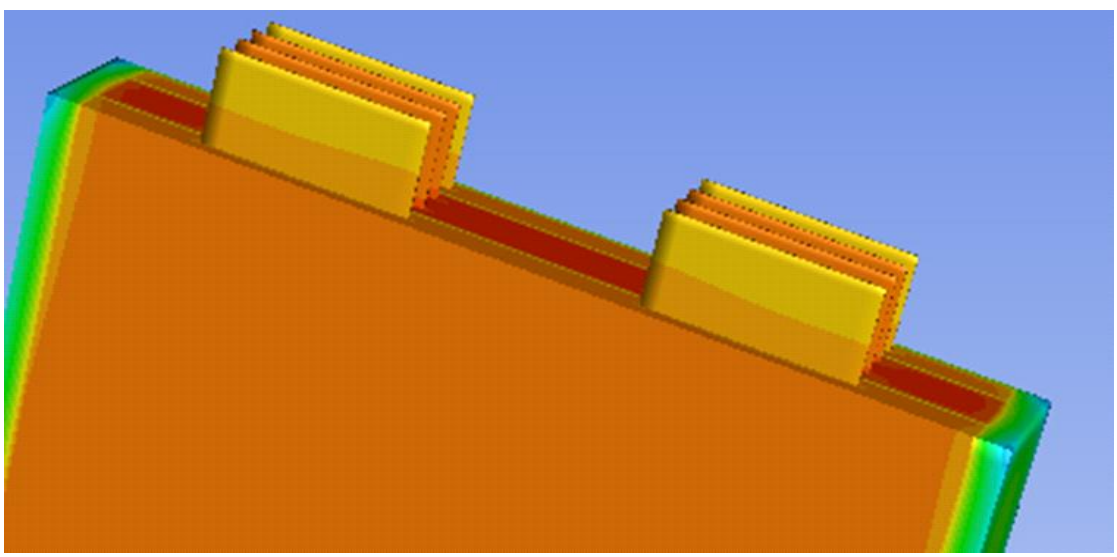

Figure 6.32 Temperature contours in sub-module surrounded with PCM

In order to have a better idea and comparison between this model and the case where PCM is not utilizes, maximum temperatures in different zones have been listed in Table 6.6

As Table 6.6 shows, cell-2 has the highest temperature which is close to cell 3. In between two cells, second foam is placed as a separator to prevent direct contact of them.

Temperature in the vertical alignment of the second cell is changing by the height. Its variation has been shown in Figure 6.33. The value of zero represents the bottom of the cell while the y=194 mm is the top of the cell, where the terminals are connected to the cell. Temperature is increasing in this direction and reaches a maximum value. Curve fitting of the temperature profile gives the maximum temperature location.

Table 6.6 Maximum temperatures in different zones of sub-module with and without PCM

Zone Name	Max. Temp. (K) With PCM	Max. Temp. (K) Without PCM
Foam 1	318.67	319.31
Cell 1	319.52	320.19
Foam 2	320.34	321.00
Cell 2	320.61	321.28
Cooling plate 1	320.60	321.27
Cell 3	320.61	321.27
Foam 3	320.23	320.89
Cell 4	319.24	319.90
Cooling plate 2	318.50	319.16
Terminals of cell 2	316.94	318.91
PCM around the sub module	319.90	319.31

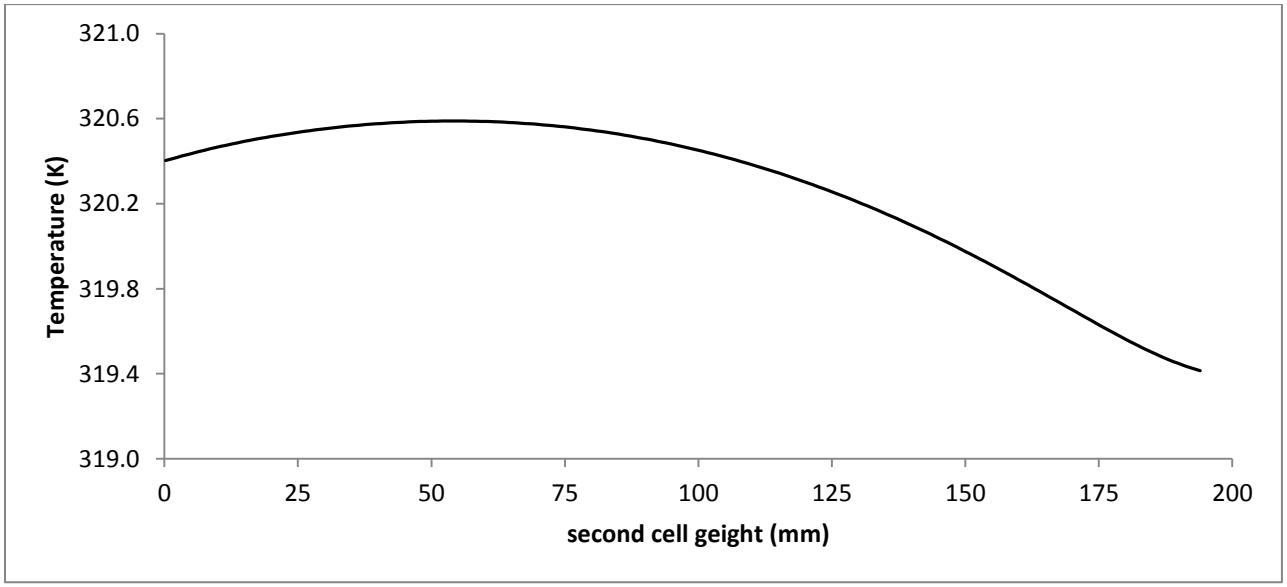

Figure 6.33 Temperature distribution along the vertical rake in cell-2 with the PCM

A vertical position of 55 mm provides the maximum temperature which is located in the cell 2 .Similar to the previous method; a horizontal rake is created in Z-direction which includes

all the 9 components of the sub module. The value of -1 mm depicts the foam 1 zone since the mesh coordinates starts at cell 1 (z = 0 indicates the corner of cell 1).

In order to verify the position of the new, two critical temperature distributions for each case have been compared. The temperatures in each critical case have been compared with each other instead of comparing the same rake in each case. Figure 6.34 shows illustrates that PCM decreases the temperature in the cell. The difference in temperatures is noticeable in two cases. This is highlighted in Table 6.7. As it mentioned in Chapter 2, two parameters which depict the effectiveness of the thermal management are the magnitude and more uniformity of temperature distribution. Both of these criteria are met by using the PCM in the sub module. This can be seen in Figure6.35.

- The maximum temperature has been decreased.
- Temperature excursion has been modified and decreased which is an important issue in the battery pack and Li-ion cells.

This conclusion can be observed in Figure 6.35 which illustrates more uniform temperature contours in the sub module in compared with the bare sub module without the PCM.

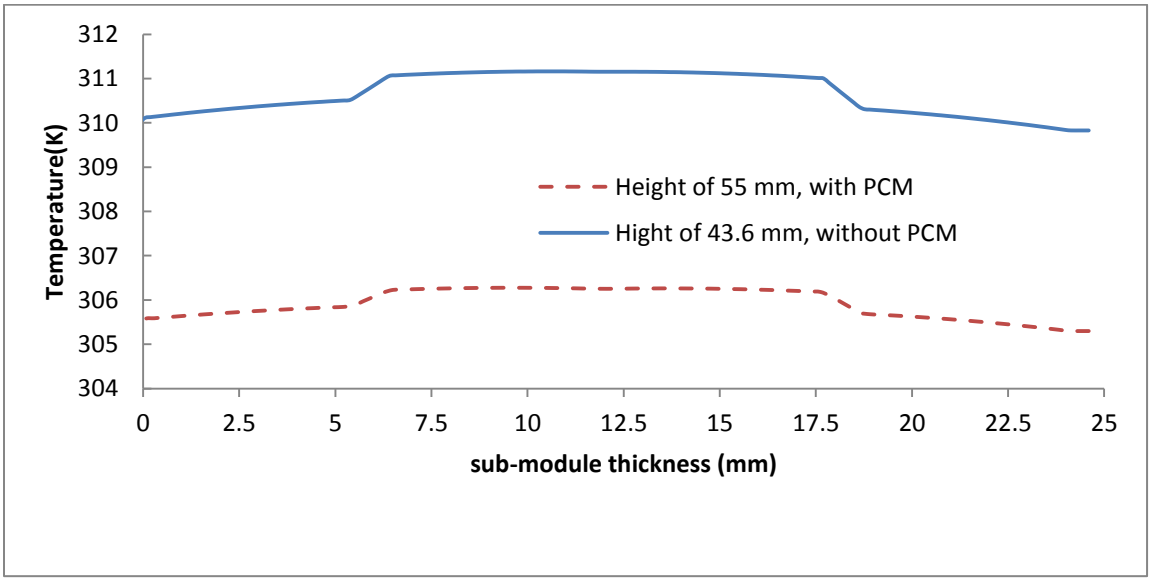

Figure 6.34 Temperature distribution in sub-module height with and without PCM

Table 6.7. Comparing temperature range in sub module with and without PCM in steady-state

Model	T_{max} (K)	T_{min} (K)	Temp. difference in sub-module (K)	Temp. difference in cell-2 (K)
Sub-module without PCM	321.28 (cell-2)	315.72 (foam-1)	5.56	2.21
Sub module with PCM	320.61 (cell-2)	315.17 (foam-1)	5.44	2.04

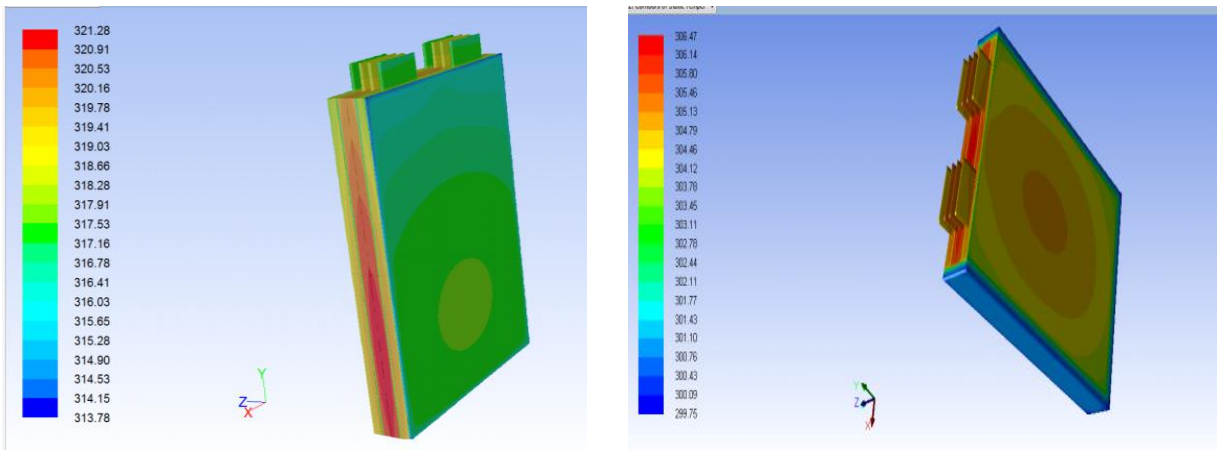

(a) (b)

Figure 6.35 Temperature contours in the sub-module a) temperature contours in sub-module without PCM b) More uniform temperature distribution using the PCM around the sub-module

6.1.2.3 Transient response of the sub-module

Thermal management system which uses the liquid cooling of active air cooling system, are operating in a steady-state condition. For the cases where the heat generation is higher than normal (Higher C-rate discharge of the battery pack) the compressor works with higher speed to compensate the cooling load. Therefore transient response is of higher importance and time-dependent temperature distribution of the cell and sub module is important. The upcoming analyses of the cell with the higher temperature are taking the transient response into account in detail.

Grid time-independency test

Time independency test is carried out for sub-module mesh by selecting time steps as follows:

- Time step size = 1 s and number of time steps = 500, flow time= 500 s
- Time step size= 5 s and number of time steps = 100 , flow time= 500 s
- Time step size = 2.5 s and number of time steps = 200 , flow time 500 s

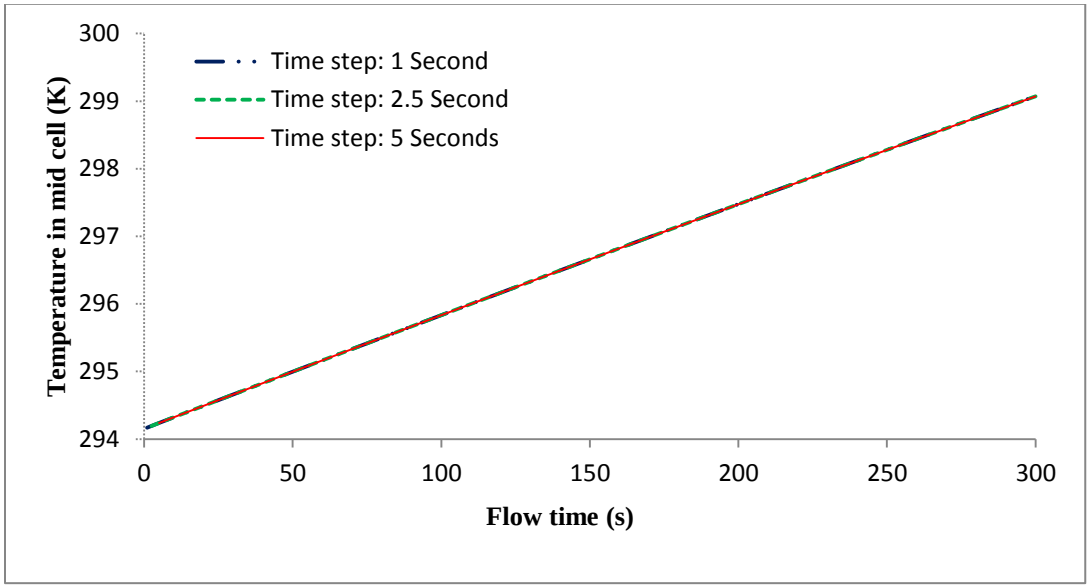

Figure 6.36 Transient response of the sub-module in different time steps

The selected mesh has 342,000 cells and the mesh squish as quality criteria is 0.06 where the idea case will have the squishiness of zero. Temperature in the mid of cell-2 has been monitored as a complementary convergence criteria. As it can be deduced from the Figure 6.36, there are ignorable differences among the time steps and therefore time-independency is confirmed. Depending on the heat generation in the Li-ion cells, the temperature increase will be different. The governing boundary conditions also will determine the changes in the temperature distribution of the sub-module.

To achieve this goal, the sub-module under the specific heat generation rate and boundary condition is considered with and without the PCM. The rakes are again created to investigate the temperature distribution in order to study the transient response of the sub module. The point in the second cell center has been monitored to compare the temperature changes in the cell as

criteria to investigate the effect of the PCM around the sub module. Figure 6.40 shows the effect of PCM in decreasing the rate at which temperature can affect the cell.

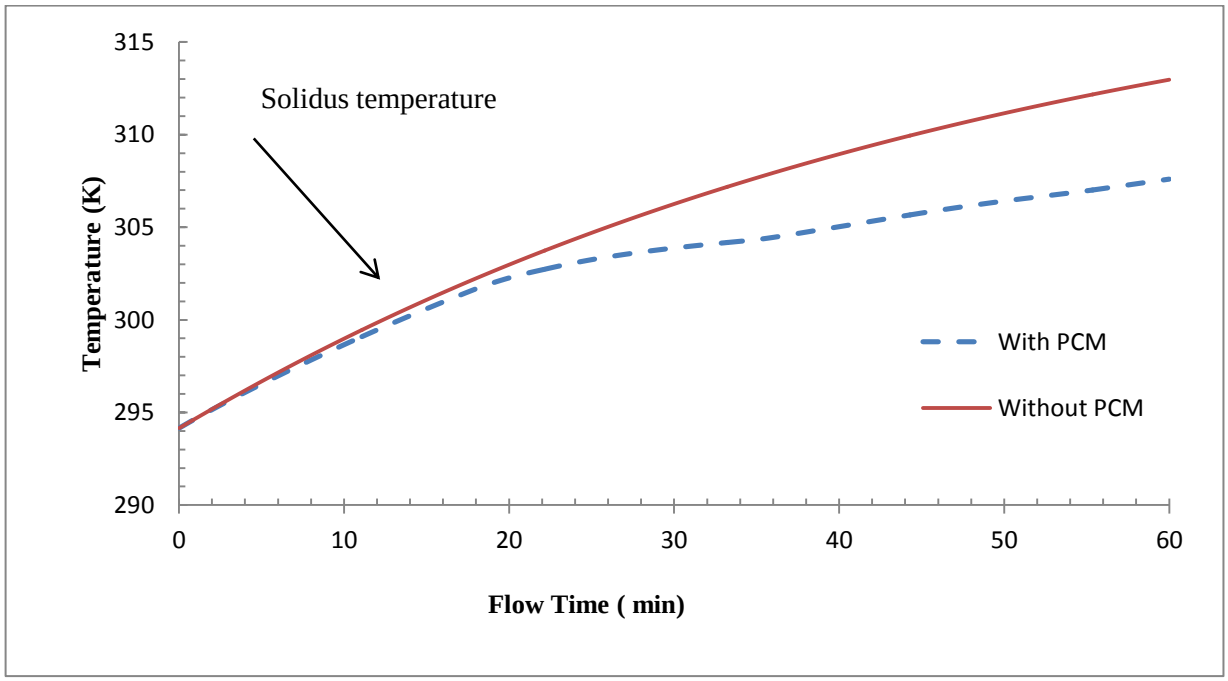

Figure 6.37 The effect of PCM in the temperature of mid cell in the sub module

It is obvious from Figure 6.37 that there is a delay in temperature increase with applying the PCM This is the main idea behind using this passive thermal management system. For further transient response of these models, Figure 6.38 compares the temperature distribution along the rake in height of 43.6 mm in two different elapsed times. After 10 minutes of operation, there is less than 0.5 K difference along the sub module thickness. After 50 minutes, the impact of PCM is more crucial ant and makes a noticeable cooling effect in the rake along the sub module thickness (more than 7 K decrease in the temperature).

The transient effect of temperature in melting the PCM around the sub module can be seen in Figure 6.39. It shows that closer to the second cell (and third one) the PCM is melting more which shows the higher temperature amount in this region.

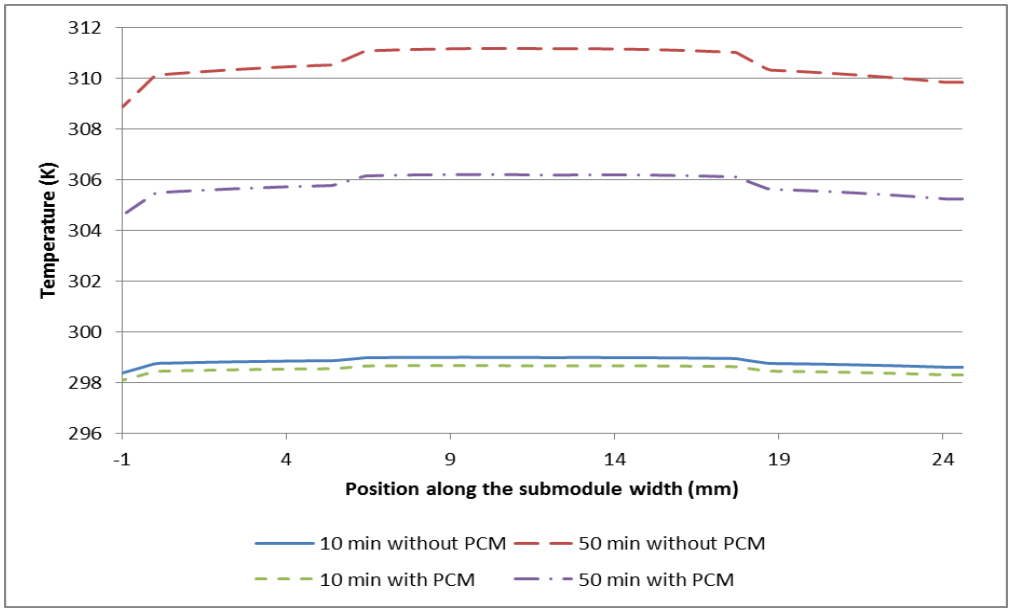

Figure 6.38 Time dependent temperature of sub-module thickness in middle point

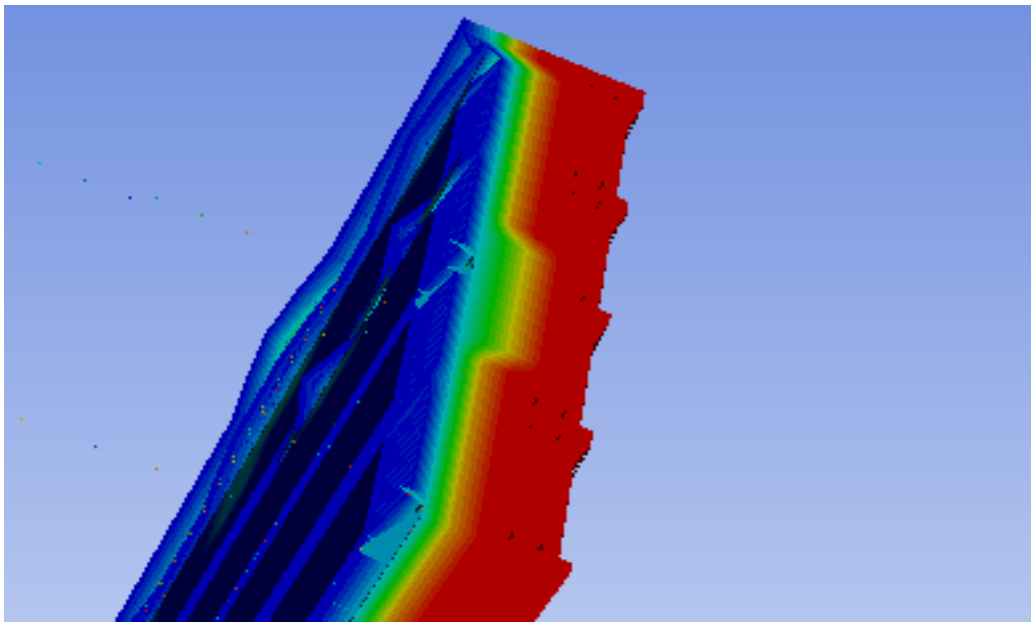

Figure 6.39 The transient effect in melting of the PCM around the sub module

6.1.2.4 Quasi-steady study of the sub-module

The quasi steady-state temperature is important to consider the thermal management critical intervals. More effort is going to be devoted for the time before system reaches the quasi steady-state situation.

The steady-state temperature in the mid cell-2 is 320.58 K. If 85% of the steady-state temperature is defined as the quasi steady-state situation and initiating temperature considered to be 294.15 K, then the times required for the sub module to increase the temperature as 22.46 ℃ (316.61 K) is quasi steady-state time. As Figure 6.40 shows the quasi steady-state temperature is satisfied within 3 hours of monitored flow time.

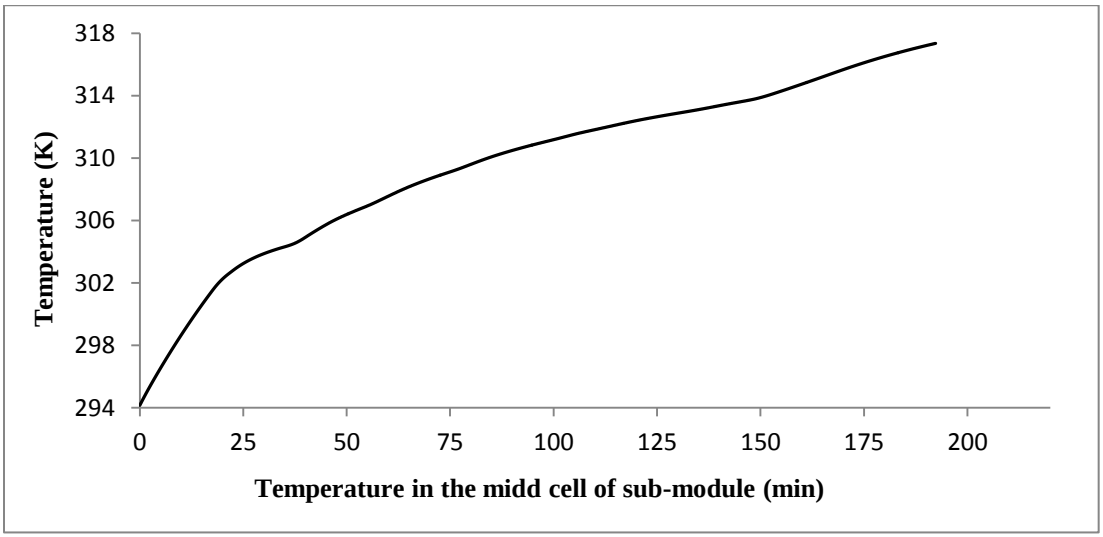

Figure 6.40 Quasi steady-state temperature dependence of sub module for heat generation of 22.8 W/liter

When higher currents are discharged from the battery pack, more heat will be generated due to internal resistance of the battery. As discussed before, the height of 43.6 mm had the highest temperature values. It can be seen that applying the PCM is an effective method in decreasing the rake temperature and therefore to provide a better thermal management system. Figure 6.41 shows the final temperature of the sub module under different heat generation rates. 6866 W/m^3 is the normal value in lithium ion cells, but final temperature is not even enough to melt the PCM in considered sub module as the model predicts. There are two reasons why one should not select another PCM with lower melting temperature. The first reason is the thermal runaway problem in the battery pack.

The Chevy Volt battery pack consists of sub modules with 90, 72 and 126 cells. When all of cells generate heat with a high value rate, the resultant temperature should be in reliable range. Secondly, in 2-C or higher discharge rates, which is possible in acceleration period, the 6855 W/m^3 will cause the sub module to attain temporarily high temperature which can keep the

temperature levels higher than the predicted temperature even after getting to its normal operating condition.

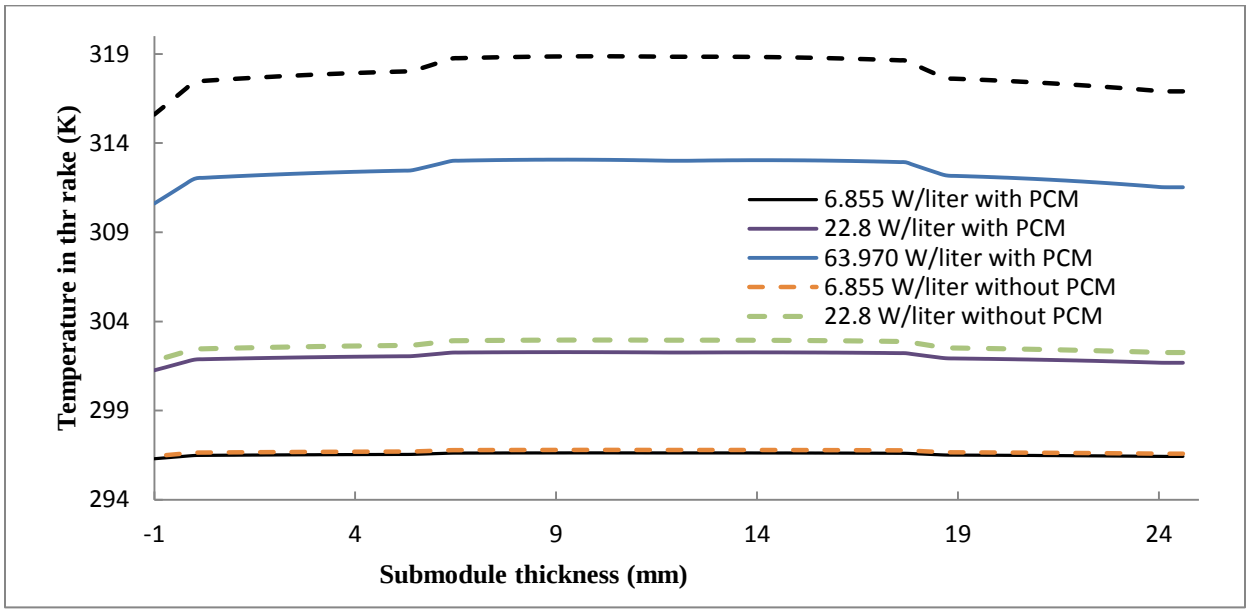

Figure 6.41 Temperature along the sub module thickness for different heat generation rates

Table 6.8 summarizes the temperature difference in the sub module in different heat generation rates. It is necessary to mention that in higher heat generation rates, the PCM has an incredible effect on cooling down or preventing temperature rise in the system. Different heat generation rates have been simulated. The results show that for the rake along the sub module thickness, the temperature will decrease more in higher heat generation.

Table 6.8 Temperature difference in the sub-module for different heat generation rates

Heat generation rate (kW/m^3)	6.885	22.800	63.970	200
Temperature difference due to PCM usage (K)	0.17	0.68	5.80	13.33

For a point in middle of cell-2 (as the critical cell for thermal runaway initiation), Figure 6.42 shows the temperature increase with respect to the flow time in different heat generation rates. For a short period of time, there is an intense current extraction from the battery pack

which causes heat generation rate of 200,000 W/m^3 in the sub module. Figure 6.43 compares the response of the cell 2 to such a heat generation rate in transient situation.

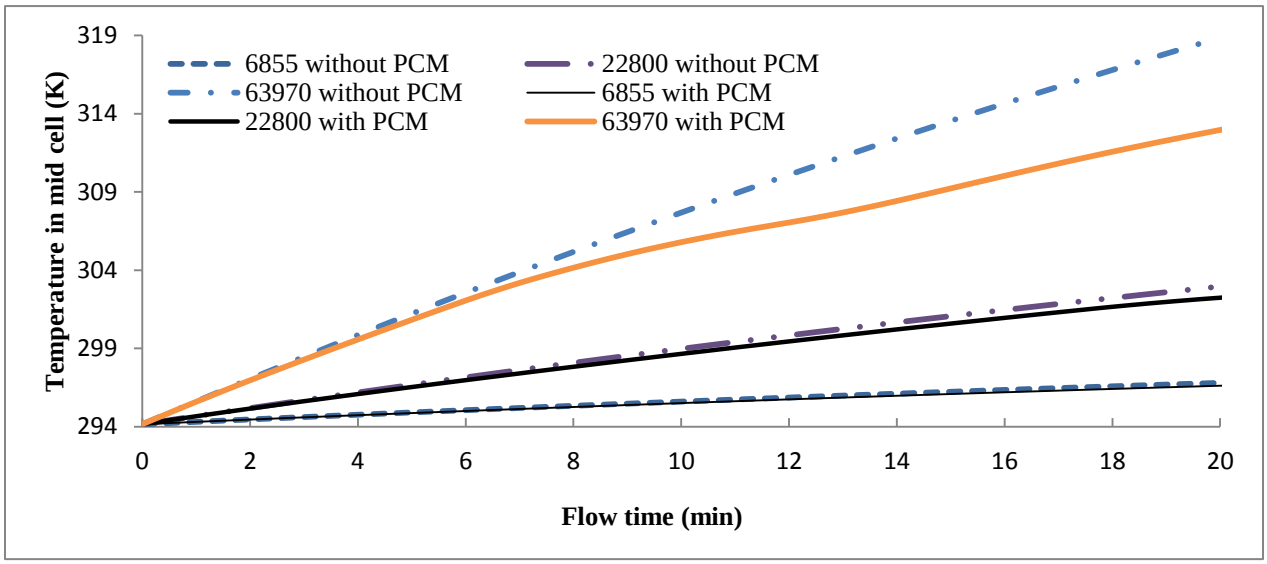

Figure 6.42 Temperature increase in the mid cell for different operational conditins of vehicle

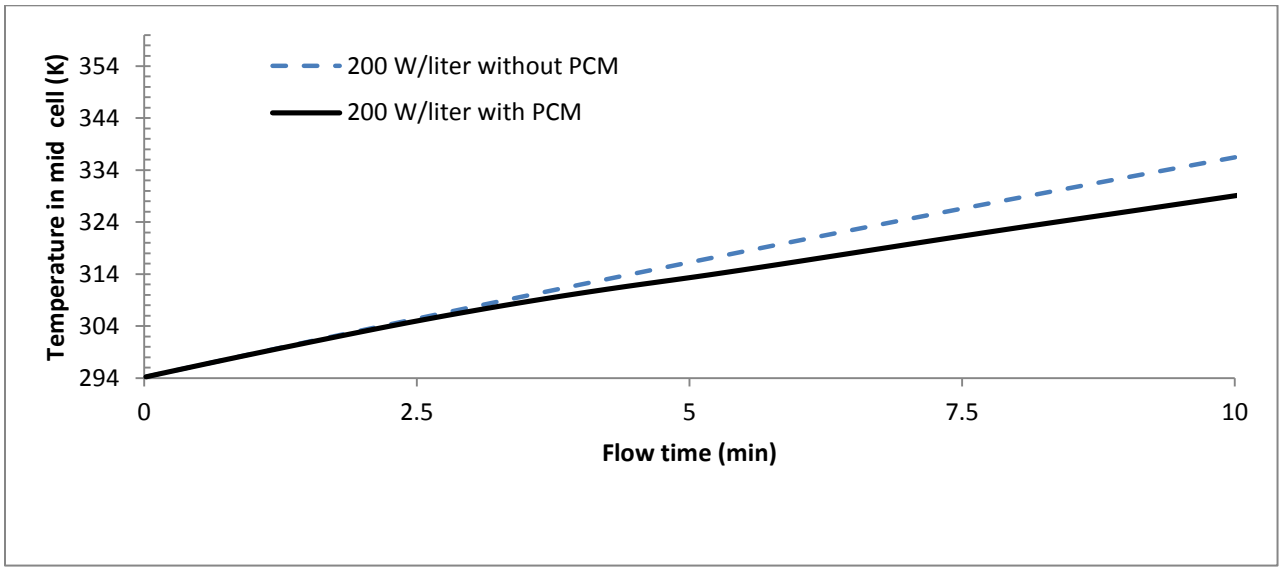

Figure 6.43 Transient response of the sub-module for the higher heat generation rate (200 kW/m^3)

6.1.3 PCM in between the cells (Cell level integration of the PCM in the battery pack)

In the third option, the foam is applied between the cells. The same sub module in the previous option will be used in this configuration. There are 288 cells in the Chevy Volt battery pack which weight around 400 lbs. (181.4 kg) with a capacity of 16 kWh Li-ion battery pack (16.5

kWh in model 2013 generation which leads to 8% extended driving range). Figure 6.44 shows one cell and the cooling fin and foam on both sides. By changing the order and number of the foams and cooling plates, the sub module has been formed. The material properties are the same as previous section. The PCM is melted and being absorbed by the foam. The amount of absorption was considered as an important criterion in selecting the foam. The thermal stability and strength of the foam are other parameter in selecting the foam.

Once the heat is generated in the cells, the heat will be transferred to the foam and this, in turn, will delay the temperature increase in the cells by charging the PCM contained in the foam and meting it.

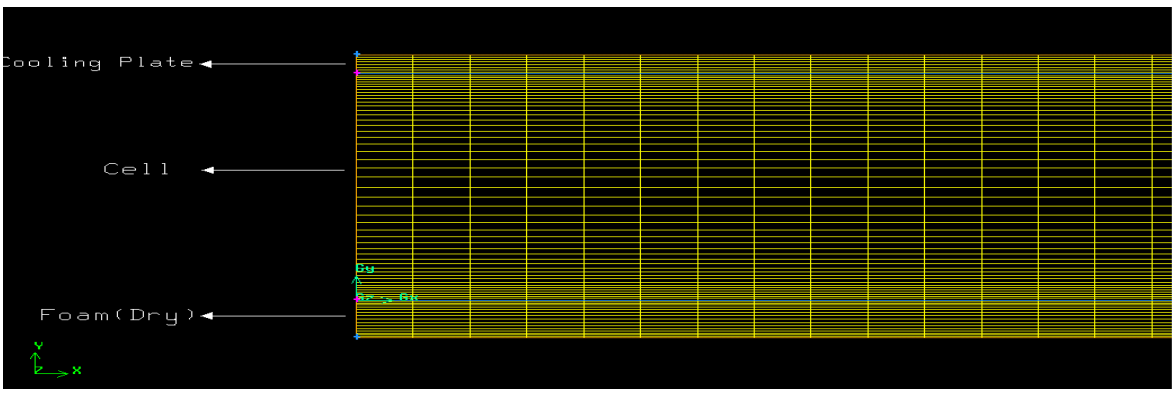

Figure 6.44 Li-ion cell, cooling fin and foam mesh

6.1.3.1 Effective properties of soaked foam

For the absorbed PCM in the foam, the following relations can be used to estimate the effective properties of the wet foam.

$$\mathrm{Cp_{aver}} = \frac{1}{\mathrm{m_{tot}}} \times \sum \mathrm{m_i\, Cp_i} = \frac{\mathrm{m_{pcm}}}{\mathrm{m_{tot}}}\ \mathrm{Cp_{pcm}} + \frac{\mathrm{m_{foam}}}{\mathrm{m_{foam}}}\ \mathrm{Cp_{foam}} \tag{6.22}$$

The mass concentration is defined as

$$\mathrm{c} = \frac{\mathrm{M_{pcm}}}{\mathrm{M_{\ total}}} \tag{6.23}$$

$$\mathrm{M_{total}} = \mathrm{M_{pcm}} + \mathrm{M_{foam}} \tag{6.24}$$

Therefore, if the mass concentration is of interest then

$$\mathrm{Cp_{ave}} = c \times \mathrm{Cp_{pcm}} + (1 - c) \times \mathrm{Cp_{foam}} \tag{6.25}$$

For the foam, if the porosity is defined in the following way, then volumetric porosity will act like volume concentration and can be written as

$$\varepsilon = \frac{V_{pcm}}{V_{tot}} \rightarrow m_{pcm} = \rho_{pcm} \times V_{pcm} = \rho_{pcm} \times \varepsilon \times V_{tot} \tag{6.26}$$

Therefore the specific heat can be calculated as in Equation 6.27.

$$Cp_{aver} = \frac{\rho_{pcm}}{\rho_{tot}} \times \varepsilon \times Cp_{pcm} + \frac{\rho_{foam}}{\rho_{tot}} \times (1 - \varepsilon) \times Cp_{foam} \tag{6.27}$$

In specific applications, the volumetric concentration should be used in terms of mass concentration. The relationship between these two parameters is found to be as follows:

$$c = \frac{M_{pcm}}{M_{total}} = \frac{\rho_{pcm} V_{pcm}}{\rho_{pcm} V_{pcm} + \rho_{foam} V_{foam}} \tag{6.28}$$

By defining density ratios and volume ratios as constitutive relations in form of density and volume ratios of foam and PCM

$$r = \frac{\rho_{pcm}}{\rho_{foam}} \tag{6.29}$$

$$x = \frac{V_{pcm}}{V_{foam}} \tag{6.30}$$

$$c = \frac{V_{pcm}}{V_{pcm} + \frac{1}{r} \times V_{foam}} = \frac{1}{\frac{1}{R} \times \frac{1}{x} + 1} \rightarrow x = \frac{c}{r(1-c)} \tag{6.31}$$

The porosity definition gives $\frac{1}{\varepsilon} = \frac{1}{x} + 1$, which is used to give the relation between mass and volume concentrations as follows:

$$\varepsilon = \frac{c}{c + r(1-c)} \tag{6.32}$$

In the simulation, the mass concentration is C=65.8 which is found the experimental measurements. The properties of normal Octadecane are given in section 4.1.3.2. Based on this information, the following effective properties are calculated for the wet foam (foam with the absorbed PCM) which is going to be placed in between the cells in the sub-module.

$$C_{p,wet\ foam} = \begin{cases} 1928 & \text{J/kgK} & \text{T}_{\text{solidus}} > \text{T} \quad \text{solid phase} \\ 148560 & \text{J/kgK} & \text{T}_{\text{solidus}} < \text{T} < \text{T}_{\text{liquidus}} \quad \text{Mushy zone} \\ 1947 & \text{J/kgK} & \text{T} > \text{T}_{\text{liquidus}} \quad \text{liquidus phase} \end{cases} \tag{6.33a}$$

$$k_{wet\ foam} = \begin{cases} 0.264 & \text{W/mK} & \text{T}_{\text{solidus}} > \text{T} \quad \text{solid phase} \\ 0.196 & \text{W/mK} & \text{T}_{\text{solidus}} < \text{T} < \text{T}_{\text{liquidus}} \quad \text{Mushy zone} \\ 0.128 & \text{W/mK} & \text{T} > \text{T}_{\text{liquidus}} \quad \text{liquidus phase} \end{cases} \tag{6.33b}$$

$$\rho_{wet\ foam} = \begin{cases} 630 & \text{kg/m}^3 & \text{T}_{\text{solidus}} > \text{T} \quad \text{solid phase} \\ 600 & \text{kg/m}^3 & \text{T}_{\text{solidus}} < \text{T} < \text{T}_{\text{liquidus}} \quad \text{Mushy zone} \\ 571 & \text{kg/m}^3 & \text{T} > \text{T}_{\text{liquidus}} \quad \text{liquidus phase} \end{cases} \tag{6.33c}$$

In this relations, the solidus and liquidus temperatures are considered as $T_{solidus}$ =301.15 K and $T_{liquidus}$ = 303.15 K.

6.1.3.2 Steady state response of the sub module

Results show that second cell has the highest temperature in the sub-module. This is mainly due to lower heat transfer coefficient for the inner components of the sub-module where the free connection with the ambient temperature is not available. The temperature difference between the critical zone, which is the second cell, as mentioned before and the cool zones, is small, but it worth to mention that for the case of sub-modules with big number of cells, any temperature gradient can lead to lower efficiency in the li-ion cells and the power extracted from the battery pack, even a small decrease in temperature can prevent thermal runaway in the larger sub modules. This means that higher number of cells in the sub-module will have higher temperature gradients which should be thermally managed to avoid thermal runaway. The values have been compared with the case of sub module without PCM (Table 6.9).

Similar to the previous analyses, the region with higher temperature is selected and a horizontal rake has been placed along the sub module thickness to include all the 9 different zones and compare the effect of PCM on the cooling of the system. Figure 6.45 reveals the effect of phase change materials in decreasing of the temperature in the sub-module.

Table 6.9 Comparison between temperatures with and without PCM in between the cells

Zone Name	Maximum Temp.(K) with PCM	Maximum Temp. (K) Without PCM
Foam 1	319.12	319.31
Cell 1	319.93	320.19
Foam 2	320.48	321.00
Cell 2	320.73	321.28
Cooling plate 1	320.72	321.27
Cell 3	320.72	321.27
Foam 3	320.40	320.89
Cell 4	319.75	319.90
Cooling plate 2	319.02	319.16
Terminals of cell 2	318.40	318.91

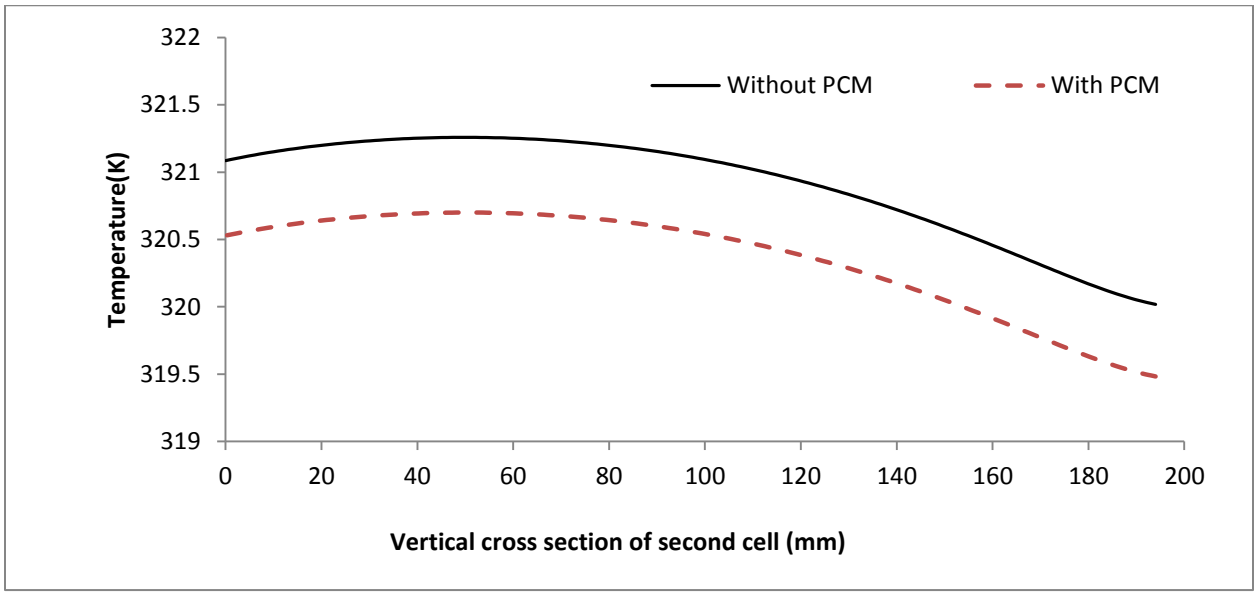

Figure 6.45 Temperature comparison in vertical direction in second cell with and without PCM

6.1.3.3 Transient response of the sub module

Transient response of the sub module is assessed in this section. At the specific times the results will be compared with each other to magnify the effect of flow time. In addition to the rake, 5

points have been defined on the surface of the second cell (the critical cell in the sub module) to compare the simulation and experimental results

6.1.3.3.1 Sub module with PCM soaked in the foam:

Figure 6.46shows the location of these points. The rake for maximum temperature location along the sub module thickness also is shown in Figure 6.46.

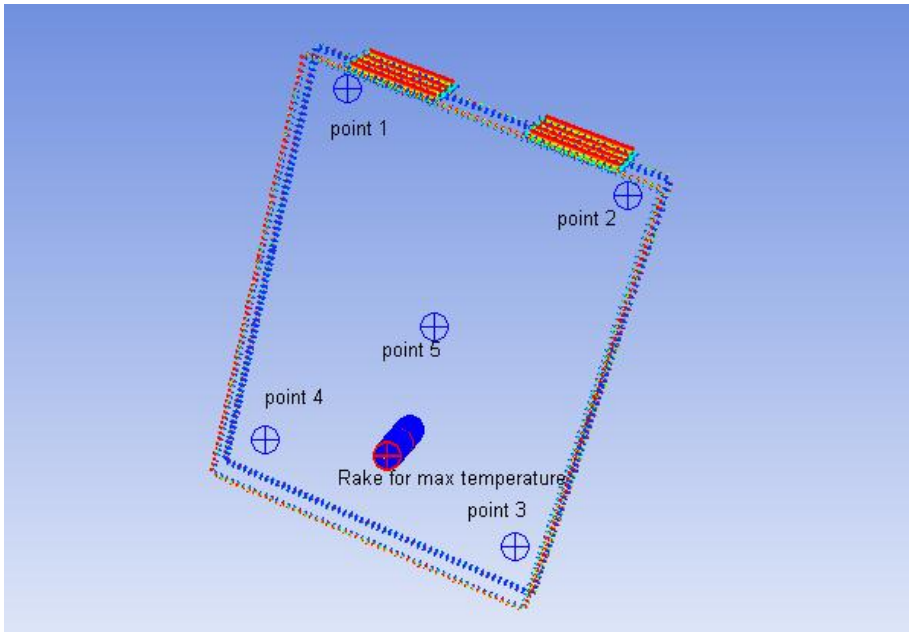

Figure 6.46 Loctaion of points on the surface of second cell and the rake through sub module

The values are compared with base line where the foams are dry (Without octadecane). It should be mentioned that points 1, 3 and 5 have been monitored due to the symmetry. It should be mentioned that this assumption is accurate if there is a uniform volume heat generation rate inside the cell. As discussed in chapter 4, the new generation of Li-ion cells have nearly uniform heat generation rate. For the other cases, the user defined functions should be integrated with the solver in the software to take into account the local heat generation rates, specially the higher rates close to the connectors, where the electrons are exchanged.

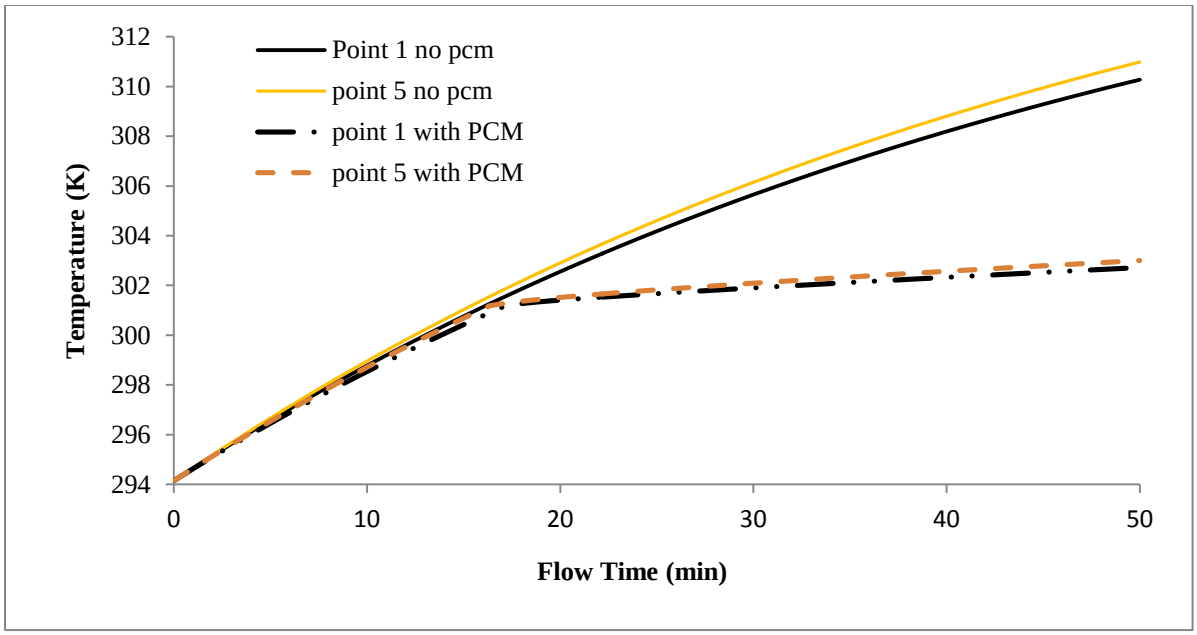

Figure 6.47 Effect of PCM on temperature increase on the cell surface

Temperature distribution in the rake after 50 min through the sub module can be seen in Figure 6.47. The PCM absorbs the generated heat by the battery and causes an abrupt decrease in the temperature trend of the sub module. When it is compared with the baseline that there is no PCM, 8.1 K has been decreased which shows the effective of the application a PCM for battery pack thermal management. The heat generation is 22.8 W/liter.

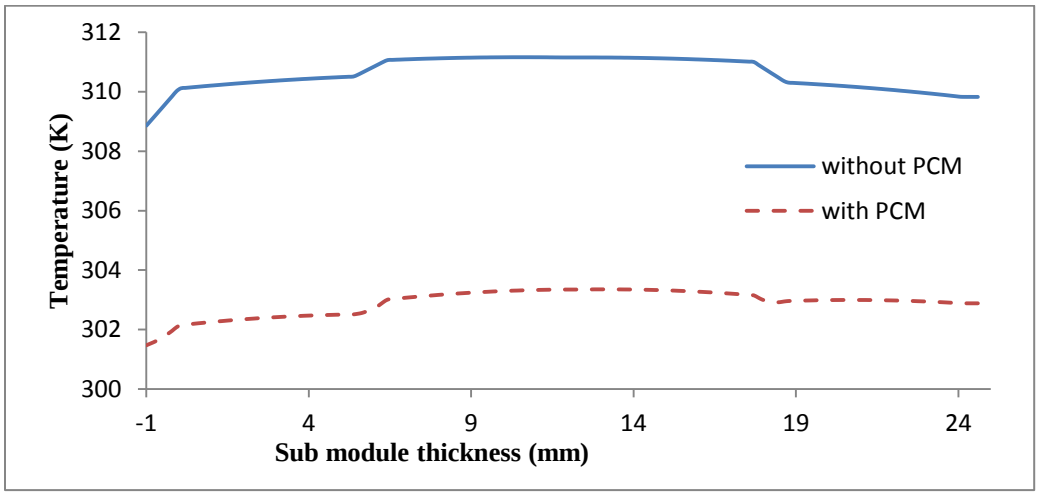

Figure 6.48 Temperature distribution along the thickness of the sub module after 50 minutes

The negative values in x axis of Figure 6.48 are simply due to the selected coordinate system. So, the value of -1 mm is the thickness of the first foam in the sub module. Table 6.10 compares the temperature changes with respect to the time and their location in both dry and wet foam sub module.

Table 6.10 Temperatures after 50 minute for different zones

Model	**Sub module with dry foam**			**Sub module with PCM in the foam**		
Zone Name	Volume average temp. (K)	Max. temperature (K)	Min. temperature (K)	Volume average temperature (K)	Max. temperature (K)	Min. temperature (K)
Cell 1	310.05	310.51	308.98	302.30	302.52	301.85
Cell 2	310.87	311.16	309.85	303.13	303.85	302.65
Cell 3	310.85	311.15	309.84	303.20	303.36	302.73
Cell 4	309.88	310.30	308.98	302.88	303.00	302.44

6.1.3.4 Sub module with dry and wet foam at higher heat generation rate

As Figure 6.49 indicates, the presence of PCM prevents temperature increase in the cells. Temperature rise changes very effectively after complete melting of PCM and starting sensible heat period. The related concern is how much a defined amount of PCM can absorb the heat to maintain the effective thermal management system. For the heat generation rate of 22.8 kW/m^3, PCM melts after 16 minutes, and continues to be effective until 50 minutes of the flow time. For discharge rate of C-2, 63.97 kW/m^3 will be generated and the corresponding transient response of the system to this high heat generation rate is shown in Figure 6.49. This figure shows that after 5 minutes, the PCM will acts as passive thermal management system. In this condition, PCM is effective to control the temperature for period of 15 minutes, before getting melted

completely. The same heat generation has been considered to find the temperature variations along the sub-module thickness (Figure 6.50).

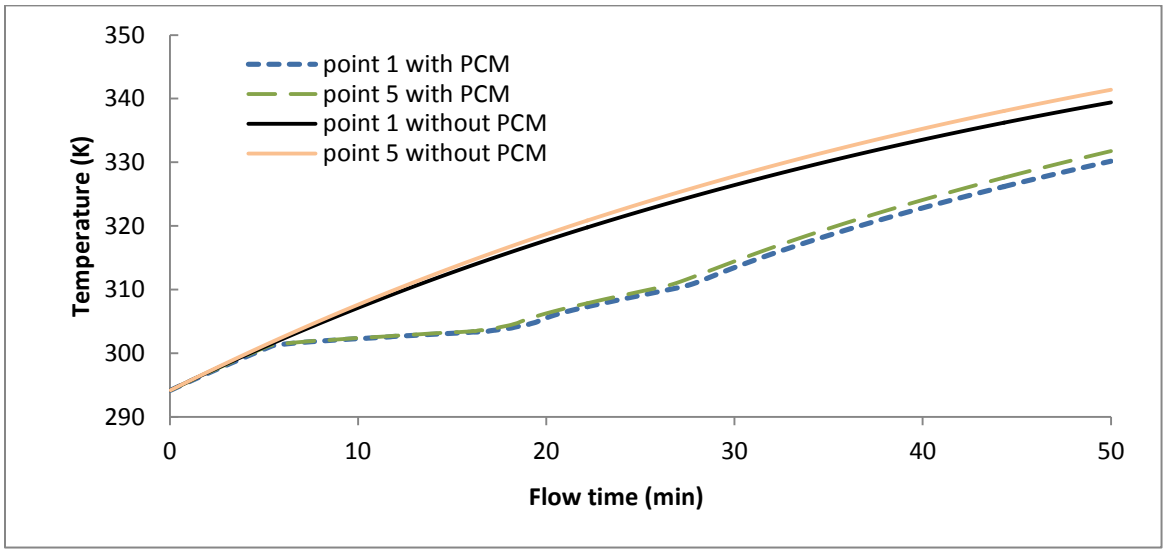

Figure 6.49 Effect of PCM on temperature increase of the cell surface (heat generating rate of 63.970 kW/m^3)

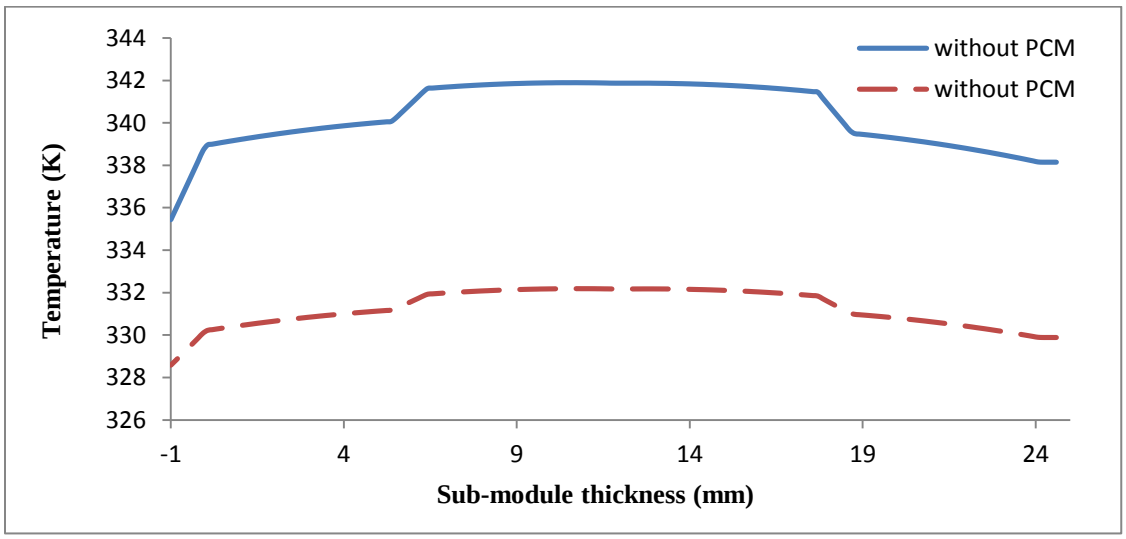

Figure 6.50 Temperature difference in sub-module thickness with and without PCM for heat generation rate of 63.970 kW/m^3

6.1.4 Model Validation

In order to assess the temperature increase on the cell surface, battery cycler applies the charging voltage and extracts the current in C/1 –Rate to the Li-ion cells. The test set up is explained in Chapter 5. In order to recall the point's location on the cell surface, Figure 6.51 shows the five

locations where the thermocouples are placed for measurement purpose. Transient response of the cells was analyzed in two situations. Firstly, the sub-module was simulated without the PCM in the foam. In this case, the foams in the sub module act as a separator to prevent cell surfaces to contact. Secondly, the foam was soaked in the PCM and the same situations for sub module were tested again.

Figure 6.51 Location of thermocouples on the surface of Li-ion cells

Figure 6.52 shows the all temperature profiles in the 10 locations on the cell surfaces. After filtering the noise in the data, and selecting points 3 and 5 (as shown in the Figure 6.52). Figure 6.53 reveals the temperature variations in the specified locations. Due to the symmetrical position of the thermocouples, points 3 and 5 are selected to simplify the monitoring process of their transient temperature increase during the testing period.

The quasi steady-state has been considered and the elapsed time has been selected to be 3 hours. The same C-rate is applied for the case of dry foam and the foam soaked with the PCM. As it can be seen from Figure6.53 and based on the simulation results, in both points, the surface temperature of the Li-ion cell decreases by replacing the dry foam with the foam soaked in PCM.

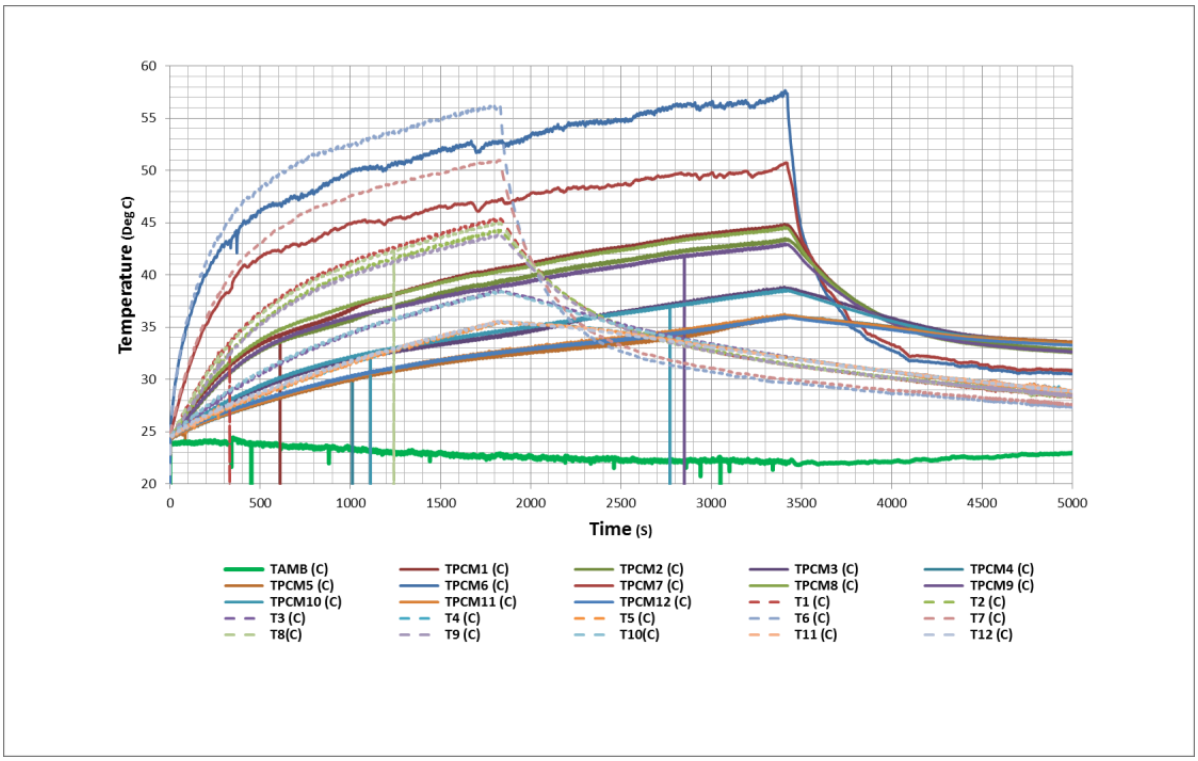

Figure 6.52 Temperature variations for all 10 points on both sides of the cell with and without the PCM

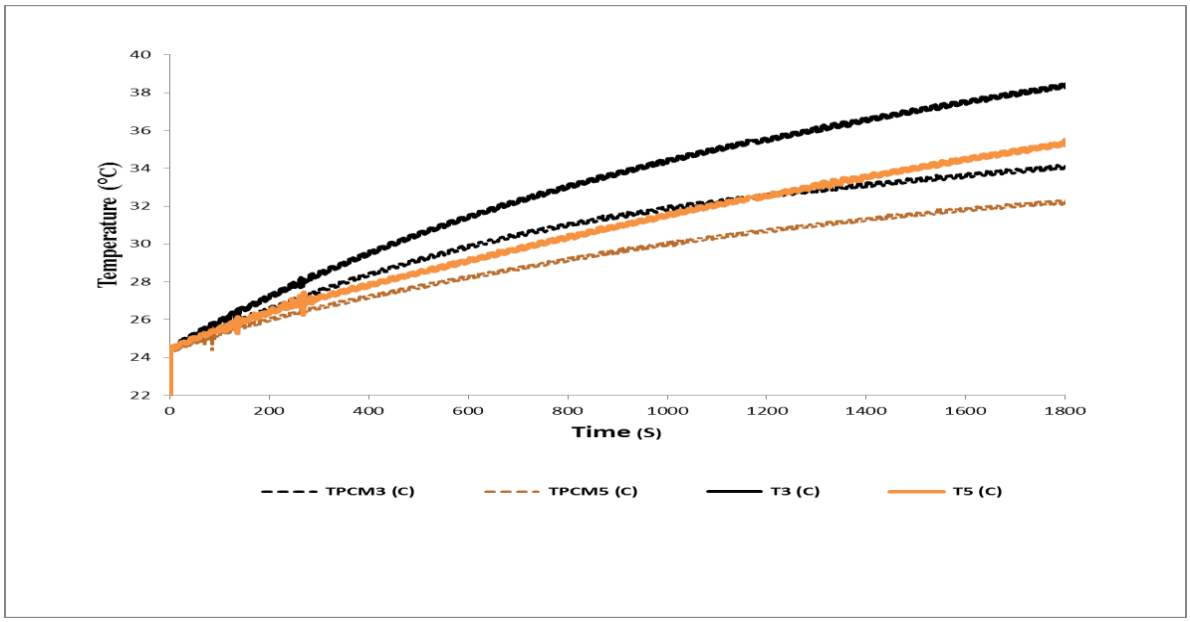

Figure 6.53 Experimentally measured cell temperature with and without PCM in between the cells.

Closing remarks

Different Thermal management methods are designed to meet two requirements: To minimize the peak temperature and to prevent the temperature excursion. Various options for passive thermal management with PCM are conducted in this section. The results show a temperature decrease in single cell case. Furthermore, maximum temperatures in the sub-module (battery pack representative) are decreasing when the PCM is used for thermal management purpose. This is in accordance with experimental results presented in other studies [38]. At elapsed time of 50 minutes, the temperature is predicted to be decreased around 7.74 K in the cell.

6.2 Design and optimization of the latent heat thermal energy storage system

The second option of using PCM in thermal management of the HEVs is the energy storage system. Thermal management system of the hybrid electric vehicles has been improved by introducing the PCM as passive cooling (heating) system. Based on the literature review the shell & tube heat exchanger has better effectiveness when the PCM fills the shell side. In this section, two tube configurations have been considered, including straight and helical tube heat exchangers. In addition, fins are studied as extended surface to investigate their effect. The optimization has been carried out based on the constraints, including limit volume and length of the heat exchanger. These design aspects are mostly caused by the fact that the heat exchanger should be placed in the vehicle's available space.

6.2.1 Objective functions, design parameters and constraints

The main criteria in the heat exchanger are the occupied volume. The length of the heat exchanger has been defined as the objective function and designed parameters are considered as:

- number of tubes
- tube inside and outside diameter
- shell diameter

When the phase change material is used as storage media, the length of the heat storage system exceeds the limits. This is due to the main drawback of phase change materials which is the low thermal conductivity. The predicted length for this case will be presented in the following sections. In order to overcome this problem, the nanoparticles have been introduced to increase the thermal conductivity and rate of heat transfer in the PCM. This will lead to more

compact storage system which satisfies the objective function. Carbon Nanotubes and Graphene Nano-platelets have been added to PCM as described in the experimental section.

6.2.2 Effective properties of the PCM and nanotubes

By mixing the nanotubes in the PCM, the effective properties will be changed. The predicted thermal conductivity of the mixture has been introduced in the designing parameters of the heat exchanger. As the equations show, the effective thermal conductivity mainly depends on the direction of the nanotubes. If they are placed in series configuration, the effective thermal conductivity increases tremendously. On the other hand, the effective thermal conductivity will not have a significant increase when the nanotubes are placed in the parallel arrangement. Figure 6.54 shows the variations of effective thermal conductivity for the parallel arrangement of the particles of carbon. This can be considered as the worst scenario.

The label pointing to the zero concentration corresponds to the following effective thermal conductivity as:

$\frac{k_{eff}}{k_{cnt_{parallel}}} = 5.067 \times 10^{-5}$ Therefore: $k_{eff,parallel} = 5.067 \times 10^{-5} \times 3000 = 0.152$ W/m K

The obtained value is identical to thermal conductivity of pure PCM. The best scenario corresponds to the case where the carbon nanotubes are set in series with the temperature gradients direction.

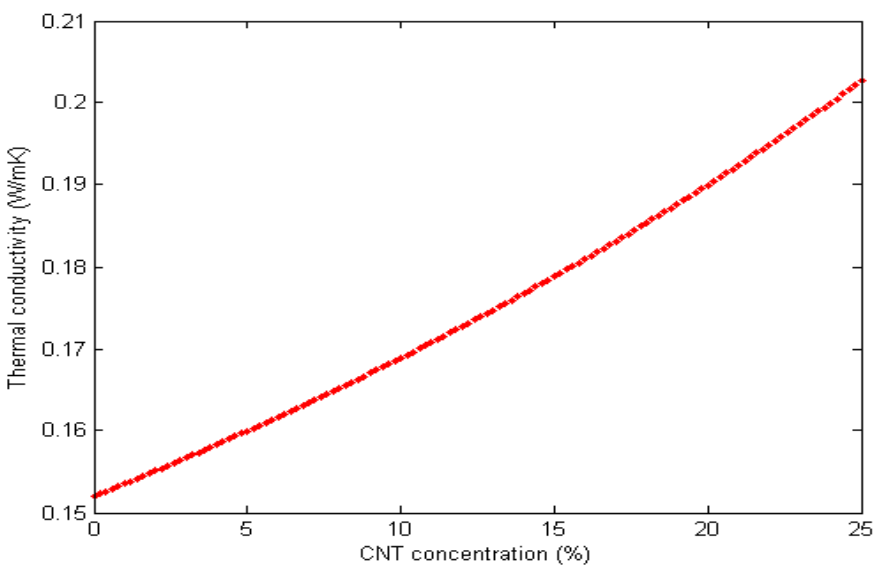

Figure 6.54 Effect of CNT concentration on the thermal conductivity of the mixture in parallel configuration

On the other hand, the highest thermal conductivity is expected for series configuration (Figure 6.55). For example in 90% concentration for PCM, which is equal to 10% concentration of CNTs we will have [160]:

$$c = \frac{V_{pcm}}{V_{tot}} = \frac{V_{pcm}}{V_{pcm}+V_{cnt}} \tag{6.34}$$

$$k_{eff}\,(parallel) = \left(\frac{c}{k_{pcm}} + \frac{1-c}{k_{cnt}}\right)^{-1} \tag{6.35}$$

$$k_{eff}\,(series) = ck_{pcm} + (1-c)k_{cnt} \tag{6.36}$$

$K_{eff} = k_{cnt} \times 0.1 = 3000 \times 0.1 = 300$ W/mK

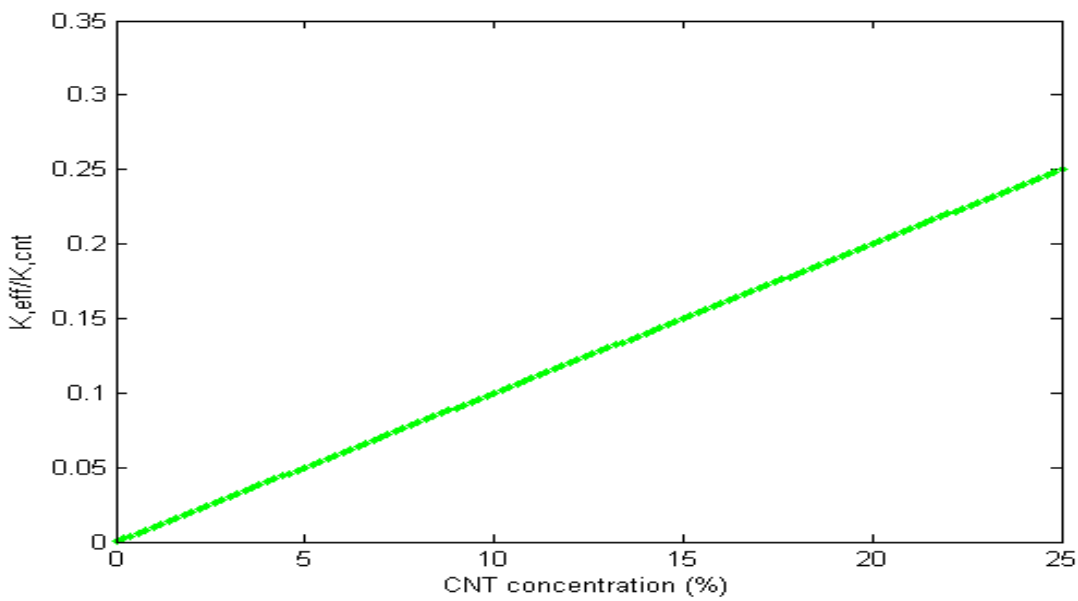

Figure 6.55 Effective thermal conductivity of the PCM and Nanoparticles in series arrangement

6.2.3 **Combined condition**

Second approach is the probability for distribution for the CNTs. In this method, we give weighting for the best (series) and worst (parallel) arrangements of CNTs in the mixture: If "P" is defined as the probability of series arrangement (best case), then the following equations can are obtained

$$k_{mix} = P \times k_{eff,s} + (1-P) \times k_{eff,p} \tag{6.37}$$

where $k_{eff,s}$ and $k_{eff,s}$ represent thermal conductivity in series and parallel configurations.

$$k_{mix} = P(c.k_{pcm} + (1-c)k_{cnt}) + (1-P)(\frac{c}{k_{pcm}} + \frac{1-c}{k_{cnt}})^{-1} \tag{6.38}$$

which shows that the concentration of nanoparticles is an effective parameter in determining the mixtures thermal conductivity. Therefore, similar to previous section where the mass and volumetric concentration is defined for soaked foam, the same idea is valid for the mixture as follows:

$$c = \frac{V_{pcm}}{V_{tot}} = \frac{V_{pcm}}{V_{pcm}+V_{cnt}} \tag{6.39}$$

$$k_{eff}\,(parallel) = (\frac{c}{k_{pcm}} + \frac{1-c}{k_{cnt}})^{-1} \tag{6.40}$$

$$k_{eff}\,(series) = ck_{pcm} + (1-c)k_{cnt} \tag{6.41}$$

$$k_{mix} = P(c.k_{pcm} + (1-c)k_{cnt}) + (1-P)(\frac{c}{k_{pcm}} + \frac{1-c}{k_{cnt}})^{-1} \tag{6.42}$$

Figure 6.56 shows the effective thermal conductivity as a function of concentration and probability.

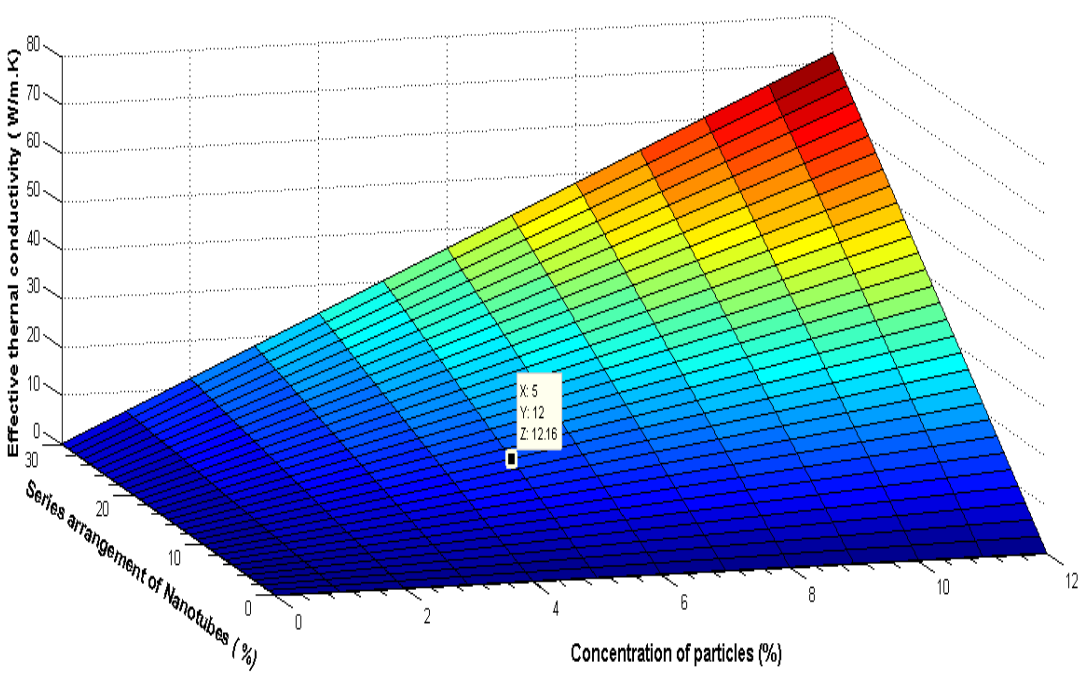

Figure 6.56 Thermal conductivity as a function of concentration and probability.

6.2.4 **Model description**

The main goal of this section is to describe the operating conditions of heat exchanger. The hot water with the minimum mass flow rate of 0.02 kg/s enters in the tube side as hot stream. The PCM is placed in the shell side to absorb the minimum 300W heat generated by the battery. The melting point of PCM is assumed to be 28.5 ^{o}C . Coolant is a 50-50 water-ethylene glycol which leaves the tubes at 29.5 ^{o}C. Two types of tubes including the straight tube and helical tubes are studied. Moreover, both finned and un-finned tube structure are considered in the straight tube.

6.2.5 **Optimization using genetic algorithm (GA)**

In this section, the length of heat exchanger considered as objective function. In order to minimize this objective, five design parameters, namely, number of tubes, index of each tube, shell (tank) diameter, CNT concentration and CNT series probability were selected. Design parameters and their range of variation are given in Table 6.11.

Table 6.11: Design parameters and their rang of variation

Variable	Lower bound	Upper bound
Number of tubes	1	200
Index of tube	1	5
Tank diameter (m)	0	0.3
CNT concentration (%)	0	10
CNT series probability (%)	0	20

Due to the specific space limitations in vehicle applications, the maximum allowable tank diameter to be selected is considered to be 0.3m. Moreover, the maximum allowable CNT concentration and the probability of series alignment are chosen to be 10% and 0.2, respectively. At mass concentration of 9%, the mixture will resemble a semi-solid. Concentrations more than 10% are rarely reported in the literature. Tube schedules, outside diameter, tube thickness and tube fin length are listed in Table. 6.12.

Table 6.12 Tube specification for the optimization (Data from [161]).

Tube schedule number	3/16	1/4	5/16	3/8	1/2
Tube outside diameter (mm)	6.10	8.13	9.86	11.456	16.00
Tube thickness (mm)	0.75	0.76	0.89	0.89	1.57
Tube fin length (mm)	5.08	5.59	6.10	6.60	8.89

The analyses for the tubes with/without fans are carried out in this section. The genetic algorithm optimization was performed for 150 generations, using a search population size of M =100 individuals, crossover probability of pc = 0.9, gene mutation probability of pm = 0.035 for both cases (with and without finned tube). The results for optimum length versus generation for both cases are shown in Figure 6.57.

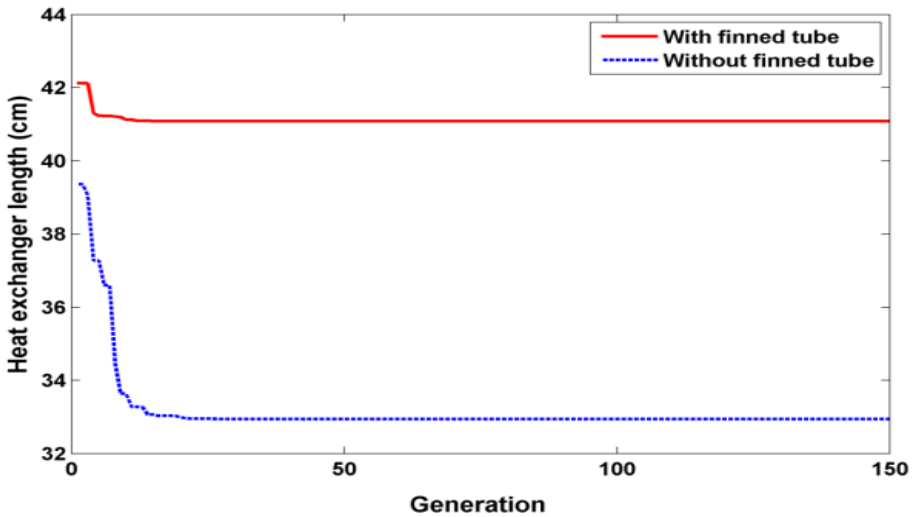

Figure 6.57 Convergence of objective function versus number of generation for both cases

The optimum values for the heat exchanger length are 32.95 cm and 41.09 cm respectively for the case of without and with finned tubes. As a result, the application of the fin for tubes is not recommended in this case. The optimal design parameters for each case are listed in table 6.13. It is worth mentioning that the tube with schedule number less than the 5/16 is not available in the market. As a result, the tube with smaller schedule number 5/16, are omitted in the optimization process.

Table 6.13 Comparing of the optimum results in cases including with and without finned tubes

Type	Tube type	Length of H.X (cm)	Tank diameter (cm)	Number of tubes	CNT concentration (%)	CNT series probability
Finned	5/16	41.09	33.97	47	10	20
No fin	5/16	32.95	27.56	62	8.6	19.7

6.2.5.1 Sensitivity analysis

The optimum value of effective thermal conductivity is determined as 34 W/mK for the case of without finned tube. The variation on length of heat exchanger versus effective thermal conductivity of the PCM is shown in the Figure 6.58. It is observed that by increasing of the effective thermal conductivity, the heat exchanger length decreases. Actually by increasing the PCM thermal conductivity, the overall heat transfer coefficient increases, and as a result, the required heat transfer surface area decreases for spesific heat duty. Consequently, by decreaseing the heat transfer surface area, the length of tube and heat exchanger decreases.

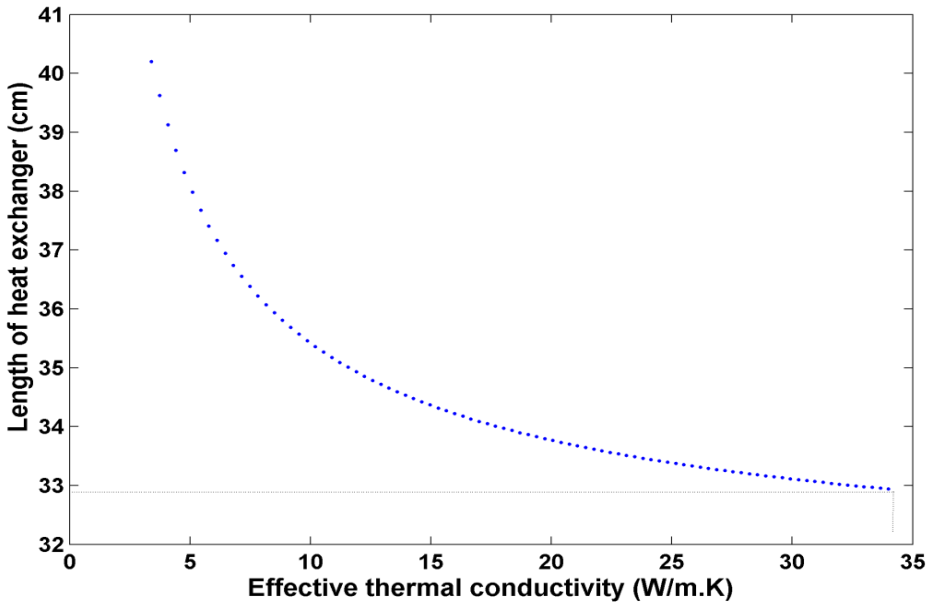

Figure 6.58 Variation on length of heat exchanger versus effective thermal conductivity of the PCM

The variation of heat exchanger length and shell diameter in terms of the variation of standard tube (with specific inner and outer diameter) are depicted in Table 6.14. It is concluded that by increasing the tube diameter, both heat exchanger length and shell diameter increases. As a result, the minimum available tube diameter in the market is suitable in this case. Essentially, by increasing the tube diameter, the Reynods number decreases, and as a result, the inner convection heat transfer coefficient and overall heat transfer coefficient decreases. By decreasing the overall heat transfer coefficient, the total heat transfer surface area (length of tubes) should increase [107].

Genetic algorithm has performed for different copper tubes. Based on the results, the available tubes in the market are considered as designing output. Figures 6.59 and 6.60 illustrate these variations for the tubes respectively.

Table 6.14 Variations of heat exchanger length and shell diameter versu tube diameter

Tube size	Index	d_i (mm)	d_o (mm)	L (mm)	D (mm)
1/16.	1	1.14	1.59	16.4	13.7
1/8.	2	1.65	3.18	16.72	13.93
3/16.	3	3.23	4.75	20.8	17.53
1/4.	4	4.83	6.35	24.7	20.74
5/16.	5	6.30	7.93	28.41	23.79
3/8.	6	7.90	9.53	32.1	26.77
7/16.	7	9.49	11.11	35.33	29.51
1/2.	8	11.13	12.70	39.33	32.64

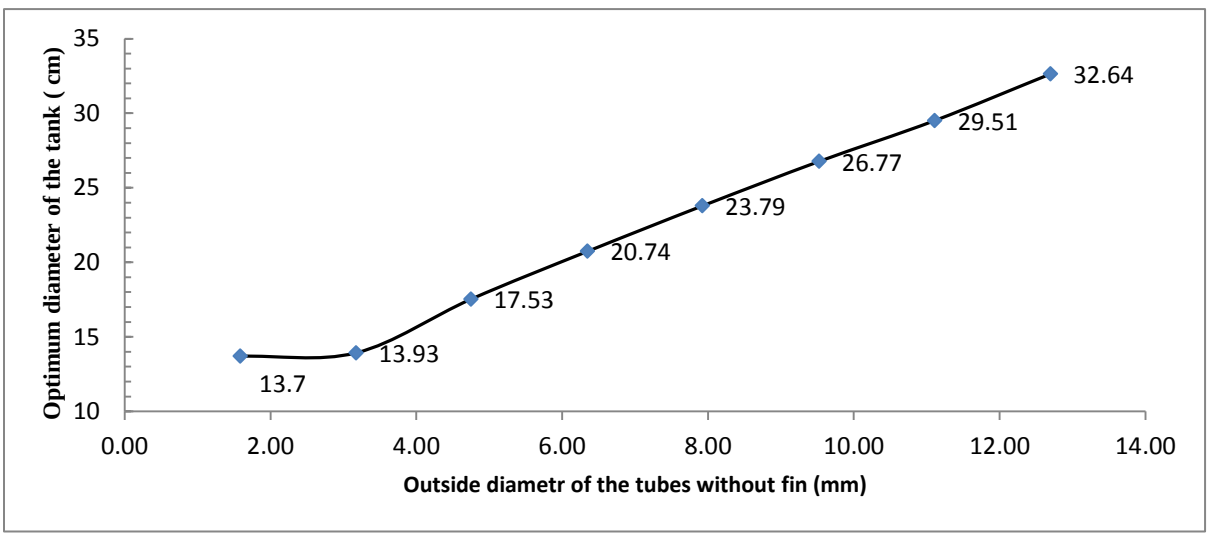

Figure 6.59 Variation of optimum shell (tank) diameter versus tube outside diameter in the case of without fin

By increasing the tube index, the tube inside and outside dimensions are also increased. It is determined that, by increasing the tube diameter, both L/d_i and D/d_o decreases. Figure 6.61 shows the variations of L/d_i and D/d_o versus the variations of tube index. It is deduced that the rate of increment in the tube inside and outside diameter, is higher than the rate of increment in the tube length and shell diameter.

The variation of optimum value of tube length versus tube inner diameter for various heat loads is shown in Figure 6.62. As it can be seen, the optimum tube length increases by increasing the tube inner diameter with a constant slope. Furthermore, the optimum value of tube length increases by an increase in the rate of heat transfer flow.

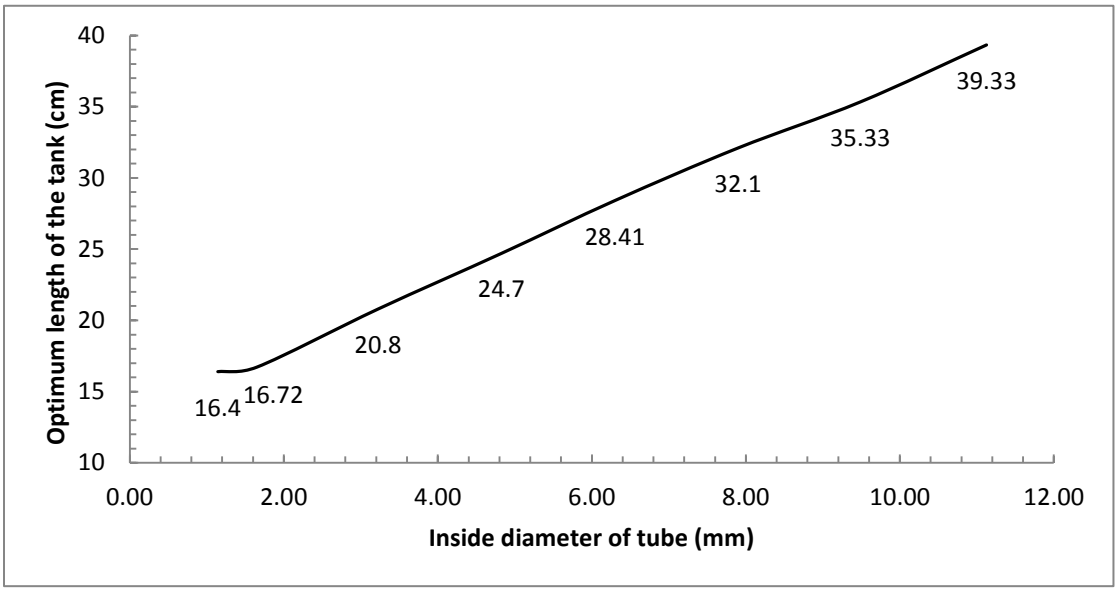

Figure 6.60 Variation of optimum tube length versus tube inside diameter in the case of without fin

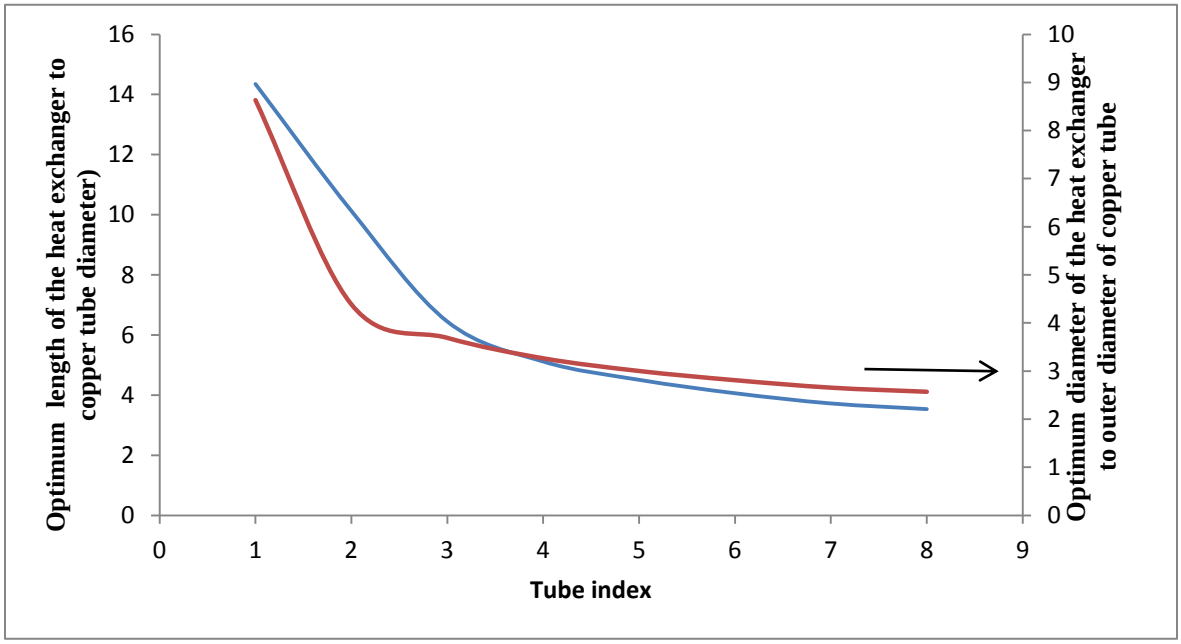

Figure 6.61 Variation of L/di and D/do with tube index

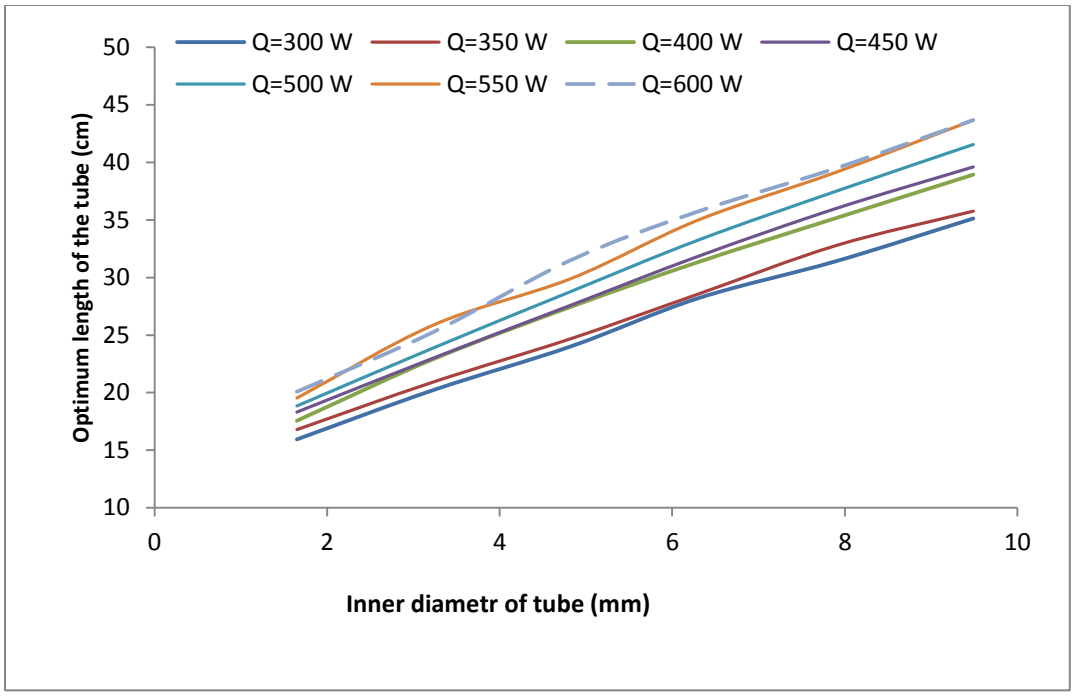

Figure 6.62 Variation of optimum value of tube length versus tube inner diameter for various rate of heat transfer

The variation of "L/d" versus Reynolds number and rate of heat transfer for various tube diameters is shown in Fig. 6.63. It can be seen that, the higher value of heat transfer needs the higher value of Reynolds number and L/d.

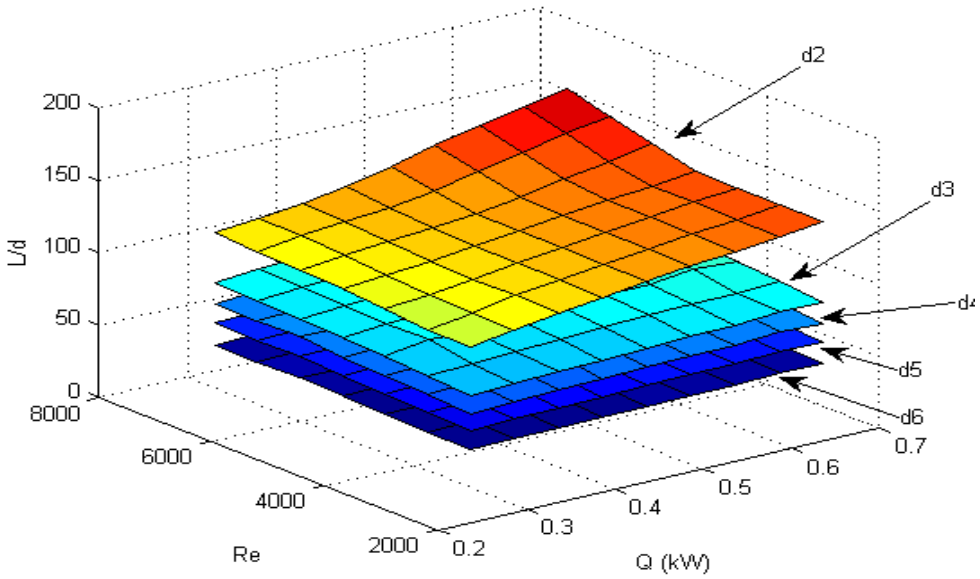

Figure 6.63 Dependency of Re, rate of heat transfer and L/d for various tube diameter

The variations of heat exchanger length versus CNT series probability and CNT concentration in optimum point are shown in Figures 6.64 and 6.65. It should be mentioned that the values of heat exchanger length which cannot satisfy the problem constrains are not illustrated in these Figures. It also can be seen that the heat exchanger length decreases by increasing both CNT probability and concentration. The maximum length is taken at the minimum possible CNT probability and concentration. Furthermore, in addition at the zero CNT probability and concentration (pure PCM) there is no optimum design to satisfy the constraint.

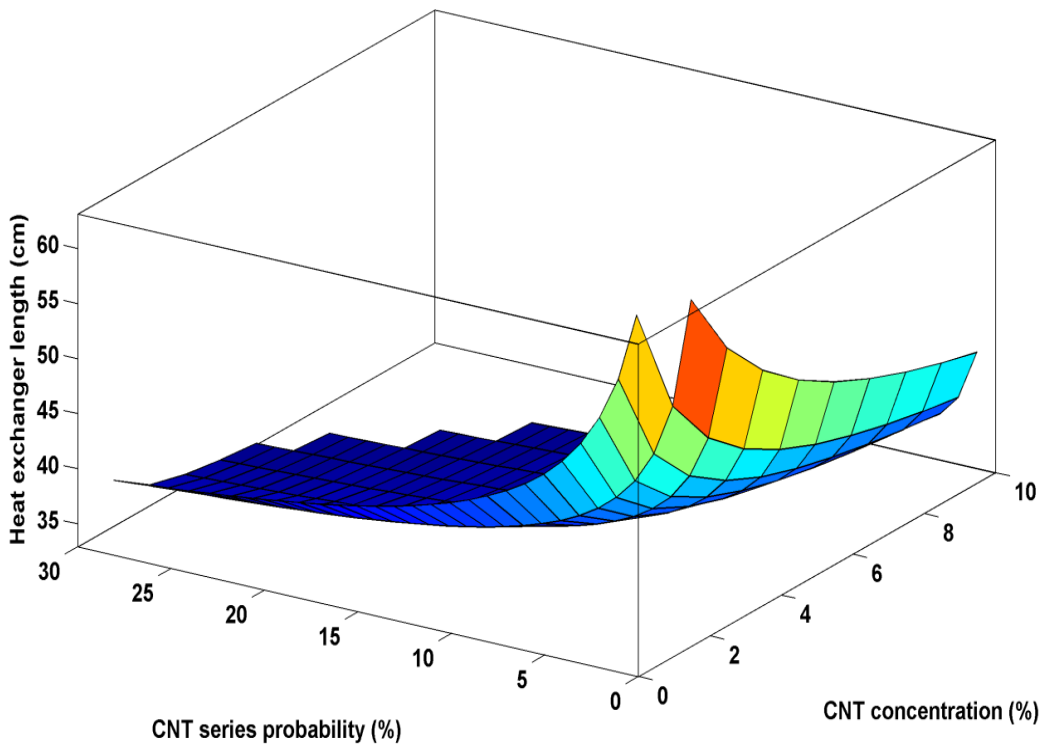

Figure 6.64 Variation of heat exchanger length with the probability of CNT in series configuration and concentration

The optimum heat exchanger length has been illustrated as a function of CNT concentration and series configuration probability in Figure 6.65. Contours reveal the regions that cannot satisfy the constraints. The bottom left corner, corresponds to the pure PCM which provides the lengths that fail to meet the requirements and to satisfy the constraint.

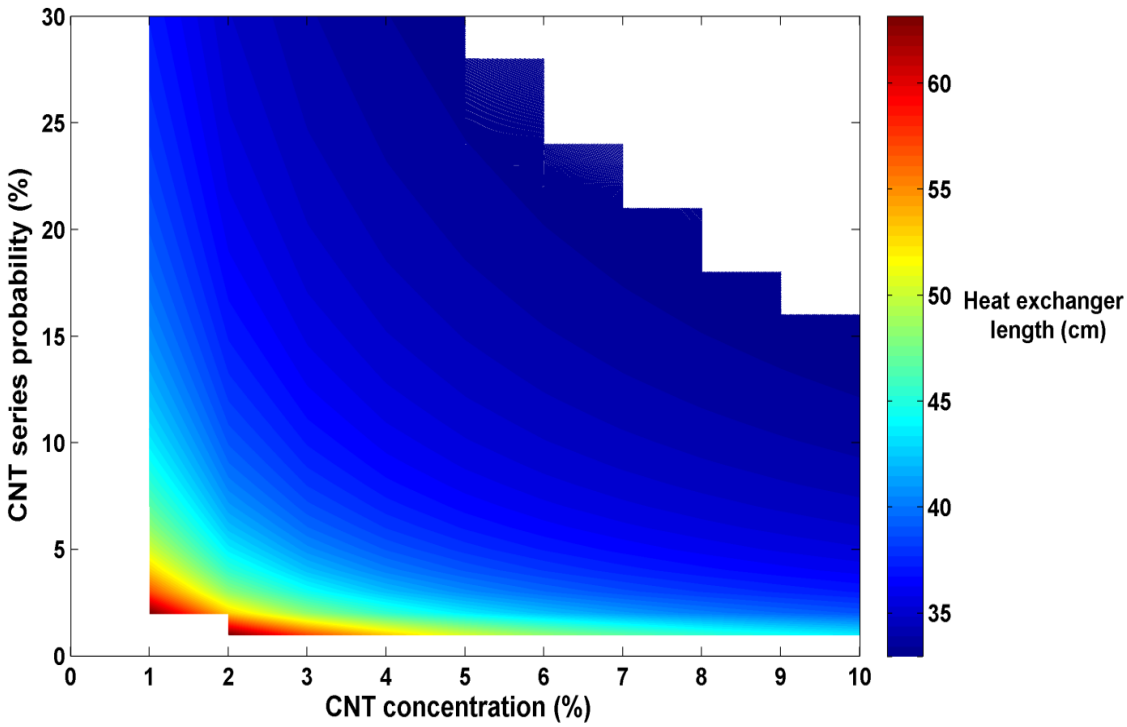

Figure 6.65 Contour of heat exchanger length versus CNT series probability and CNT concentration in

The optimum length has been obtained for different values of heat generation (Q) and various mass flow rates which give different Reynolds numbers. Once all the available tubes, starting from 1/16" diameter up to 1" diameter are investigated with respect to the variable mass flow rates and heat transfer to be handled in through the heat exchanger, the following relationship fits the set of diagrams with the least error.

$$\frac{\mathrm{LD}}{\mathrm{d}^2} = 471.55 + \mathrm{Re}\ (1 + 381.28 \times \mathrm{Q/L\_melt}\ (1 + \mathrm{Re}/893)) \qquad (6.43)$$

"L" and "D" are optimum length and diameter of the tank. L_{melt} is latent heat of fusion for the phase change material. It is also worth mentioning that Re number is calculated based on the total mass flow rate:

$$D_H = \frac{AA}{P} \qquad (6.44)$$

where DH is the hydraulic diameter. If "N" is the number of tubes in heat exchanger, then

$D_H = d\sqrt{N}$. Also Reynolds number is calculated as $R_e = \frac{4\dot{m}_{total}}{\mu \pi D_H}$

6.2.6 **Helical tube heat exchanger**

Another alternative for the tube configuration is helical. Helical tubes increase the rate of heat transfer due to the curvature in the tube. At the same time, they apply specific geometrical limitation in the design. In order to minimize the heat exchanger length, seven design parameters including number of tubes, index of each tube, shell (tank) diameter, CNT concentration, CNT series probability, helical radius and aspect ratio (ratio of helical pitch to the tube diameter) are selected. Design parameters and their variation range are shown in Table 6.15. Tube schedules and corresponding tube outside diameter, tube thickness and tube fin length are listed in the Table 6.16.

Table 6.15 Design parameters and their rang of variation in the case of helical tubes

	Lower bound	Upper bound
Number of tubes	1	200
Index of tube	1	6
Tank diameter (m)	0	0.3
CNT concentration (%)	0	10
CNT series probability (%)	0	20
Helical radius	0.02	0.1
Aspect ratio	1.5	10

Table 6.16 Soft copper tube specifications for optimization

Size (O.D, inch.)	Outer diameter (mm)	Inner diameter (mm)	Wall thickness (mm)
1/8"	3.16	1.65	0.762
3/16"	4.76	3.24	0.762
1/4"	6.35	4.83	0.762
5/16"	7.94	6.31	0.813
3/8"	9.53	7.90	0.813
1/2"	12.70	11.07	0.813

The genetic algorithm optimization was performed for 150 generations, using a search population size of M = 100 individuals, crossover probability of pc = 0.9, gene mutation probability of pm = 0.035. The optimum value for the heat exchanger length obtains 21.1 cm. The optimal values of design parameters are listed in Table 6.17. The designed helical heat exchanger with 4 coils and dimensions are given in Figure 6.66

Table 6.17 Optimum values of design parameters in the case of helical tube

Tube type	Length of H.X (cm)	Tank diameter (cm)	Number of tubes	CNT concentration (%)	CNT series probability	Helical radius (cm)	Aspect ratio
3/16	21.1	17.5	4	9.9	21	20	6.24

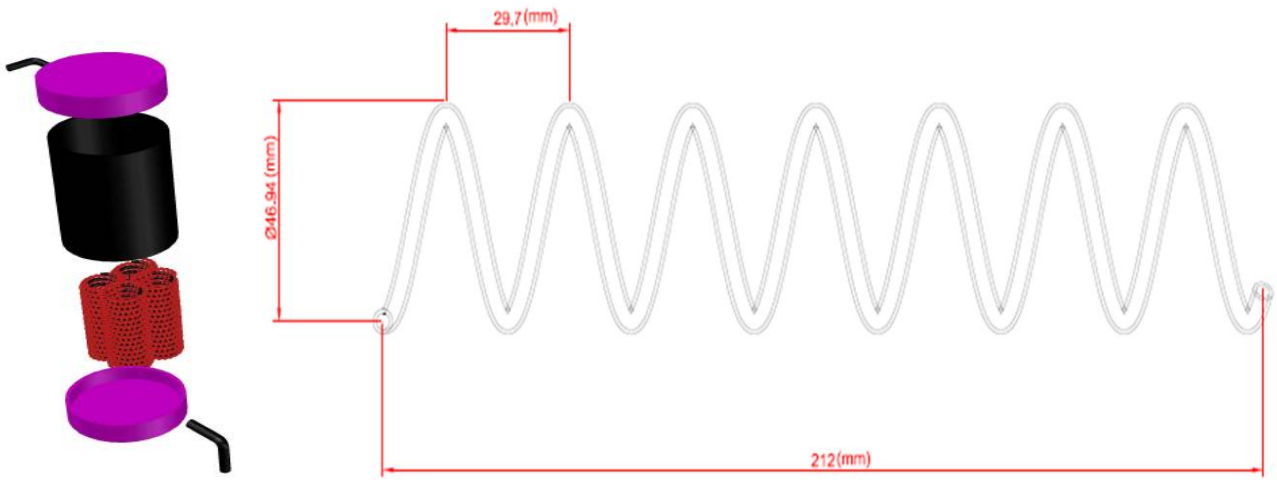

Figure 6.66 Schematic diagram of optimum helical tube heat exchanger

The variations of heat exchanger length versus CNT series probability and CNT concentration in optimum point is shown in Figure 6.67. It should be mentioned that the values of heat exchanger length which cannot satisfied the constraints are not illustrated in these Figures. It can be seen that the heat exchanger length decreases by increase of both CNT probability and concentration and the maximum length is taken at the minimum possible CNT probability and concentration. In additions, at the zero CNT probability and concentration (pure PCM) there is no optimum design to satisfy the constraint as the case for straight copper tubes.

6.3 Exergy analysis results

A software code in EES was developed to analyze a baseline model, with respect to the balance equations and system parameters provided in Section 4.3. Based on the baseline analysis, the exergy efficiencies and exergy destruction rates associated with each component are provided in Figure 6.68. Throughout the exergy analysis; the exergy efficiencies and exergy destruction rates are calculated for each component in the thermal management system. Among these components, the heat exchangers have the lowest exergy efficiencies with respect to the high

temperature differences and phase change which results in more entropy generation between the refrigerant and coolants. In the evaporator, the exergy losses are relatively high since (aside from the frictional losses) only part of the heat rejection occurs during the phase change process with large temperature differences between the working fluid in the evaporator and the vehicle cabin. Thus, reducing the mean temperature difference would reduce the exergy losses. One way of reducing the mean temperature difference is to increase the evaporator surface area; however, it should be weighed against the increase in the cost of installation [162].

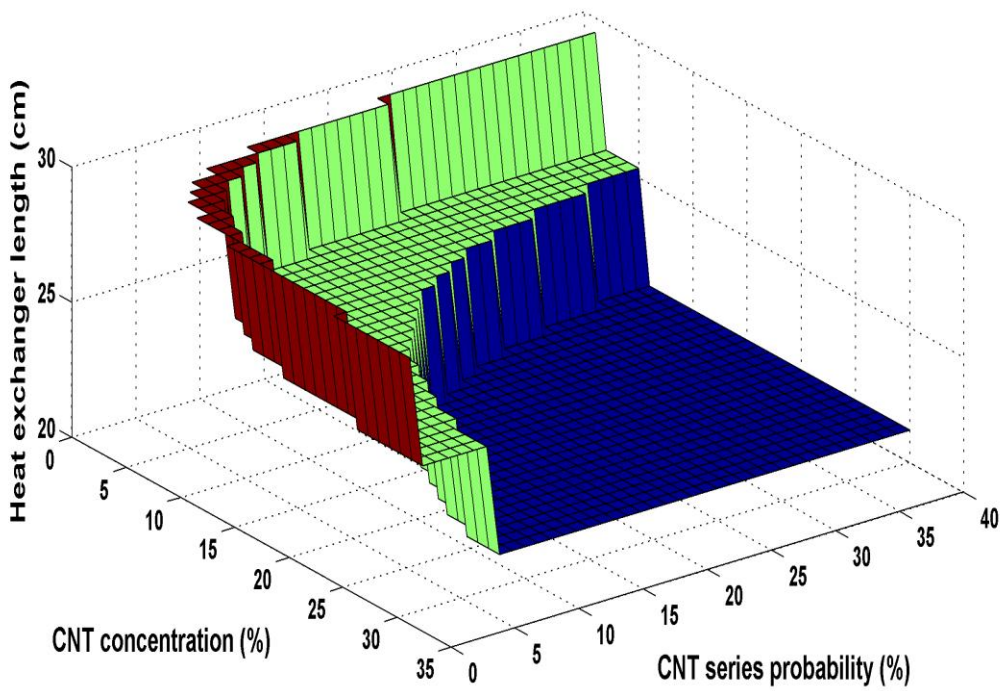

Figure 6.67 The variation of heat exchanger length versus CNT series probability and CNT concentration in optimum point

The condenser is calculated to have a lower exergy efficiency than the evaporator and the chiller, mainly due to the relatively higher temperature difference between the condenser exit and ambient air (taken at 35ºC), when compared to the differences between the evaporator exit and vehicle cabin temperature as well as the refrigerant and coolant temperatures. Among the remaining components, the compressor has high compression pressure ratio and change in temperature of the refrigerant passing through the compressor, which contributes to an increase in exergy destruction. The exergy loss in the compressor can be reduced by using a compressor

with higher isentropic efficiencies. Moreover, since the compressor power is highly dependent of the inlet and outlet pressures, proper sealing inside the compressor, heat exchanger improvements (such has reducing ΔT) and the implementation of multistage compression would reduce the exergy losses, thus reducing the compressor power. Furthermore, since a part of the irreversibilities occurs with respect to the frictional losses inside the compressor, utilizing appropriate lubricating oil that is miscible with the refrigerant (such as R-134a) would reduce the respective exergy losses.

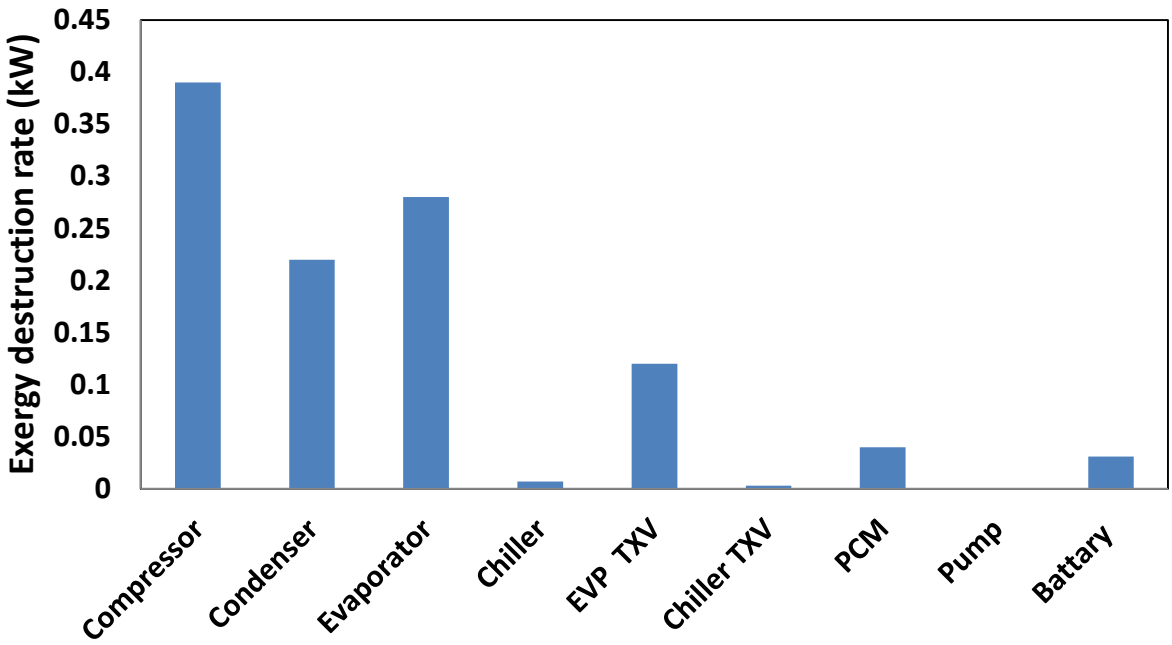

Figure 6.68 Exergy destruction rates for the system and its components

There is also significant research conducted [163] on the effects of using additives with a high conductivity (certain lubricant based nano-fluids) in the refrigerant in order to improve the heat transfer rate, thus reducing the difference in the operating temperatures, which also reduced the exergy losses. However, proper care must be taken in the utilization of the lubricant in order to prevent the deposition of the lubricant in the evaporator wall. The interaction between the cooling and battery coolant cycles also helps in reducing the compressor requirements significantly. The transfer of excess heat from the battery coolant to the cooling cycle via the chiller helps allocate the thermal energy appropriately, since otherwise, the cooling cycle would need to supply the additional energy which uses a compressor. Therefore, further utilizing this interaction would also be beneficial. Moreover, irreversibilities in the system occur due to high

temperature differences in heat exchangers, and therefore reducing these differences would reduce the associated irreversibilities [164].

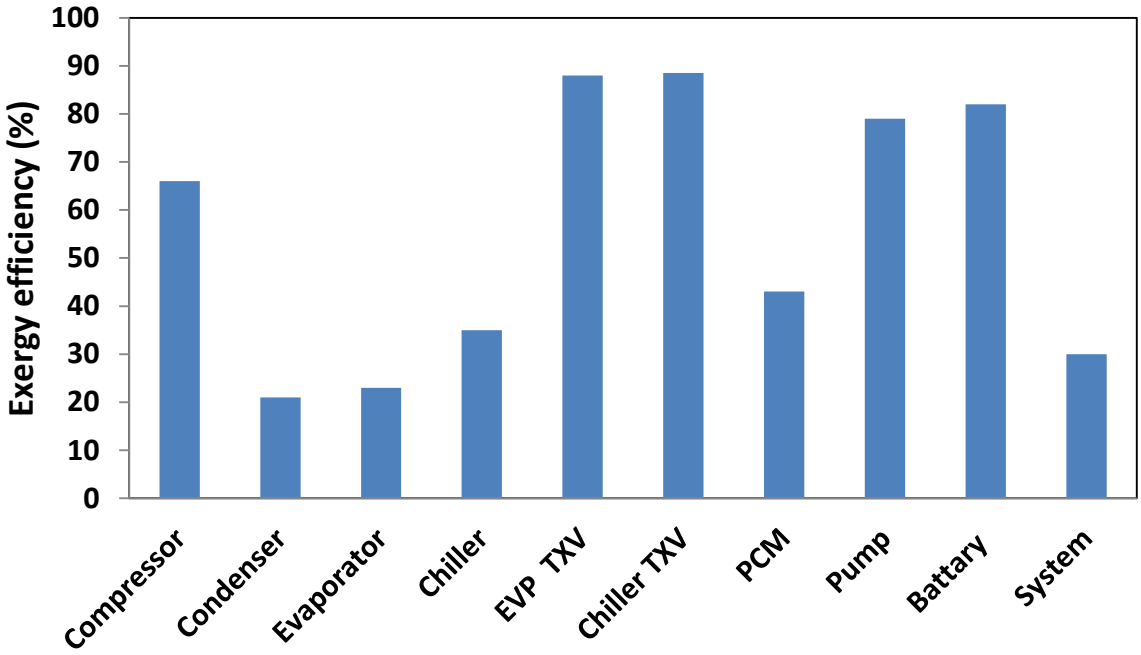

Figure 6.69 Exergy efficiency rates for the system and its components

The exergy efficiencies for the evaporator TXV and chiller TXV are higher (over 80%) since the processes are isenthalpic and have little or no heat loss (Figure 6.69). Therefore the exergy losses occur mainly due to a pressure drop in the expansion valve. The exergy losses in these TXVs can be reduced by lowering (or sub-cooling) the temperature of the refrigerant exiting the condenser, which can be feasible by utilizing the refrigerant vapour exiting the evaporator [165, 166]. The coolant pump also has a relatively higher efficiency (81%) since there is no significant heat loss from the pump.

It should be noted that the battery is modeled as a system and thus the internal efficiencies for the battery are not considered in this analysis. In this regard, the battery has high efficiencies within the target operating temperature range (up to 50ºC). However, the associated efficiency would decrease significantly as the battery is heated up beyond this range.

6.3.1 **Parametric Studies**

The system considered in the model is also analyzed based on the effects of condensing and evaporating temperatures, as well as compressor pressure ratio. Baseline values are used for all non-varied parameters in the parametric studies. The effect of variations of several design parameters on the thermodynamic performance of the system is assessed. Since PCM mass fraction, PCM heat exchanger pinch point temperature, evaporator temperature and condenser temperature affect system performance parameters we focus on them here. Figure 6.70 shows the effect of PCM mass fraction the system exergy and COP of the system. It is observed that an increase in PCM mass fraction results in an increase in both system exergy efficiency and system COP of the system.

When the PCM mass fraction increases, the cooling load of the PCM increases and the compressor work decreases due to the reduced mass flow rate entering the compressor. Therefore, according to the definition of exergy efficiency of the system the lower the compressor work the higher the exergy efficiency of the system. It is also concluded form Figure 6.70 that COP of the system is much higher than the system exergy efficiency of the system which is due to the fact that exergy associated with heat is multiplied by a small number which finally leads to decrease the exergy efficiency.

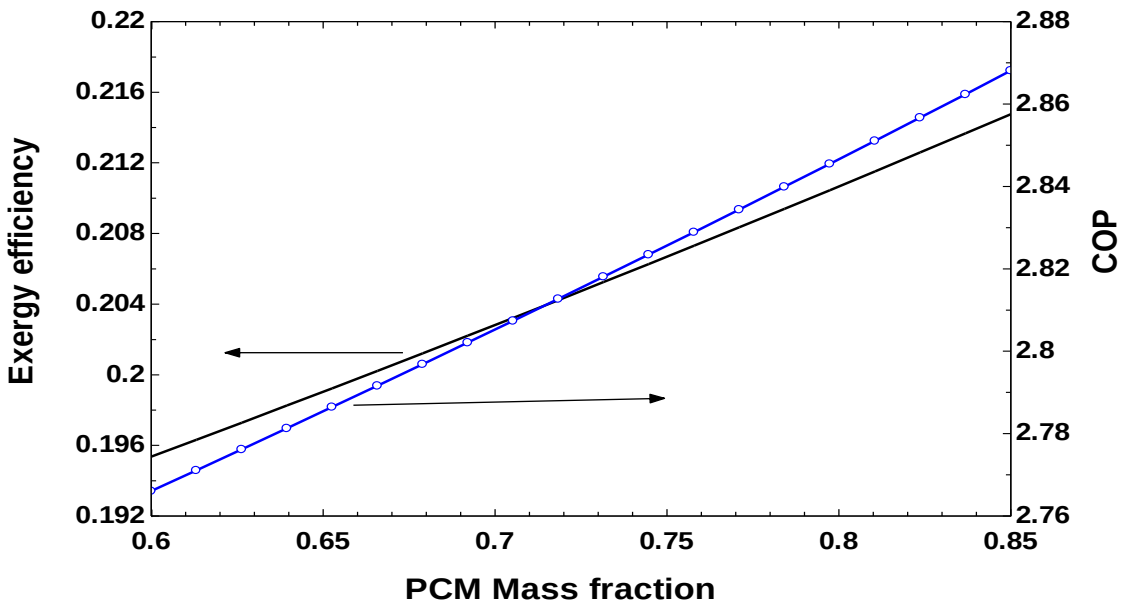

Figure 6.70 Effect of PCM mass fraction on exergy efficiency and COP of the system

Figure 6.71 shows the effect of PCM mass fraction on compressor work. It is shown that, an increase in PCM mass furcation results in decrease in compressor work. The effect of PCM variation on chiller cooling load and PCM cooling load is illustrated in Figure 6.72. It is observed that an increase in PCM mass flow rate decreases the chiller load and increase the PCM cooling load while decreases the compressor work as explained in Figure 6.76 Therefore, the combination of all these effects results in an increase in the system exergy efficiency.

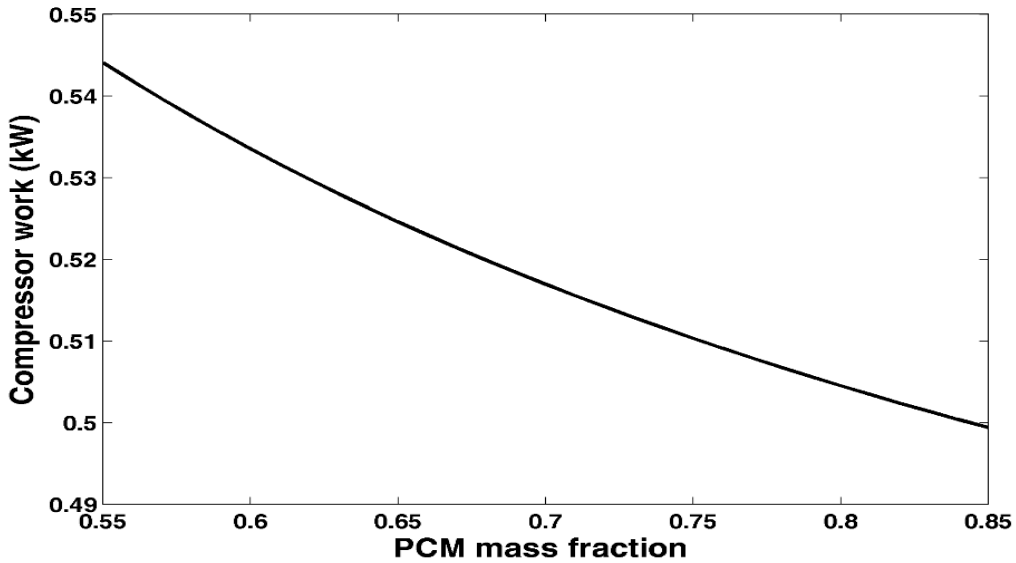

Figure 6.71 the effect of PCM mass fraction on compressor work

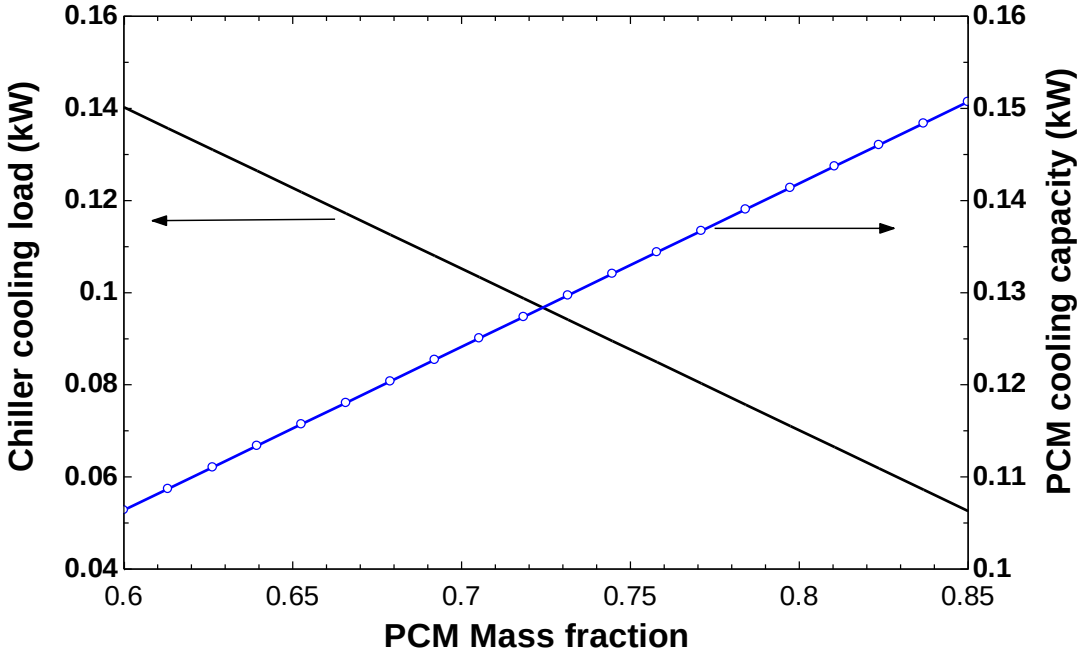

Figure 6.72 Effect of PCM mass fraction on chiller cooling load and PCM cooling capacity.

Figure 6.73 shows the variation of PCM mass fraction on the amount of PCM used in the system. As shown in Figure 6.73, an increase in PCM mass fraction ratio increases the amount of PCM for the system in kg. The reason is due to the increase in the PCM cooling load capacity as the higher the cooling load the higher the PCM mass used for the system to meet the cooling capacity of the system to reach the desired temperature. In order to enhance the understanding of the PCM heat exchanger, the effect of heat exchanger pinch point temperature on system exergy efficiency and COP of the system is shown in Figure 6.74. As it is shown in this Figure, an increase in heat exchanger pinch point temperature leads to a decrease in system exergy efficiency.

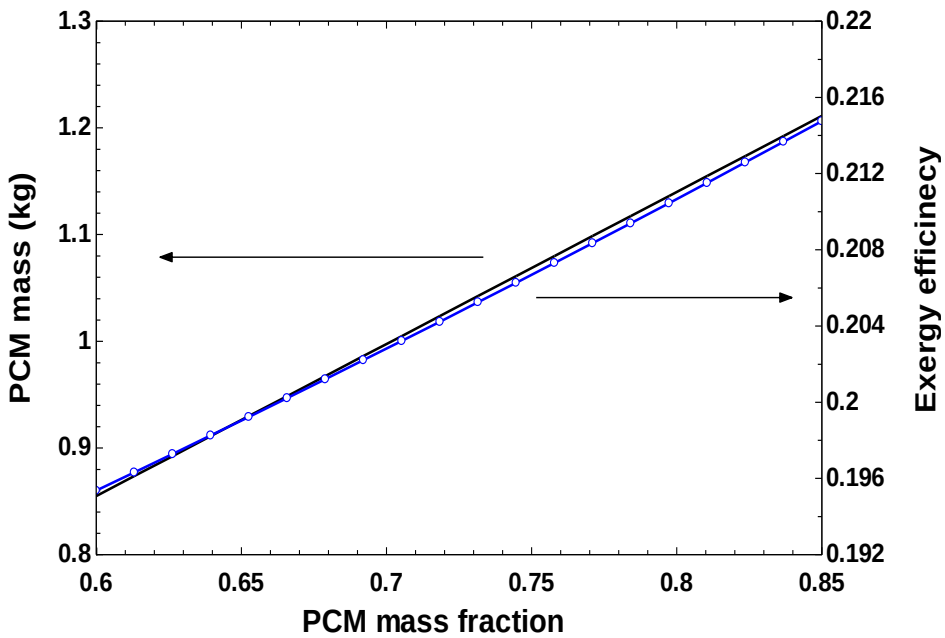

Figure 6.73 Effect of PCM mass fraction on PCM mass and exergy efficiency of the system.

This is due to the fact that the higher the pinch point temperature, the lower the energy being utilized in heat exchanger which leads to a reduction of PCM cooling load of the system. On the other side, an increase in pinch point temperature while fixing other design parameters, results in a decrease in heat transfer area for the heat exchanger. This is will lead to a decrease in the total cost rate of the system. Another important parameter that affects the system performance is evaporator temperature. As the evaporator temperature increases, the temperature of the refrigerant vapour before entering the compressor also increases.

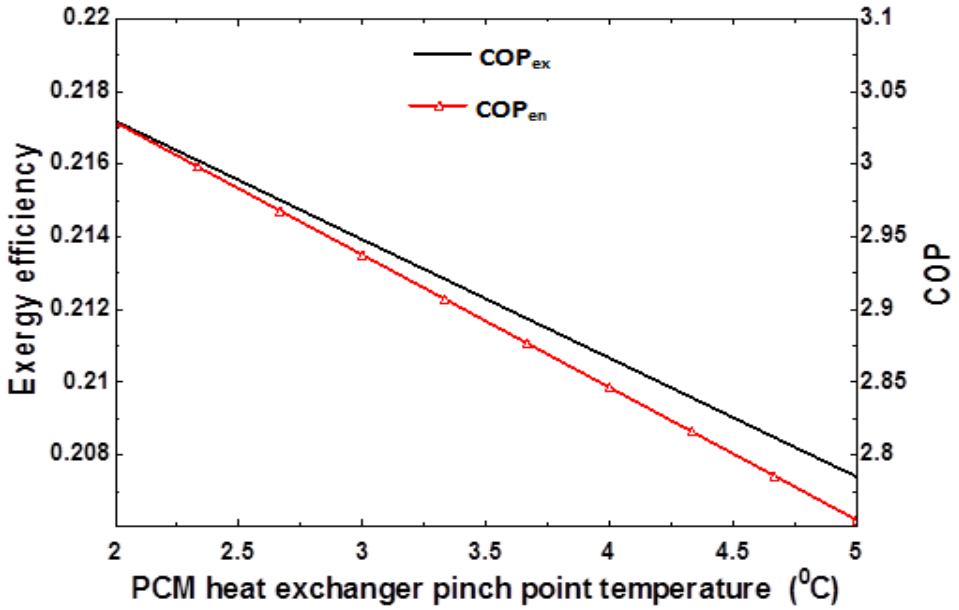

Figure 6.74 PCM heat exchanger on system exergy efficiency and COP

The refrigerant vapour specific volume reduction increases the associated refrigerant mass flow rate, therefore increases the system cooling output. On the other hand, an increase in the condensing temperature leads to an increase in the temperature of the refrigerant discharged from the compressor along with the compression ratio. However, the compression capacity of the compressor will be reduced. Moreover, the refrigerant circulated per unit of time will be lower, which reduces the cooling load as shown in Figure 6.75

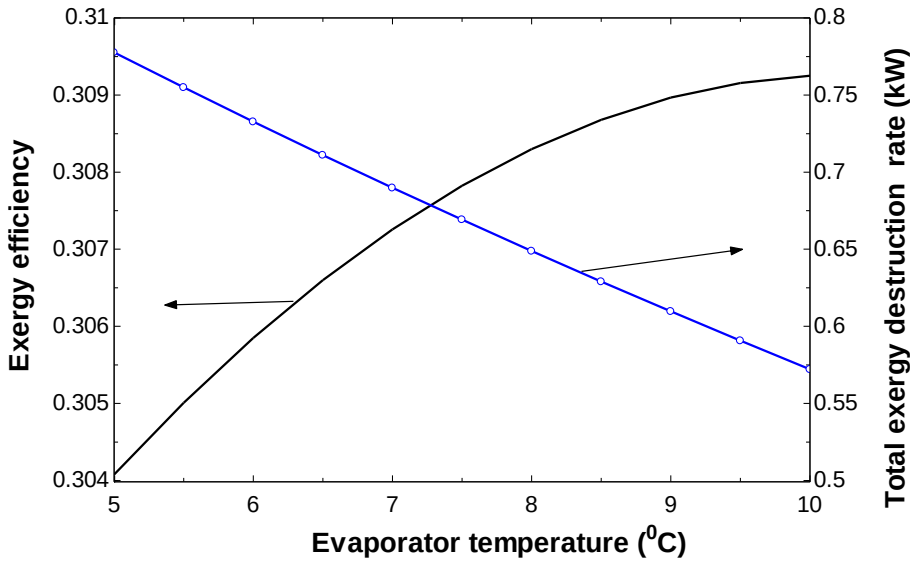

Figure 6.75 Effect of evaporator temperature on system exergy efficiency and total exergy destruction of the system

Since energy consumption of the compressor is also proportional to the pressure ratio, this reduction in the condensing temperature or increase in the evaporator temperature increases the COP of the system by reducing the compression ratio. This indicates that the required compressor power to a certain cooling capacity drops as the condensing temperature decreases or the evaporating temperature increases. Moreover, the throttling losses also decrease with decreasing temperature change, hence leading to an increase in the COP as shown in Figure 6.76. Furthermore, the exergetic COP of the system also increases since reducing the condensing temperatures reduces the mean temperature difference between the refrigerant and the ambient air.

Increasing the evaporating temperatures reduces the mean temperature difference between the refrigerant and the cabin air, both reducing the associated exergy destruction (See Figure 6.77 and Figure 6.78). The compressor ratio is another important parameter since it has a significant impact on compressor work, cooling capacity and energetic and exergetic COPs of the system. As the compressor speed increases, the average compressor work also increases, resulting in higher refrigerant mass flow rates, discharge pressure, compression ratio and lower suction pressure and volumetric efficiency.

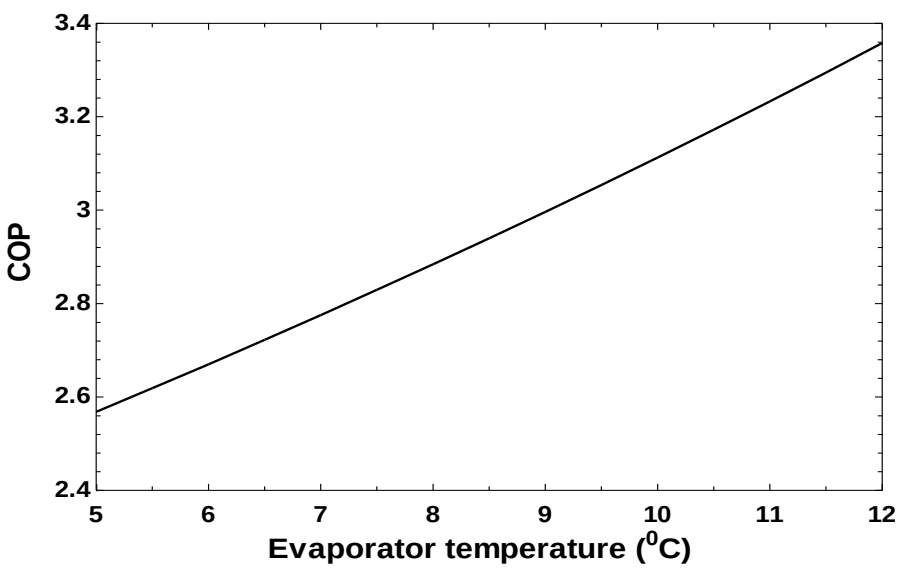

Figure 6.76 Effect of evaporator temperature on system COP of the system.

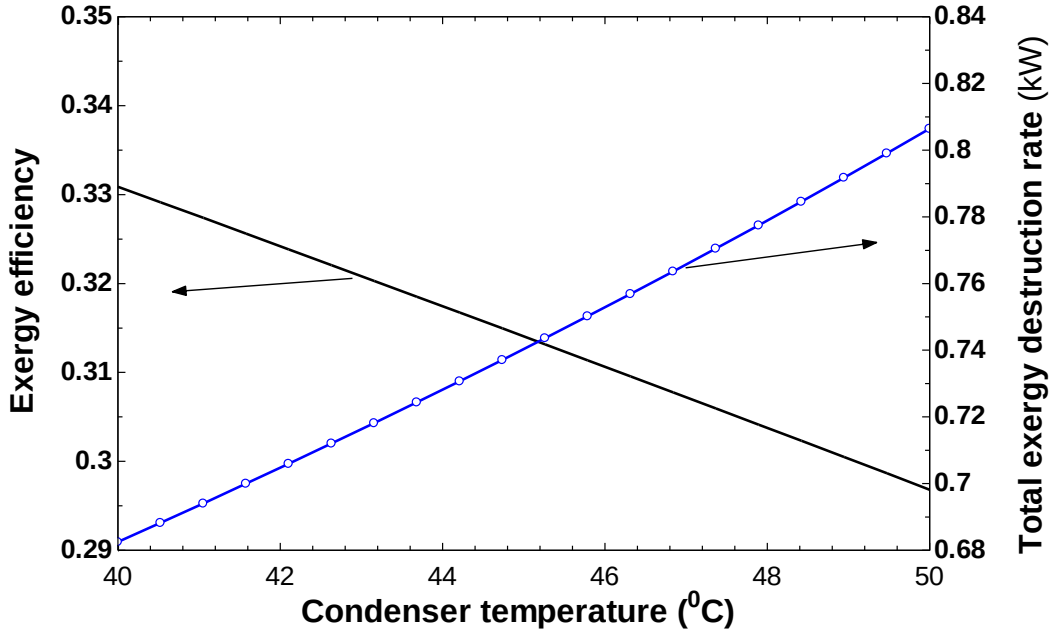

Figure 6.77 Effect of condenser temperature on system exergy efficiency and total exergy destruction

It is also found that the increase in the compressor ratio leads to an increase in the cooling capacity while decreasing the corresponding energetic COP of the system. The exergetic COP of the system also decreases since the associated pressure difference across the compressor and expansion valve increases the overall exergy destruction of the system [167]. The effects of the resulting compression ratio on the system exergetic COP and exergy destruction rate are shown in Figure 6.79.

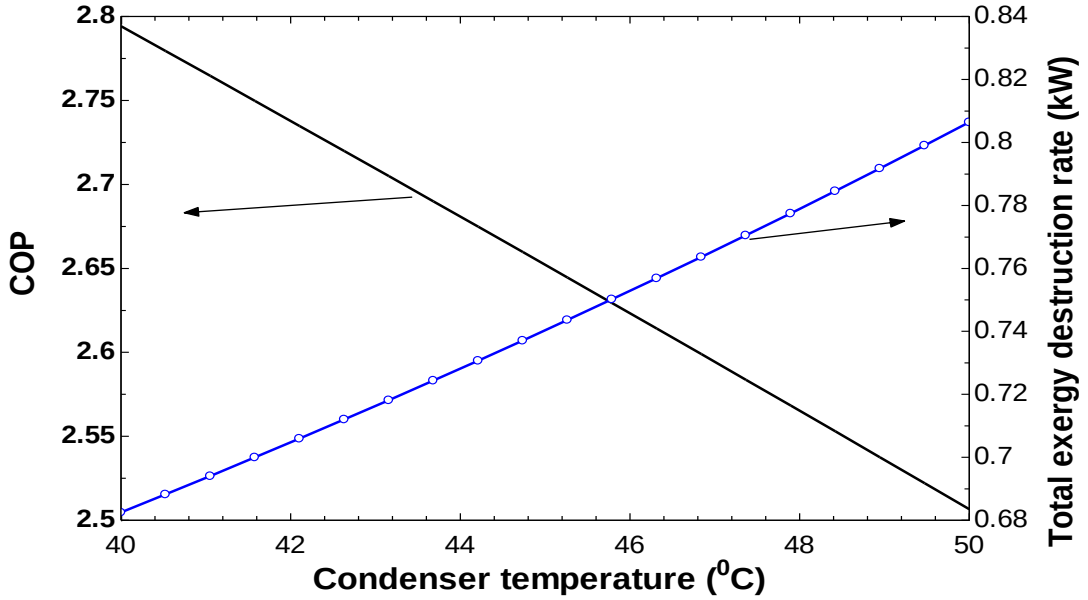

Figure 6.78 Effect of condenser temperature on system COP and total exergy destruction of the system.

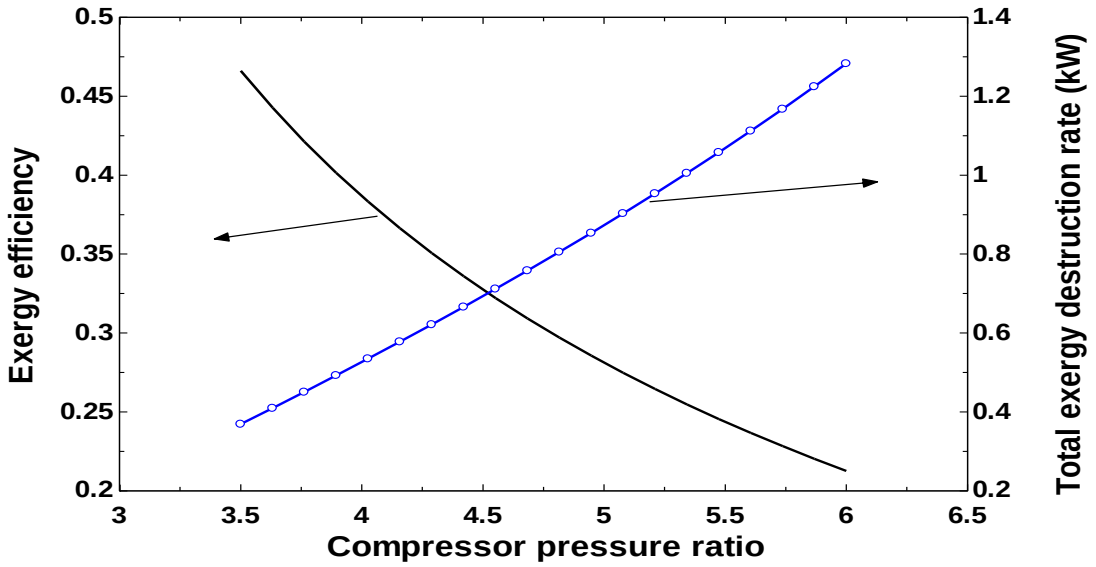

Figure 6.79 Effect of compressor pressure ratio on system exergy efficiency and total exergy destruction of the system.

The sustainability index is a good indicator of how efficiently the resources are utilized in the TMS. Thus, it is therefore directly related to the exergetic COP and exergy destruction rates associated with each TMS. Moreover, the indirect GHG emissions are produced from electricity generation associated with the compressor and pump for the TMS. Figure 6.80 shows the GHG emissions and sustainability index with respect to the exergetic COP for the baseline TMS using R134a. In Figure 6.80, as the efficiency of the baseline TMS increases, the power input required for the TMS decreases under the same cooling loads. Hence, the corresponding emissions decrease and the sustainability index increases. It should be noted that the emissions in Figure 6.80a are determined based on the U.S average energy generation mix composed of 49% coal, 20% natural gas, 20% nuclear, 7% hydro and 4% other renewables [168].

Therefore, the associated indirect emissions will be different under other energy generation options with different carbon intensities. Figure 6.80b shows that the emissions produced from electricity generation almost double under a high-carbon scenario, where the electricity is primarily generated using coal. This reduces significantly under a low-carbon scenario, where electricity is produced through a natural gas combined cycle.

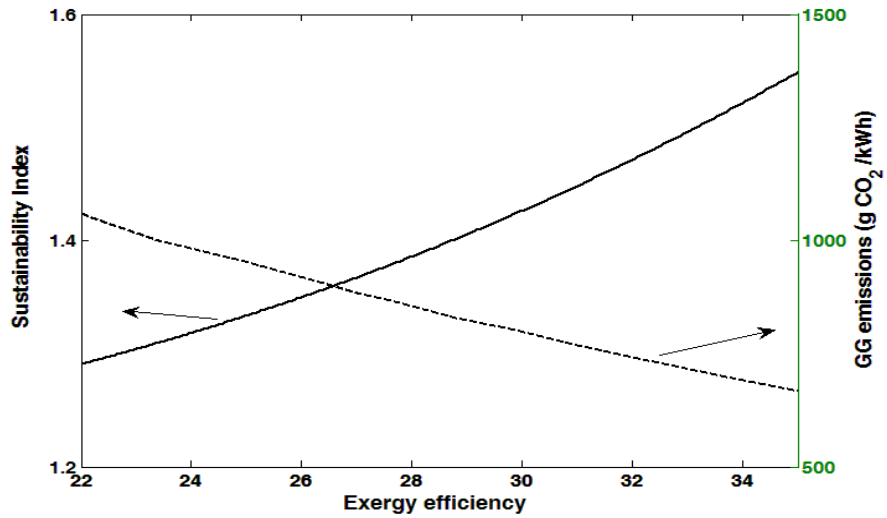

(a)

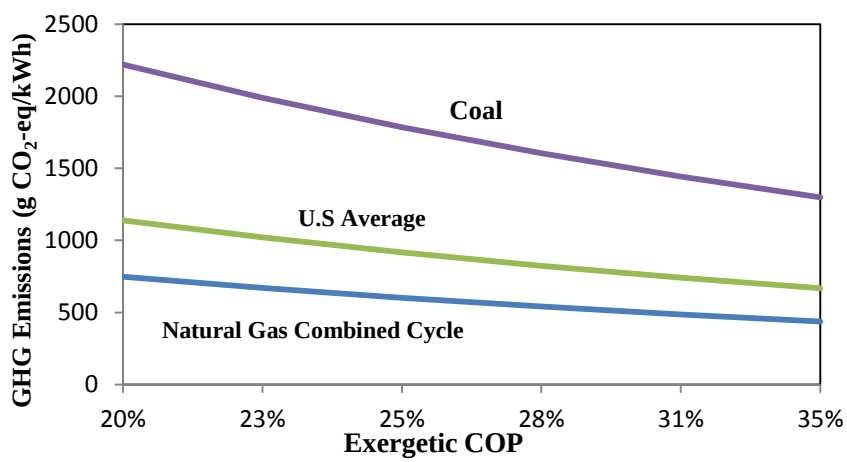

(b)

Figure 6.80 (a) GHG emissions and sustainability index with respect to baseline TMS exergetic COPs (b) under various carbon intensity of electricity generation.

6.3.2 **Optimization results**

The exergy efficiency and total cost rate are considered as two objective functions. To maximize the exergy efficiency and to minimize the total cost rate, nine design parameters including compressor speed, compression ratio, evaporating air temperature, superheating temperature, evaporator air mass flow rate, cooling capacity, condensing air temperature, condenser air mass flow rate and sub-cooling temperature are selected. Design parameters (decision variables) and the range of their variations are listed in Table 6.18

Table 6.18 Range of parameters used in the analysis

Parameter	Range of variation
Compressor speed (rev/min)	1,500-5,000
Compression Ratio	1 – 5
Evaporating Air Temperature (℃)	0 – 15
Superheating Temperature (℃)	0 – 12
Evaporator Air Mass Flow Rate (kg/s)	0.1 – 0.5
Cooling Capacity (kW)	1 – 5
Condensing Air Temperature (℃)	40 – 55
Condenser Air Mass Flow Rate (kg/s)	0.1 – 0.5
Sub-cooling Temperature (℃)	0 – 12

The genetic algorithm optimization is performed for 500 generations, using a search population size of M = 100 individuals, crossover probability of pc is 0.90, gene mutation probability of pm is 0.03 and controlled elitism value will be c = 0.60. The results of optimum exergy efficiency and total cost rate for all points evaluated over 500 generations are depicted in Fig. 6.81. The Pareto-optimal front (best rank) is clearly visible in the lower part of the Figure which is separately shown in Fig. 6.82.

A clear approximation of the Pareto front is visible on the lower part of the curve. The Pareto optimum results clearly reveal the conflict between two objectives, the exergy efficiency and the total cost rate. Any change that increases the exergy efficiency, leads to an increase in the total cost rate and vice versa. This shows the need for multi-objective optimization technique in optimal design of cycle. It is shown in Figure. 6.82, which the maximum exergy efficiency exists at design point *A* (0.3479), while the total cost rate is the biggest at this point.

On the other hand the minimum total cost rate occurs at design point *C* (1.377 $/hr), with a smallest exergy efficiency value (0.3217) at that point. Design point *A* is the optimal situation

at which, exergy efficiency is a single objective function, while design point *C* is the optimum condition at which the total cost rate is a single objective function.

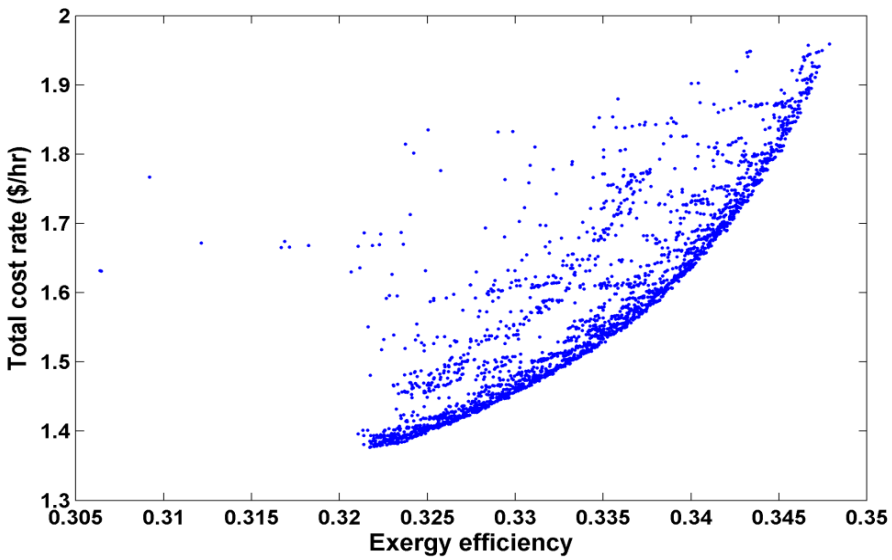

Figure 6.81 Results of all evaluations during 500 generations using NSGA-II.

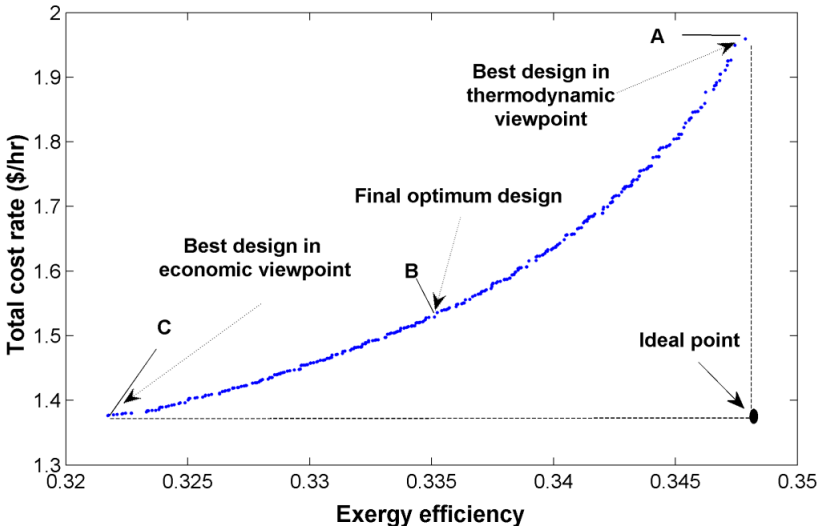

Figure 6.82 The distribution of Pareto-optimal points solutions using NSGA-II

Based on procedure presented in final optimum solution, the optimum design point *B* is selected as final optimum design using LINMAP method. Optimum values of two objectives for three typical points from *A* to *C* (Pareto-optimal fronts) are listed in Table. 6.19.

Table 6.19 Values of two objectives for three typical points from *A* to *C*

Objectives	A	B	C
Exergy efficiency	0.3479	0.3351	0.3217
Total cost rate ($/hr)	1.959	1.529	1.377

In order to provide a useful tool for the optimal design of this cycle, Equation 6.45 for exergy efficiency versus the total cost rate is curved for the Pareto curve (Figure 6.82).

$$C_{total}(\$/hr) = \frac{1.04\varepsilon^2 - 0.7551\varepsilon + 0.137}{\varepsilon^2 - 0.7132\varepsilon + 0.1271} \tag{6.45}$$

which is valid in the range of $0.3217 < \varepsilon < 0.3479$ for exergy efficiency. In this equation, for any considered exergy efficiency, it will provide corresponding the minimum total cost rate for that optimal point.

6.3.3 **Stefan problem and transient exergy analyses**

For a shell and tube tank with the PCM in the shell side, the exergy analysis is developed below. The total heat transferred from the copper tube to the PCM includes sensible heat storage in the solid and liquid phases along with the mushy zone, which are shown in Figure 6.83.

$$\dot{Q} = \frac{d}{dt}(Q_{melt}) + \frac{d}{dt}(Q_{msh}) + \frac{d}{dt}(Q_{solid}) = \underset{(1)}{\frac{d}{dt}(\rho_L V_m L_m)} + \underset{(2)}{\frac{d}{dt}(m_s h_s + m_{L,msh} L)} + \underset{(3)}{\frac{d}{dt}(\rho_s + V_s h_s)} \tag{6.46}$$

The second term in the right hand of above equation, deals with the mushy zone, which is analysed as follows:

$$x = \frac{m_l}{m_{tot}} \tag{6.47}$$

$$m_{tot} = m_l + m_s, \quad m_{tot} = \frac{m_l}{x} = \frac{\rho_L V_{Lm}}{x} \tag{6.48}$$

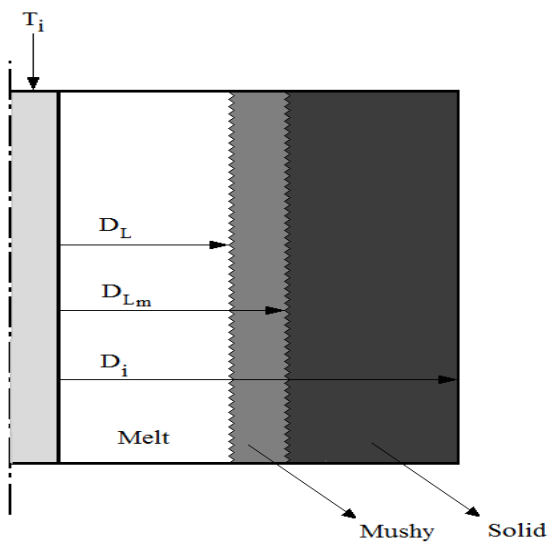

Figure 6.83 Phase change material in LHTES system in transient condition

By applying of this definition for mass concentration, the heat rate in the mushy zone is calculates as below:

$$m_s = (1-x).m_{tot} \tag{6.49}$$

$$m_l = x.m_{tot} \tag{6.50}$$

$$\dot{Q}_{msh} = \frac{d}{dt}(m_{tot}((1-x)h_s + x.L) = \frac{d}{dt}(\frac{\rho_L V_{Lm}}{x}((1-x)h_s + x.L)) = \frac{d}{dt}(\rho_L V_{Lm}(\frac{1}{x}-1)h_s + L)) \tag{6.51}$$

$$V_{L,m} = \frac{\pi(D^2{}_{L,msh} - d^2)}{4}.H = A_{L,msh}(t)H \rightarrow \frac{dV_{L,msh}}{dt} = \frac{dA_{L,msh}(t)}{dt}H \tag{6.52}$$

$$\dot{Q}_{msh} = \rho_L \frac{dV_{Lm}}{dt}((\frac{1}{x}-1)h_s + L)) + \rho_L V_{Lm}\frac{d}{dt}((\frac{1}{x}-1)h_s + L)) \tag{6.53}$$

where, H is the length of the heat storage tank and A denotes the occupied area mushy zone

$$V_{L,msh} = HA_{L(t)} \tag{6.54}$$

$$\dot{Q}_{msh} = \rho_L(H.\frac{dA_{Lm}}{dt}(\frac{1}{x}-1)h_s + L) - \frac{HA_{L,m}h_s}{x^2}) \tag{6.55}$$

$$\dot{Q}_{msh} = \rho_L h_s H.(\frac{dA_{Lm(t)}}{dt}((\frac{1}{x}-1)h_s + L) - \frac{A_{L_m(t)}}{x^2}) \tag{6.56}$$

$$\dot{Q}_{mshy} = f(A_{L(t)}, x) \tag{6.57}$$

$$A_{L_{m(t)}} = \frac{\pi}{4}(D_{L_m}^2 - D_L^2) \tag{6.58}$$

For term (1) in Equation 6.46

$$\frac{d}{dt}(\rho_L V_L L) = \rho_L.LH\frac{d}{dt}(A_{L(t)}) \tag{6.59}$$

$$A_L = \frac{\pi(D_L^2 - d^2)}{4} \rightarrow \frac{dA_L}{dt} = \frac{\pi}{4}\frac{d}{dt}(D_L^2 - d^2) = \frac{\pi}{2}D_L\frac{dD_L}{dt} \tag{6.60}$$

Therefore, term 1 will be $\rho_L.LH\frac{\pi}{2}D_L\frac{dD_L}{dt}$ (6.61)

For term (3) which is Solid region of the solution, the calculation can be given as follows:

$$\frac{d}{dt}(\rho_s V_s h_s) \rightarrow \frac{d}{dt}(\rho_s V_s h_s) = \rho_s h_s H\frac{dA_{L(t)}}{dt}$$
$$= \rho_s h_s H\frac{dA_{L(t)}}{dt} = \rho_s h_s H\frac{\pi}{4}\frac{d(D_i^2 - D_{L,m}^2)}{dt} = -\frac{\pi}{2}D_{L,m}\rho_s h_s H\frac{dD_{L,m}}{dt} \tag{6.62}$$

where Di is the internal diameter of cylinder in Figure 6.83. Therefore the result will be

$$\dot{Q}_{msh} = \rho_L.LH\frac{\pi}{2}D_L\frac{dD_L}{dt} + \rho_L h_s H.(\frac{dA_{Lm(t)}}{dt}((\frac{1}{x}-1)h_s + L) - \frac{A_{L_m(t)}}{x^2}) + \rho_L.LH\frac{d}{dt}(\frac{\pi}{2}D_L\frac{dD_L}{dt}) \tag{6.63}$$

Based on this equation, the transient exergy is given as

$$\dot{EX}_{(t)} = \dot{Q}(1-\frac{T_0}{T_m}) = (1-\frac{T_0}{T_m})[\rho_L.LH\frac{\pi}{2}D_L\frac{dD_L}{dt} + \rho_L h_s H.(\frac{dA_{Lm(t)}}{dt}((\frac{1}{x}-1)h_s + L) - \frac{A_{L_m(t)}}{x^2})$$
$$+ \rho_L.LH\frac{d}{dt}(\frac{\pi}{2}D_L\frac{dD_L}{dt})] \tag{6.64}$$

It worth to mention that the contribution of mushy zone in exergy efficiency of the heat exchanger is smaller, compared to those corresponding to solid or liquid parts.

To have an idea about this process, The ANSYS FLUENT simulation is conducted to demonstrate the size of the mushy zone (Figure 6.84). It can be seen that the size of the mushy zone is considerably smaller as compared to those of solid and liquid phases; therefore, exergy related to mushy becomes considerably smaller than those of solid and liquid regions in

accordance with equations. Simulation domain consists of a tube zone with 1.62mm diameter, in which the hot water flows. The tube is placed in middle of tank with diameter of 64 mm; therefore the problem is axisymmetric (2D). Domain length is 250 mm and mesh consists of 9000 element (104 x 60). The top boundary is considered insulated, while left and right boundaries are imposed to free convection. Hot water enters to the tube from left side and PCM in the shell side melts.

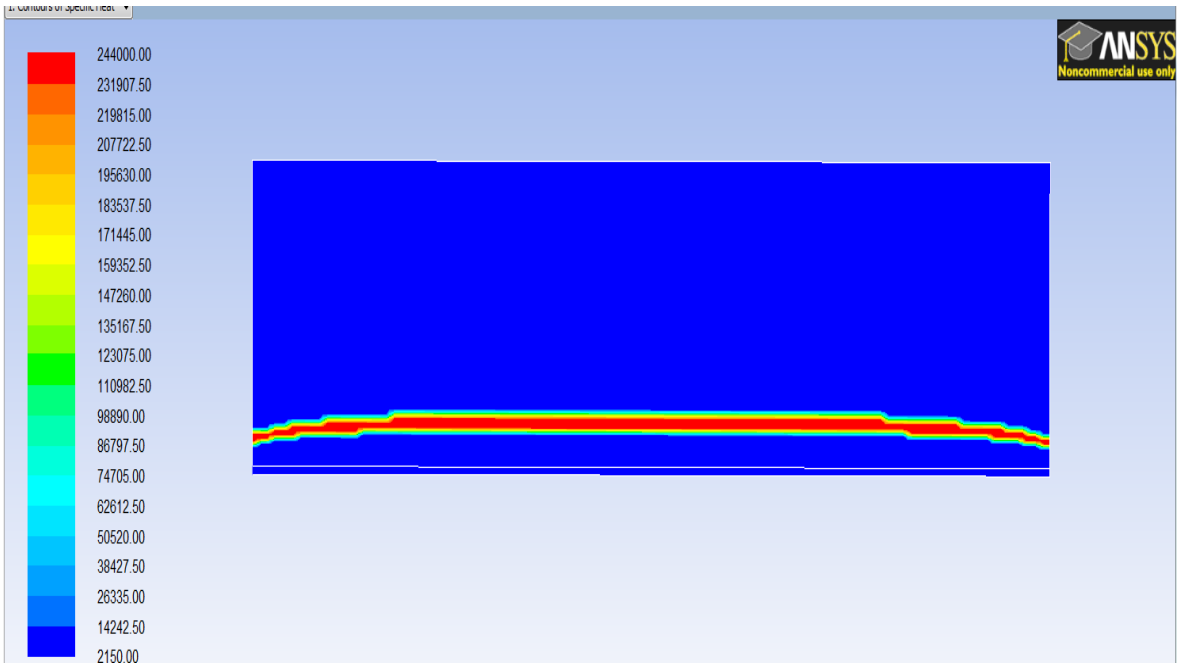

Figure 6.84 Mushy zone thickness in vicinity of tube in the heat exchanger

Away from the surface of the tube, 4 points have been defined, each one with 1 mm distance in between. The liquid fraction or changes in specific heat at the specified locations are monitored to give the melting front speed. Figure 6.85 shows specific heat transient response in each location, with respect to the elapsed time. It can be seen that for the locations near to the tube, the front speed is higher than other points. This can be justified based on the low thermal conductivity of the PCM.

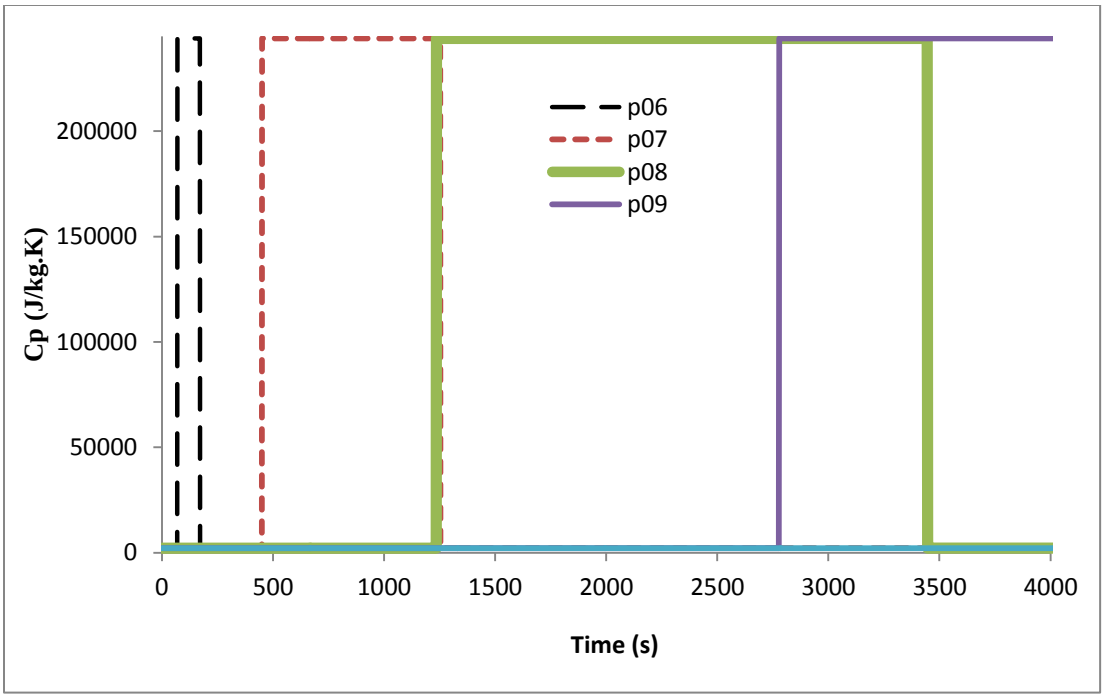

Figure 6.85 Speed of the melting front in radial direction at four points

6.4 Experimental results

First set of experimental data presented in section 6.1 to assess the numerical simulations of PCM applications between the Li-ion cells in the sub-module. In this section, the results for heat exchanger are presented. First the results for charging and discharging of pure and technical grade PCM will be presented following by the PCM mixed with CNT and carbon nanotubes are given.

6.4.1 Thermal conductivity enhancement by Nanoparticles

Different methods for enhancement of thermal conductivity are discussed in Chapter 2 (section 2.4.2). Results of adding carbon nanotubes and grapheme nano-platelets are presented in this section. Differential scanning calorimetry (DSC) tests are carried out for the samples that are prepared in the UOIT lab. The main reason to add these nanoparticles is to increase the thermal conductivity. This is why the thermal conductivity of mixtures can be measured directly. At the same time, a method is developed in this section to calculate and compare the effect CNT and

grapheme additives in the PCM based on the DSC data. DSC method for the 4 samples has been carried out. Table 6.20 shows the 4 samples which are tested and results are analyzed.

Table 6.20 Samples of PCM and Nano-particles prepared for the tests

No.	Sample
1	Technical Grade PCM
2	Pure PCM
3	6% Graphene platelets mixed in technical grade PCM
4	6% CNT mixed in in pure PCM

The properties of CNT and grapheme nano-platelets are described in chapter 4. In brief, carbon Nano-tubes (CNT) are 8-10 nm in diameter and 10-50 micrometer in length. Normal octadecane is either pure or technical grade, with the purity of 99.66% and 90.8% , respectively. Cooling of the samples starts from 55℃ to -10℃ at 10C/min temperature ramp. Figures 6.86 and 6.87 show the heating and cooling DSC results for pure and technical grade octadecane PCMs, respectively. Nanoparticles are added to the pure and technical paraffin as described in table 6.20. The same methodology is applied in order to obtain the DSC diagrams of these mixtures of PCM and nanoparticles. The related DSC graphs are given in in Figures 6.88 and 6.89.

One result that can be deduced comparing these DSC graphs is reduced latent heat of fusion for pure material by increasing the impurities. This value for pure PCM is 226,107 J/kg which has been reduced to 187,322 J/kg for technical grade PCM. This value is the area under the power curve and horizontal axis.

In order to calculate the thermal conductivity based on the DSC test for specific heat, the following relations are improved. The following equation can be obtained by solving the heat differential equation [169]:

$$\frac{d(\Delta P)}{dT} = \frac{2}{R} \tag{6.65}$$

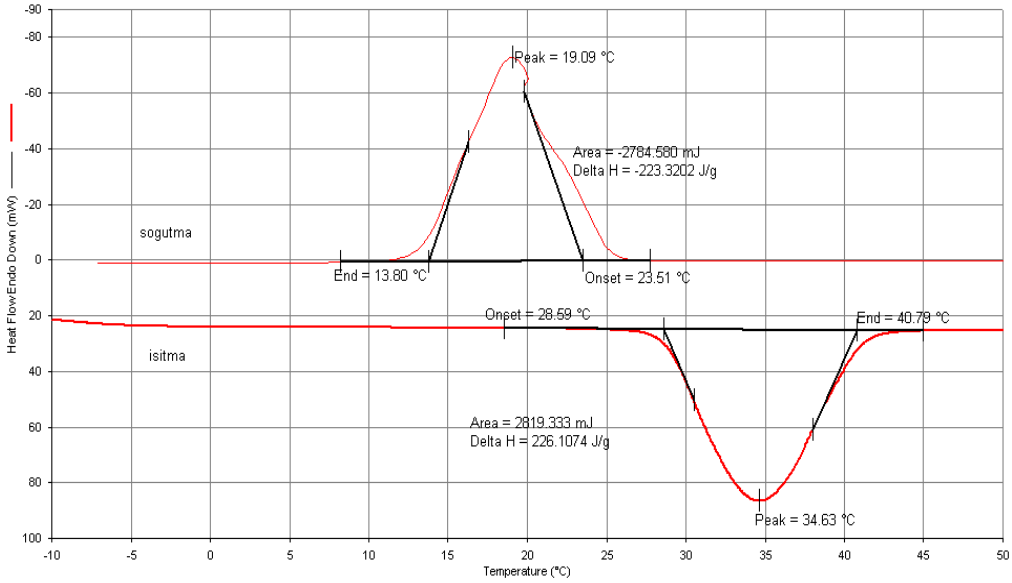

Figure 6.86 Differential scanning calorimetry results for pure n-octadecan (99 %) in heating and cooling periods.

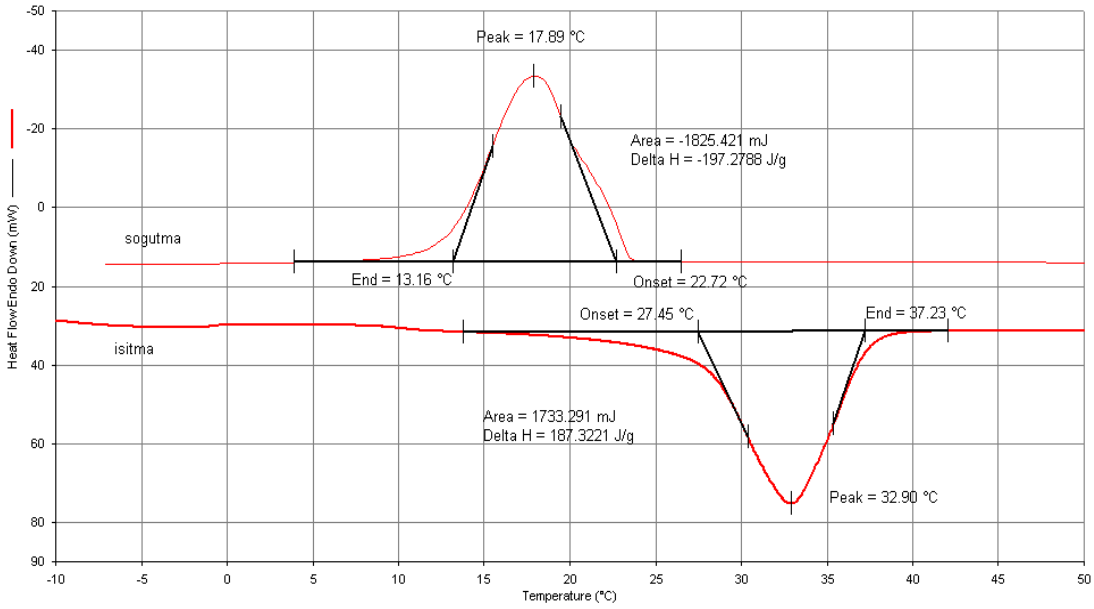

Figure 6.87 Results of DSC for technical grade octadecane (90.8%)

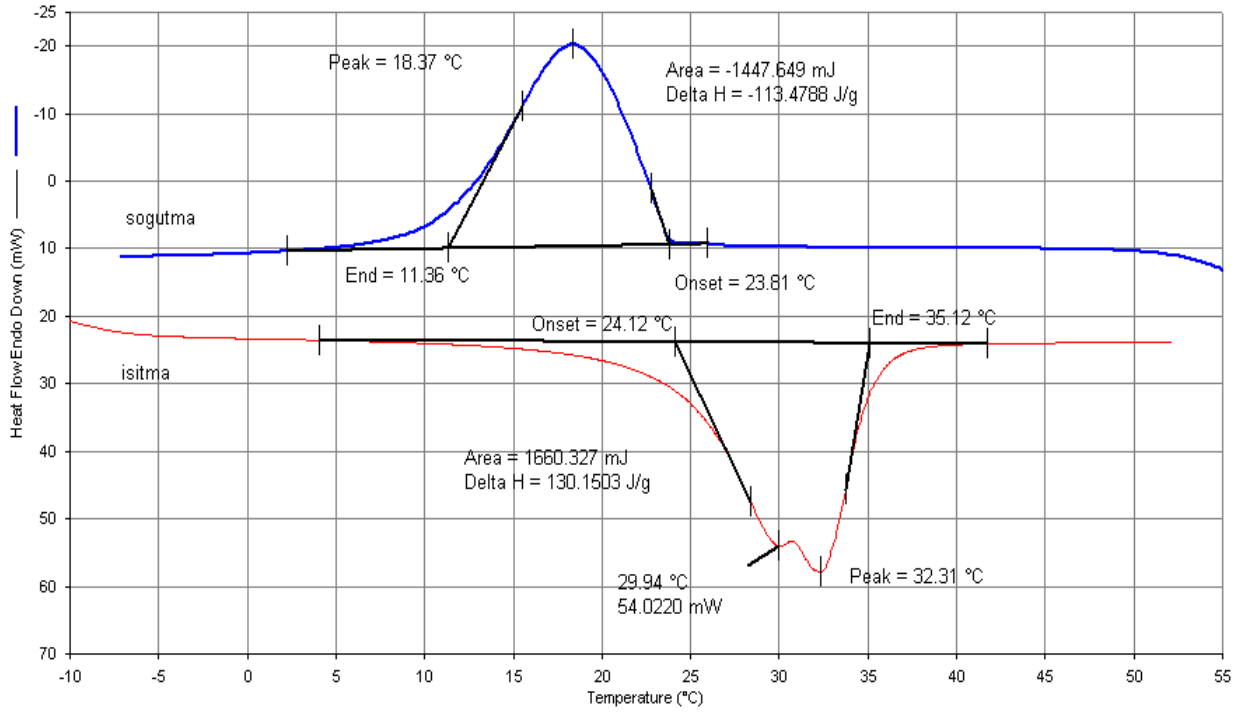

Figure 6.88 DSC test results for mixture of 6% mass concentration of CNT and 99% (pure) PCM

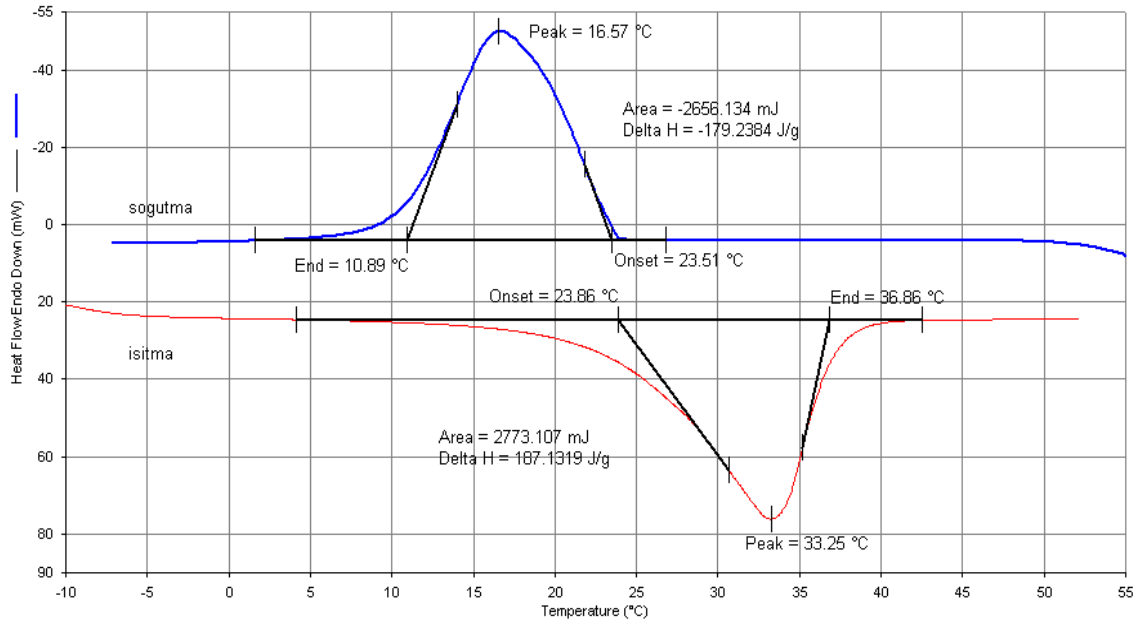

Figure 6.89 DSC test results for the mixture of 6% graphene platelets mixed with technical grade PCM

The slope is considered in general form as it can be seen from DSC diagrams for the samples. In general, it can be written in the following form:

$$\frac{d(\Delta P)}{dT} = \frac{C_1}{R} \tag{6.66}$$

where ΔP represents the differential power of calorimeter and R is the total thermal resistance.

$$R = R_1 + R_2 + R_s \tag{6.67}$$

Here, R_1 , R_2 and R_3 are thermal contact resistance between the sample and the sample furnace, the thermal contact resistance between the sample and the calibration substance and thermal resistance of the sample, respectively.

The device related resistance C_2 is defined as $C_2 = R_1 + R_2$

$$\frac{d(\Delta P)}{dT} = \frac{C_1}{R_1+R_2+R_3} = \frac{C_1}{C_2+R_s} \tag{6.68}$$

The thermal conductivity can be calculated from the following thermal contact resistance, R_s:

$$R_s = \frac{L_s}{k_s A_s} \tag{6.69}$$

where L_s , k_s , $and\ A_s$ are the height of the sample, thermal conductivity of the sample and a horizontal cross-section area; respectively.

Defining: $C_3 = \frac{L_s}{A_s}$ leads to

$$\frac{d(\Delta P)}{dT} = \frac{C_1}{C_2 + \frac{C_3}{k_s}} \tag{6.70}$$

$$\frac{C_3}{k_s} = \frac{C_1}{\frac{d(\Delta P)}{dT}} - C_2 \tag{6.71}$$

By arranging and re-writing the corresponding values for PCM and mixture of PCM and CNT

$$k_{s,PCM} = \frac{C_3 \frac{d(\Delta P)_{PCM}}{dT}}{C_1 - C_2 \frac{d(\Delta P)_{PCM}}{dT}} \tag{6.72}$$

$$k_{s,PCM+CNT} = k_{s,mix} = \frac{C_3 \frac{d(\Delta P)_{mix}}{dT}}{C_1 - C_2 \frac{d(\Delta P)_{mix}}{dT}} \tag{6.73}$$

The ratio of thermal conductivities is

$$k_{ratio} = \frac{\frac{d(\Delta P)_{mix}}{dT}}{\frac{d(\Delta P)_{PCM}}{dT}} . \frac{C_1 - C_2 d(\frac{(\Delta P)}{dT})_{PCM}}{C_1 - C_2 d(\frac{(\Delta P)}{dT})_{mix}} \tag{6.74}$$

It can be noticed that the following ratio is always greater than unit.

$$\frac{C_1 - C_2 d(\frac{\Delta P}{dT})_{PCM}}{C_1 - C_2 d(\frac{\Delta P}{dT})_{mix}} > 1 \tag{6.75}$$

If the terms C_1 and C_2 are considered, then, it can be observed that inequalities of 6.76 and 6.77 are always satisfied as explained below:

$$C_1 - C_2 d(\frac{\Delta P}{dT}) > 0 \tag{6.76}$$

$$(\frac{\Delta P}{dT})_{mix} > (\frac{\Delta P}{dT})_{PCM} \tag{6.77}$$

In order to have a positive thermal conductivity, inequality 6.77 should be positive. The second inequality is true because the results of the experiment also show that the slope of power to temperature for sample with CNT is higher than that for pure PCM and indicates that carbon additives will lead to higher thermal conductivity. These two, implies that the ratio will be positive. Based on the given calculations, the ratio of effective thermal conductivity of 99% CNT to technical grade (90.8%) octadecane is shown in Figure 6.90.

Comparing 6% mass concentration CNT mixed with PCM and the same concentration of graphene platelet mixed with PCM is shown in Figure 6.91. It should be noticed that the values needs modification in terms of multiplication in a coefficient. As it was mentioned, this coefficient is a positive number and greater than one. This means that even if the ratio become near 1, after multiplication by this coefficient, it will be improved.

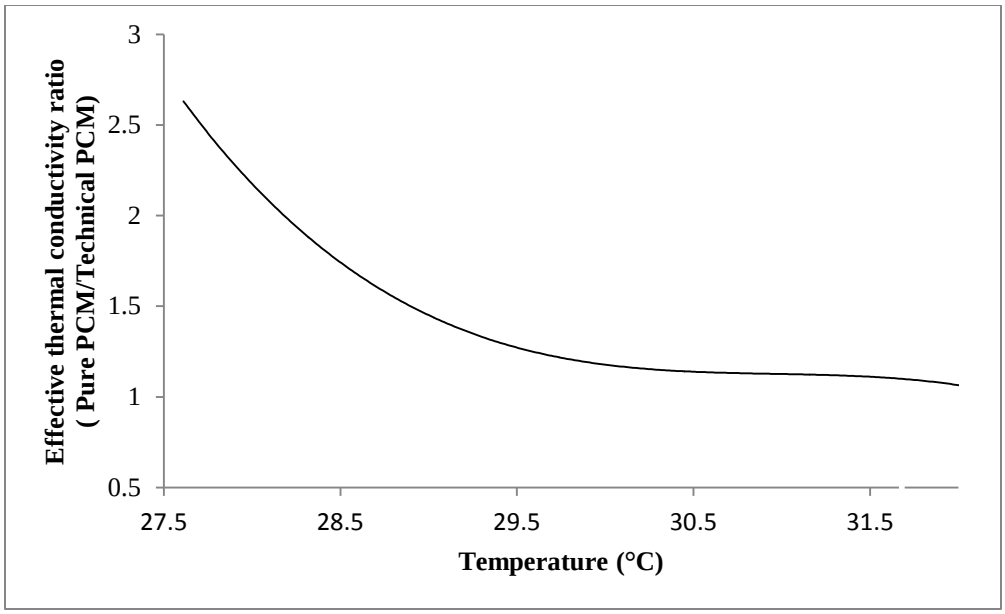

Figure 6.90 Ratio of effective thermal conductivity of 99% CNT to technical grade (90.8%) octadecane

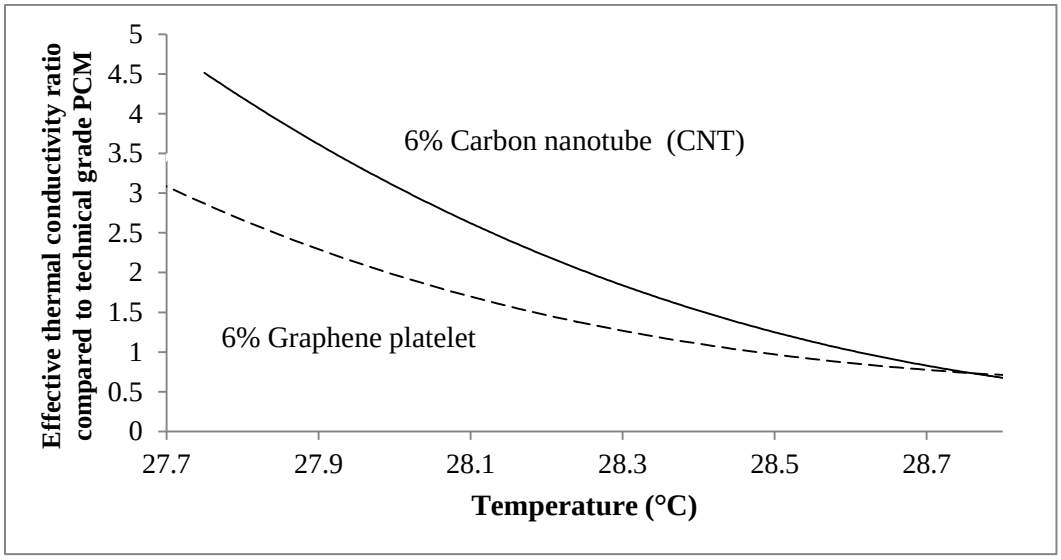

Figure 6.91 Comparing CNT and Platelets of graphene effective thermal conductivity

Dependency of this coefficient to other parameters is an important concept. It is worth to mention that the ratios for other temperatures are not shown in Figure 6.91, since this ratio is for phase change region. Therefore, for the solid part, which is expected to have higher thermal conductivity due to CNT presence, other methods are used. Figure 6.91 also shows that the thermal conductivity of CNT is around 1.6 higher than graphene platelets at T= 27.9 °C.

Secondly, the thermal conductivity can be up to 5 times greater than that for technical PCM, as the test results show.

6.4.2 Results for pure and technical grade PCM used in LHTES

The error related to temperature measurements is in the order of 5 %. The data are recorded for 5 hours and even more for the pure PCM. Massive data is recorded which are used to draw Figure 6.92. The uncertainty analysis should be done, once working with measurement numbers. Two items that should be noticed in this regards are

- Precision uncertainty
- Bios uncertainty

The first one relates to precision of the available apparatus and data acquisition systems. The second one is about the meaningful digits in the calculations. This is more obvious source of error generation, when there is calculations which involve with small numbers due to subtracting of two small numbers. As an example, in the ANSYS FLUENT calculations, the convergence criteria should be satisfied which can be of order -12. In these cases, the bios uncertainty will play a role. In the conducted calculations and data acquisition, these aspects are tried to be taken into account. Temperature at 3 points away from the copper tube is shown in Figure 6.92. The melting process in the PCM zone is obvious from this figure. A rake is put at T= 27.45 ℃ . This temperature is selected based on information for technical grade PCM. Based on Figure 6.92, it takes 20 minutes in order to reach the temperature of 27.45℃. Since the distance is 3 mm, therefore the velocity is defined

$V = X/t = 0.15$ mm/min.

The melting front velocity is used to calculate the transient exergy in the heat exchanger. By increasing the elapsed time, the temperature of the PCM, becomes identical to the inlet temperature due to sensible heat capacity of the PCM (Figure 6.93). From this Figure, the quasi steady-state time also can be found.

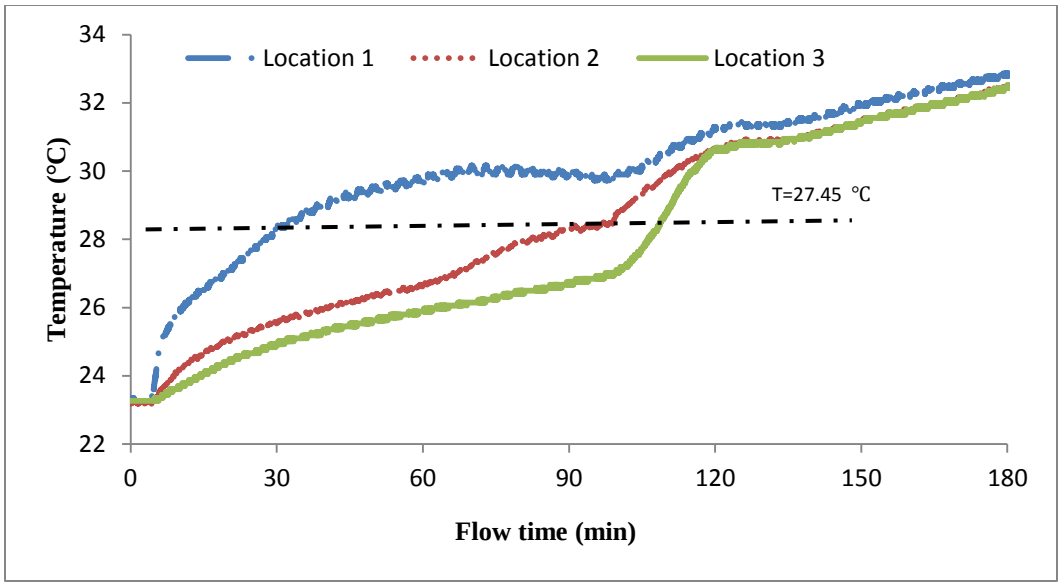

Figure 6.92 Temperature profile at points 1, 2 and 3 that are located 3, 6 and 9 mm away from copper tube outer surface.

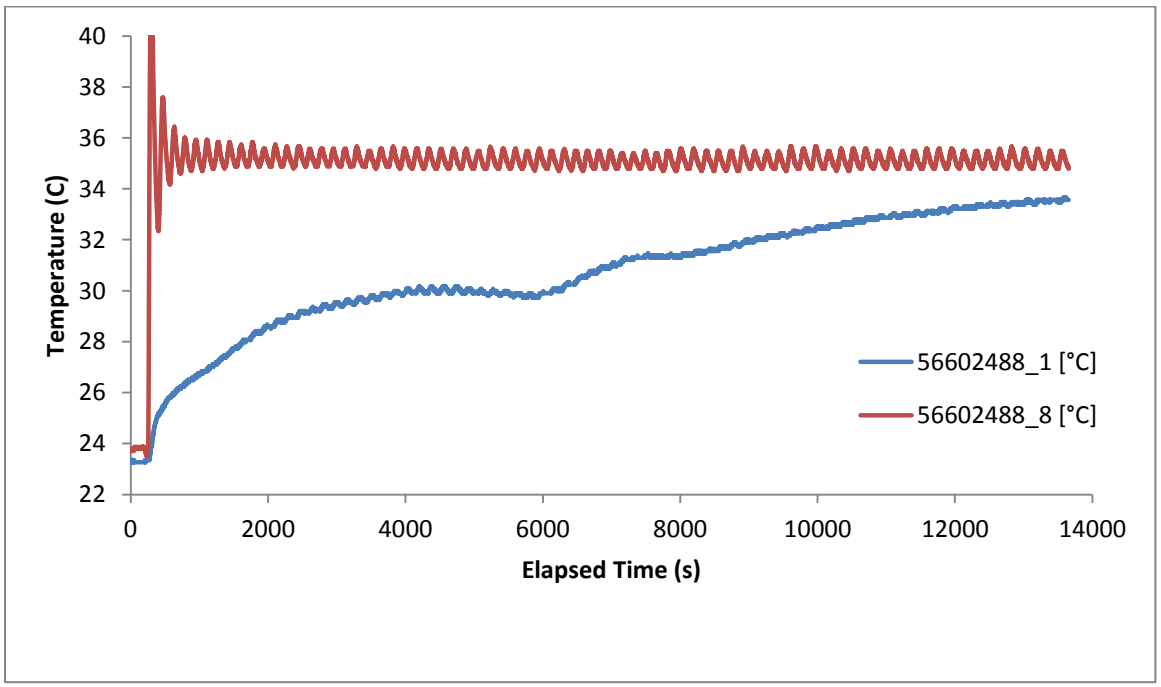

Figure 6.93 Temperature of entering flow (T_8) and PCM temperature 3mm away from the tube.

Data for the case of pure PCM (99% purity)

Temperature in different locations in the pure PCM is shown in Figure 6.94. The time starts from the moment that hot water enters to the heat exchanger.

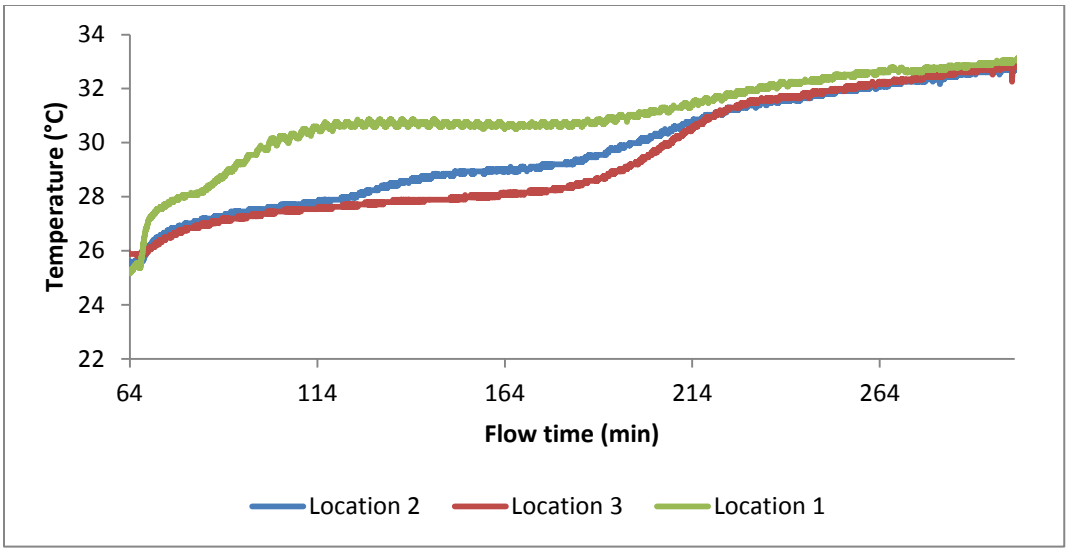

Figure 6.94 Temperature in locations 1, 2 and 3 in the case of pure PCM

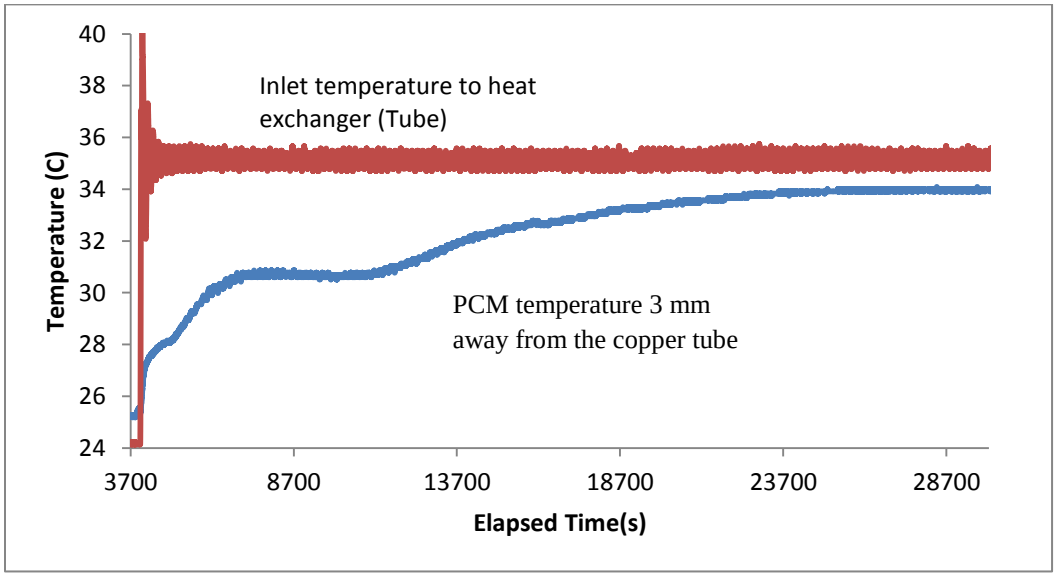

Figure 6.95 Temperature increase in the pure PCM compared to the inlet temperature.

In case of pure n-octadecane, phase changing process takes shorter time than that for technical grade PCM. The trend of pure PCM can be seen in Figure 6.102. The pure PCM behaves differently in melting process. While the technical grade (Figure 6.92) takes longer to absorb, the pure PCM shows sharper increase. This can also indicate that melting effect of the pure PCM and interaction of neighborhood tubes carrying the hot flow is faster than the case for technical grade. The experimental results presented in this thesis, also shows higher thermal conductivity for pure PCM compared to technical PCM (Figure 6.95).

6.4.3 Transmission and reflection optical microscopy studies of PCM and nanoparticle mixture

In order to get better understanding of the CNT configuration in the PCM mixture, the optical microscopic method is implemented. Furthermore, transmission optical microscopy is carried out in order to study the samples. This is a type of light microscopy where the lights pass through the source and then incidence onto the lens. Optics properties of PCM and mixture along with their morphological characteristics are obtained through this method. CNT and graphene platelets mixed with pure and technical grade PCM, are prepared and studied.

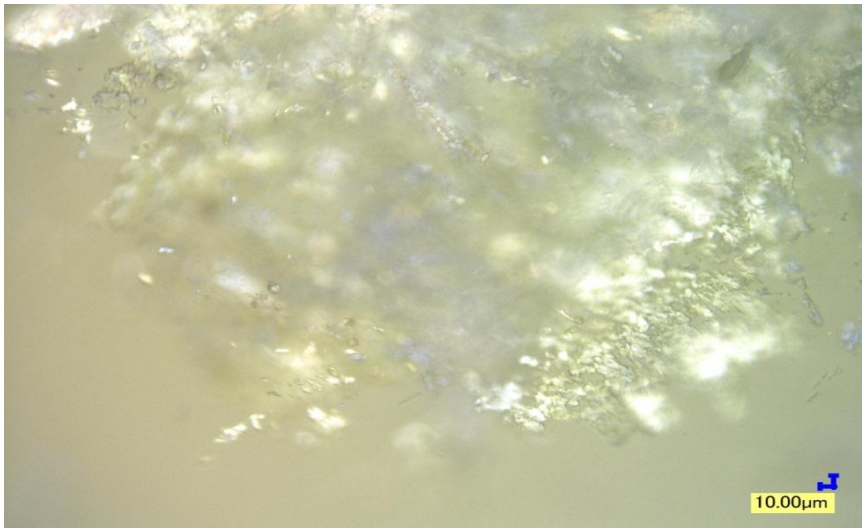

Figure 6.96 Optical image of pure PCM

Figure 6.96 shows optical image of pure PCM (99 % purity). Prior to melting, Structural morphology demonstrates granulated and smooth surfaces. The granulated part is formed during the solidification at a high cooling rate, which indicates the initial solidification region in the PCM. It should be noted that initial temperature difference in the PCM should be sufficiently high to initiate the solidification process in line with the solidification characteristic [170].

Figure 6.97 shows optical micrograph of technical grade PCM in solid phase. The surface morphology dictates the presence of irregular structure, closely situated at the surface. The distinguishing feature appears to be the boundaries in the heterogeneous structure.

These boundaries can act as thermal boundary resistance suppressing the heat flow across the structure similar to grain boundaries in solids. Therefore, the melting initiation and competition is longer than that of the case observed for pure PCM. This can also be observed from the differential scanning calorimeter graphs as discussed earlier in this chapter.

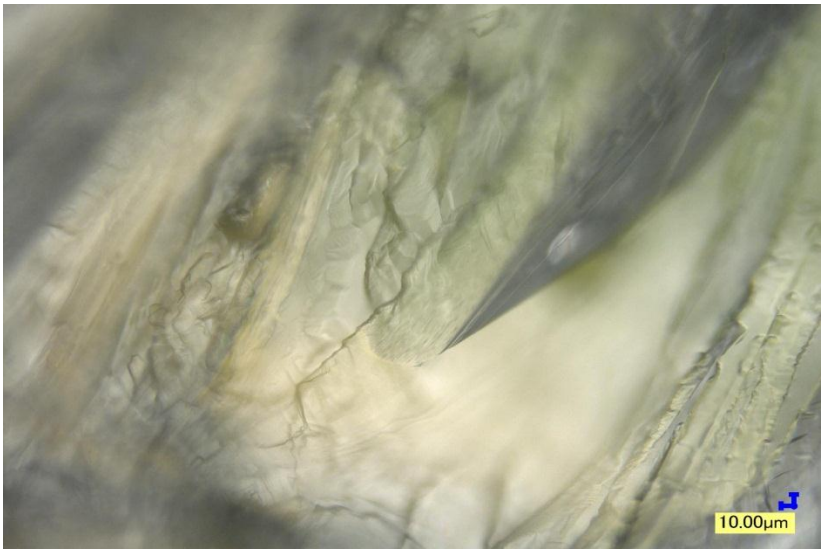

Figure 6.97 Structure of technical grade PCM with x500 magnification using optical microscope

Figure 6.98 shows optical image of 1.25% of CNT and pure PCM mixture onset of melting. The morphology of the structure reveals the minor and local scattered agglomeration of carbon nanotubes. The coverage area of agglomeration is only a small fraction of total are, shown in Figure 6.98. Agglomerated CNT appears to be dark inclusions with round appearance as it can be seen from the Figure. It should be noted that the maximum magnification of the lens used in the optical microscope is not capable of capturing the images of the nano sized particles, such as nano particles. The image presented has the resolution of 10 micrometer per o.5 cm on the captured picture. This only allows observing the agglomerated nano carbon tubes or graphine pellets on the image. Figure 6.99a shows 3% CNT and pure PCM mixture. The morphology of the image shows locally agglomerated CNT with circular appearance at the surface. In addition, partially dissolved solid structure is also visible in the photographic image. The size of CNT agglomerations is different at the surface.

However for all sizes, spacing between inclusions is not close enough to merge forming a large size clustered CNT regions in the PCM. The morphology in Figure 6.99b indicates small size and large number of agglomerated platelets at the solid surface. This Figure shows a 1.25% of graphene platelet and technical PCM mixture. The presence of small size agglomeration is associated with the small Van der Waals and other small forces such as surface tension forces. However their increased number in the PCM is expected to improve the thermal conductivity.

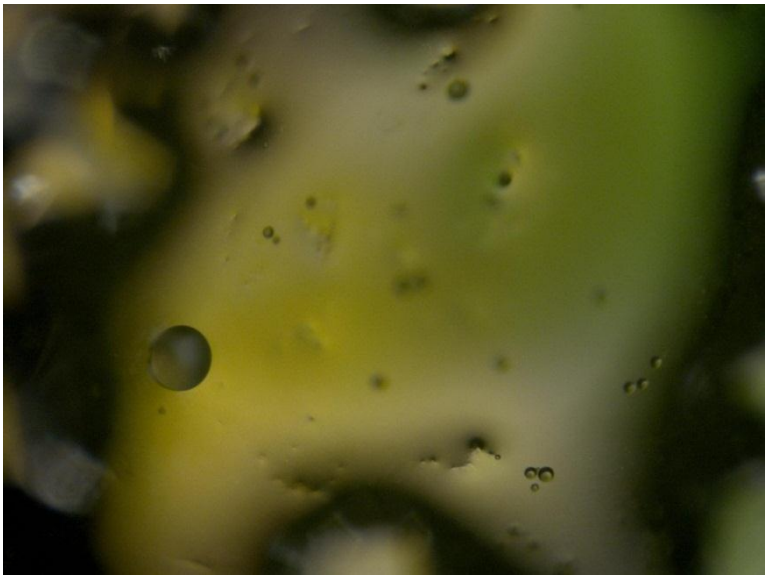

Figure 6.98 Optical image of 1.25% CNT and pure PCM mixture

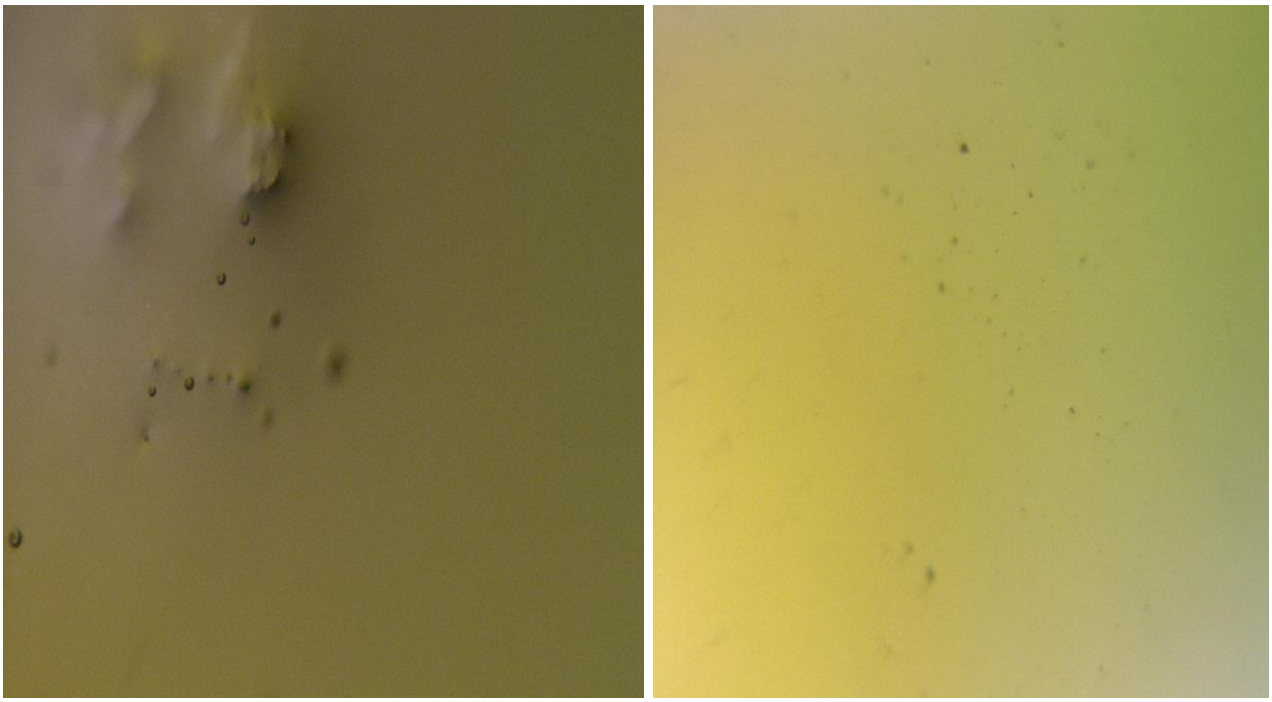

(a) (b)

Figure 6.99 a) Optical image of 3% CNT and pure PCM mixture b)Graphene platelets with 1.25% mass fraction mixed with technical PCM

Figure 6.100 shows 6% of CNT and pure PCM mixture onset of melting. The radiation source is provided to melt the PCM during the microphotography. Since the absorption

characteristic of CNT and PCM are different for the incident radiation, the topology of the image shows fine hilly like structures. In this case, the volume concentration of the CNT is high and agglomerated size of the CNT becomes large.

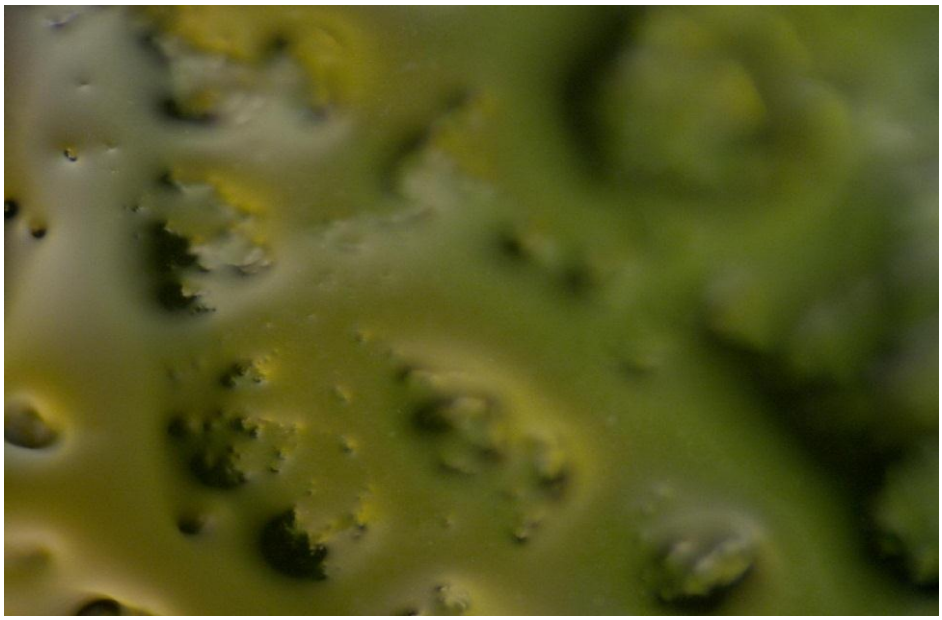

Figure 6.100 Optical image of 6% CNT and pure PCM mixture

This, in turn, absorbs more radiation and generates more heat in these regions than that corresponding to the PCM. Consequently, the local melting where the PCM concentration is high forms the valley-like structure in the topology. Nevertheless, this structure is scattered without interconnecting at the surface, while indicating no total merging of agglomerated CNT sites.

Figure 6.101 shows transmission optical image of 1.25 % of CNT and pure PCM when it is partially melted. The melted regions appear to be bright color due to higher transmittance characteristics of molten PCM than solid PCM because of incident radiation emanating from optical microscope. The image shows the convection current forming streamline flow characteristics in the molten phase. This shows feather like appearance in the bright region of the image.

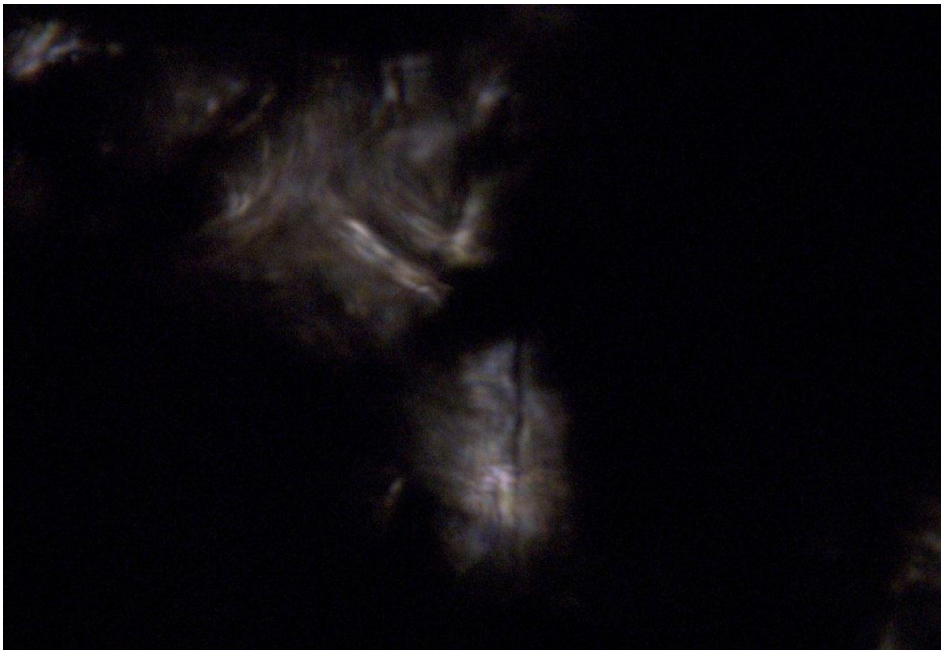

Figure 6.101 Transmission optical image of the 1.25% CNT and pure PCM mixture.

The convection current is formed because of temperature and density variations in the molten phase of PCM. It is also possible that melted PCM (n-octadecane) molecules can enter into the nanotube while modifying the buoyancy forces. The molecular diameter (length of the molecular chain) is in the order of 1 nm [171] which is smaller than the carbon nanotube (CNT) inner diameter (10 nm -30 nm). The reduced buoyancy force facilitates CNT participating in convection current. This enhances the optical image where the convection current is developed. Moreover, streamlined flow enhances the concentration of CNT in this region which further increases the absorption of incidence radiation emanating from the optical microscope. Hence, temperature variations in this region further enhances the convection current intensity. Figure 6.102 shows transmission image of 6% CNT and pure PCM for partially molten mixture. The image consists of dark and bright regions. Dark regions represent solid while bright regions corresponds to liquid phases.in the bright region, there appears to be scattered patterns of radiation emitted from the microscope.

Figure 6.102 Transmission optical image of 6 % CNT and pure PCM mixture.

The scattered pattern is circular and its origin is associated with the presence of CNT agglomeration sites. Concentrated CNT regions undergo early melting because of high rate of absorption of incident radiation, emanating from the microscope. These regions melt sooner, therefore, the dark regions in neighbourhood of bright region indicates the presence of less concentration of CNT sites. This behaviour inherently indicates that high concentration of CNT causes: i) reduction in the latent heat of melting, and ii) enhancement of the thermal conductivity. Figure 6.104 shows the effect of stainless steel mesh with 20 μm mesh size. Observations show that he mesh decreases the convection flow of the graphene platelets and CNTs. The agglomerated mass of nanoparticles are seen, beneath the mesh in Figure 6.103.

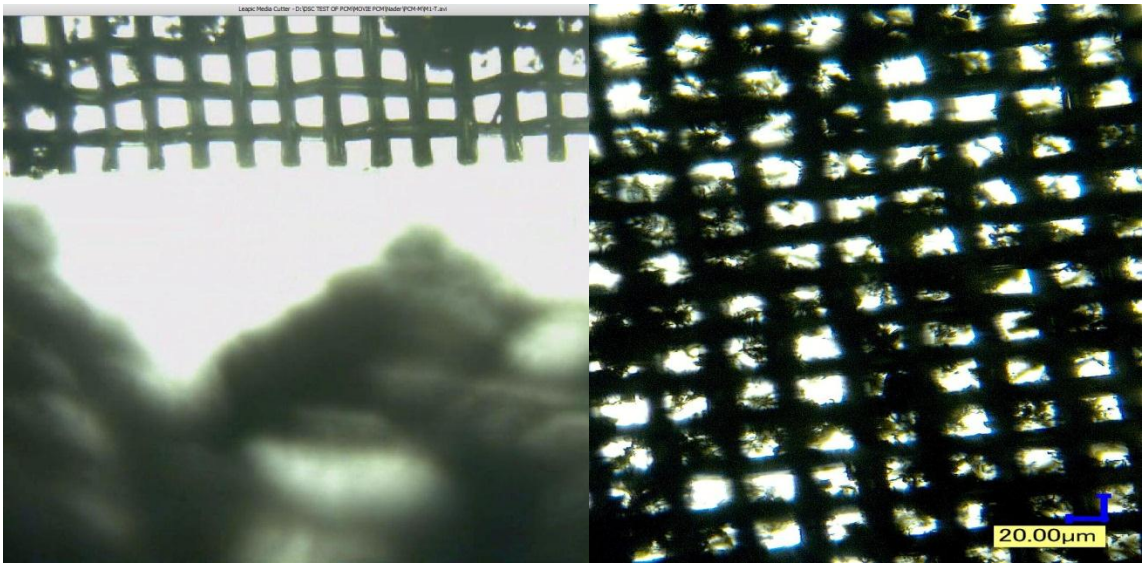

Figure 6.103 Effect of metal micro-mesh on agglomeration of nano-particles

Chapter 7 Conclusions and Recommendations

In this chapter, the main concluding remarks are presented, and some recommendations are made for future studies in the field.

7.1 Conclusions

In this thesis, the specific options for using phase change materials (PCMs) for passive thermal management systems (TMSs) are studied. Two main requirements for any TMS in the battery pack of a hybrid electric vehicle (HEV) are the ability to minimize the peak temperature and to prevent temperature gradients. The goal of using PCM in cooling systems is to lessen the reliance on the active refrigeration cooling cycle which currently predominates. This will lead to overall improvements in vehicle efficiency.

The first part of the study includes numerical simulation of the system with ANSYS FLUENT version 12.0.1. Three options are considered in the simulations: PCM is introduced around the Li-ion battery with test thicknesses of 3, 6, 9 and 12 mm. Then, a sub-module consisting of four Li-ion cells is modeled with PCM applied around it. Furthermore, the separating foams in the battery pack are replaced by foam soaked in the PCM and placed between cells. Temperature variations and distribution are calculated and compared.

The second part of the study deals with design and optimization of latent heat thermal energy storage systems (LHTES) to be integrated in parallel with the current active TMS of HEVs. Due to volume restriction in the vehicle, the heat exchanger length is taken as the objective function and a genetic algorithm is applied to find its optimum values. Also of concern is that the PCM in the shell side has low thermal conductivity (0.152 W/mk). In order to overcome this issue, carbon nano-tubes (CNT) and graphene nano-platelets are added to the pure and technical grade octadecane to improve the thermal conductivity of the mixture. Optical microscopic methods are implemented to study the PCM and nano-particles mixture, specifically to monitor the agglomeration of nanoparticles. Transmission and reflection optical microscopy methods are carried out in order to study the prepared samples. Furthermore, CNT and graphene platelets mixed with pure and technical grade PCM, are studied through differential scanning calorimetry (DSC) in order to compare the thermal conductivity of the mixtures.

In the experimental investigation, a test bench is established to conduct the trials. The test bench represents the cooling system of the vehicle, and is instrumented with temperature sensors, pressure gauges and flow meters before and after the storage system. In order to verify the numerical results, temperature variations in the four-cell Li-ion sub-module cells are measured. Experimental results confirm the cooling effect of the PCM holders in between the cells in the sub-module.

Furthermore, thermodynamic analysis of the considered thermal management is investigated. The exergy analysis is carried out by using EES software. The storage system is used in parallel with the chiller in a conventional vapour compression refrigeration cycle. The results of multi-objective optimization provide good insight into the system. Two objective functions are considered: exergy efficiency of the system (to be maximized) and total cost rate of the system (to be minimized). A developed genetic algorithm code is used to find the best optimal point of the multi-objective optimization. In the economic consideration of the study, the investment cost rates are calculated with respect to equipment costs and capital recovery factors. Subsequently, by combining it with previously conducted exergy analysis, an exergoeconomic analysis is conducted.

The main findings of this study are summarized as follows:

- When the PCM is applied in a 3 mm thickness around the Li-ion cell, the temperature distribution becomes 10% more uniform. Results show that phase change material with 12 mm thickness decreases the maximum temperature by 3.04 K. The corresponding value for thinner layers of 3 mm, 6 mm and 9 mm are 2.77 K, 2.89 K and 2.98 K, respectively. The results are calculated for the time of 20 minutes in transient conditions.
- For the sub-module with PCM around it, more than a 7.7 K decrease in volume-average temperature occurs. Difference between the maximum and minimum temperatures in the sub-module with PCM around it are decreased 0.17 K, 0.68 K, 5.80 K and 13.33 K for the volumetric heat generation rates of 6.885, 22.8, 63.97 and 200 kW/m^3, respectively.
- Experimental study of five different foams shows that the maximum mass concentration of PCM possible in this medium is 65.8%.

- Maximum temperature of the sub-module with dry foams decreases from 310.87 K to 303.13 K when PCM is applied in the foam in between the cell. Moreover, the critical cell shows reduced temperature variation (9% less temperature excursion).
- The numerical results on temperature distribution of cells in the sub-module are found to be in accordance with experimentally measured data in both cases with and without PCM.
- Contact resistance in the cell and connectors boundary is 7.8×10^{-6} m^2K/W, which is smaller than air film resistance by an order of 10^{-4} and therefore is not considered in simulations. This is mainly due to the high temperature gradients in the direction of heat transfer.
- The application of finned tubes to the latent heat thermal storage gives 41.1 cm for the length of the heat exchanger, which is larger than the 22.9 cm required for bared copper tubes due to more heat transfer resistance and specific geometrical constraint.
- Smaller tube diameters minimize the heat exchanger length. For 3/8 inch copper tube, the optimized length and diameter are 32.1 cm and 26.7 cm respectively. The corresponding values for the 3/16 inch copper tube are 20.8 cm and 17.5 cm. Regarding the pressure drop, the calculation gives less than 2 kPa pressure drops for a 5/16 inch diameter tube, which is selected as the optimum diameter for manufacturing purposes. The obtained pressure drop is not beyond the pump power in the loop.
- The agglomeration effect can be challenging in practical applications. Using a micro-mesh reduces CNT agglomeration in the mixture by reducing the convection in the melting process.
- In phase changing processes, the ratio of total heat (sensible and latent heat) to the latent heat of fusion is used for calculating the heat exchanger length. The new parameter takes into account the sub-cooled heat; therefore it is used instead of the Stefan number, which is the ratio of sensible superheat energy to latent heat.
- The optical observations of technical PCMs show boundaries in their structure. These boundaries can act as a source of thermal boundary resistance, suppressing the heat flow across the structure similar to grain boundaries in solids.
- A high concentration of CNTs (6%) increases the thermal conductivity of the mixture. The effective thermal conductivity of a CNT and pure PCM mixture is 4 times higher

compared to a mixture with technical grade octadecane. At the same time, this concentration decreases the latent heat of the mixture by 6%.

- An increase in PCM mass fraction from 65% to 80% will increase the COP and exergetic efficiency of the system from 2.78 to 2.85 and from 19.9% to 21%, respectively.
- An increase of 15% in PCM mass fraction (from 60% to 75%) results in a compressor work decrease of 25 Watts.
- An increase in heat exchanger pinch point temperature from 2.5 K to 4.5 K decreases the exergy efficiency of the system from 21.5% to 20.9%. This is due to the fact that the higher the pinch point temperature, the lower the energy being utilized in the heat exchanger, which leads to a reduction of the PCM cooling load of the system. Also, an increase in evaporator temperature and condenser temperature results in a decrease in system exergy efficiency and an increase in total exergy destruction rate.
- A 5.04% increase in exergy efficiency is calculated when the PCM is used compared to no PCM. At the same time, the total cost rate increases 12.42% when PCM is used.
- The thermal expansion valve and pump have higher exergy efficiencies of 87% (similar to the case without the PCM tank), while the evaporator, condenser and chiller feature lower efficiencies (21%). The lower efficiency can potentially be improved by reducing the mean temperature difference between the working fluids.
- Finding the final optimum solution among the optimum points in the Pareto front using the LINMAP method yields an exergy efficiency and total cost rate of 0.3351 and 1.529 $/hr for this point, respectively.

7.2 Recommendations

The main recommendations for future studies are summarized as follows:

- For simulation purposes, the whole battery pack should be simulated and a whole picture of the temperature in different locations needs to be obtained under different operational conditions.
- The discharging period of PCMs (solidification period) releases the stored heat in the melting process. This period should be simulated for heating the battery pack in the winter season.

- For experimental study, user defined functions (UDF) should be introduced to ANSYS/FLUENT software to simulate the local volumetric heat generation rates in the cell zone.
- For simulation and experimental studies, different PCMs, particularly eutectics, should be selected and tested.
- Cooling jackets of PCM should be added to outer surfaces of the battery pack, as vehicle space allows. Temperature gradients must be measured experimentally to assess the effect of the PCM.
- In PCM and nano-particle mixtures, the alignment of CNTs or nano-platelets should be in the same direction as heat transfer. The possibility of aligning functionalized CNTs using magnetic fields warrants investigation. Thermal conductivity should be studied for different configurations.
- New technologies such as heat pipes or thermoelectric units should be investigated for extracting the heat out of the melted PCM and accelerating the solidification time of the latent heat storage system.
- An optimized helical heat exchanger should be manufactured and experimental and numerical results should be compared with those of straight tube heat exchangers.
- Life cycle assessment (LCA) should be conducted for the TMSs with PCM and results compared with those without PCM with the aim of assessing associated environmental impact.
- Advanced exergy analysis for the TMS should be useful to further study the performance and potential improvements.

References

[1] Rosen, M. A., Dincer, I., and Kanoglu, M., 2008, "Role of Exergy in Increasing Efficiency and Sustainability and Reducing Environmental Impact," Energy Policy, 36, pp. 128-137.

[2] Wang, Q., Yuan, X., Zhang, J., Mu, R., Yang, H., and Ma, C., 2013, "Key Evaluation Framework for the Impacts of Urbanization on Air Environment–a Case Study," Ecological Indicators, 24, pp. 266-272.

[3] Geelen, L. M., Huijbregts, M. A., Jans, H. W., Ragas, A. M., Den Hollander, H. A., and Aben, J. M., 2013, "Comparing the Impact of Fine Particulate Matter Emissions from Industrial Facilities and Transport on the Real Age of a Local Community," Atmospheric Environment, pp. 138-144.

[4] Høyer, K. G., 2008, "The History of Alternative Fuels in Transportation: The Case of Electric and Hybrid Cars," Utilities Policy, 16, pp. 63-71.

[5] Suganthi, L., and Samuel, A. A., 2012, "Energy Models for Demand Forecasting—a Review," Renewable and Sustainable Energy Reviews, 16, pp. 1223-1240.

[6] Rosen, M. A., 2009, "Energy Sustainability: A Pragmatic Approach and Illustrations," Sustainability, 1, pp. 55-80.

[7] Gordon, D., and Burwell, D., 2013, Transport Beyond Oil, Springer, The Role of Transportation in Climate Disruption1.

[8] Park, S., Kim, Y., and Chang, N., 2013, "Hybrid Energy Storage Systems and Battery Management for Electric Vehicles," Proceedings of the 50th Annual Design Automation Conference, pp. 97.

[9] Van Mierlo, J., Van Den Bossche, P., and Maggetto, G., 2004, "Models of Energy Sources for Ev and Hev: Fuel Cells, Batteries, Ultracapacitors, Flywheels and Engine-Generators," Journal of power sources, 128, pp. 76-89.

[10] Sharma, A., Tyagi, V., Chen, C., and Buddhi, D., 2009, "Review on Thermal Energy Storage with Phase Change Materials and Applications," Renewable and Sustainable energy reviews, 13, pp. 318-345.

[11] Kristoffersen, T. K., Capion, K., and Meibom, P., 2011, "Optimal Charging of Electric Drive Vehicles in a Market Environment," Applied Energy, 88, pp. 1940-1948.

[12] Conte, F., 2006, "Battery and Battery Management for Hybrid Electric Vehicles: A Review," e & i Elektrotechnik und Informationstechnik, 123, pp. 424-431.

[13] Kampman , B., Leguijt, C., Bennink, D., Wielders, L., Rijkee, X., Buck, A. D., and Braat , W., 2010, "Green Power for Electric Cars–Development of Policy Recommendations to Harvest the Potential of Electric Vehicles," Technical Report No. CE Delft, Delft.

[14] Streimikiene, D., Baležentis, T., and Baležentienė, L., 2013, "Comparative Assessment of Road Transport Technologies," Renewable and Sustainable Energy Reviews, 20, pp. 611-618.

[15] Halford, B., 2013, Preventing Battery Fires, August 2013, http://cen.acs.org/articles/91/i15/Preventing-Battery-Fires.html.

[16] Tang, Z. J., Zhu, Q. Z., Lu, J. W., and Wu, M. Y., 2013, "Study on Various Types of Cooling Techniques Applied to Power Battery Thermal Management Systems," Advanced Materials Research, 608, pp. 1571-1576.

[17] Fan, L., Khodadadi, J., and Pesaran, A., 2013, "A Parametric Study on Thermal Management of an Air-Cooled Lithium-Ion Battery Module for Plug-in Hybrid Electric Vehicles," Journal of Power Sources, 238, pp. 301-312.

[18] Shiau, C.-S. N., Samaras, C., Hauffe, R., and Michalek, J. J., 2009, "Impact of Battery Weight and Charging Patterns on the Economic and Environmental Benefits of Plug-in Hybrid Vehicles," Energy Policy, 37, pp. 2653-2663.

[19] Chau, K., and Wong, Y., 2002, "Overview of Power Management in Hybrid Electric Vehicles," Energy Conversion and Management, 43, pp. 1953-1968.

[20] Nelson, P., Dees, D., Amine, K., and Henriksen, G., 2002, "Modeling Thermal Management of Lithium-Ion Pngv Batteries," Journal of power sources, 110, pp. 349-356.

[21] Yap, W., and Karri, V., 2010, "Performance Simulation and Predictive Model for a Multi-Mode Parallel Hybrid Electric Scooter Drive," International Journal of Energy Research, 34, pp. 67-83.

[22] Gutmann, G., 1999, "Hybrid Electric Vehicles and Electrochemical Storage Systems-a Technology Push–Pull Couple," Journal of power sources, 84, pp. 275-279.

[23] Khateeb, S. A., Farid, M. M., Selman, J. R., and Al-Hallaj, S., 2004, "Design and Simulation of a Lithium-Ion Battery with a Phase Change Material Thermal Management System for an Electric Scooter," Journal of Power Sources, 128, pp. 292-307.

[24] Shukla, A., Venugopalan, S., and Hariprakash, B., 2001, "Nickel-Based Rechargeable Batteries," Journal of Power Sources, 100, pp. 125-148.

[25] Fthenakis, V., 2009, "Sustainability of Photovoltaics: The Case for Thin-Film Solar Cells," Renewable and Sustainable Energy Reviews, 13, pp. 2746-2750.

[26] Kitoh, K., and Nemoto, H., 1999, "100 Wh Large Size Li-Ion Batteries and Safety Tests," Journal of power sources, 81, pp. 887-890.

[27] Al Hallaj, S., Maleki, H., Hong, J., and Selman, J., 1999, "Thermal Modeling and Design Considerations of Lithium-Ion Batteries," Journal of power sources, 83, pp. 1-8.

[28] Lahiri, I., and Choi, W., 2013, "Carbon Nanostructures in Lithium Ion Batteries: Past, Present, and Future," Critical Reviews in Solid State and Materials Sciences, 38, pp. 128-166.

[29] Chan, C. C., and Chau, K., 2001, *Modern Electric Vehicle Technology*, Oxford University Press.,

[30] Gerssen-Gondelach, S. J., and Faaij, A. P., 2012, "Performance of Batteries for Electric Vehicles on Short and Longer Term," Journal of power sources, 212, pp. 111-129.

[31] Nelson, R. F., 2000, "Power Requirements for Batteries in Hybrid Electric Vehicles," Journal of power sources, 91, pp. 2-26.

[32] Patil, P. G., 2008, "Developments in Lithium-Ion Battery Technology in the Peoples Republic of China," Technical Report No. Argonne National Laboratory (ANL).

[33] Matheys, J., Timmermans, J.-M., Van Mierlo, J., and Meyer, S., 2009, "Comparison of the Environmental Impact of Five Electric Vehicle Battery Technologies Using Lca," International Journal of Sustainable Manufacturing, 1, pp. 318-329.

[34] Duvall, M. S., 2005, "Battery Evaluation for Plug-in Hybrid Electric Vehicles," Vehicle Power and Propulsion, pp. 338-343.

[35] Howell, D., 2007, "Electrical Energy Storage. Plug-in Hybrid Electric Vehicle Battery Research and Development Activities," Technical Report No. US Department of Energy PHEV Stakeholder Workshop, Washington DC (June 13, 2007), DOE.

[36] Pesaran, A. A., Burch, S., and Keyser, M., 1999, "An Approach for Designing Thermal Management Systems for Electric and Hybrid Vehicle Battery Packs," Proceedings of the 4th Vehicle Thermal Management Systems, pp. 24-27.

[37] Chen, Y., and Evans, J. W., 1996, "Thermal Analysis of Lithium-Ion Batteries," Journal of the Electrochemical Society, 143, pp. 2708-2712.

[38] Al-Hallaj, S., and Selman, J., 2002, "Thermal Modeling of Secondary Lithium Batteries for Electric Vehicle/Hybrid Electric Vehicle Applications," Journal of power sources, 110, pp. 341-348.

[39] Wang, Q., Ping, P., Zhao, X., Chu, G., Sun, J., and Chen, C., 2012, "Thermal Runaway Caused Fire and Explosion of Lithium Ion Battery," Journal of power sources, 208, pp. 210-224.

[40] Mahamud, R., and Park, C., 2011, "Reciprocating Air Flow for Li-Ion Battery Thermal Management to Improve Temperature Uniformity," Journal of Power Sources, 196, pp. 5685-5696.

[41] Kuper, C., Hoh, M., Houchin-Miller, G., and Fuhr, J., 2009, "Thermal Management of Hybrid Vehicle Battery Systems," EVS24, Stavanger, Norway, pp. 1-10.

[42] Pesaran, A. A., Kim, G.-H., and Keyser, M., 2009, "Integration Issues of Cells into Battery Packs for Plug-in and Hybrid Electric Vehicles," 24th International Batterie, Hybrid and Fuel Cell Electric Vehicle Symposium (EVS24), Stavanger, pp.

[43] Gm-Volt, 2010, The Chevrolet Volt Cooling/Heating Systems Explained, August 2013, http://gm-volt.com/2010/12/09/the-chevrolet-volt-coolingheating-systems-explained.

[44] Lamonica, M., 2009, Gm: Chevy Volt Battery Tech on Track, http://news.cnet.com/8301-11128_3-10199252-54.html.

[45] Al-Hallaj, S., Kizilel, R., Lateef, A., Sabbah, R., Farid, M., and Selman, J. R., 2005, "Passive Thermal Management Using Phase Change Material for Ev and Hev Li-Ion Batteries," Vehicle Power and Propulsion, 2005 IEEE Conference, pp. 0-7803-9280-9.

[46] Dennis, K., 1995, "Phase Change Materials & Heat Pump Analysis for an Electric Vehicle, Department of Mechanical Engineering," Technical Report No. Lakehead University

[47] Abhat, A., 1983, "Low Temperature Latent Heat Thermal Energy Storage: Heat Storage Materials," Solar energy, 30, pp. 313-332.

[48] Jegadheeswaran, S., and Pohekar, S. D., 2009, "Performance Enhancement in Latent Heat Thermal Storage System: A Review," Renewable and Sustainable Energy Reviews, 13, pp. 2225-2244.

[49] Jegadheeswaran, S., Pohekar, S., and Kousksou, T., 2010, "Exergy Based Performance Evaluation of Latent Heat Thermal Storage System: A Review," Renewable and Sustainable Energy Reviews, 14, pp. 2580-2595.

[50] Sharma, S., and Sagara, K., 2005, "Latent Heat Storage Materials and Systems: A Review," International Journal of Green Energy, 2, pp. 1-56.

[51] Iijima, S., 1991, "Helical Microtubules of Graphitic Carbon," nature, 354, pp. 56-58.

[52] Aqel, A., El-Nour, K. M., Ammar, R. A., and Al-Warthan, A., 2012, "Carbon Nanotubes, Science and Technology Part (I) Structure, Synthesis and Characterisation," Arabian Journal of Chemistry, 5, pp. 1-23.

[53] Xu, J., and Fisher, T. S., 2006, "Enhancement of Thermal Interface Materials with Carbon Nanotube Arrays," International Journal of Heat and Mass Transfer, 49, pp. 1658-1666.

[54] Xu, Y., Zhang, Y., Suhir, E., and Wang, X., 2006, "Thermal Properties of Carbon Nanotube Array Used for Integrated Circuit Cooling," Journal of Applied Physics, 100, pp. 074302-074302-5.

[55] Reilly, R. M., 2007, "Carbon Nanotubes: Potential Benefits and Risks of Nanotechnology in Nuclear Medicine," Journal of Nuclear Medicine, 48, pp. 1039-1042.

[56] Rosshirt, M., Fabris, D., Cardenas, C., Wilhite, P., Tu, T., and Yang, C. Y., 2009, "Comparison of Carbon-Based Nanostructures with Commercial Products as Thermal Interface Materials," MRS Proceedings, 1158, pp. 1.

[57] De Volder, M. F., Tawfick, S. H., Baughman, R. H., and Hart, A. J., 2013, "Carbon Nanotubes: Present and Future Commercial Applications," science, 339, pp. 535-539.

[58] Kelly, B., 1981, *Physics of Graphite*, Applied Science, London.

[59] Ma, F., Zeng, Y., Wang, J., Yang, Y., Yang, X., and Zhang, X., 2012, "Thermogravimetric Study and Kinetic Analysis of Fungal Pretreated Corn Stover Using the Distributed Activation Energy Model," Bioresource Technology, 128, pp. 417-422.

[60] Solé, A., Miró, L., Barreneche, C., Martorell, I., and Cabeza, L. F., 2013, "Review of the T-History Method to Determine Thermophysical Properties of Phase Change Materials (Pcm)," Renewable and Sustainable Energy Reviews, 26, pp. 425-436.

[61] Agyenim, F., Hewitt, N., Eames, P., and Smyth, M., 2010, "A Review of Materials, Heat Transfer and Phase Change Problem Formulation for Latent Heat Thermal Energy Storage Systems (Lhtess)," Renewable and Sustainable Energy Reviews, 14, pp. 615-628.

[62] Prakash, J., Garg, H., and Datta, G., 1985, "A Solar Water Heater with a Built-in Latent Heat Storage," Energy conversion and management, 25, pp. 51-56.

[63] Esen, M., Durmuş, A., and Durmuş, A., 1998, "Geometric Design of Solar-Aided Latent Heat Store Depending on Various Parameters and Phase Change Materials," Solar Energy, 62, pp. 19-28.

[64] Selman, J. R., Al Hallaj, S., Uchida, I., and Hirano, Y., 2001, "Cooperative Research on Safety Fundamentals of Lithium Batteries," Journal of power sources, 97, pp. 726-732.

[65] Arcaklıoğlu, E., Çavuşoğlu, A., and Erişen, A., 2005, "An Algorithmic Approach Towards Finding Better Refrigerant Substitutes of Cfcs in Terms of the Second Law of Thermodynamics," Energy conversion and management, 46, pp. 1595-1611.

[66] Özkaymak, M., Kurt, H., and Recebli, Z., 2008, "Thermo-Economic Optimization of Superheating and Sub-Cooling Heat Exchangers in Vapor-Compressed Refrigeration System," International Journal of Energy Research, 32, pp. 634-647.

[67] Dincer, I., and Rosen, M. A., 2012, *Exergy: Energy, Environment and Sustainable Development*, Newnes,

[68] Weiller, C., 2011, "Plug-in Hybrid Electric Vehicle Impacts on Hourly Electricity Demand in the United States," Energy Policy, 39, pp. 3766-3778.

[69] Doucette, R. T., and Mcculloch, M. D., 2011, "Modeling the Prospects of Plug-in Hybrid Electric Vehicles to Reduce Co< Sub> 2</Sub> Emissions," Applied Energy, 88, pp. 2315-2323.

[70] Samaras, C., and Meisterling, K., 2008, "Life Cycle Assessment of Greenhouse Gas Emissions from Plug-in Hybrid Vehicles: Implications for Policy," Environmental Science & Technology, 42, pp. 3170-3176.

[71] Doyle, M., Fuller, T. F., and Newman, J., 1993, "Modeling of Galvanostatic Charge and Discharge of the Lithium/Polymer/Insertion Cell," Journal of the Electrochemical Society, 140, pp. 1526-1533.

[72] Pals, C. R., and Newman, J., 1995, "Thermal Modeling of the Lithium/Polymer Battery. I. Discharge Behavior of a Single Cell," Journal of the Electrochemical Society, 142, pp. 3274-3281.

[73] Pals, C. R., and Newman, J., 1995, "Thermal Modeling of the Lithium/Polymer Battery. Ii. Temperature Profiles in a Cell Stack," Journal of the Electrochemical Society, 142, pp. 3282-3288.

[74] Al Hallaj, S., Prakash, J., and Selman, J., 2000, "Characterization of Commercial Li-Ion Batteries Using Electrochemical–Calorimetric Measurements," Journal of power sources, 87, pp. 186-194.

[75] Rao, L., and Newman, J., 1997, "Heat-Generation Rate and General Energy Balance for Insertion Battery Systems," Journal of The Electrochemical Society, 144, pp. 2697-2704.

[76] Kelly, K., Mihalic, M., and Zolot, M., 2001, "Battery Usage and Thermal Performance of the Toyota Prius and Honda Insight for Various Chassis Dynamometer Test Procedures," Proceeding of the 17th Annual Battery Conference on Applications and Advances, pp. 1-6.

[77] Lee, J., Choi, K., Yao, N., and Christianson, C., 1986, "Three-Dimensional Thermal Modeling of Electric Vehicle Batteries," Journal of The Electrochemical Society, 133, pp. 1286-1291.

[78] Duan, X., and Naterer, G., 2010, "Heat Transfer in Phase Change Materials for Thermal Management of Electric Vehicle Battery Modules," International Journal of Heat and Mass Transfer, 53, pp. 5176-5182.

[79] Kizilel, R., Sabbah, R., Selman, J. R., and Al-Hallaj, S., 2009, "An Alternative Cooling System to Enhance the Safety of Li-Ion Battery Packs," Journal of Power Sources, 194, pp. 1105-1112.

[80] Kizilel, R., Lateef, A., Sabbah, R., Farid, M., Selman, J., and Al-Hallaj, S., 2008, "Passive Control of Temperature Excursion and Uniformity in High-Energy Li-Ion Battery Packs at High Current and Ambient Temperature," Journal of Power Sources, 183, pp. 370-375.

[81] Sabbah, R., Kizilel, R., Selman, J., and Al-Hallaj, S., 2008, "Active (Air-Cooled) Vs. Passive (Phase Change Material) Thermal Management of High Power Lithium-Ion Packs: Limitation of

Temperature Rise and Uniformity of Temperature Distribution," Journal of Power Sources, 182, pp. 630-638.

[82] Jabardo, J., Mamani, W. G., and Ianella, M., 2002, "Modeling and Experimental Evaluation of an Automotive Air Conditioning System with a Variable Capacity Compressor," International Journal of Refrigeration, 25, pp. 1157-1172.

[83] Kaynaklı, Ö., and Horuz, I., 2003, "An Experimental Analysis of Automotive Air Conditioning System," International communications in heat and mass transfer, 30, pp. 273-284.

[84] Pesaran, A. A., 2001, "Battery Thermal Management in Ev and Hevs: Issues and Solutions," Battery Man, 43, pp. 34-49.

[85] Keller, A., and Whitehead, G., 1991, "Thermal Characteristics of Electric Vehicle Batteries. In: Electric Vehicle R & D," Technical Report No. 1560911727,

[86] Mi, C., Li, B., Buck, D., and Ota, N., 2007, "Advanced Electro-Thermal Modeling of Lithium-Ion Battery System for Hybrid Electric Vehicle Applications," Vehicle Power and Propulsion Conference, 2007. VPPC 2007. IEEE, pp. 107-111.

[87] Bernardi, D., Pawlikowski, E., and Newman, J., 1985, "A General Energy Balance for Battery Systems," Journal of the Electrochemical Society, 132, pp. 5-12.

[88] Krein, P. T., 2007, "Battery Management for Maximum Performance in Plug-in Electric and Hybrid Vehicles," pp. 2-5.

[89] Van Mierlo, J., Maggetto, G., and Lataire, P., 2006, "Which Energy Source for Road Transport in the Future? A Comparison of Battery, Hybrid and Fuel Cell Vehicles," Energy Conversion and Management, 47, pp. 2748-2760.

[90] Farid, M. M., Khudhair, A. M., Razack, S. a. K., and Al-Hallaj, S., 2004, "A Review on Phase Change Energy Storage: Materials and Applications," Energy conversion and management, 45, pp. 1597-1615.

[91] Zalba, B., MaríN, J. M., Cabeza, L. F., and Mehling, H., 2003, "Review on Thermal Energy Storage with Phase Change: Materials, Heat Transfer Analysis and Applications," Applied thermal engineering, 23, pp. 251-283.

[92] Trp, A., 2005, "An Experimental and Numerical Investigation of Heat Transfer During Technical Grade Paraffin Melting and Solidification in a Shell-and-Tube Latent Thermal Energy Storage Unit," Solar energy, 79, pp. 648-660.

[93] Quanying, Y., Chen, L., and Lin, Z., 2008, "Experimental Study on the Thermal Storage Performance and Preparation of Paraffin Mixtures Used in the Phase Change Wall," Solar Energy Materials and Solar Cells, 92, pp. 1526-1532.

[94] Hong, J. S., Maleki, H., Al Hallaj, S., Redey, L., and Selman, J., 1998, "Electrochemical-Calorimetric Studies of Lithium-Ion Cells," Journal of the Electrochemical Society, 145, pp. 1489-1501.

[95] Doughty, D. H., Butler, P. C., Jungst, R. G., and Roth, E. P., 2002, "Lithium Battery Thermal Models," Journal of power sources, 110, pp. 357-363.

[96] Wu, M.-S., Liu, K., Wang, Y.-Y., and Wan, C.-C., 2002, "Heat Dissipation Design for Lithium-Ion Batteries," Journal of power sources, 109, pp. 160-166.

[97] Saito, Y., Takano, K., and Negishi, A., 2001, "Thermal Behaviors of Lithium-Ion Cells During Overcharge," Journal of power sources, 97, pp. 693-696.

[98] Bellecci, C., and Conti, M., 1993, "Phase Change Thermal Storage: Transient Behaviour Analysis of a Solar Receiver/Storage Module Using the Enthalpy Method," International journal of heat and mass transfer, 36, pp. 2157-2163.

[99] Akgün, M., Aydın, O., and Kaygusuz, K., 2008, "Thermal Energy Storage Performance of Paraffin in a Novel Tube-in-Shell System," Applied Thermal Engineering, 28, pp. 405-413.

[100] Trp, A., Lenic, K., and Frankovic, B., 2006, "Analysis of the Influence of Operating Conditions and Geometric Parameters on Heat Transfer in Water-Paraffin Shell-and-Tube Latent Thermal Energy Storage Unit," Applied Thermal Engineering, 26, pp. 1830-1839.

[101] Sarı, A., and Karaipekli, A., 2007, "Thermal Conductivity and Latent Heat Thermal Energy Storage Characteristics of Paraffin/Expanded Graphite Composite as Phase Change Material," Applied Thermal Engineering, 27, pp. 1271-1277.

[102] Mazman, M., Cabeza, L. F., Mehling, H., Paksoy, H. Ö., and Evliya, H., 2008, "Heat Transfer Enhancement of Fatty Acids When Used as Pcms in Thermal Energy Storage," International Journal of Energy Research, 32, pp. 135-143.

[103] Vyshak, N., and Jilani, G., 2007, "Numerical Analysis of Latent Heat Thermal Energy Storage System," Energy conversion and management, 48, pp. 2161-2168.

[104] Ettouney, H., Alatiqi, I., Al-Sahali, M., and Al-Hajirie, K., 2006, "Heat Transfer Enhancement in Energy Storage in Spherical Capsules Filled with Paraffin Wax and Metal Beads," Energy conversion and management, 47, pp. 211-228.

[105] Py, X., Olives, R., and Mauran, S., 2001, "Paraffin/Porous-Graphite-Matrix Composite as a High and Constant Power Thermal Storage Material," International Journal of heat and mass transfer, 44, pp. 2727-2737.

[106] Foli, K., Okabe, T., Olhofer, M., Jin, Y., and Sendhoff, B., 2006, "Optimization of Micro Heat Exchanger: Cfd, Analytical Approach and Multi-Objective Evolutionary Algorithms," International Journal of Heat and Mass Transfer, 49, pp. 1090-1099.

[107] Sanaye, S., and Hajabdollahi, H., 2010, "Multi-Objective Optimization of Shell and Tube Heat Exchangers," Applied Thermal Engineering, 30, pp. 1937-1945.

[108] Fukai, J., Kanou, M., Kodama, Y., and Miyatake, O., 2000, "Thermal Conductivity Enhancement of Energy Storage Media Using Carbon Fibers," Energy Conversion and Management, 41, pp. 1543-1556.

[109] Maxwell, J. C., 1904, *Electricity and Magnetism, Part 2*, Clarendon Press, United Kingdom.

[110] Shaikh, S., Lafdi, K., and Hallinan, K., 2008, "Carbon Nanoadditives to Enhance Latent Energy Storage of Phase Change Materials," Journal of Applied Physics, 103, pp. 094302-094308.

[111] Kumaresan, V., Velraj, R., and Das, S. K., 2012, "The Effect of Carbon Nanotubes in Enhancing the Thermal Transport Properties of Pcm During Solidification," Heat and Mass Transfer/Waerme- und Stoffuebertragung, 48, pp. 1345-1355.

[112] S. Alquaity, A., Al-Dini, S., and Yilbas, B., 2012, "Entropy Generation in Microchannel Flow with Presence of Nanosized Phase Change Particles," Journal of Thermophysics and Heat Transfer, 26, pp. 134-140.

[113] Zhang, G., and Zhao, C., 2013, "Thermal Property Investigation of Aqueous Suspensions of Microencapsulated Phase Change Material and Carbon Nanotubes as a Novel Heat Transfer Fluid," Renewable Energy, 60, pp. 433-438.

[114] Amama, P. B., Cola, B. A., Sands, T. D., Xu, X., and Fisher, T. S., 2007, "Dendrimer-Assisted Controlled Growth of Carbon Nanotubes for Enhanced Thermal Interface Conductance," Nanotechnology, 18, pp. 385303.

[115] Tong, T., Zhao, Y., Delzeit, L., Kashani, A., Meyyappan, M., and Majumdar, A., 2007, "Dense Vertically Aligned Multiwalled Carbon Nanotube Arrays as Thermal Interface Materials," Components and Packaging Technologies, IEEE Transactions on, 30, pp. 92-100.

[116] Hamut, H., Dincer, I., and Naterer, G., 2012, "Exergy Analysis of a Tms (Thermal Management System) for Range-Extended Evs (Electric Vehicles)," Energy, 46, pp. 117-125.

[117] Hamut, H., Dincer, I., and Naterer, G., 2013, "Performance Assessment of Thermal Management Systems for Electric and Hybrid Electric Vehicles," International Journal of Energy Research, 37, pp. 1-12.

[118] Ahmadi, P., Dincer, I., and Rosen, M. A., 2011, "Exergy, Exergoeconomic and Environmental Analyses and Evolutionary Algorithm Based Multi-Objective Optimization of Combined Cycle Power Plants," Energy, 36, pp. 5886-5898.

[119] Endo, T., Kawajiri, S., Kojima, Y., Takahashi, K., Baba, T., Ibaraki, S., and Takahashi, T., 2007, "Study on Maximizing Exergy in Automotive Engines," SAE World Congress & Exhibition, pp. 2007-01-0257.

[120] Li, H., 2001, *Optimization of an Automotive Cooling System Based on Exergy and Energy Analysis*, Clemson University,

[121] Figliola, R., Tipton, R., and Li, H., 2003, "Exergy Approach to Decision-Based Design of Integrated Aircraft Thermal Systems," Journal of aircraft, 40, pp. 49-55.

[122] Ansys Inc., 2009, *Ansys Fluent 12.0.1 User's Guide.*

[123] Keyser, M. A., Pesaran, A., Mihalic, M., Yu, J.-S., Kim, S.-R., Alamgir, M., and Rivers, D., 2003, "Thermal Characterization of Advanced Lithium-Ion Polymer Cells," Third Advanced Automotive Battery Conference, pp. 1-6.

[124] Keyser, M., Mihalic, M., Pesaran, A., and Rivers, D., 2007,

[125] Malalasekra, W., 2007, *An Introduction to Computational Fluid Dynamics: The Finite Volume Method*, Pearson Education UK,

[126] Ramandi, M. Y., 2012, "Numerical Modeling of Transient Transport Phenomena in Molten Carbonate Fuel Cells," Ph.D. thesis, University of Ontario Institute of Technology,

[127] Shah, R. K., Sekulic P., 2003, *Fundamental of Heat Exchanger Design*, John Wiley & Sons, Inc.,

[128] Caputo, A. C., Pelagagge, P. M., and Salini, P., 2008, "Heat Exchanger Design Based on Economic Optimisation," Applied Thermal Engineering, 28, pp. 1151-1159.

[129] Kakac, and Liu, 2000, *Heat Exchangers Selection Rating, and Thermal Design*, CRC Press, New York.

[130] Ghaffarizadeh, A., 2006, "Investigation on Evolutionary Algorithms Emphasizing Mass Extinction," Ph.D. thesis, B. Sc. Thesis, Shiraz University of Technology-Shiraz, Iran,

[131] Goldberg, D., 1989, "Genetic Algorithms in Optimization, Search and Machine Learning," Addison Wesley, New York. Eiben AE, Smith JE (2003) Introduction to Evolutionary Computing. Springer. Jacq J, Roux C (1995) Registration of non-segmented images using a genetic algorithm. Lecture notes in computer science, 905, pp. 205-211.

[132] Holland, J. H., 1992, *Adaption in Natural and Artificial Systems*, The MIT Press, London.

[133] Dincer, I., 2007, "Environmental and Sustainability Aspects of Hydrogen and Fuel Cell Systems," International Journal of Energy Research, 31, pp. 29-55.

[134] Yumrutaş, R., Kunduz, M., and Kanoğlu, M., 2002, "Exergy Analysis of Vapor Compression Refrigeration Systems," Exergy, an International Journal, 2, pp. 266-272.

[135] Dincer, I., and Kanoglu, M., 2011, *Refrigeration Systems and Applications*, Wiley. com,

[136] Bejan, A., 1997, *Thermodynamic Optimization of Heat Transfer and Fluid Flow Processes*, Cambridge University Press, UK.

[137] Javani, N., Dincer, I., and Naterer, G., 2012, "Thermodynamic Analysis of Waste Heat Recovery for Cooling Systems in Hybrid and Electric Vehicles," Energy, 46, pp. 109-116.

[138] Sonntag, R. E., Borgnakke, C., Van Wylen, G. J., and Van Wyk, S., 1998, *Fundamentals of Thermodynamics*, Wiley New York,

[139] Selbaş, R., Kızılkan, Ö., and Şencan, A., 2006, "Thermoeconomic Optimization of Subcooled and Superheated Vapor Compression Refrigeration Cycle," Energy, 31, pp. 2108-2128.

[140] Tsatsaronis, G., and Lin, L., 1990, "On Exergy Costing in Exergoeconomics," 21, pp. 1-11.

[141] Lazzaretto, A., and Tsatsaronis, G., 2006, "Speco: A Systematic and General Methodology for Calculating Efficiencies and Costs in Thermal Systems," Energy, 31, pp. 1257-1289.

[142] Bejan, A., and Moran, M. J., 1996, *Thermal Design and Optimization*, Wiley, New Jersey.

[143] Abusoglu, A., and Kanoglu, M., 2009, "Exergetic and Thermoeconomic Analyses of Diesel Engine Powered Cogeneration: Part 1–Formulations," Applied Thermal Engineering, 29, pp. 234-241.

[144] Valero, A., Lozano, M. A., Serra, L., Tsatsaronis, G., Pisa, J., Frangopoulos, C., and Von Spakovsky, M. R., 1994, "Cgam Problem: Definition and Conventional Solution," Energy, 19, pp. 279-286.

[145] Sanaye, S., and Niroomand, B., 2009, "Thermal-Economic Modeling and Optimization of Vertical Ground-Coupled Heat Pump," Energy Conversion and Management, 50, pp. 1136-1147.

[146] Al-Otaibi, D., Dincer, I., and Kalyon, M., 2004, "Thermoeconomic Optimization of Vapor-Compression Refrigeration Systems," International communications in heat and mass transfer, 31, pp. 95-107.

[147] Hensley, R., Newman, J., and Rogers, M., 2012, Battery Technology Charges Ahead, August 2013, http://www.mckinsey.com/insights/energy_resources_materials/battery_technology_charges_ahead

[148] Peterson, R., 2012, Chevrolet Volt Math Everybody Can Understand, Sept. 2012, http://www.chevroletvoltage.com

[149] Leibson, S., 2012, Driving the Chevy Volt, August 2013, http://low-powerdesign.com/sleibson/2012/08/04/driving-the-chevy-volt/

[150] Wang, S., Gu, J., Dickson, T., Dexter, J., and Mcgregor, I., 2005, "Vapor Quality and Performance of an Automotive Air Conditioning System," Experimental Thermal and Fluid Science, 30, pp. 59-66.

[151] Schaffer, J. D., 1985, "Multiple Objective Optimization with Vector Evaluated Genetic Algorithms," Proceedings of the 1st international Conference on Genetic Algorithms, pp. 93-100.

[152] Srinivas, N., and Deb, K., 1994, "Muiltiobjective Optimization Using Nondominated Sorting in Genetic Algorithms," Evolutionary computation, 2, pp. 221-248.

[153] Deb, K., Pratap, A., Agarwal, S., and Meyarivan, T., 2002, "A Fast and Elitist Multiobjective Genetic Algorithm: Nsga-Ii," Evolutionary Computation, IEEE Transactions on, 6, pp. 182-197.

[154] Deb, K., and Goel, T., 2001, "Controlled Elitist Non-Dominated Sorting Genetic Algorithms for Better Convergence," Evolutionary Multi-Criterion Optimization, pp. 67-81.

[155] Deb, K., 2001, "Multi-Objective Optimization," Multi-objective optimization using evolutionary algorithms, pp. 13-46.

[156] Sayyaadi, H., and Mehrabipour, R., 2012, "Efficiency Enhancement of a Gas Turbine Cycle Using an Optimized Tubular Recuperative Heat Exchanger," Energy, 38, pp. 362-375.

[157] Amrollahi, A., Hamidi, A., and Rashidi, A., 2008, "The Effects of Temperature, Volume Fraction and Vibration Time on the Thermo-Physical Properties of a Carbon Nanotube Suspension (Carbon Nanofluid)," Nanotechnology, 19, pp. 315701.

[158] Bayramoglu, E. Ç. L., 2011, "Thermal Properties and Stability of N-Octadecane Based Composites Containing Multiwalled Carbon Nanotubes," Polymer Composites, 32, pp. 904-909.

[159] Chen, G., 1998, "Thermal Conductivity and Ballistic-Phonon Transport in the Cross-Plane Direction of Superlattices," Physical Review B, 57, pp. 14958.

[160] Strauss, M. T., and Pober, R. L., 2006, "Nanotubes in Liquids: Effective Thermal Conductivity," Journal of applied physics, 100, pp. 084328-084328-9.

[161] Dayco, I., Integral High-Finned Copper Tube, July 2013, http://www.daycoindustries.com/pdfs/CopperHiFinnedTubing.pdf

[162] Hepbasli, A., Erbay, Z., Icier, F., Colak, N., and Hancioglu, E., 2009, "A Review of Gas Engine Driven Heat Pumps (Gehps) for Residential and Industrial Applications," Renewable and Sustainable Energy Reviews, 13, pp. 85-99.

[163] Lee, C., Cho, S., Hwang, Y., Lee, J., Lee, B., Park, J., and Jung, J., 2007, "Effects of Nano-Lubricants on the Friction and Wear Characteristics at Thrust Slide-Bearing of Scroll Compressors," International Congress of Refrigeration, Paris, pp. ICR07-B2-1014.

[164] Behr, http://www.behrgroup.com/Internet/behrcms_eng.nsf

[165] Kumar, S., Prevost, M., and Bugarel, R., 1989, "Exergy Analysis of a Compression Refrigeration System," Heat Recovery Systems and CHP, 9, pp. 151-157.

[166] Arora, A., and Kaushik, S., 2008, "Theoretical Analysis of a Vapour Compression Refrigeration System with R502, R404a and R507a," International journal of refrigeration, 31, pp. 998-1005.

[167] Hosoz, M., and Direk, M., 2006, "Performance Evaluation of an Integrated Automotive Air Conditioning and Heat Pump System," Energy Conversion and Management, 47, pp. 545-559.

[168] Yang, C., and Mccarthy, R., 2009, Electricity Grid: Impacts of Plug-in Electric Vehicle Charging, June 2013,

[169] Camirand, C. P., 2004, "Measurement of Thermal Conductivity by Differential Scanning Calorimetry," Thermochimica Acta, 417, pp. 1-4.

[170] Bejan, A., Lorente, S., Yilbas, B., and Sahin, A., 2013, Why Solidification Has an S-Shaped History, http://www.nature.com/srep/2013/130424/srep01711/full/srep01711.html

[171] Sun, L., Siepmann, J. I., and Schure, M. R., 2007, "Monte Carlo Simulations of an Isolated N-Octadecane Chain Solvated in Water-Acetonitrile Mixtures," Journal of Chemical Theory and Computation, 3, pp. 350-357.